THE TRANSACTIONS OF

The Royal Institution of Naval Architects

Vol 160 Part A2 2018

International Journal of Maritime Engineering

The Transactions of The Royal Institution of Naval Architects – Part A

International Journal of Maritime Engineering

The International Journal of Maritime Engineering (IJME) provides a forum for the reporting and discussion on technical and scientific issues associated with the design and construction of marine vessels and offshore structures. The IJME is published four times a year as Part A of the Transactions of The Royal Institution of Naval Architects. Contributions in the form of scientific and technical papers and notes on all aspects of maritime engineering, together with comment on published papers are welcomed.

PAPERS

Papers may introduce new theory or evaluate existing theory, or describe experimental or novel practical work, Papers presenting case histories will report on new or existing techniques, including design and production. Papers may also provide literary reviews which appraise and evaluate published work. All papers are refereed.

TECHNICAL NOTES

Technical notes will provide early announcement of new ideas, findings, procedures, applications, interim results, etc., which might later on form part of a full paper. Technical notes are refereed as for papers, but due allowance will be made for their immediate nature.

DISCUSSION

Comments on papers and technical notes will normally be published in the first available issue of the *IJME* following that in which the paper was published. Discussion may be continued in subsequent issues, at the discretion of the Editor. Authors will be invited to respond to published comment.

ISSN 1479-8751

The Transactions of The Royal Institution of Naval Architects

Vol 160 Part A2 2018 **ISSN 1479-8751**

International Journal of Maritime Engineering

CONTENTS

PAPERS

TECHNICAL NOTES

There are no Technical Notes published in this issue of IJME

DISCUSSION

Trans RINA, Vol 160, Part A2, Intl J Maritime Eng, Apr-Jun 2018

AN EXPERIMENTAL STUDY OF SHIP MOTIONS DURING REPLENISHMENT AT SEA OPERATIONS BETWEEN A SUPPLY VESSEL AND A LANDING HELICOPTER DOCK

(DOI No: 10.3940/rina.ijme.2018.a2.427)

J Mathew and **D Sgarioto**, Defence Science Technology, Australia, **J Duffy, G Macfarlane, S Denehy, J Norman, A Cameron, N Eutick,** University of Tasmania Australian Maritime College, Australia and **F van Walree,** Maritime Research Institute Netherlands, Netherlands

SUMMARY

Hydrodynamic interactions during Replenishment at Sea (RAS) operations can lead to large ship motions and make it difficult for vessels to maintain station during the operation. A research program has been established which aims to validate numerical seakeeping tools to enable the development of enhanced operator guidance for RAS. This paper presents analysis of the first phase of scale model experiments and focuses on the influence that both the lateral and longitudinal separations between two vessels have on the interactions during RAS. The experiments are conducted in regular head seas on a Landing Helicopter Dock (LHD) and a Supply Vessel (SV) in intermediate water depth. The SV is shorter than the LHD by approximately 17%, but due to its larger block coefficient, it displaces almost 16% more than the LHD. Generally, the motions of the SV were larger than the LHD. It was found that hydrodynamic interactions can lead to large SV roll motions in head seas. Directions for future work are provided.

NOMENCLATURE

B_{OA}	Beam overall
C_B	Block coefficient
COs	Commanding officers
DOF	Degree of freedom
Fr	Froude length number
GM_T	Transverse metacentric height
h	Water depth
k	Wave number
K_{xx}	Roll radius of gyration
K_{yy}	Pitch radius of gyration
K_{zz}	Yaw radius of gyration
LCG	Longitudinal centre of gravity
LHD	Landing helicopter dock
L_{OA}	Length overall
L_{PP}	Length between perpendiculars
MS	Midships
T_{AP}	Draft at aft perpendicular
TCG	Transverse centre of gravity
T_{FP}	Draft at forward perpendicular
R	Scale ratio
RAS	Replenishment at sea
SV	Supply vessel
v	Vessel speed
VCG	Vertical centre of gravity
z	Heave
Δ	Displacement
θ	Pitch angle
ϕ	Roll angle
ω_e	Encounter wave frequency
ω_w	Incident wave frequency
λ	Wave length
ζ_a	Wave amplitude
μ	Incident wave direction (180°, Head seas)
σ	Standard deviation

1. INTRODUCTION

Replenishment at Sea (RAS) is a critical capability for all modern navies as it allows vessels to be deployed for extended periods away from home ports. RAS operations typically involve the transfer of fuel, supplies and/or personnel between vessels operating in close proximity at moderate forward speeds (approximately 12 to 16 knots). The vessels travel alongside one another on parallel paths with lateral separations typically ranging between 20 to 60 m (inner side to inner side). Due to the close proximity of the vessels, hydrodynamic interaction loads develop between the hull forms. These loads impact upon both the motions and manoeuvring capability of the vessels.

Hydrodynamic interactions can cause vessels to be drawn into or pushed away from one another, making it difficult for vessels to maintain the desired heading, speed and lateral (transverse) and longitudinal separations in RAS operations. Interactions can also lead to large vessel motions, which can inhibit the crew's ability to conduct the operation safely. Excessive relative motions may cause the lines passed between vessels to break posing a significant risk to the safety of the crew on deck. In the case of replenishment of solid supplies, large relative motions can result in the payload dipping into the water. Increased wave heights between the vessels, due to interactions, also increases the risk of payload submergence and deck wetness. The hydrodynamic interaction loads are highly dependent on the amplitude, encounter angle and frequency of the incident waves as well as the ship speed and load conditions.

Hydrodynamic interactions are unavoidable during RAS operations. Commanding Officers (COs) therefore look to identify a 'sweet spot' operationally, where minimal rudder inputs are required to allow the vessels to safely maintain station for the duration of the operation. This 'sweet spot' will be different for each RAS operation based on the wave environment, the relative size and shape of the vessels involved and their loading conditions. Giving consideration to all these factors the COs need to determine the most appropriate replenishment speed, heading and vessel separation distance (both lateral and longitudinal) at which to conduct RAS. COs are generally required to make these decisions based mainly on experience as existing operational guidance for RAS is limited and quite general in nature.

Defence Science and Technology (DST) are currently undertaking a research program into multi-vessel hydrodynamic interactions during RAS. This program aims to validate numerical seakeeping tools that will enable the development of enhanced operator guidance for the Royal Australian Navy (RAN) during RAS operations. There is very limited experimental data available in the open literature that can be used to validate these tools for RAS.

DST and the Australian Maritime College (AMC), a specialist institute of the University of Tasmania, have setup a collaborative research project to obtain the experimental dataset required to validate the numerical tools. RAS operations between a Landing Helicopter Dock (LHD) and a Supply Vessel (SV) have been selected as a case study for validation. RAS operations between these vessels are of particular interest to the RAN given that the LHD is much larger than any other RAN vessel that would typically receive replenishment. The SV is shorter than the LHD by approximately 17%, but due to its larger block coefficient, it displaces almost 16% more than the LHD. Figure 1 illustrates the roll motion experienced by the supply vessel HMAS Sirius when conducting RAS operations with the LHD HMAS Canberra, during first of class acceptance trials.

Figure 1: RAS operation between HMAS Canberra and HMAS Sirius during the LHD’s first of class acceptance trials [1]

This paper presents results of the first phase of scale model experiments investigating the influence of the lateral and longitudinal separation between vessels in regular head seas on the resulting hydrodynamic interactions.

2. LITERATURE REVIEW

In calm water, the interaction forces, moments and motions are predominantly dependent on the vessel geometry, the vessel speed and the relative longitudinal and lateral positions of the vessels. The influence of the interaction between the calm water wave patterns from the vessels will vary depending on the above factors. In waves, the forces, moments and motions are also dependent on the incident wave height and frequency, encountering angle, the interaction between the diffracted waves, the radiated waves due to the ship motions as well as the calm water wave patterns. Traditionally, RAS interactions have been investigated using numerical techniques, physical model scale experiments and, to a lesser extent, full scale trials.

The problem of hydrodynamic interactions between vessels operating in close proximity has been investigated numerically using potential flow solvers, in calm water Skejic *et al.* (2009); Skejic and Berg (2010); Fonfach *et al.* (2011) and also in waves Chen and Fang (2001); Rafiqul Islam and Murai (2013); von Graefe *et al.* (2015); Yuan *et al.* (2015); Thomas et al. (2010); Yuan *et al.* (2016); Kashiwagi *et al*. (2005). The applicability of these simulation techniques to the analysis of hydrodynamic interactions is limited due to the lack of viscosity in the numerical models.

To inform the design of the scale model experiments presented in this paper Mathew *et al.* (2016) made use of a frequency domain 3D panel method tool. This study highlighted the importance of applying appropriately tuned artificial damping to the free surface between vessels when using such codes. McTaggart and Turner (2006) also used a 3D panel method to investigate interaction forces and moments on ships during RAS in the frequency domain. This study included the prediction of viscous forces based on the work of Schmitke (1978) and Himeno (1981).

RANS simulations have been conducted to capture viscous effects in both calm water Sadat-Hosseini *et al.* (2011); Fonfach *et al.* (2011) and in waves Mousaviraad *et al.* (2016). RANS simulation methods offer significant advantages for the analysis of hydrodynamic interactions. These techniques however, remain highly computationally expensive.

Lataire *et al.* (2009) conducted semi-captive physical model scale experiments in calm, shallow water to investigate interaction between an Aframax tanker and a Very Large Crude Carrier (VLCC) with operating propellers during a lightering operation. It was found that the interaction forces and moments were significantly influenced by the ship speed and the relative longitudinal and lateral positions of the vessels.

The interaction between ships operating in regular waves was investigated by McTaggart *et al.* (2003). Head sea tests were conducted on a frigate and supply ship at speeds up to 12 knots at one lateral separation and two longitudinal separations. Zero forward speed tests were also conducted at 120 and 150 degrees encountering angles. It was found that the presence of the larger ship significantly influenced the motions of the smaller ship operating in close proximity.

Thomas et al. (2010) conducted experiments on a frigate and supply tanker undergoing RAS in head seas. This study focussed on the influence of the longitudinal separation between vessel and supply vessel displacement, on the resulting ship motions. Increasing the supply vessel displacement significantly increased the frigate roll response. Whereas, increasing the longitudinal separation (frigate aft of the supply vessel) reduced the motions of the frigate. Andrewartha *et al.* (2007) performed head sea semi-captive model tests on a generic frigate and a larger supply vessel. It was found that the roll, pitch and heave motions of the frigate were strongly influenced by the relative longitudinal and lateral position of the vessels.

Mousaviraad *et al.* (2016) considered the problem of hydrodynamic interactions more generally and reported on semi-captive model tests in deep calm water and regular waves for headings ranging from following to head seas. The longitudinal and lateral positions of the vessels were also varied.

Quadvlieg *et al.* (2011) conducted free sailing model scale experiments in waves using a variety of ship models. It was observed that the entrapped waves between the vessels had a significant influence on the behaviour of the vessels. Full scale trials were also conducted in the Gulf of Mexico.

Physical scale model experiments specifically looking at hydrodynamic interactions during RAS, published in the open literature have typically considered the scenario where the supply vessel is significantly larger than the vessel being replenished. These experiments have also been typically limited to head seas with semi-captive models. To improve understanding of hydrodynamic interactions during RAS and enable validation of numerical tools for analysis of this problem the available experimental dataset needs to be developed further.

3. PHYSICAL SCALE MODEL EXPERIMENTS

3.1 MODEL DETAILS

The experiments were conducted using 1:70 scale ship models of a LHD and a SV. The LHD was fitted with fore and aft bilge keels and ballasted to its full load condition. The SV did not have appendages fitted and was tested at its minimum operating condition. The two extreme loading conditions were chosen as they are expected to represent the worst-case scenario and were kept constant for the entire testing program. The SV was tested without appendages to provide a simplified benchmark case for validation.

Each model was constructed to standards defined by International Towing Tank Conference (ITTC) specifications for geometric tolerances and turbulence stimulation ITTC (2011). To obtain the correct model scale mass distribution, roll decay and inclining tests were performed iteratively. The model scale and full scale particulars are given in Table 1.

Table 1: Ship and Model Particulars

Particular	**LHD**		**SV**	
	Model Scale	**Full Scale**	**Model Scale**	**Full Scale**
L_{OA} (m)	3.30	230.8	2.73	191.3
B_{OA} (m)	0.43	29.9	0.44	31.0
L_{PP} (m)	2.96	207.2	2.4	168.0
T_{FP} (m)	0.10	7.10	0.10	7.18
T_{AP} (m)	0.10	7.10	0.12	8.38
Trim (m)	0.00	0.00	0.02	1.2
Δ	78.2 kg	27486 t	92.9 kg	32662 t
C_B	0.61	0.61	0.80	0.80
LCG (m)	1.43	100	1.27	88.58
VCG (m)	0.19	13.51	0.12	8.08
TCG (m)	0.0	0.0	0.0	0.0
GM_T (m)	0.05	3.72	0.09	6.33
K_{xx} (m)	0.20	13.9	0.16	11.55
K_{yy} (m)	0.76	53.7	0.63	43.82
K_{zz} (m)	0.76	53.7	0.63	43.82

3.2 EXPERIMENTAL SETUP

All tests were performed at the AMC's Model Test Basin (MTB). The MTB is 35 metres long, 12 metres wide and has a maximum depth of 1m. It has a multi-paddle, piston-type wave maker at one end and an artificial wave-dampening beach at the other.

The experiments used an overhead rail system, capable of towing the models at an equivalent full scale speed of 14 knots (Figure 2). Both models were attached to the overhead carriage using a two-post system, with a ball joint connection on the forward post and a ball joint and slide on the aft post. This arrangement allowed the models to freely heave, pitch and roll but constrained them in surge, sway and yaw. The posts were connected to each model on their centreline at heights corresponding to their respective vertical centre of gravity, allowing the presented data to be easily used for numerical validation purposes.

It is noted that constraining the models may induce motions that would not be experienced during an actual RAS operation. Since the centre of roll will move throughout the experiments based on the wetted hull surface, restraining the model to roll about the *VCG* will have some small influence on the measured roll motions. Similarly, a small artificial pitching moment will exist due to towing the models from above their thrust line. Numerical tools could be used to further investigate these affects by conducting simulations with the vessels constrained as in the model testing and a free sailing condition.

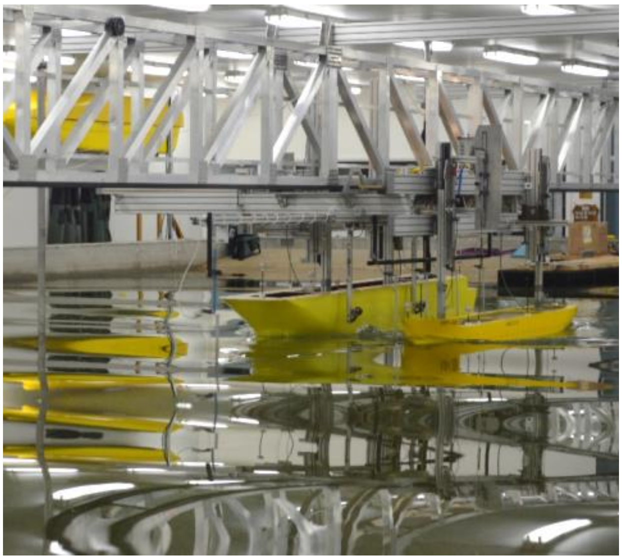

Figure 2: MTB and Testing Apparatus

3.3 INSTRUMENTATION

These experiments made use of the newly upgraded QUALISYS three-dimensional digital video motion tracking system in the MTB. This type of non-contact motion capture system offers a number of advantages for multi-vessel seakeeping experiments over the traditional the Linear Variable Differential Transformers (LVDTs). The non-contact sensors remove the potential for physical interference. They also provide flexibility in the design of the experimental test rig and simplify both the experimental setup and calibration process.

LVDTs were also used to independently measure the motions to provide benchmark data to assess the viability of the upgraded QUALISYS system for this type of multi-vessel experiment. LVDTs were mounted to the forward and aft posts of each model. To acquire roll motion data, a third LVDT was attached to each model on the outboard extremity, having the same longitudinal position as the forward LVDT.

Resistance type wave probes were used to measure the free surface elevation. Two static wave probes were used to capture the incident wave train properties and any dissipation or reflection of this wave over the length of the test basin. A third wave probe was mounted to the carriage forward of the models to measure the encountering waveform. All signals were recorded at a sample rate of 200 Hz.

To assist in understanding the interaction effects and free surface environment, three cameras were also attached to the carriage. Two were focused on the SV's waterline on the inner side of the model. The third camera was mounted forward of both models and aligned to monitor the overall free surface elevation in the gap between vessels.

3.4 TEST CONFIGURATIONS

The model experiments were conducted in regular head seas with a nominal model scale wave amplitude of 0.015 m, equivalent to 1.05 m full scale. The models were towed in parallel at a constant forward speed of 0.86 m/s model scale, equivalent to 14 knots full scale, which is a typical speed for RAS operations. This equates to a Froude Length Number (*Fr*) of approximately 0.16 for LHD and 0.18 for the SV.

Two lateral separations of 40 m and 60 m (full scale, inner side to inner side) were selected as they represent typical real-world separation distances for RAS operations involving two larger vessels (NATO Standardization Agency, 2001). Two longitudinal separations have been tested which represent alignment of a single RAS station on the SV with two RAS stations on the LHD. The longitudinal separations are 15.5 m and 58.9 m between vessels midships, with the SV forward of the LHD in both cases. A schematic of the vessel configurations in each test condition is provided in Figure 3.

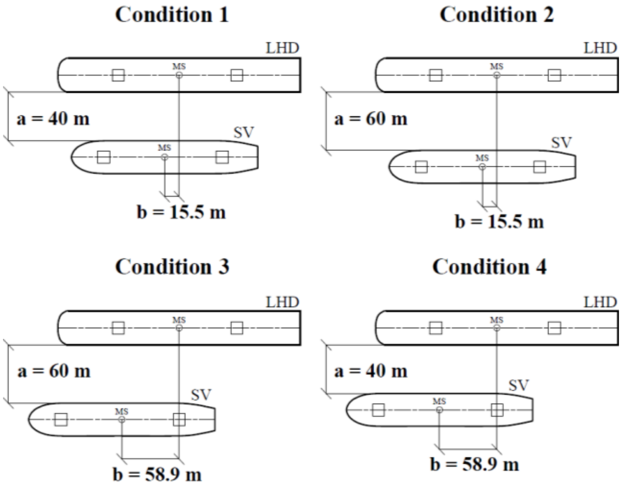

Figure 3: Lateral and longitudinal separations between vessels for each condition. Dimensions of the lateral separation are inner side to inner side and longitudinal separations are midships to midships. Full scale dimension shown in the schematic and model scale dimensions are summarised below:

Condition 1: a = 0.571 m, b = 0.221 m
Condition 2: a = 0.857 m, b = 0.221 m
Condition 3: a = 0.857 m, b = 0.841 m
Condition 4: a = 0.571 m, b = 0.841 m

The water depth in the MTB was 0.75 m for testing which is approximately 53 m at full scale. To avoid wave reflections in the dataset an appropriate time delay between the start of the wave maker and the start of the carriage was established for each wave frequency tested. The lowest practical circular wave frequency was found to be 2.95 rad/s model scale.

For all conditions tested, the circular wave frequency was varied between 2.95 and 6.41 rad/s model scale, equivalent to 0.35 and 0.77 rad/s full scale. Due to the limited water depth in the basin and the frequency range of interest, the majority of experiments were not undertaken in deep water ($h > \lambda/2$) Bhattacharyya (1978), but rather in intermediate water depths. Bottom effects are therefore present in the waves encountered by the models. When using this data to validate the chosen numerical tool it may be possible to account for the effects of the intermediate water depth waves in the simulations.

3.5 ROLL DECAY EXPERIMENTS

Free floating, calm water roll decay experiments were conducted for both vessels at zero speed. The experiments were undertaken in a water depth of 0.75 m and the roll displacement (ϕ), was measured using the non-contact QUALISYS motion capture system. To gauge the influence of the semi-captive test setup on the roll behaviour of the models, further calm water roll decay experiments were conducted for each of the models while attached to the carriage.

Example roll decay time series for both the free and semi-captive experiments are shown at full scale in Figure 4. The average natural roll frequencies in both the free and semi-captive arrangement are summarised in Table 2. The semi-captive natural roll frequency is lower than that of the free response for both vessels.

Table 2: Average full scale natural roll frequencies of the LHD and Supply Vessel

Natural Roll Frequency	**LHD**	**SV**
Free (rad/s)	0.436	0.705
Semi-captive(rad/s)	0.359	0.675

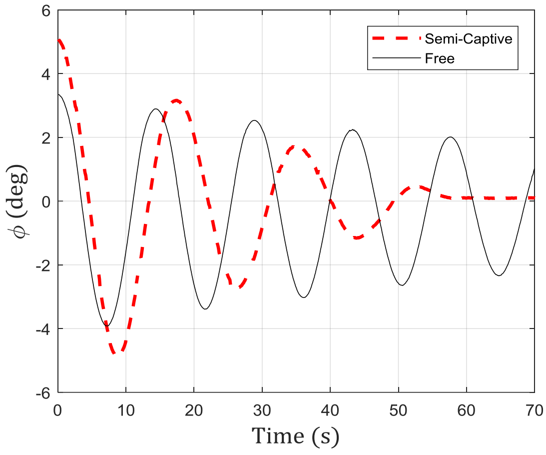

(a) LHD

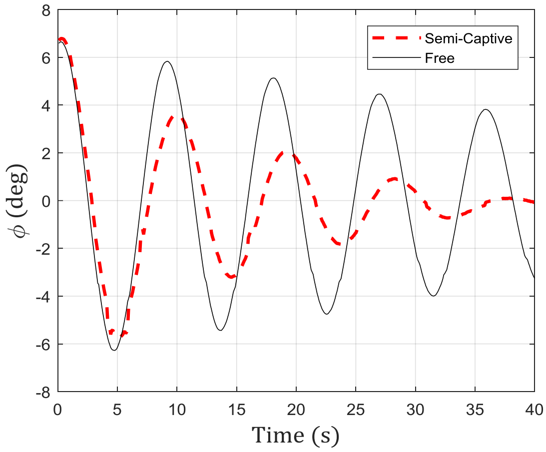

(b) SV

Figure 4: Examples of free and semi-captive roll decay time series

4. RESULTS AND DISCUSSION

The heave (z), roll (ϕ), and pitch (θ) motion responses of the vessels in regular waves are presented as a function of full scale encounter frequency. The motions are non-dimensionalised as per Equations 1-3, and the full scale encounter frequency is calculated as per Equation 4. The motion ordinates are calculated based on the standard deviation of the steady state portion of the time series. This approach has been used to account for the irregularity observed in some of the time domain motion traces. For cases where the water depth was classified as intermediate, the wave length was determined using the method presented by Fenton and McKee (1990).

$$Heave = \frac{\sigma_z}{\sigma_{\zeta_a}} \quad (1)$$

$$Roll = \frac{\sigma_\phi}{\sigma_{\zeta_a}.k} \quad (2)$$

$$Pitch = \frac{\sigma_\theta}{\sigma_{\zeta_a}.k} \quad (3)$$

$$\omega_e = \omega_w.\left(1 - \frac{\omega_w.v}{g}\cos(\mu)\right).\frac{1}{\sqrt{R}} \quad (4)$$

To investigate the influence of the relative vessel positions on the free surface elevation between vessels, a qualitative analysis of the calm water wave interactions between the vessels in each condition is made. This visual comparison is then extended to the wave interactions between vessels in head seas for two example cases.

4.1 QUALISYS AND LVDT COMPARISON

To obtain confidence in the use of the non-contact motion measuring system for this application, the motion results were benchmarked against that of the traditionally used LVDT arrangement. Figure 5 shows an example of the derived motion results based on the LVDT and Qualisys measurements, for the SV motion in Condition 3. The motion measurements from the two systems match closely in all cases. It is noted that there are some data points missing for the roll motion derived from the LVDT measurements. This is due to a technical issue encountered with one of the LVDTs. This issue was promptly identified and addressed during the experiments but due to time constraints it was decided not to re-run these cases. The heave and pitch motions derived from the LVDTs were not affected by this issues.

4.2 VESSEL MOTION RESPONSES

For each combination of lateral and longitudinal separation between vessels, the resulting heave (z), roll (ϕ) and pitch (θ) responses of the SV are shown in Figure 6. All results are presented at full scale, as a function of encounter frequency. Generally, the peak motion responses are larger for the SV than for the LHD. Therefore, the discussion focusses mainly on the SV motions. However, the LHD pitch response is shown in Figure 7 to illustrate that the lateral and longitudinal separation influence the motion response of the LHD and SV differently.

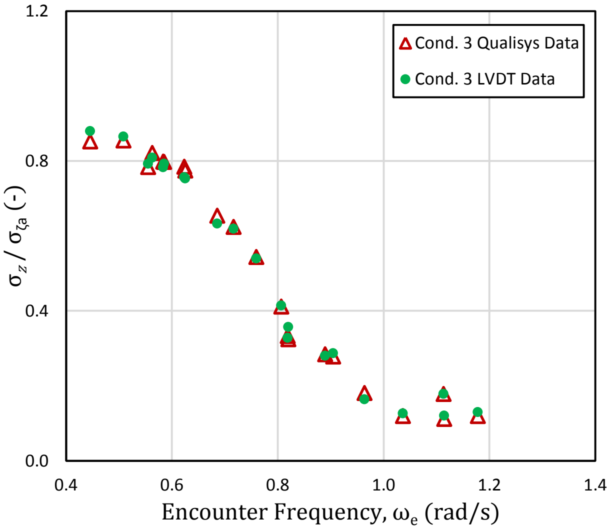

(a) Heave

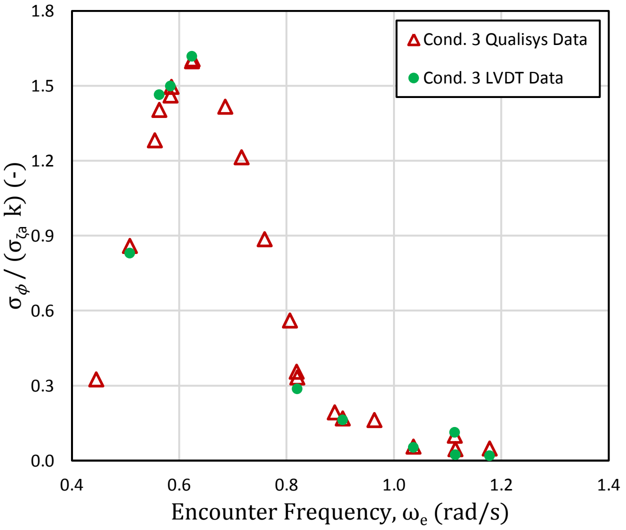

(b) Roll

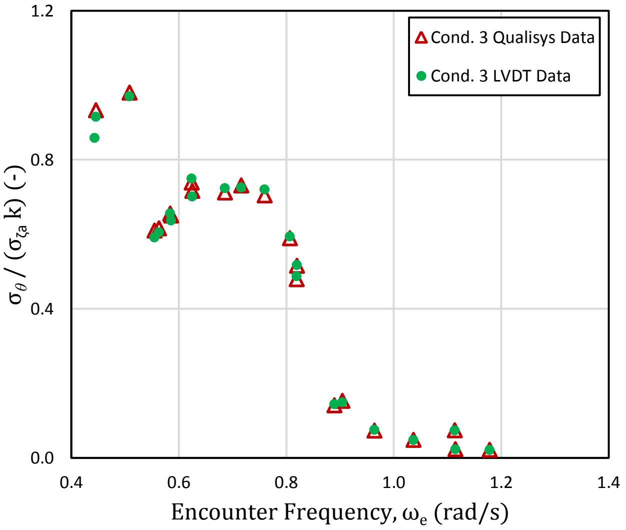

(c) Pitch

Figure 5: Non-dimensional motion responses resulting from Qualisys and LVDT measurements.

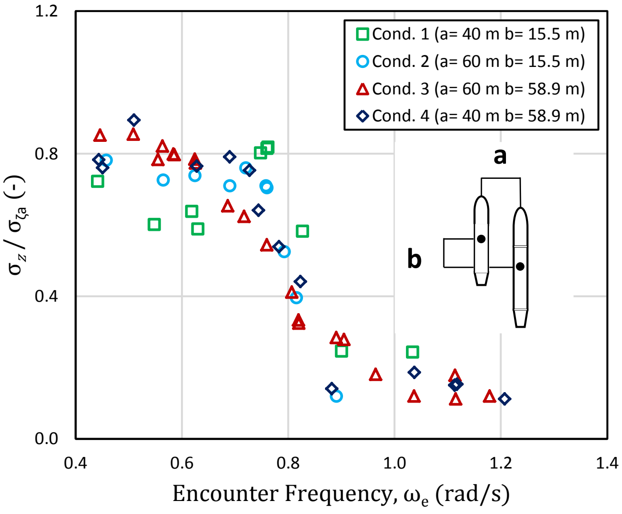

(a) Heave

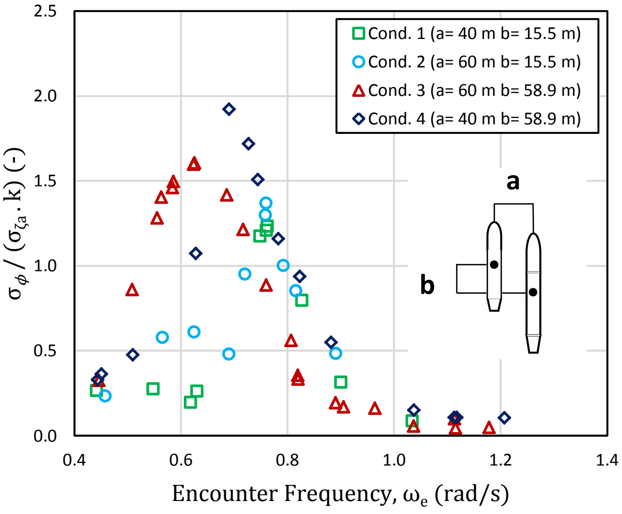

(b) Roll

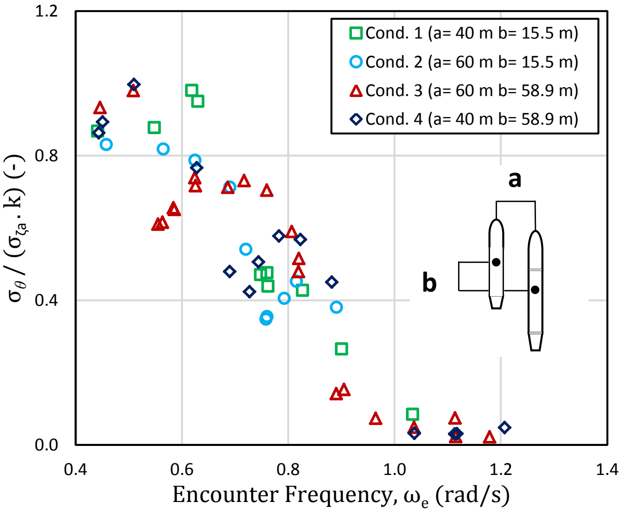

(c) Pitch

Figure 6: SV non-dimensional motion response

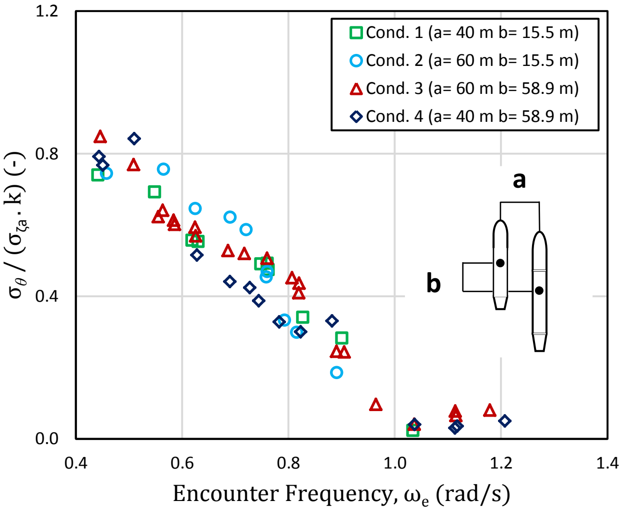

Figure 7: LHD non-dimensional pitch motion response

4.2 (a) SV Heave Response

The largest SV peak heave response occurred with a lateral separation of 40 m and longitudinal separation of 58.9 m (Condition 4). The smallest peak heave response was observed with a lateral separation of 60 m and a longitudinal separation of 15.5 m (Condition 2). The peak heave response for Conditions 2, 3 and 4 occurred in the encounter frequency range of 0.44 – 0.51 rad/s. However, for the case with the smallest tested lateral and longitudinal separation (Condition 1), the peak heave response occurred at a higher encounter frequency (0.76 rad/s).

Increasing the lateral separation between vessels, whilst maintaining a longitudinal separation of 15.5 m (Conditions 1 to 2), slightly reduces the peak heave response of the SV. With a longitudinal separation of 58.9 m, increasing the lateral separation (Conditions 4 to 3) also reduces the peak heave motion response.

Increasing the longitudinal separation between vessels, with a lateral separation of 40 m (Conditions 1 to 4) increased the peak heave response. Similarly, with a lateral separation of 60 m between vessels increasing the longitudinal separation (Conditions 2 to 3) results in an increase in peak heave response.

The vessel configuration that results in the smallest heave response is largely dependent on the encounter frequency. For example, in the frequency range of 0.56 to 0.62 rad/s Condition 1 results in the lowest heave response. Contrastingly, in the range of 0.69 to 0.76 rad/s the smallest response occurs in Condition 3.

4.2 (b) SV Roll Response

It can be seen that hydrodynamic interactions induce significant SV roll motions in all conditions tested. This means that during RAS operations in head seas the SV will need to withstand not only the typically dominant longitudinal motions but also significant lateral plane motions.

The largest peak SV roll response occurred with a lateral separation of 40 m and longitudinal separation of 58.9 m (Condition 4), the same condition that resulted in the largest peak heave response. The peak response in this condition occurs at an encounter frequency close to the semi-captive natural roll frequency of the SV (0.68 rad/s), as seen in Table 2. Smaller frequency spacing around the peak roll response would be desirable to more accurately capture the peak values.

Increasing the lateral separation between vessels at a longitudinal separation of 58.9 m (Condition 4 to 3) reduces the peak roll response. However, at a longitudinal separation of 15.5 m the peak roll response is marginally increased when the lateral separation is increased from 40 m to 60 m (Condition 1 to 2).

Increasing the longitudinal separation between vessels with a lateral separation of 40 m (Condition 1 to 4) increases the magnitude of the peak roll response and shifts it to a lower encounter frequency. The same trends are seen as a result of increasing the longitudinal separation between vessels with a lateral separation of 60 m.

Given the lack of appendages on the SV, its roll damping will be low and mainly due to wave radiation. The large variations seen in the peak roll response with change in lateral and longitudinal separation can be partially attributed to its low roll damping. This causes the magnitude of the peak roll response to be highly sensitive to variations in the amount of damping present. The semi-captive experimental setup may compound these effects as the radiated waves can become somewhat captured between the models. The way in which the waves between the models interact is a complex problem and may have a significant effect on the peak roll response of the SV. The resulting interaction loads will vary greatly depending on whether the wave interactions are constructive or destructive. This is discussed further in section 4.3.

As is the case for heave motion, the vessel configuration that provides the smallest roll motion varies with encounter frequency. Between 0.56 and 0.62 rad/s the smallest roll response occurs in Condition 1. This is the same condition that produced the smallest heave response in this frequency range. For encounter frequency of 0.76 rad/s and above, Condition 3 results in the smallest roll response.

In Condition 1 the peak heave and roll responses occur at the same encounter frequency. For all other configurations, at the encounter frequency corresponding to the peak roll response, the magnitude of the heave response is also close to its peak value. This indicates that the roll and heave excitation forces due to hydrodynamic interactions vary in a similar way. These interactions cause the roll response of the SV to change dramatically especially at resonance. The variations in heave response due to these interactions are less severe because the heave motions are more heavily damped.

4.2 (c) SV Pitch Response

The magnitude of the SV peak pitch response is similar for Conditions 1, 3 and 4. Condition 2 results in the smallest peak pitch response. With a longitudinal separation of 15.5 m, increasing the lateral separation between vessels (Condition 1 to 2) reduces the peak SV pitch response. In contrast, the peak SV pitch response is relatively unaffected as a result of increasing the lateral separation between vessels with a constant longitudinal separation of 58.9 m (Conditions 4 to 3). The peak pitch response for Conditions 2, 3 and 4 occurred within the encounter frequency range of 0.44 –0.51 rad/s.

Contrastingly, for Condition 1 the frequency of the peak pitch response was higher at 0.62 rad/s. This trend is similar to that discussed in section 4.2 (a) for the peak SV heave response. As in the case of both the SV heave and roll responses, the condition that produces the smallest pitch response varies with the encounter frequency.

4.2 (d) LHD Pitch Response

In general, the longitudinal and lateral separations between the vessels have a smaller influence on the pitch motion response of the LHD than on the SV. This may be partly attributed to the differences in hull form, loading condition and that the SV was not fitted with bilge keels.

The magnitude of the peak pitch motion is greatest for the largest longitudinal separation (Conditions 3 and 4). Some consistent trends can be identified over small ranges of encounter frequency. For example, for encounter frequencies between 0.56 and 0.72 rad/s the pitch motion is largest for Condition 2. For encounter frequencies between 0.62 rad/s and 0.82 rad/s the pitch motion response is consistently lowest for Condition 4.

4.3 FREE SURFACE ENVIRONMENT OBSERVATIONS

4.3 (a) Calm Water Patterns

The wave patterns from the vessels moving in calm water were investigated using photographs and video footage to provide insight into their influence on the motions experienced by the vessels. The wave patterns between the two models when moving through calm water with an equivalent full scale speed of 14 knots can be seen in Figure 8 for each condition.

(a) Condition 1 (a = 40 m, b = 15.5 m (full scale))

(b) Condition 2 (a = 60 m, b = 15.5 m (full scale))

(c) Condition 3 (a = 60 m, b = 58.9 m (full scale))

(d) Condition 4 (a = 40 m, b = 58.9 m (full scale))

Figure 8: Wave patterns between models in calm water, (LHD Left, SV Right).

In Conditions 1 and 2, where the midship sections of the vessels are more closely aligned longitudinally, the waves from each vessel meet closer to the centre of the gap between the vessels. While in Conditions 3 and 4 where the SV is further forward of the LHD, the waves meet closer to the LHD. This is due to the waves from the SV travelling further before meeting the waves off the LHD in Conditions 3 and 4.

In Condition 1, 2 and 4 it appears that after the waves meet, the diffracted waves that travel in the direction of the SV contact the aft starboard side of the SV. In contrast, for Condition 3 (largest tested lateral and longitudinal separation) it appears that the waves do not contact the SV but rather pass behind its aft extent. The waves that contact the aft extent of the SV may contribute to roll motion, not only by exerting an exciting moment on the vessel, but also by altering the instantaneous wetted surface area of the hull and therefore its transverse stability.

The observations conducted in calm water were used to provide an understanding of the free surface environment for a simplified case. However, the wave patterns from the vessels in calm water will be influenced when the vessels move into a head sea.

4.3 (b) Free Surface Environment in Waves

The effect that interactions have on vessels in calm water is largely a function of their speed, hull geometry and relative positions. In head seas however, the forces, moments and motions are also dependent on the incident wave amplitude and frequency, the interaction between the diffracted waves, the radiated waves due to the ship motions as well as the calm water wave patterns discussed in section 4.3 (a).

The free surface elevation observed between the two vessels advancing in waves was chaotic and highly irregular. It also varied significantly for changes in both vessel configuration and encounter frequency. Wave trapping between the hulls due to vertical motions as described by Faltinsen (2005) may potentially contribute to the observed free surface characteristics for some of the conditions tested. Figures 9 and 10 illustrate the free surface elevation between vessels for Conditions 3 and 4 respectively, at an encounter frequency of 0.73 rad/s full scale. Each figure contains three sequential images with a time step 0.6 seconds full scale between images. The images were taken from the aft camera between the vessels.

In Condition 3 the free surface environment is relatively undisturbed in the region of the aft starboard shoulder of the SV. As discussed in Section 4.3 (a), the bow wave of the LHD contacts the aft quarter of the SV in Condition 4 but not in Condition 3.

The wave elevation is notably larger and more chaotic in Condition 4 than in Condition 3. It is also noted that there is a distinct forward propagation of a wave along the hull of the SV in Condition 4. Both of these features may influence the excitation moments on the SV and may contribute to the larger SV roll response seen in Condition 4.

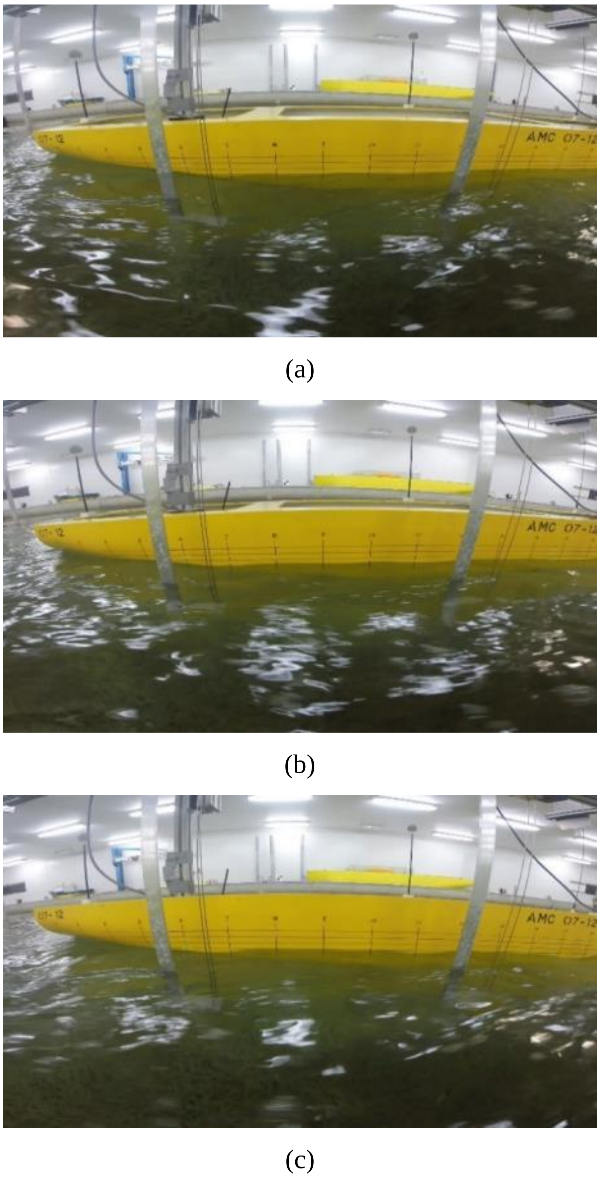

(a)

(b)

(c)

Figure 9: Sequential images of the free surface elevation between vessels in Condition 3 at encounter frequency of 0.73 rad/s full scale. The time step between images is 0.6 s full scale.

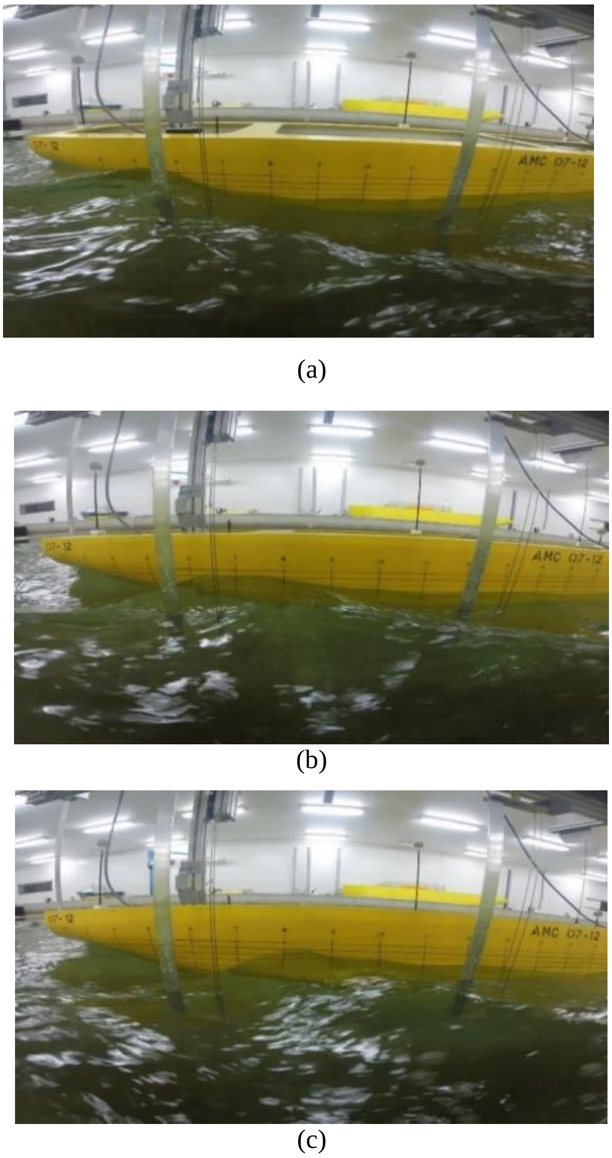

(a)

(b)

(c)

Figure 10: Sequential images of the free surface elevation between vessels in Condition 4 at encounter frequency of 0.73 rad/s full scale. The time step between images is 0.6 s full scale.

5. CONCLUSIONS

This paper presents analysis of physical scale model experimental results of hydrodynamic interactions during RAS. These studies focussed on the influence of lateral and longitudinal separation between vessels on interactions between a supply vessel (SV) and a landing helicopter dock (LHD) operating in head seas.

Variations in the lateral and longitudinal separation between vessels were found to have more influence on the pitch response of the SV than that of the LHD. The LHD roll response was close to zero for all conditions. In contrast, it was found that hydrodynamic interactions could result in large SV roll motions. This means that during RAS operations in head seas the SV will need to withstand not only the typically dominant longitudinal motions but also significant lateral plane motions.

A single configuration resulted in the largest peak SV heave, roll and pitch motion responses. In this configuration the vessels were separated by 58.9 m longitudinally and 40 m laterally. The vessel configuration that resulted in the smallest SV heave, roll and pitch responses varied with encounter frequency.

The lateral and longitudinal separations between vessels were found to have a large influence on the peak roll response of the SV. Increasing the longitudinal separation increased the peak SV roll response. Increasing the lateral separation between vessels reduced the peak SV roll response at a longitudinal separation of

58.9 m. In contrast, increasing the lateral separation at a longitudinal separation of 15.5 m marginally increased the peak roll response.

Visual comparison was made of the free surface elevation between the vessels in calm water and for a selected case when advancing in head waves. The selected comparison considered the influence of changing the lateral separation between vessels with a constant longitudinal separation of 58.9 m. With 60 m lateral separation, the bow wave of the LHD was found not to contact the SV. When the lateral separation was reduced to 40 m, the bow wave of the LHD made contact with the aft extent of the SV. The reduced lateral separation also resulted in larger wave elevations and a more chaotic free surface between the vessels. These features may influence the excitation moments on the SV and contribute to the increase in roll response with reduced lateral separation which was seen for these conditions.

6. FUTURE WORK

Future scale model experiments will aim to quantify all hydrodynamic loads acting on the models as well as the wave elevation between them. This will enable a thorough understanding of the way in which the waves between the models interact and the resulting hydrodynamic interactions. As part of this study the potential for wave-trapping between the hulls as described by Faltinsen (2005) will be investigated in detail. The additional experimental data will also be highly valuable when it comes to validating numerical tools.

Another valuable experimental dataset for validation could be obtained by conducting single vessel radiation and diffraction experiments. This would be similar to the approach taken by Carette (2016) when considering the problem of validating numerical tools for analysis of hydrodynamic interactions during launch and recovery. This will enable validation of numerical tools for a simplified case before moving to the more complicated case with two vessels operating in close proximity.

Validation of the chosen numerical tool will be undertaken in multiple phases. The experimental dataset presented here will be used as the basis for the first phase of validation. Once the influence of lateral and longitudinal separation between vessels on hydrodynamic interactions in head seas is well understood, the focus of studies will be expanded to include consideration of vessel heading and forward speed.

To inform the development of an efficient test program for the next phase of scale model experiments, parametric studies will be conducted using the partially validated numerical tool. A key focus of these studies will be how each of the contributions to the roll exciting moment is influenced by variation in the lateral and longitudinal separation between vessels as well as vessel heading and speed. Numerical studies will also be used to examine the influence of the semi-captive experimental setup by conducting simulations with the vessels constrained as they were in the experiments and also in free sailing condition.

7. ACKNOWLEDGEMENTS

The authors acknowledge the valuable input of both Mr Adam Rolls (AMC) and Mr Peter Graham (DST) whilst undertaking the experimental component of this work.

8. REFERENCES

1. http://images.navy.gov.au/20151124ran 8100087_069.jpg (Accessed 20th July 2016)
2. SKEJIC, R., BREIVIK, M., FOSSEN, T. I. & FALTINSEN, O. M. (2009) *Modeling and control of underway replenishment operations in calm water*. Proceedings of 8th IFAC Int. Conference on Manoeuvering and Control of Marine Craft, Trondheim, Norway, 2009.
3. SKEJIC, R. & BERG, T. E. (2010) *Combined seakeeping and maneuvering analysis of a two ship lightering operation*. Proceedings of the 29th International Conference on Ocean, Offshore and Arctic Engineering – OMAE, Shanghai, China, 2010.
4. FONFACH, J. M. A., SUTULO, S. & GUEDES SOARES, C. (2011) *Numerical study of ship-to-ship interaction forces on the basis of various flow models*. 2nd International Conference on Ship Manoeuvring in Shallow and Confined Water, Trondheim, Norway, 2011.
5. CHEN, G. R. & FANG, M. C. (2001) *Hydrodynamic Interactions Between Two Ships Advancing in Waves*. Ocean Engineering, Elsvier Science Ltd., 28**,** 1053-1078, 2001.
6. RAFIQUL ISLAM, M. & MURAI, M. (2013) *Dynamic interaction of parallel moving ships in close proximity*. Journal of Marine Science Application, 12**,** 261-271, 2013.
7. VON GRAEFE, A., SHIGUNOV, V. & EL MOCTAR, O. (2015) *Rankine source method for ship–ship interaction problems*. Journal of Offshore Mechanics and Arctic Engineering 137, 2015.
8. YUAN, Z. M., INCECIK, A., S. DAI, ALEXANDER, D., JI, C. Y. & ZHANG, X. (2015) *Hydrodynamic interactions between two ships travelling or stationary in shallow waters*. Ocean Engineering, 108**,** 620-635, 2015.
9. THOMAS, G., TURNER, T., ANDREWARTHA, T. & MORRIS, B. (2010) *Ship Motions During Replenishment at Sea Operations in Head Seas*. Trans RINA. Vol. 152, Part A4, Intl J Maritime Eng, Oct-Dec 2010.
10. YUAN, Z., JI, C., INCECIK, A., ZHAO, W., DAY, A. (2016) *Theoretical and Numerical Estimation of Ship-to-Ship Hydrodynamic*

Interaction Effects, Ocean Engineering, 121, 239-253, 2016.

11. KASHIWAGI, M., ENDO, K., YAMAGUCHI, H. (2005) *Wave Drift Forces and Moments on Two Ships Arranged Side by Side in Waves*, Ocean Engineering, 32, 529-535, 2005.
12. MATHEW, J., SGARIOTO, D., TURNER, T. & LIN, F. (2016) *Numerical Exploration of Ship Motions during Replenishment at Sea between a Supply Vessel and a Landing Helicopter Dock*. Proceedings of the Maritime/Air Systems and Technologies Europe Conference and Exhibition (MAST Europe), Amsterdam, 2016.
13. MCTAGGART, K. & TURNER, T. (2006) *Ship Motions Including Interaction Forces During Replenishment at Sea*. Pacific Internation Maritime Conference, 2006 Sydney, Australia.
14. SCHMITKE, R. T. (1978) *Ship Sway, Roll and Yaw Motions in Oblique Seas*. Transactions, Society of Naval Architects and Marine Engineers, 86**,** 26-46, 1978.
15. HIMENO, Y., *Prediction of Ship Roll Damping. A State of the Art*. The University of Michigan College of Engineering, 1981.
16. SADAT-HOSSEINI, S. H., WU, P., TODA, Y., CARRICA, P. & AND STERN, F. (2011) *URANS Studies of ship-ship interactions in shallow-water*. 2nd International Conference on Ship Manoeuvring in Shallow and Confined Water, Trondheim, Norway, 299-309, 2011.
17. MOUSAVIRAAD, S. M., SADAT-HOSSEINI, S. H., CARRICA, P. M. & STERN, F. (2016) *Ship–Ship interactions in calm water and waves. Part 2: URANS validation in replenishment and overtaking conditions*. Ocean Engineering, 111**,** 627-638, 2016.
18. LATAIRE, E., VANTORRE, M. & DELEFORTRIE, G. (2009) *Captive model testing for ship-to-ship operations*. MARSIM, 2009.
19. MCTAGGART, K., CUMMING, D., HSIUNG, C. C. & LI, L. (2003) *Seakeeping of Two Ships in Close Proximity*. Ocean Engineering, 30**,** 1051-1063, 2003.
20. ANDREWARTHA, T., THOMAS, G., TURNER, T. & LIN, F. (2007) *Replenishment at Sea: Motions of Ships Operating Side-by-Side in Head Seas*. International Journal of Maritime Engineering 149 63-72, 2007.
21. MOUSAVIRAAD, S. M., SADAT-HOSSEINI, S. H. & STERN, F. (2016) *Ship–ship interactions in calm water and waves. Part 1: Analysis of the experimental data*. Ocean Engineering, 111, 2016.
22. QUADVLIEG, F. H. H. A., HALLMANN, R., HUGHES, G. & HARRIS, D. H. (2011) *Using dynamic positioning for side-by-side cargo transfer operations*. 2nd International Conference on Ship Manoeuvring in Shallow and Confined Water, Trondheim, Norway, 2011.
23. ITTC, *Recommended Procedures and Guidelines*, *Ship Models*, 7.5-01-01-01, Revision 3, 2011
24. NATO STANDARDIZATION AGENCY, *ATP 16(D)/MTP 16(D) Replenishment at Sea*. 2001.
25. BHATTACHARYYA, R., Dynamics of Marine Vehicles, New York, USA, John Wiley and Sons Inc. 1978.
26. FENTON J.D., MCKEE, W.D. (1990) *On calculating the lengths of water waves*, Coastal Engineering, 14 (1990), pp. 499-513, 1990.
27. FALTINSEN, O. M. (2005) *Hydrodynamics of High-Speed Marine Vehicles*. Cambridge University Press.
28. CARETTE, N. (2016) *Physical testing of RHIB and mother ship interactions for launch and recovery simulation validation*. Proceedings of Launch and Recovery Symposium, 2016 Linthicum Heights, MD, USA.

PRESSURE-IMPULSE DIAGRAM OF THE FLNG TANKS UNDER SLOSHING LOADS

(DOI No: 10.3940/rina.ijme.2018.a2.436)

S E Lee, The Korea Ship and Offshore Research Institute (Lloyd's Register Foundation Research Centre of Excellence) at Pusan National University, Korea and Southampton Marine and Maritime Institute, University of Southampton, UK,
J K Paik, Pusan National University, Korea and University College London, UK.

SUMMARY

Sloshing impact loads can cause severe structural damage to cargo tanks in liquefied natural gas floating production storage offloading units (LNG-FPSOs or FLNGs). Studies of sloshing can be classified into two types, namely, hydrodynamics-related and structural mechanics-related studies. This study is a sequel to the authors' previous studies (Paik et al. 2015; Lee et al. 2015), but is more related to issues of structural mechanics. In this study, a new method for probabilistic sloshing assessment, which has been previously developed by the authors, is briefly explained. The nonlinear impact structural response characteristics under sloshing impact loads are examined by a nonlinear finite element ANSYS/LS-DYNA method. An iso-damage curve, representing a pressure-impulse diagram, is derived for the self-supporting prismatic-shape IMO B type LNG cargo containment system of a hypothetical FLNG. The insights developed from this work can be useful for the damage-tolerant design of cargo tanks in FLNGs.

NOMENCLATURE

C	Cowper-Symonds coefficient
D	Maximum deformation level (mm)
I_a	Impulsive asymptote (bar·s)
I_o	Impulse (bar·s)
K	Spring stiffness (N/mm)
T	Natural period (s)
P_a	Quasi-static asymptote (bar)
P_o	Peak pressure (bar)
q	Cowper-Symonds coefficient
t_{dec}	Decay time of an impact action (ms)
t_{dur}	Duration time of an impact action (ms)
t_{dur}'	Idealized duration time of an impact action (ms)
t_o	Rise time of an impact action (ms)
$x_{\max}$	Maximum dynamic displacement (mm)
α , β	Constants
$\dot{\varepsilon}$	Strain rate (mm/s)
ε_f	Fracture strain under a static load (mm)
ε_{fd}	Fracture strain under a dynamic load (mm)
ν	Poisson's ratio
ρ	Density of a material (kg/m^3)
σ_Y	Yield stress under a static load (N/mm^2)
σ_{Yd}	Yield stress under a dynamic load (N/mm^2)
ω	Natural circular frequency (rad/s)

1. INTRODUCTION

Tank sloshing is unavoidable in a liquefied natural gas floating production storage offloading unit (LNG-FPSO or FLNG), due to the continuous loading and unloading processes, together with the effects of winds, waves and currents (Paik and Thayamballi, 2003, 2007). In many cases, repetitive sloshing impact loads can cause severe structural damage to LNG cargo containment systems (CCS) and their sub-structures.

Studies of sloshing can be classified into two kinds: hydrodynamics-related studies that aim to identify the impact pressure profile over time, and structural mechanics-related studies that aim to calculate the dynamic structural damage. To quantify structural damage under sloshing impact loads, a number of extensive studies have been conducted over the last 50 years.

Classification societies, shipyards and third-party authorities have proposed their own assessment procedures (ABS 2006; DNV GL 2006; LR 2009; BV 2011; Hwang *et al* 2014; Ito *et al*. 2008; Nam *et al*. 2006; Pastool *et al*. 2005; Graczyk *et al*. 2007; Graczyk and Moan 2008; Kuo *et al*. 2009). In recent years, numerical and experimental studies on loads and strength of sloshing impacts have also been undertaken in the literature (Paik and Shin 2006; Nasar *et al*. 2008; Hirdaris *et al*. 2010; Brizzolara *et al*. 2011; Zhao *et al*. 2013; Jiang *et al*. 2015; Kim *et al*. 2017; Liu *et al*. 2017; Xu *et al*. 2017; Zhang *et al*. 2017).

It has been widely recognised, however, that the sloshing impact loads obtained from current procedures might not represent the entire set of credible sloshing scenarios, as these procedures have been conducted for specific environmental conditions or for limited ranges of tank resonant periods.

To improve the sloshing scenario sampling, the authors have previously proposed a fully probabilistic design procedure that provides guidelines to be followed in all the tasks involved, from selecting credible scenarios probabilistically to determining the design sloshing loads (Paik *et al*. 2015), and conducting the nonlinear dynamic structural analysis under sloshing loads (Lee *et al*. 2015). As a sequel to that design procedure, this study applies a new approach as shown in Figure. 1 that utilises a pressure-impulse (P-I) diagram for assessing the extent of damage to the cargo tanks in FLNG units.

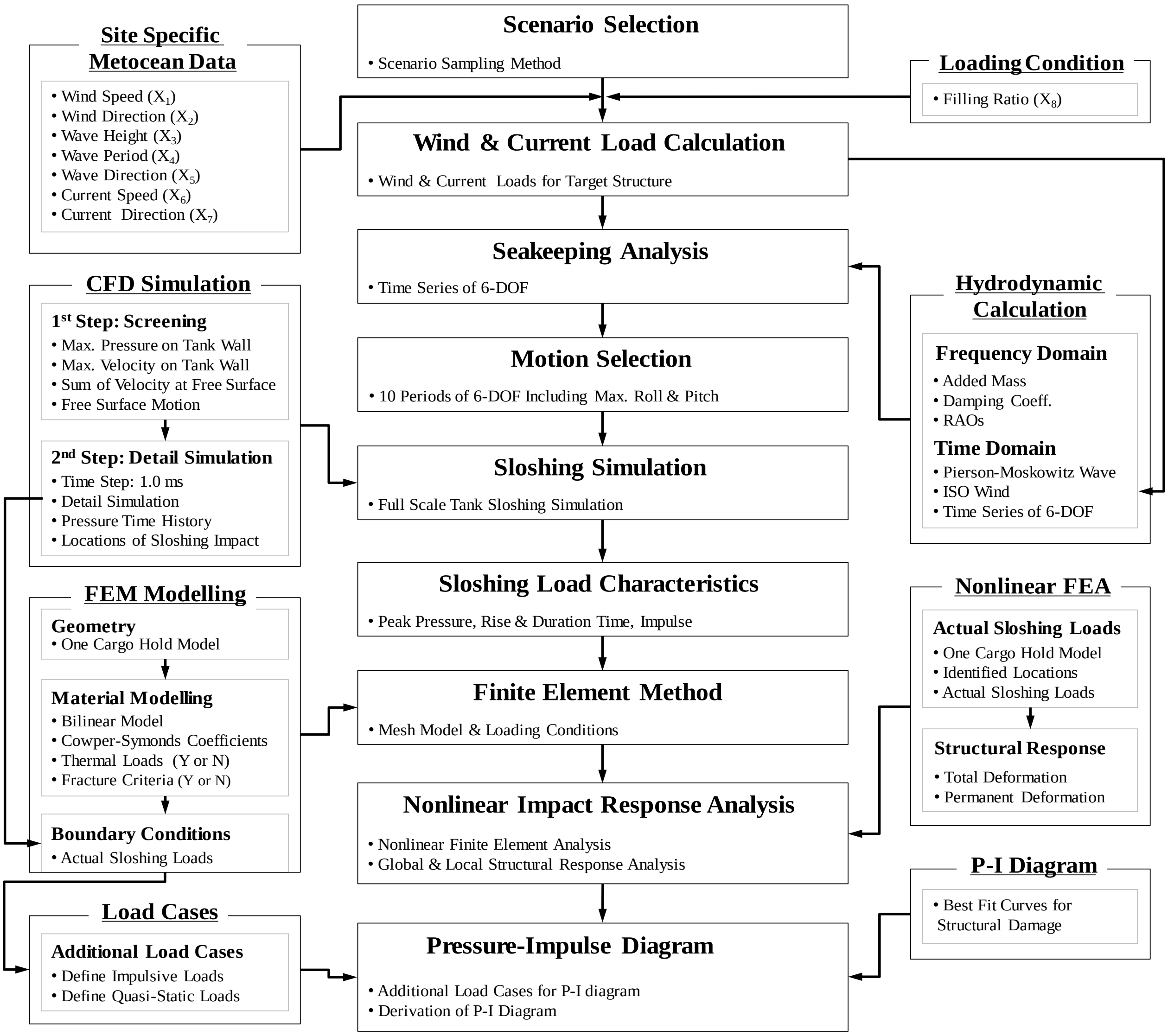

Figure 1: Procedure of a probabilistic design approach to assessing structural damage under sloshing impact loads.

In general, the P-I diagram is a useful design tool that structural design engineers are able to easily assess the response to applied loads. With defined damage level, the diagram indicates the combinations of load and impulse that will cause a specific damage level. In the early days, the P-I diagram method has most commonly been used for assessing animal and human injuries or for analysing structural damage from blast loads (Jarrete 1968; Smith and Hetherington 1994; Baker *et al*. 1983; Mays and Smith 1995; Merrifield 1993; Li and Meng 2002a, 2002b; Fallah and Louca 2007; Ma *et al*. 2007; Parlin *et al*. 2014; Lan and Crawfird 2003; Scheider 1998; Wesevich and Oswald 2005; Shi *et al*. 2008; Sohn *et al*. 2013). This method involves applying a single degree of freedom (SDOF) model (Li and Meng 2002b; Fallah and Louca 2007; Ma *et al*. 2007; Parlin *et al*. 2014; Lan and Crawfird 2003; Scheider 1998) and a finite element method (FEM) (Lan and Crawfird 2003; Scheider 1998; Wesevich and Oswald 2005; Shi *et al*. 2008; Sohn *et al*. 2013). In this study, the authors examine the feasibility of using the P-I method to quantify structural damage to cargo tanks in FLNG units as shown in Figure. 2.

Figure 2: A hypothetical FLNG (Lee *et al*. 2015).

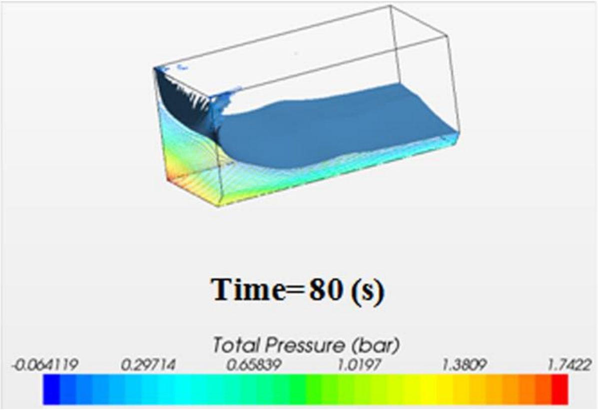

Figure 3: An example of the pressure distribution inside the LNG tank (Paik *et al*. 2015)

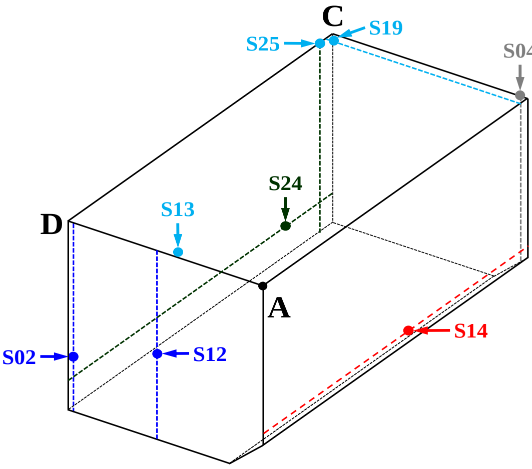

Figure 4: identified sloshing impact locations from 30 credible scenarios (Lee *et al*. 2015)

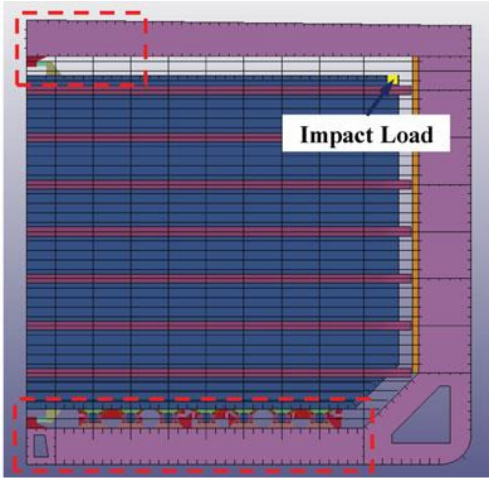

Figure 5: An example of the FE model and the boundary conditions (Lee et al. 2015)

2. PROBABILISTIC PROCEDURE OF SLOSHING ASSESSMENT

This chapter briefly summarises the developed probabilistic procedure of sloshing assessment. It can be outlined as follows:

Step 1

- Selecting credible sloshing scenarios through a probabilistic sampling method
- Finite volume method (FVM) mesh modelling for the wind and current loads
- Estimating the wind and current loads for all directions by computational fluid dynamics (CFD)
- Seakeeping analysis in the frequency- and time-domains taking into account the wind, wave, and current loads
- Selecting a range of motion for sloshing simulations
- FVM mesh modelling of tank sloshing in full scale
- Performing sloshing CFD simulation (Figure. 3)
- Analysing the sloshing load characteristics for peak pressure, impulse and rise time
- Identifying locations of the sloshing impact (Figure. 4)

Step 2

- FEM mesh modelling
- Defining material modelling and boundary conditions (Figure. 5)
- Analysing a series of nonlinear structural responses under parametric sloshing loads
- Identifying the weakest location in a tank

Step 3

- Identifying the range of actual sloshing impact profiles from the CFD simulations
- Nonlinear FEM (NLFEM) series analyses for the weakest location
- Quantifying the extent of damage
- Deriving the P-I diagram of maximum deformation
- Estimating the impulsive and quasi-static asymptotes
- Evaluating the unit’s structural capacity and safety

3. CHARACTERISTICS OF THE P-I DIAGRAM

For structural designers, the primary objective for assessing the loading capacity of a target structure can be either to determine the maximum deflection or to assess the stress level at the end of the loading state. However, in the structural design of a dynamic system, the time history of the dynamic responses is also very significant. For practical design purposes, structural behaviour in response to an impact-pressure event can be conceptualised within three domains, depending on the ratio between the duration of an impact event, and the natural period of the structure. This evaluation is conducted as follows (NORSOK 2009):

- Quasi-static domain: $t_{dur} / T \geq 3$
- Dynamic domain: $0.3 \leq t_{dur} / T < 3$
- Impulsive domain: $t_{dur} / T \leq 0.3$

By plotting known responses, the spectra of maximum peak responses to the abovementioned three domains can be illustrated, and the structural behaviour under a given loading can be clarified, as shown in Figure. 6. There are various forms of response spectra plots that can describe the relationships between the maximum value of a response parameter and characteristics of the dynamic system. Among these forms, the P-I diagram is widely used to represent the response spectrum for structural damage assessment, as illustrated in Figure. 7.

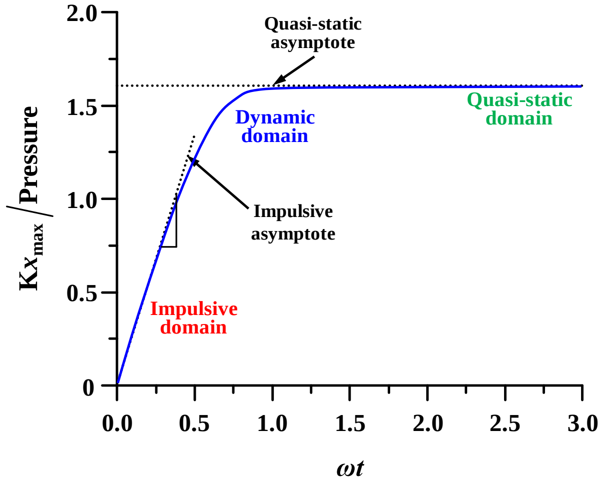

Figure 6: Typical response spectrum.

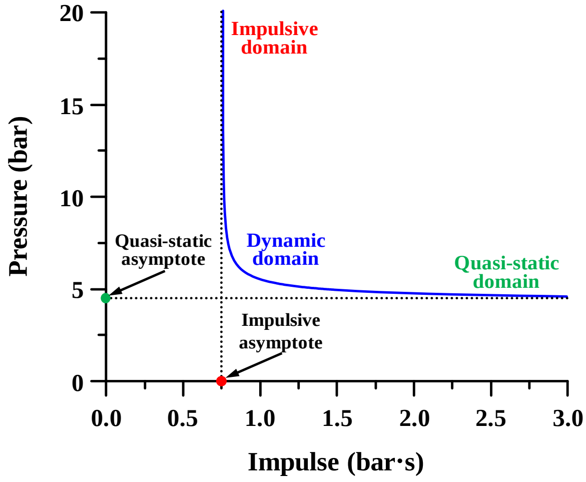

Figure 7: Typical pressure-impulse diagram.

Unlike the typical response spectrum plot, the P-I diagram allows a simple differentiation between behaviour domains, in the form of impulsive and quasi-static asymptotes. For estimating the structural safety of a dynamic system under combined pressure-impulse forces, plots in the diagram's left area and below a basis level indicate no specified damage, but plots in the right area and above the basis level indicate damage in excess of that level.

As shown in Figure. 8, if the dynamic system shows multiple plots of damage-level events in the P-I diagram, then each of these events represents damage, which may range from negligible to extreme, according to the damage criteria. In this regard, the P-I diagram method can serve as an efficient approach to quantifying structural damage levels, and this method can help structural engineers to systematically identify the safety limits and the structural capacity of a unit in response to expected impact pressure events.

4. FINITE ELEMENT MODELLING

4.1 GEOMETRY

A hypothetical barge-type FLNG with a Self-supporting, Prismatic-shape IMO type B (SPB) tank was developed, as shown in Figure. 5. This target structure has the following dimensions: length 411 m, breadth 80 m, depth 40 m, draft 15.1 m and total capacity 628 K. The details of the tank arrangement and a schematic drawing of a mid-ship section were presented in the authors' previous study (Paik *et al*. 2015).

4.2 MATERIAL MODEL

In the dynamic structural response analysis using the NLFEM, material properties are the major factors of concern, as yield stress and fracture strain vary along with the dynamic effects, and specifically the strain rate effects. The Cowper–Symonds model is usually applied to evaluate strain rate effects (Jones 1970; Paik 2003).

$$\frac{\sigma_{Yd}}{\sigma_Y} = 1.0 + \left(\frac{\dot{\varepsilon}}{C}\right)^{1/q} \tag{1}$$

$$\frac{\varepsilon_{fd}}{\varepsilon_f} = \left[1.0 + \left(\frac{\dot{\varepsilon}}{C}\right)^{1/q}\right]^{-1} \tag{2}$$

where σ_Y and ε_f are the yield stress and the fracture strain under static load; σ_{Yd} and ε_{fd} are the yield stress and the fracture strain under dynamic load; $\dot{\varepsilon}$ is the strain rate; and C and q is the experimentally determined Cowper-Symonds coefficients. MAT_PIECEWISE_LINEAR_PLASTICITY in ANSYS /LS-DYNA is adopted to take the elasto-plastic behaviour and strain rate into account. This analysis characterises not only the nonlinear stress-strain relationships of the material, but also the yield stress with factors C and q (ANSYS/LS-DYNA 2014).

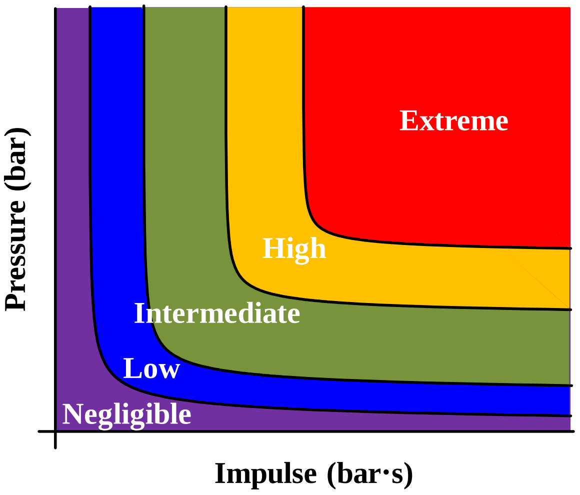

Figure 8: Damage level of P-I diagram.

The materials composing the tank and hull structures are aluminum and mild steel, respectively. The SPB tank and its supporting structures are assumed to be constructed of aluminum alloy at a temperature of -163°C, and the hull structures are of mild steel constructed at room temperature. The effects of thermal loads within the cargo tanks are not considered because this study is focused on the dynamic structural behaviour. The applied material properties obtained by the material coupon test are shown in Table 1. The insulation system is not included in this study.

Table 1: Material properties of cargo tanks

Units	Al. at -163℃	Mild steel at RT
ρ	2700	7889
ν	0.33	0.3
σ_Y	133.25	235.0
C	6500	40.4
q	4	5

4.3 LOADING AND BOUNDARY CONDITIONS

Characterising the sloshing impact load is one of the most challenging tasks in determining structural requirements. The actual sloshing loads can be conceptualised as impulsive loading, and characterised by the peak pressure, impulse and rise time, as shown in Figure. 9. In the parametric analyses, each sloshing load is conceptualised, and the results in terms of its ideal duration time, t_{dur}' are summarised in Table 2.

To simplify the NLFEM computations, the boundary conditions are set as symmetrical around the centre plane, and fixed at both ends of the hull structure, as explained in the authors' previous study (Lee *et al*. 2015). The total simulation time is set as three times the duration of an applied sloshing load, as a means to consider the dynamic stress propagation in the structural model.

Table 2: Actual sloshing load profiles

No.	t_o	P_o	t_{dec}	I_o	t_{dur}'
Scenario-02	18	15.31	292	0.95	124
Scenario-04	10	1.32	195	0.06	88
Scenario-12	67	7.45	1,388	1.33	356
Scenario-13	18	3.22	269	0.17	108
Scenario-14	35	0.71	643	0.10	279
Scenario-19	27	5.36	578	0.93	345
Scenario-24	22	0.59	769	0.09	316
Scenario-25	34	8.58	966	1.50	350

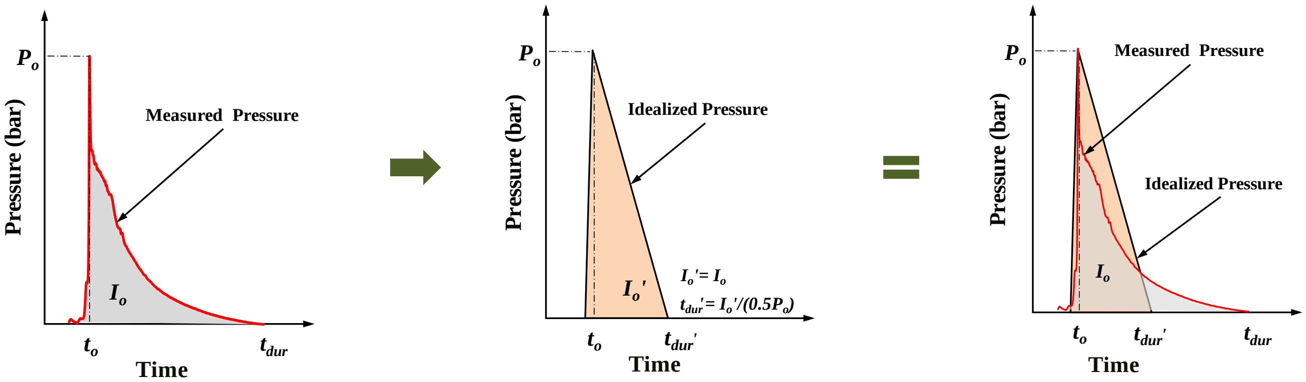

Figure 9: Idealisation of measured sloshing impact pressure characteristics applied in the dynamic structural analysis.

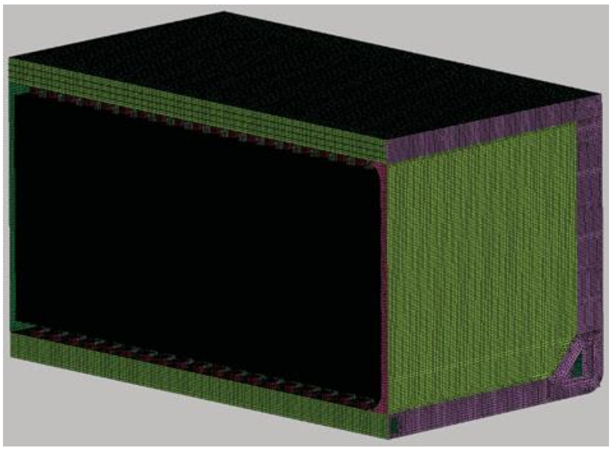

Figure 10: An example of the generated mesh model (Lee *et al*. 2015).

Table 3: Calculated impulse for parametric studies

P_o	t_{dur}'				
	88	108	124	316	350
0.592	0.026	0.032	0.037	0.094	0.103
1.324	0.058	0.071	0.082	0.209	0.231
3.225	0.142	0.174	0.199	0.510	0.564
5.361	0.236	0.289	0.331	0.847	0.926
8.587	0.378	0.463	0.530	1.357	1.502
15.312	0.674	0.825	0.946	2.420	2.678

Table 4: Impulsive conditions

P_o	I_o	
	0.250	0.500
5.361	93	187
8.587	58	116
15.312	33	65
20.000	25	50

4.4 MESH CONVERGENCE STUDY

In authors' previous work (Lee *et al*. 2015), a mesh convergence study was performed for six types of mesh sizes under a sloshing load. As a result, the element sizes for the SPB tank and the hull structure were determined as 100 and 400 mm, respectively. For this study, the number of elements generated and applied is approximately 3.4 million as shown in Figure. 10.

5. NUMERICAL RESULTS

According to the author's previous paper (Lee *et al*. 2015), it was found that the location of Scenario-19 (Figure. 4) was the weakest structural component in the SPB tank. Thus, the parametric studies to derive the P-I diagram is performed only for this location.

5.1 PARAMETRIC STUDIES

To derive the P-I diagram of the FLNG CCS, the peak pressure and the ideal duration time from the actual sloshing loads are selected as input parameters. 30 case series analyses are performed. The parameters considered in this part of the process are as follows:

- P_o : 0.592, 1.324, 3.225, 5.361, 8.587, 15.312 bars
- t_{dur}' : 88, 108, 124, 316, 350 ms

The calculated impulse values, according to the selected peak pressures and ideal duration times, are summarised in Table 3. Furthermore, to capture the damage level near-impulsive domain in the P-I diagram, 8 more cases of series analyses are performed. The parameters considered in this part of the analysis are as follows:

- I_o : 0.250, 0.500 bar·s
- P_o : 5.361, 8.587, 15.312, 20.000 bars

The calculated duration of time for the various impulse levels and peak pressures are presented in Table 4. The dynamic structural response characteristics of the FLNG CCS are investigated using ANSYS/LS-DYNA (2014). Maximum deformation is defined as the maximum value, and the permanent deflection is the average value of event duration.

Figure. 11 describes the deformation time histories for variations in the peak pressure and the ideal duration of pressure events. Figures. 12 and 13 illustrate the maximum and the permanent deformations of the FLNG CCS. It is observed that as the impulse and peak pressure increase, the maximum deformation increases. It is found that the level of permanent deformation is not severe when the sloshing peak pressure is under 6.0 bars. However, the damage level increases significantly when peak pressures rise to over 6 bars.

Figure. 14 reveals the sensitivity of the maximum and permanent deformation to peak pressure and impulse. It appears that the main factor for increasing the maximum and permanent deformation is the peak pressure and impulse respectively.

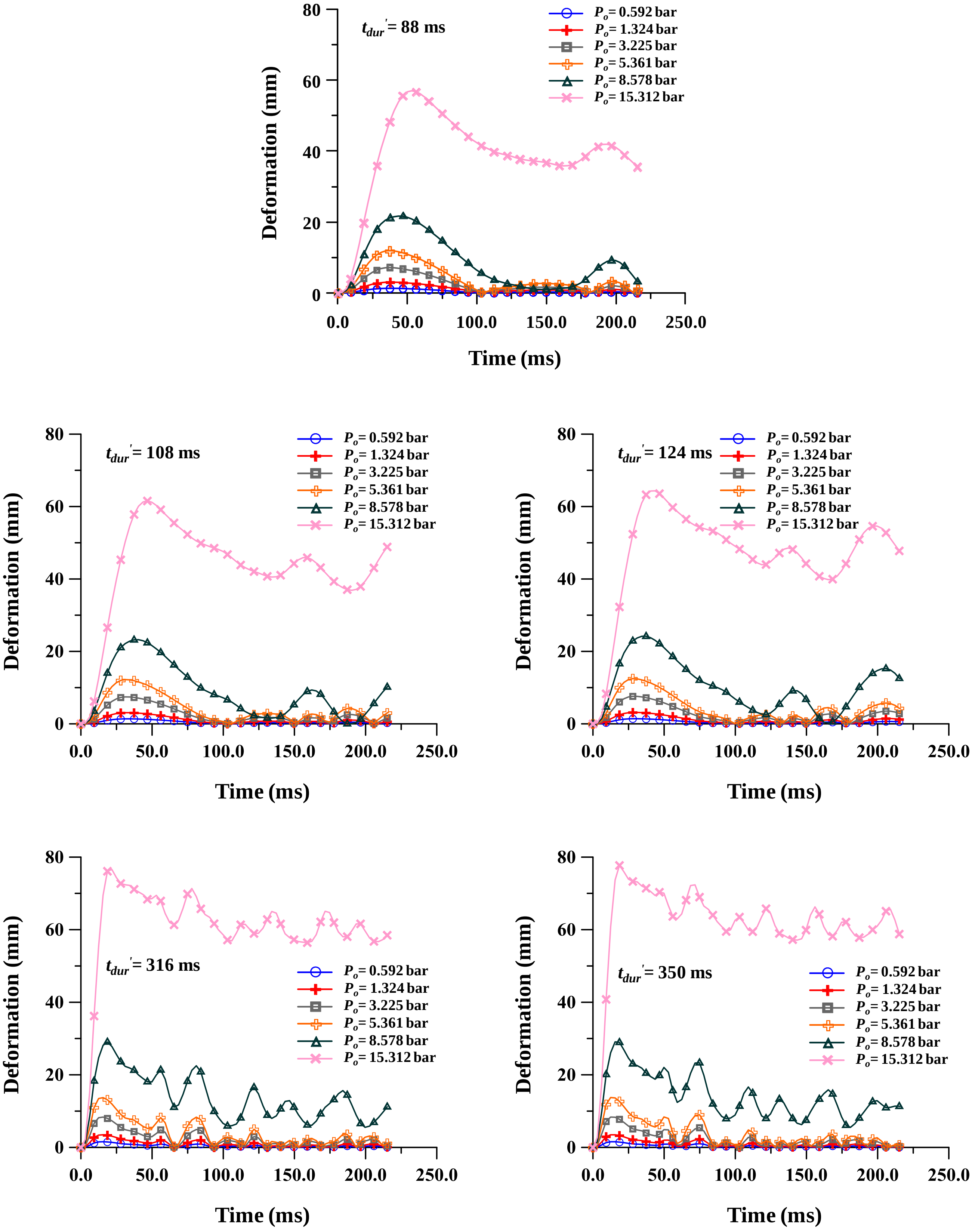

Figure 11: Deformation time-histories of the FLNG CCS under sloshing impact loads.

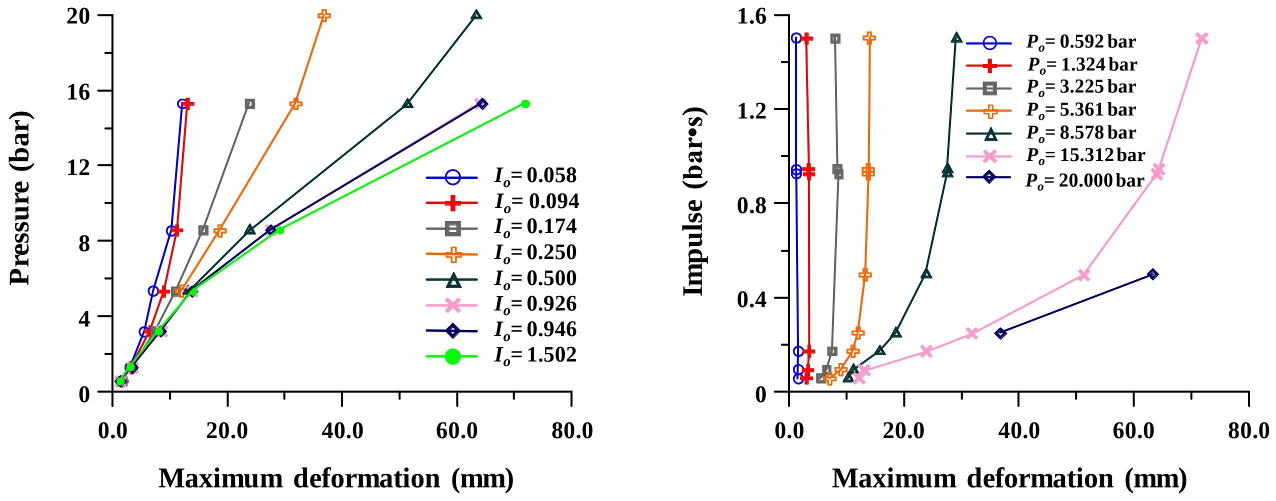

Figure 12: Maximum deformation of the FLNG CCS with varying impact load profiles.

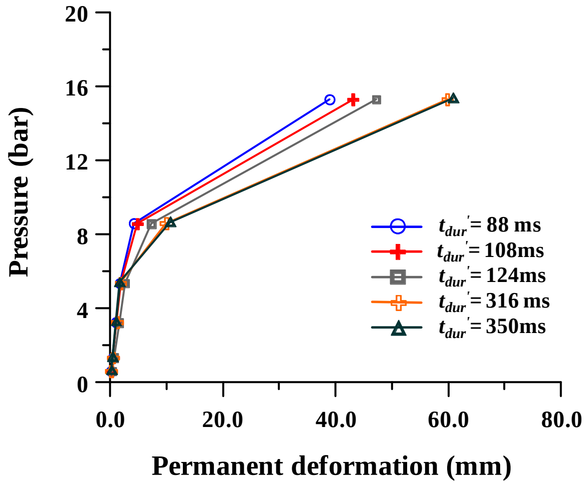

Figure 13: Permanent deformation of the FLNG CCS with varying impact load profiles.

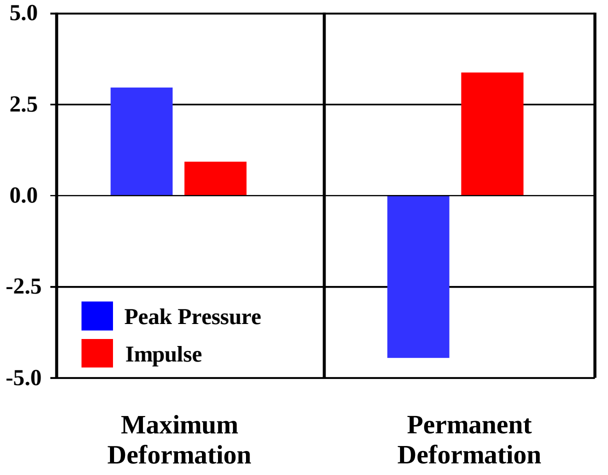

Figure 14: Sensitivities of the peak pressure and impulse on the maximum and permanent deformation.

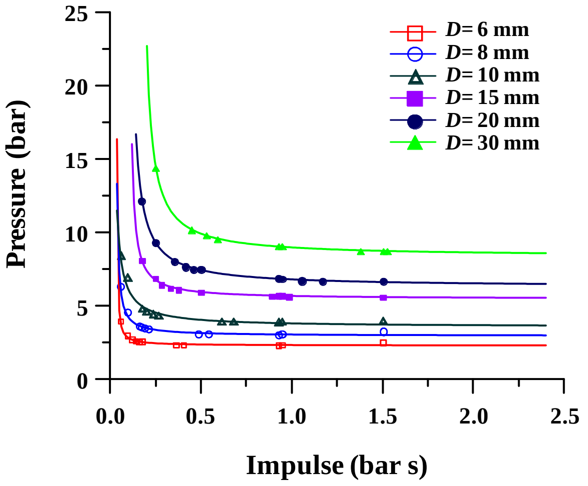

Figure 15: Pressure-impulse diagram of the FLNG CCS according to the damage level.

5.2 DERIVATION OF THE P-I DIAGRAM

To generate the P-I diagram for the FLNG CCS, a series of NLFEM analyses are conducted. The sloshing impact loads, such as the peak pressures and impulses that correspond to the LNG CCS damage levels, are plotted in the P-I space, based on the maximum deformation levels. Finally, the iso-damage curves, which are the boundary lines between different damage levels, can be obtained by using the curve fitting method.

In the present study, the simple hyperbolic function recommended by Oswald and Sherkut (1994) was used. It has been applied some engineering studies (Shi et al. 2008; Mutalib and Hao 2011) and the good results were achieved. The general form is written as follows:

$$(P-P_a)(I-I_a)=\alpha(P_a/2+I_a/2)^{\beta} \tag{3}$$

where P_a is the pressure asymptote for the maximum deformation level D; I_a is the impulsive asymptote for maximum deformation level D; and α and β are constants that determine the shape of the hyperbola which can be obtained by numerical curve fitting.

Figure. 15 illustrates the P-I diagram of the FLNG CCS. The estimated values of the asymptotes and constants are summarised in Table 5, along with the maximum deformation level.

Table 5: Approximated asymptotes and constants

D	P_a	I_a	α	β
6	2.284	0.038	0.083	-5.989
8	2.957	0.031	0.143	-1.131
10	3.516	0.010	0.464	-1.183
15	5.408	0.102	0.221	-0.135
20	6.254	0.096	0.547	-0.150
30	8.334	0.163	0.813	-0.303

6. DISCUSSION

Sloshing impact loads in cargo tanks such as LNGCs, FPSOs, FLNGs or VLCCs are among the most challenging issues for structural designers. For over the last 50 years, a number of design procedures have been proposed and applied for industrial purposes.

Apart from the industrial use of existing design procedures, the issue of how to accurately determine the sloshing scenarios and to design for sloshing loads is still controversial. To resolve this issue, the authors have introduced a novel concept, utilising a probabilistic approach to sample sloshing scenarios and to analyse the sloshing impact load profiles. Previously, the feasibility of this approach had been fully reviewed through an applied example (Paik *et al*. 2015).

In the present paper, the authors introduced a novel method to the assessment of the sloshing damage on the hypothetical FLNG tank structure and confirmed the feasibility of sloshing damage assessment. Once designers or engineers have the P-I diagram, they will be able to assess the damage level immediately. However, it is numerically very expensive to derive the P-I diagram which requires a full set of parametric simulations.

7. CONCLUSIONS

The aim of this study is to briefly introduce the developed probabilistic procedure for sloshing assessment in FLNG CCSs, and to derive a P-I diagram based on parametric studies of sloshing impact loads. The following conclusions can be drawn from the results obtained from this study.

(1) A new procedure to generate a P-I diagram of an FLNG CCS under sloshing impact loads is introduced, based on a series of NLFEM analyses. A P-I diagram of a model FLNG CCS is successfully derived, indicating the iso-damage levels.

(2) The effect of impulse and peak pressure is proportional to the maximum and permanent deformations. It was found that the peak pressure and impulse respectively play a primary role in increasing the maximum and permanent deformation.

(3) Regardless of the duration of pressure, very similar levels of permanent deformation appear when the peak pressure is under 6.0 bars.

(4) The probabilistic approach to assessing sloshing impact damage is fully presented. It includes a full series of steps, from selecting credible scenarios of tank sloshing to deriving the P-I diagram of tank structures. The feasibility of the developed procedure is confirmed by testing an applied example of a hypothetical FLNG.

It is believed and hoped that the probabilistic procedure developed in this study will be helpful for engineers and designers in the shipbuilding and offshore industries. The authors will continue their research on sloshing-induced impact loads and design loads, as there is a need to further refine the industry standards for resolving these issues. It is noted that to improve the accuracy of the proposed procedure, the effects of insulation systems and of thermal loads in the cargo tanks should be considered.

8. ACKNOWLEDGEMENTS

This study was undertaken at the Korea Ship and Offshore Research Institute at Pusan National University which has been a Lloyd’s Register Foundation Research Centre of Excellence. This research was also supported by Basic Science Research Program through the National Research Foundation of Korea (NRF) funded by the Ministry of Education (NRF-2015R1A6A3A01060166, NRF-2017R1A6A3A03003742).

9. REFERENCES

1. ABS (2006) *Guidance Note on Strength Assessment of Membrane-Type LNG Containment Systems Under Sloshing Loads*. American Bureau of Shipping, Houston, TX, US.
2. ANSYS/LS-DYNA, (2014) *User’s manual* (version 15.0). ANSYS Inc., Pennsylvania, US, 2014.
3. BAKER, W.E. COX, P.A. WESTINE, P.S. KULESZ, J.J. and STREHLOW, R.A. (1983)

Explosion Hazards and Evaluation. Elsevier Scientific Pub. Co., New York, US.

4. BRIZZOLARA, S., SAVIO, L., VIVIANI, M., CHEN, Y., TEMAREL, P. and COUTY, N. (2011). *Comparison of Experimental and Numerical Sloshing Loads in Partially Filled Tanks. Ships and Offshore Structures*, Vol. 6(1-2), pp. 15-43.
5. BV (2011) *Strength Assessment of LNG Membrane Tanks under Sloshing Loads* - Guidance Note NI 564 DTR00 E. Bureau Veritas, Paris, France.
6. DNV GL (2006) *Sloshing Analysis of LNG Membrane Tanks,* DNV classification notes no.30.9. Det Norske Veritas, Oslo, Norway.
7. FALLAH, A.S. and LOUCA, L.A. (2007) *Pressure–Impulse Diagrams for Elastic–Plastic Hardening and Softening Single-Degree-of-Freedom Models subjected to Blast Loading.* International Journal of Impact Engineering, Vol. 34, pp. 823-842.
8. GRACZYK, M. MOAN, M.K. and WU, M.K. (2007) *Extreme Sloshing and Whipping-Induced Pressures and Structural Response in Membrane LNG Tanks*. Ships Offshore Structures, Vol. 2(3), pp. 201–216.
9. GRACZYK, M. and MOAN, T. (2008) *A Probabilistic Assessment of Design Sloshing Pressure Time Histories in LNG Tanks*. Ocean Engineering, Vol. 35(8-9), pp. 834–855.
10. HIRDARIS, S.E., WHITE, N.J., ANGOSHTARI, N., JOHNSON, M.C., LEE, Y. and BAKKERS, N. (2010). *Wave Loads and Flexible Fluid-Structure Interactions: Current Developments and Future Directions.* Ships and Offshore Structures, Vol. 5(4), pp. 307-325
11. HWANG, J.O. CHUN, S.E. JOH, K.H. SAMBOS, P. DE LAUZON, J. WHITE, N. KIM, M.S. PARK, J.B. and LEE, J.M. (2014) *Direct Assessment of Structural Capacity Against Sloshing Using Dynamic Nonlinear FE Analysis*. The 24h International Offshore and Polar Engineering Conference, ISOPE, Busan, Korea, June 15–20.
12. ITO, H. SUH, Y.S. CHUN, S.E., SATISH KUMAR, Y.V. HA, M.K. PARK, J.J. YU, H.C. and WANG, B. (2008) *A Direct Assessment Approach for Structural Strength Evaluation of Cargo Containment System Under Sloshing inside LNGC Tanks based on Fluid Structure Interaction.* The 27th International Conference on Offshore Mechanics and Arctic Engineering, Estoril, Portugal, June 15-20.
13. JARRETT, D.E. (1968) *Derivation of British Explosives Safety Distances*. Annals of New York Academy of Science. 152(1), pp. 18-35.
14. JONES, N. (1970) *Structural impact*. Cambridge University Press, Cambridge, UK.
15. KIM, S.Y., KIM, Y.H. and LEE, J.H. (2017). *Comparison of Sloshing-Induced Pressure in Different Scale Tanks*. Ships and Offshore Structures, Vol. 12(2), pp.244-261.
16. KUO, J.F. CAMPBELL, R.B. DING, Z. HOIE, S.M. RINEHART, A.J. SANDSTORM, R.E. YUNG, T.W. GREER, M.N. and DNANCZKO, M.A. (2009) *LNG tank sloshing assessment methodology: The new generation*. International Journal of Offshore and Polar Engineering, ISOPE, Vol. 19(4), pp. 241-253.
17. LAN, S.R. and CRAWFORD, J.C. (2003) *Evaluation of the Blast Resistance of Metal Deck Proofs*. Proceedings of the fifth Asia-Pacific conference on shock & impact loads on structures, Changsha, Hunan, China, November 12-14.
18. LEE, S.E., KIM, B.J. SEO, J.K. HA, Y.C. MATUSUMOTO, T. BYEON, S.H. and PAIK, J.K. (2015) *Nonlinear Impact Response Analysis of LNG FPSO Cargo Tank Structures under Sloshing Loads*. Ships and Offshore Structures.
19. LI, Q.M. and MENG, H. (2002a) *Pressure-Impulse Diagram based on Dimensional Analysis and Single-Degree-of-Freedom Model*. Journal of Engineering Mechanics, Vol. 128(1), pp. 87–92.
20. LI, Q.M. and MENG, H. (2002b) *Pulse Loading Shape Effects on Pressure-Impulse Diagram of Elastic Plastic Structures*. International Journal of Mechanical Sciences, Vol. 44, pp. 1985-1998.
21. LIU, D., TANG, W., WANG, J., XUE, H. and WANG, K. (2017). *Hybrid RANS/LES Simulation of Sloshing Flow in a Rectangular Tank with and without Baffles*. Ships and Offshore Structures, Vol. 12(8), pp. 1005-1015.
22. LR (2009) *Ship Right-Sloshing Assessment Guidance Document for Membrane Tank LNG Operations*. Lloyd’s Register, London, UK.
23. MA, G.W. SSHI, H.J. and SHU, D.W. (2007) *P-I Diagram Method for Combined Failure Modes if Rigid-Plastic Beams*. International Journal of Impact Engineering, Vol. 34, pp. 1081-1094.
24. MAYS G.C. and SMITH, P.D. (1995) *Blast Effects on Buildings: Design of Buildings to Optimize Resistance to Blast Loading*. Thomas Telford Services Ltd.
25. MERRIFIELD, R. (1993) *Simplified Calculations of Blast Induced Injuries and Damage*. Report no. 37, Health and Safety Executive Specialist Inspector.
26. MUTALIB, A.A. and HAO, H. (2011) *Development of PI Diagrams for FRP Strengthened RC Columns,* Int. J. Impact Eng. Vol. 38 (5), pp. 290–304.
27. NAM, S.K. KIM, W.S. NOH, B.J. SHIN, H.C. and CHOI, I.H. (2006) *The Parametric Study on the Response of Membrane Tanks in a Mark III Type LNG Carrier Using Fully Coupled Hydro-*

Elastic Model. International Conference on Ship and Offshore Technology, ICSOT, Busan, Korea, September 14-15.

28. NASAR, T., SANNASIRAJ, S.A. and SUNDAR, V. (2008). *Sloshing Pressure Variation in a Barge Carrying Tank*. Ships and Offshore Structures, Vol. 3(3), pp. 185-203.
29. NORSOK (1999) *Actions and action effects*, Norwegian Standards.
30. OSWALD, C. and SHERKUT, D. (1994) *FACEDAP Theory Manual Version 1.2*, US Army Corps of Engineers Omaha District, Omaha. Nebraska.
31. PAIK, J.K., KIM, K.J., LEE, J.H., JUNG, B.G. and KIM, S.J. (2016). *Test Database of the Mechanical Properties of Mild, High-Tensile and Stainless Steel and Aluminium Alloy Associated with Cold Temperatures and Strain Rates.* Ships and Offshore Structures, Vol. 12(S1), pp. S230-S256.
32. PAIK, J.K. LEE, S.E. KIM, B.J. SEO, J.K. HA, Y.C. MATSUMOTO, T. and BYEON, S.H. (2015) *Toward A Probabilistic Approach to Determine Nominal Values of Tank Sloshing Loads in Structural Design of LNG FPSOs*. Journal of Offshore Mechanics and Arctic Engineering, Vol. 137(2).
33. PAIK, J.K. and SHIN, Y.S. (2006). *Structural Damage and Strength Criteria for Ship Stiffened Panels under Impact Pressure Actions Arising from Sloshing, Slamming and Green Water Loading*. Ships and Offshore Structures, Vol.1(3), pp.249-256.
34. PAIK, J.K. and THYAMBALLI, A.K. (2003) *Ultimate limit state design of steel-plated structure*. John Wiley & Sons, Chichester, UK.
35. PAIK, J.K. and THYAMBALLI, A.K. (2007). *Ship-shaped Offshore Installations: Design, Building, and Operation*. Cambridge University Press, Cambridge, UK.
36. PASTOOL, W. OSTVOLD, T.K. BYKLUM, E. and VALSGARD, S. (2005) *Sloshing Load and Response in LNG Carriers for New Designs, New Operations and New Trades*. GasTech 2005, Bilbao, Spain, March 14-17.
37. PARLIN, N.J. DAVIDS, W.G. NAGY, E. and CUMMINS, T. (2014) *Dynamic Response of Lightweight Wood-based Flexible Wall Panels to Blast and Impulse Loading*. Construction and Building Materials, Vol. 50, pp. 237-245.

38 SCHENEIDER, P. (1998) *Predicting Damage of Slender Cylindrical Steel Shells under Pressure Wave Load.* Journal of Loss Prevention in the Process Industries, Vol. 11(3), pp. 223-228.

39. SHI, Y. HAO, H. and LI, Z.H. (2008) *Numerical Derivation of Pressure-Impulse Diagrams for Prediction of RC Column Damage to Blast Loads*. International Journal of Impact Engineering, Vol. 35, pp. 1213-1227.
40. SMITH, P.D. and HETHERINGTON, J.G. (1994) *Blast and Ballistic Loading of Structures*. Butterworth Heinemann, London, UK.
41. SOHN, J.M. KIM, S.J., KIM, B.H. and PAIK, J.K. (2013) *Nonlinear Structural Consequence Analysis of FPSO Topside Blast Walls*. Ocean Engineering, Vol. 60.
42. XU, Q., HU, Z. and JIANG, Z. (2017). *Experimental Investigation of Sloshing Effect on the Hydrodynamic Responses of an FLNG System during Side-by-Side Operation. Ships and Offshore Structures*, Vol. 12(6), pp.804-817.
43. WESEVICH, J.W. and OSWARD, C.J. (2005) *Empirical based Concrete Masonry Pressure–Impulse Diagrams for Varying Degrees of Damage*. Structures Congress 2005, New York, US.
44. ZHANG, J., WU, W. and HU, J. (2017). *Parametric Studies on Nickel Ore Slurry Sloshing in a Cargo Hold by Numerical Simulations*. Ships and Offshore Structures, Vol.12(2), pp.209-218.
45. ZHAO, W., YANG, J. and HU, Z. (2013). *Effects of Sloshing on the Global Motion Responses of FLNG*. Ships and Offshore Structures, Vol. 8(2), pp.111-122.

FRICTIONAL DRAG REDUCTION: REVIEW AND NUMERICAL INVESTIGATION OF MICROBUBBLE DRAG REDUCTION IN A CHANNEL FLOW

(DOI No: 10.3940/rina.ijme.2018.a2.460)

S Sindagi, **R Vijayakumar,** Indian Institute of Technology, Madras, India and **B K Saxena**, Tolani Maritime Institute, Pune, India

SUMMARY

The reduction of ship's resistance is one of the most effective way to reduce emissions, operating costs and to improve EEDI. It is reported that, for slow moving vessels, the frictional drag accounts for as much as 80% of the total drag, thus there is a strong demand for the reduction in the frictional drag. The use of air as a lubricant, known as Micro Bubble Drag Reduction, to reduce that frictional drag is an active research topic. The main focus of authors is to present the current scenario of research carried out worldwide along with numerical simulation of air injection in a rectangular channel. Latest developments in this field suggests that, there is a potential reduction of 80% & 30% reduction in frictional drag in case of flat plates and ships respectively. Review suggests that, MBDR depends on Gas or Air Diffusion which depends on, Bubble size distributions and coalescence and surface tension of liquid, which in turn depends on salinity of water, void fraction, location of injection points, depth of water in which bubbles are injected. Authors are of opinion that, Microbubbles affect the performance of Propeller, which in turn decides net savings in power considering power required to inject Microbubbles. Moreover, 3D numerical investigations into frictional drag reduction by microbubbles were carried out in Star CCM+ on a channel for different flow velocities, different void fraction and for different cross sections of flow at the injection point. This study is the first of its kind in which, variation of coefficient of friction both in longitudinal as well as spanwise direction were studied along with actual localised variation of void fraction at these points. From the study, it is concluded that, since it is a channel flow and as the flow is restricted in confined region, effect of air injection is limited to smaller area in spanwise direction as bubbles were not escaping in spanwise direction.

NOMENCLATURE

ACS	Air Cavity Ship
ALDR	Air Layer Drag Reduction
BDR	Bubble Drag Reduction
CFD	Computational Fluid Dynamics
EEDI	Energy Efficiency Design Index
MBDR	Micro Bubble Drag Reduction
PCDR	Partial Cavity Drag Reduction
SWR	Super Water- Repellent
TBL	Turbulent Boundary Layer
R_F	Frictional Resistance of Ship
C_F	Coefficient of Friction
C_{F0}	Coefficient of friction without bubbles
S	Wetted surface area of Ship
U	Speed of ship or Flow speed in pipe
τ_w	Shear Stress
μ	Dynamic Viscosity
$\frac{du}{dy}$	Velocity Gradient
$\rho U'V'$	Reynold's Stress
ν	Kinematic Viscosity
u_0^*	friction velocity of the fully-wetted flow
l_v	Viscous wall unit
$\frac{A_B}{A_{Total}}$.	Ratio of Area of Bubble to the total Area of flow
d_b	Diameter of Bubble
D_P	Diameter of Pipe
Q	Flow of Fluid in Pipe
$C_{f0}(Q_a)$	Corrected C_{f0} at the air flow rate (Q_a)
$U(Q_a)$	Average flow speed at Q_a
α_m	Void Fraction
Q_w	Flow rate of water
Q_a	Flow rate of air
δ	Boundary-layer thickness
δ^*	Displacement thickness,
b	Width of the injector section
t_b	Equivalent air layer thickness
Ba	Width of the plate
H	Height of the channel
C_T	Coefficient of Total Resistance
C_W	Coefficient of Wave making Resistance
F_d	Depth Froude Number
D	Depth of ship
1+K	Form factor
W	Work rate to propel a ship
ΔW	Reduction in Work rate to propel a ship due to injection of bubbles.
W_{pump}	Pumping power for air injection
W_o	Work rate to propel a ship in non-bubble condition
W_{net}	Net work rate to propel a ship in Bubble condition
R_{TO}	Ship's Drag in Non Bubble condition
R_T	Ship's Drag in Bubble condition
H	Water depth at injection point
C_P	Local pressure coefficient at injection point
r_D	Ratio of wave Drag to Viscous Drag
P_{saved}	Net power savings
P_D	Power required to overcome the ship's total drag
η_{Prop}	Propeller efficiency

1. INTRODUCTION

Anybody moving through a fluid experiences resistive force, which is divided into two components: Viscous drag (Frictional drag) and Pressure drag (Form drag or profile drag) (Lewis, n.d). Viscous drag originates from friction between the fluid particles itself and friction between particles of fluid and the surfaces over which it is flowing. The Frictional Drag is a component of Viscous drag, depends on the viscosity of liquid and of course the density. As per 2003 figures (Kim, 2011), worldwide, ocean shipping consumes about 2.1 billion barrels of oil per year. If we can save 30% of the fuel consumption by a flow-control scheme through the frictional drag, it would result in a saving of $38 billion per year (based on $60 per barrel) for shipping industries. It has also been reported by (Watanabe, 1991) that NOx and SOx emissions from ship engines in maritime transport account for 7% and 4% of total NOx and SOx contaminants, respectively, in the entire world. It is reported that, the fluid frictional drag accounts for as much as 60% of the total drag for cargo ship, and about 80% of that for a tanker, thus there is a strong demand for the reduction in the fluid frictional drag.

Numerous technologies (Sindagi, et al, 2016) have been studied and utilized to reduce the frictional drag of a surface. It is concluded that, MBDR has added advantages over other drag reducing technologies, such as environmental friendly, easy operations, low costs and high saving of energy. It is also reported that the MBDR is able to achieve 80% reduction in frictional drag, which can result in a substantial fuel savings for both commercial and naval ships.

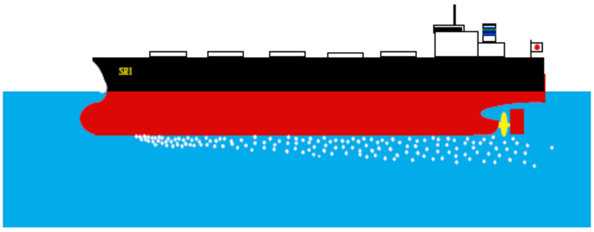

Figure 1 An image of microbubbles applied to a full-scale Ship (Yoshiaki, et al, n.d)

The most significant contribution regarding microbubble drag reduction was presented (McCormick & Bhattacharyya, 1973) by demonstrating hydrogen bubbles generated by electrolysis to reduce frictional drag on a fully submerged body of revolution. Since then, a large number of studies have been carried out on MBDR. As mentioned in the study (Yoshiaki, et al, 2000), Skin friction reduction of full-scale ships has its own difficulties in terms of higher value of Reynolds number and scaling up of skin friction device, which becomes more difficult to apply, along with fouling problem in the sea environment, which makes the application still more difficult. Displacement ships such as tankers especially VLCC & ULCC and Cargo Ships shown in Figure 1 are very large and move very slowly. They are especially suited to MBDR as, their skin friction drag component is about 80% of the total drag and their shape is like a box with wide flat bottom, forcing bubbles injected at the bottom near the bow to stay close to the hull bottom by buoyancy (Yoshiaki, et al, n.d). Thus, the injected bubbles can cover the whole hull bottom efficiently.

The Cement Carrier is also suitable for MBDR (Kodama, et al, 2004) as is generally equipped with blowers and related piping for feeding air to load and unload cement, which can be used to supply air for microbubbles. The energy required for microbubble injection is not small, as large ships have higher values of drafts resulting in escalation of hydrostatic pressure below the hull, which makes injection below hull more energy consuming, thus reducing the efficiency of entire MBDR system. Therefore, it is necessary to reduce the amount of air and/or increase the drag reduction by studying the drag reduction mechanism and minimizing the amount of injected air (Yoshiaki, et al, n.d). MBDR is expected to be suited for slow moving vessels with a target speed range of Froude numbers between 0.05 and 0.15 (MARIN, 2011) and of course to vessels operating in shallow water, where there is reduction in pressure below the hull due to shallow water effect (Sindagi, et al, 2016). Considering the importance and impending obligations, this paper reviews MBDR based on following significant points, which shall become platform for the researchers worldwide.

- Mechanisms inducing the microbubble drag reduction
- Methodology used for microbubble generation and Injection
- Effect of Void Fraction/Flow rate on drag reduction
- Effect of Bubble size distributions and coalescence
- Effect of Surfactant solution and salinity of water on bubble size formation
- Effect of position of Microbubble Injection
- Effect of Depth of water
- Effect of Microbubbles on the performance of Propeller
- Net savings in power considering Power required to inject microbubbles
- Suggestions to improve the drag reduction/ future scope for the researchers

Moreover, work on 3D numerical investigations into frictional drag reduction by microbubbles in Star CCM+ on a channel for different flow velocities, different void fraction and for different cross sections of flow at the injection point are presented in the paper. This study is the first of its kind in which, variation of coefficient of friction both in longitudinal as well as spanwise direction were studied along with actual localised variation of void fraction at these points.

2. MECHANISMS INDUCING THE MICROBUBBLE DRAG REDUCTION

To improve upon the efficiency of MBDR, one must understand the mechanisms by which there is considerable a reduction in the frictional drag. In alignment with observations of researchers, a close examination of the experimental and numerical results revealed that following mechanisms could be attributed to the reduction in the frictional drag

- Bubble/ Transitional Layer/Air Layer/ Air cavity formation
- Reduction in Density
- Reduction in Reynold's Stress
- Bubble Stratification
- Near wall Phase composition
- Reduction of Turbulence intensity in the Streamwise direction
- Prevention of Formation of spanwise vorticity near the wall

Frictional drag of any body is given by the expression

$$R_F = C_F \frac{1}{2} \rho S U^2$$

From the above expression, it can be concluded that, to reduce the frictional drag, one must reduce the C_F, density of liquid flowing and reduce the wetted surface area. In Bubble Drag Reduction (BDR), as shown in Figure 3, combined effect of density and wetted surface area reduction along with reduction in C_F due to alteration of flow properties and modification of turbulent momentum transport due the presence of bubbles causes considerable reduction in frictional drag (Jinho, et al, 2014). If the amount of injected air increases, air bubbles begin to coalesce into patches that cover the surface continuously, and a transitional air layer is formed, where the patches coexist with air bubbles. Figure 2 shows different mechanisms of air lubrication techniques (Mäkiharju, et al. 2012). If sufficiently high flux of air is injected, transition takes place from a bubbly flow to a Transitional Air Layer (Elbing, et al, 2008). This can be identified, if the microbubbles start coalescing and persistent drag reduction increases to more than 20%. As the air flow is increased further, the fraction of the surface covered by clusters of uneven air layer increases, until finally a continuous layer covers the entire surface, which reduces the wetted surface area. This in turn causes considerable reduction in frictional drag and reaches to almost 80%. In PCDR, a recess is created on the bottom of the hull that captures a volume of gas and creates a cavity of air between the hull and outer flow (Mäkiharju, et al. 2012). Researchers in the former USSR (Butuzov, 1967) (Butuzov, et al, 1999) studied PCDR for decades and developed several ships that utilize this method. These ships are sometimes called ACS or ship with artificial cavity (SAC) (Butuzov, et al, 1999), (Zverkhovskyi, et al, 2015). In the last decade, many research groups have studied PCDR through numerical modelling (Matveev, 2003), small scale experiments (Arndt, et al, 2009) (Gokcay, et al, 2004), and large scale experiments (Lay, et al, 2010), (Mäkiharju, et al. 2012). A recent review by (Ceccio, 2010) discusses relevant topics related to PCDR.

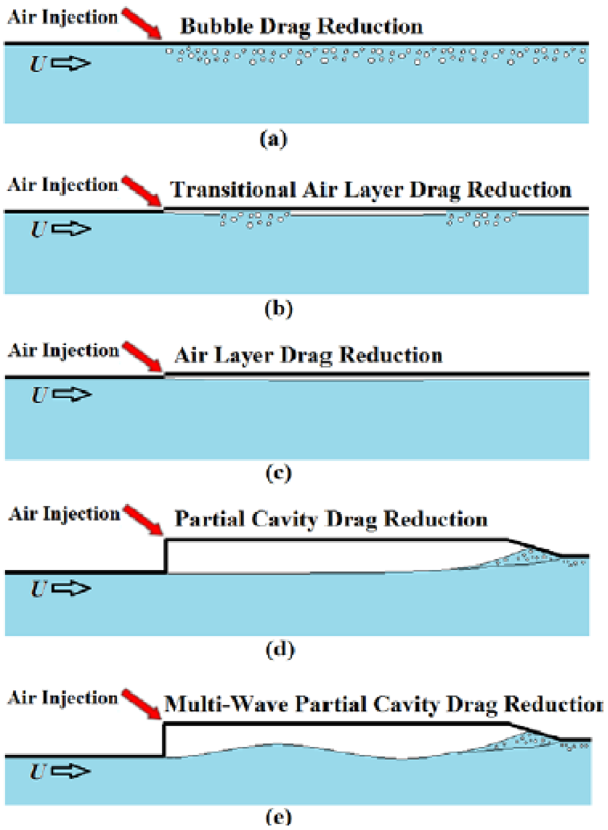

Figure 2 Conceptual sketches illustrating the different air lubrication techniques (Mäkiharju, et al. 2012) & (Jinho, et al, 2014).

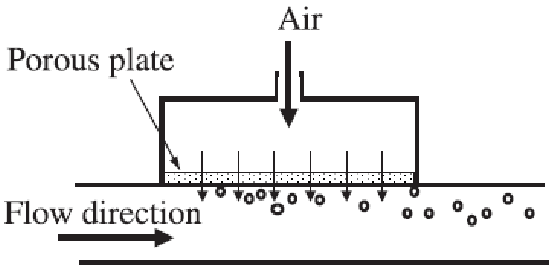

Figure 3 Air injection chamber and bubble generation through a porous plate (Madavan, et al. 1984).

The shear stress developed due to viscosity of liquid can be estimated by using

$$\tau_w = \mu \frac{du}{dy} - \rho U'V'$$

When air bubbles are present, the density of mixture decreases and accordingly shear stress is reduced. The second term in the above equation is Reynolds stress, which reduces as the density (ρ) decreases. It is opined that, (Thomas, et al, 2016), (Madavan, et al, 1984) & (Yoshiaki, et al, n.d) small bubbles or minute particles in liquid increases the effective viscosity of liquid. This originates the increase in first term of above equation. Thus, MBDR is effective only if, reduction in density and in turn reduction in Reynold's Stress is greater than increase in viscosity of liquid. In order for this mechanism to work, bubbles must be very small with diameter ranging from 0.5mm to 1mm. However, there is a possibility that much smaller bubbles can also contribute to reduction in frictional drag. The study by MARIN's research projects (Foeth, n.d), PELS (Project Energy-saving air-Lubricated Ships) and SMOOTH (Sustainable Methods for Optimal design and Operation of ships with air lubricated Hulls) pointed out that, when the bubbles are within 300 viscous wall units (l_v) ─defined as below, then reduction effect can be seen.

$$l_v = \frac{v}{u_0^*}$$

Where,

$$u_0^* = \sqrt{\frac{\tau_w}{\rho}}$$

As per the study carried out by (Mohanarangam, et al, 2009), it pointed out that, an additional momentum source caused due to the injection of gas redistributes the flow structure within the boundary layer, which increases the normal water velocities and in turn noticeable reduction in the mean streamwise velocities. Secondly, the presence of the micro-bubbles causes appreciable turbulence modification or the turbulence suppression effect results in considerable reduction in the frictional drag. The formation of a low-void-fraction layer, e.g. bubble stratification (Sanders, et al, 2006), has been observed when buoyancy acts to move microbubbles away from the solid surface when plate of observation is placed below. Conversely, buoyancy can lead to the formation of air layer when it forces microbubbles onto the plate surface. At higher speeds, fluctuating lift and drag forces on the individual microbubbles can overcome buoyancy, and the process of turbulent diffusion and mixing dominates and in turn loss in the drag reduction. Sanders, et al (2006) and Moriguchi & Kato, (2002) observed that, near wall Phase composition plays an important role in the MBDR. There is a strong relationship between the concentration of bubbles near the wall and the drag reduction which depends on the observed area ratio, $\frac{A_B}{A_{Total}}$, void fraction with small bubbles in close proximity to the wall. Figure 4, depicts the distribution of the local void ratio and the mean void ratios (Moriguchi & Kato, 2002). It seems that microbubbles gather in the centre of the channel when the mean void ratio is large. It is concluded (Kitigawa, et al, 2005) that, when the microbubbles are injected, the liquid turbulence intensity in the streamwise direction is decreased slightly in a few regions while that in the wall-normal direction decreases slightly in the whole of the region. The observation of the vortical structure (Kanai & Miyata, 2001) indicates that, injection of microbubbles prevents formation of sheet-like structure of the spanwise vorticity near the wall. The bursting phenomenon of turbulence is depressed as the streamwise vorticity (streamwise vorticity is considered to be created from the spanwise vorticity) is detached from the wall which causes weakening of streamwise vorticity. Accordingly, the low-speed streaks below the detachment position of the spanwise vorticity disappeared, in turn, the turbulent energy is reduced causing reduction in the frictional drag.

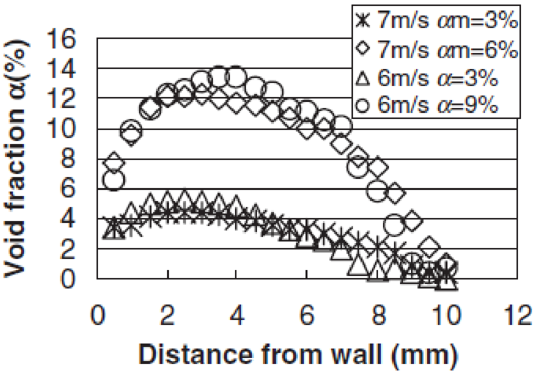

Figure 4 Distribution of Bubbles for different flow speeds (Moriguchi & Kato, 2002)

3. METHODOLOGY USED FOR MICROBUBBLE GENERATION AND INJECTION:

Since generating microbubbles needs energy, it is necessary to optimize the size of the bubbles and their distribution in the boundary layer in order to achieve a net gain in frictional drag reduction. It is anticipated that, bubbles larger than a certain diameter have no effect on frictional drag reduction (Kato, et al, 1998). Literature survey suggests that, following different methods were proposed and tested to generate smaller size of bubbles.

- Porous material (Figure 3)
- 2D convex shape with an ejection hole (Figure 5(a)
- 2D convergent-divergent nozzle with an ejection hole at the throat (Figure 5(b)
- Transverse wire (Figure 5(c))
- Change of Channel height at the point of Bubble Injection (Figure 6)
- Using an air injection plate with an array of air-injecting holes
- Foaming of dissolved water
- Use of Venturi tube

The most commonly practised method to generate microbubbles is by making use of Porous material, where in, air is injected into the flow through the porous medium. Although intuition suggests that, the pore size would be an important parameter, however, literature survey indicates that, the bubble size and in turn the reduction in the frictional drag is not determined primarily by the size of the pores used for injection, but by the characteristics of the flow. Madavan, et al, (1987) used two widely different pore sizes, 0.5mm and 100mm and found that, pore size does not have any substantial effect on the skin-friction results for the conditions tested. These results are of practical importance since with the larger-pore-size material, less energy is needed to inject microbubbles. (Yoshiaki, et al., 2000) pointed out that with porous material, generated bubbles do not uniformly distributed on the porous plate. In order to solve above problem, a new plate called plate with array of-holes was used (Yoshiaki, et al., 2000). From the experiment it is confirmed that, skin friction reduction by the array-of-holes plate is comparable to that by the porous plate. (Kato, et al, 1998) used three devices shown in Figure 5(a), Figure 5(b) Figure 5(c) for generating smaller size of bubbles. The bubbles downstream of the 2D convergent- divergent (Figure 5(b)) diffuse rather rapidly as the flow separates at the divergent part of the nozzle, which is completely undesirable. Among the three methods used, the 2D convex section shown in Figure 6(a) seems the best for drag reduction by microbubbles as the diameter of the bubbles became about one-third the size of the reference ejection on a flat plate.

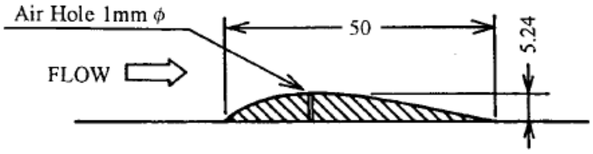

Figure 5(a) 2D convex section with air hole

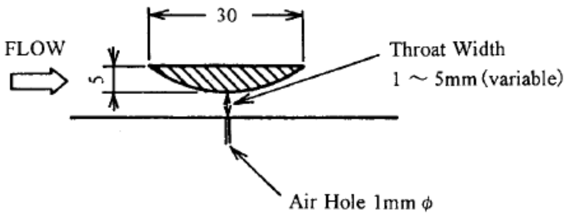

Figure 5(b) 2D convergent- divergent nozzle

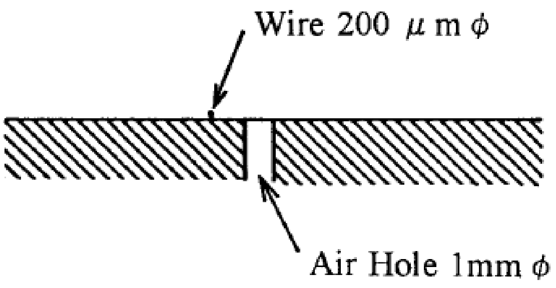

Figure 5(c) Transverse wire

Figure 5 Methods used for the generation of different sized Bubbles (Kato, et al, 1998)

Another way by which size of microbubbles was changed by using three different channels shown in Figure 6 (Moriguchi & Kato, 2002). To change size of microbubbles, flow velocity was altered by choosing different channel heights. Channel 1 has an air injection channel height of 10 mm, Channel 2 has an air injection channel height of 5mm and Channel 3 has an air injection channel height of 20mm. From the experiment it was found that, channel 2, where the channel height was small, generates smaller bubbles than other two channels. As shown in the Figure 7 and as per the empirical relation below, the mean microbubble diameter reduces as the main flow velocity at the injection point is increased.

$$\frac{d_b}{D_P} = 2.4\sqrt{\frac{Q}{UD^2}}$$

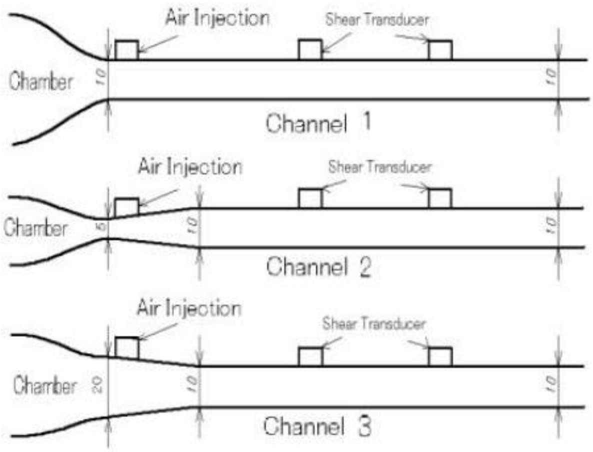

Figure 6: Change of channel height at the air injection point (Moriguchi & Kato, 2002)

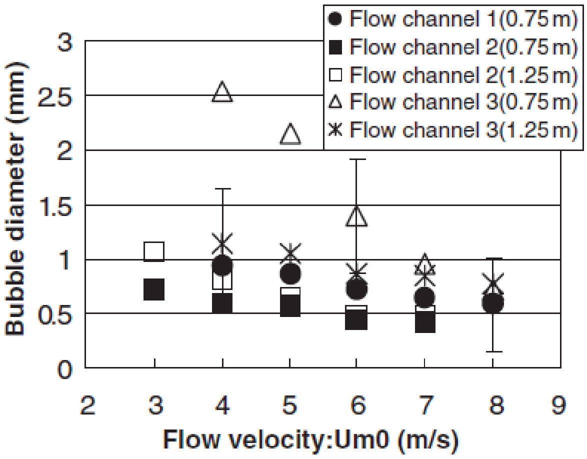

Figure 7 Effect of main flow velocity on mean microbubble Diameter (Moriguchi & Kato, 2002)

Technique with a convergent-divergent nozzle shown in Figure 8 known as venturi tube (Kitigawa, et al, 2005) & (Kawashima, et al, n.d) was introduced. As shown in Figure 8, the liquid velocity at the throat increases and the pressure is decreased, which in turn reduces the size of microbubbles.

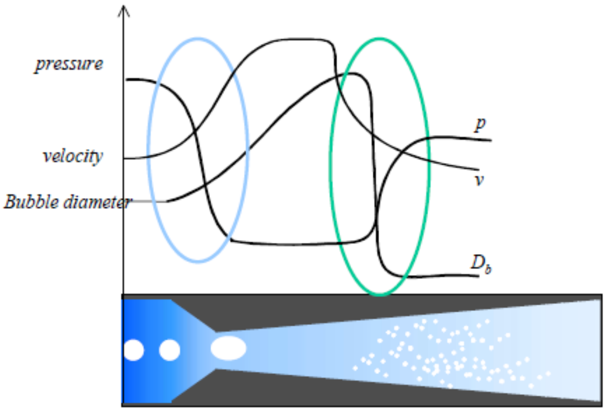

Figure 8 Schematic of venturi tube (Kitigawa, et al, n.d)

Another type of injector is used by (Shen, et al, 2006) to generate smaller bubbles is shown in Figure 9, wherein compressed nitrogen and lipid bubbles are forced through the injector by a manifold with seven evenly distributed ports in the cross-stream direction. As shown, the injector is also placed at angle of 15^0 to flow, which simply helps in evenly distribution of bubbles below the plate.

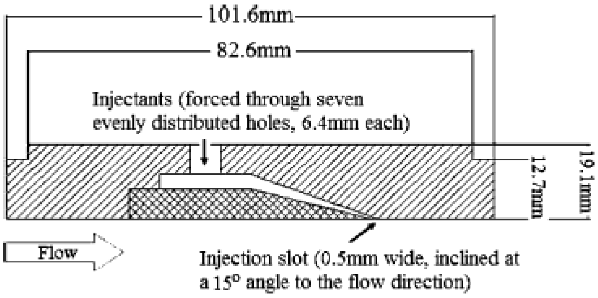

Figure 9 Cross-section schematic of the injector. (Shen, et al, 2006).

4. EFFECT OF VOID FRACTION ON DRAG REDUCTION

It has been proved experimentally and numerically that, MBDR depends on the air flow fraction or commonly known as Void fraction. In fact, research mentions MBDR in terms of void fraction. The air flow fraction or Void fraction is defined as the ratio of volumetric flowrate of air divided by the total flow rate in the boundary layer

$$\alpha_m = \frac{Q_a}{Q_a + Q_w}$$

Where, $Q_w = U(\delta - \delta^*)b$

Measurements of the cross-stream variation of the bubble volumetric concentration at various locations along the surface (Madavan, et al, 1984) & (Madavan, et al, 1983) concludes that, the bubble concentration starts from zero near the wall, increases rapidly to a peak value of 0.6 and at some locations increases to 0.8, and then falls off gradually again to zero in the free stream. For the plate above the boundary layer, substantial skin-friction reductions persist for some 35δ for low air flow rates and up to 60δ -70δ for high air flows. For the plate below the boundary layer, the reductions persist for somewhat shorter distance of 50δ. The persistence of the skin-friction reduction beyond the location of microbubble injection is a function of the gravitational orientation of the plate and the freestream velocity (Madavan, et al, 1985). The local void fraction was measured in an experiment (Kawashima, et al, n.d) & (Takahashi, et al, 2001). Typical observations are presented in Figure 10, which are in line to observations made by Madavan, et al, (1985).

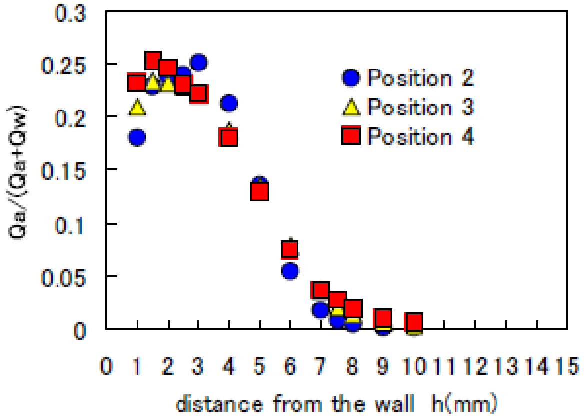

Figure 10 Local void ratio (Array-of-holes plates) (Takahashi, et al, 2001)

The local skin-friction measurements with microbubbles is generally presented in terms of the skin-friction coefficient, C_F, normalized to the corresponding skin friction coefficient without microbubbles, C_{F0} as a function of the void fraction as presented by (Kitigawa, et al, n.d), (Madavan, et al, 1985), & (Wu, et al, 2008). Typical variation obtained from the experiments is presented in Figure 11.

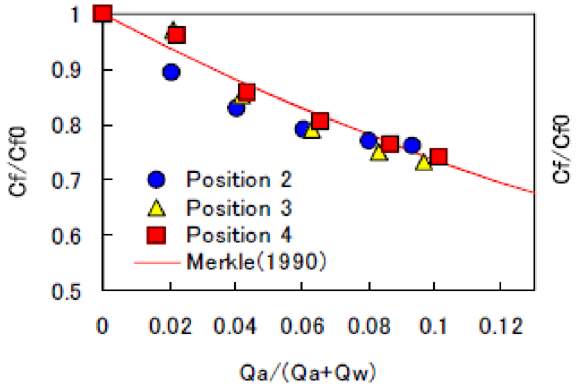

Figure 11 Skin friction reduction by (Moriguchi & Kato, 2002)

5. EFFECT OF FLOW RATE (AIR INJECTION) ON DRAG REDUCTION

As mentioned earlier, it is proved that, MBDR depends on the Void fraction. However, as per the formula of void fraction, it also depends on the injection flow rate of air. Thus, it is common interest of all researchers to understand the effect of changing flow rate on the frictional drag reduction. Figure 12 describes the relationship between the injection airflow rate and the drag reduction effect at different flow speeds (Wu, et al, 2008). As shown, as the airflow rate increases, the reduction effect increases. However, drag reduction effect start dropping when the airflow rate exceeds the critical value. Possible reason could be, excessive microbubble injection destroys the favourable turbulent boundary layer and in doing so decreases the drag reduction effect.

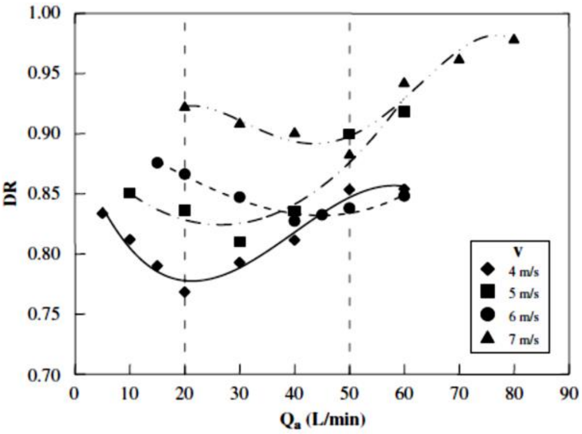

Figure 12 Effect of air injection on drag ratio (Wu, et al, 2008).

It is a common practise to express air injection flow rate into the air layer thickness using the expression

$$t_b = \frac{Q_a}{B_a U}$$

World's first trial on newly built carrier was conducted by (Mizokami, et al, 2010) in a seakeeping tank at MHI's Nagasaki Research & Development Centre. The trial test was carried out by varying air blow-off rate with the equivalent air thickness as 3mm, 5mm and 7mm. Table 1 shows the effect of air layer thickness on the drag reduction effect, which shows that, drag reduction effect increases with increasing air layer thickness and in turn on injection flow rate.

Table 1 Effect of Flow rate on Air Layer thickness and intern effect on Drag Reduction (Mizokami, et al, 2010)

Air Layer Thickness	**Net energy-saving effect**
7mm	12%
5mm	10%
3mm	8%

6. EFFECT OF BUBBLE SIZE DISTRIBUTIONS, COALESCENCE, STRATIFICATION AND DEFORMATION EFFECT ON DRAG REDUCTION

The intuition says that, the bubble size is one of the major factor which influences the reduction in the frictional drag. Actually, the bubble size depends on how the injected air or gas stream interacts with the local flow structure. From MBDR experiments carried out by (Shen, et al, 2006) (Winkel, et al, 2004), it is found that bubbles were generated by the injection of air or gas through either a slot injector or a porous plate. It is mentioned that; the importance of bubble size can be readily established by considering the ratio

$$d^+ = \frac{d_b}{l_v}$$

In TBL flows, the buffer region extends between $5y^+$ to $30y^+$ (where, $y^+ = \frac{y}{l_v}$ and y is the wall normal coordinate or normal distance from the wall or plate). If the bubbles injected in the buffer layer are smaller than or comparable to a viscous wall unit, then the bubbles will reduce the water density as they are smaller than the size of an overturning eddy. On the other hand, if the bubbles are much larger than $30l_v$, it may not be possible for them to alter the fluid momentum exchange in the buffer layer unless they are present in sufficient number to substantially increase the buffer layer thickness. In the nitrogen injection test (Shen, et al, 2006), the bubble size was varied from 476µm in fresh water, to 322µm in a 20ppm Triton X-100 solution, to 254µm in a 35ppt saltwater solution. From the experimental results, it is concluded that, MBDR is strongly related to the injected air or gas volumetric flow rate and the static pressure in the boundary layer and does not depend on the bubble size. Figure 13 shows the effect of the mean microbubble diameter on the frictional resistance reduction (Moriguchi & Kato, 2002).

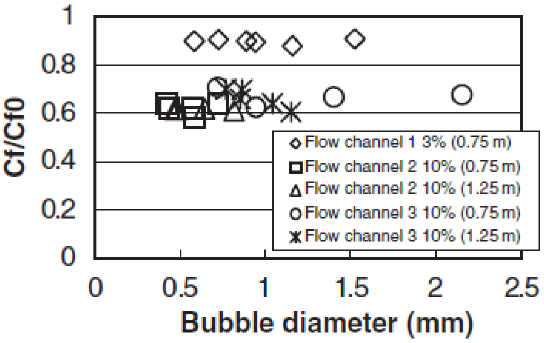

Figure 13 Effect of mean microbubble diameter on frictional resistance reduction (Moriguchi & Kato, 2002)

In another experiment by (Sanders, et al, 2006), bubble sizes and the extent of bubble coalescence was varied with downstream distance and flow speed. It is observed that, for slow speeds, the injected bubbles coalesced into an intermittent or continuous air film and at higher speeds, discrete bubbles were observed all along the plate. It is also observed that, for both lower and higher flow speeds, the mean bubble diameter increases by an average of about 30%, while the number density decreases by 50% to 80%. Contradictory observations were made by (Thomas, et al, 2016), where it is mentioned that, bubbles of a few millimetres in diameter increased the frictional resistance. It has happened possibly because of the turbulence generated by the wake of bubble. The research work also pointed that, the bubble size is a critical factor in deciding the drag reduction and it will be achieved when the bubble diameter is less than about 1 mm; and the drag reduction rate is generally higher when the bubble diameter is smaller. SR 239 Research Committee performed a full-scale experiment using the Seiun-Maru (Kato & Kodama, 2003). From the experiment, it is concluded that, the ejected air bubbles did not stay in the inner region of the boundary layer well and did not spread thinly over the hull but flowed like chimney smoke and they were slightly away from the hull surface. Also, it is interesting to note that, the air ejection rate was not maximum when the best result was obtained. By considering all these results, it is concluded that, the location of bubbles in the boundary layer is extremely important for the skin friction reduction. In other words, microbubbles are very effective in reducing skin friction, if they can be concentrated in the inner region of the boundary layer, close the wall.

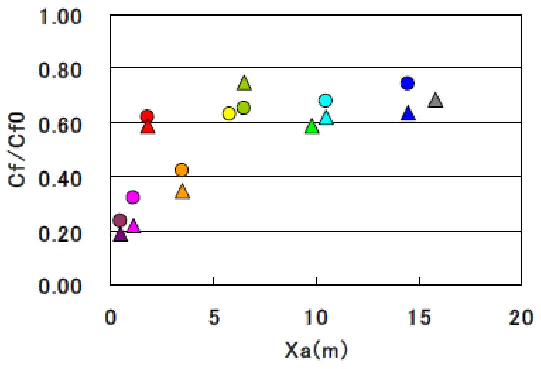

Figure 14(a) Streamwise direction

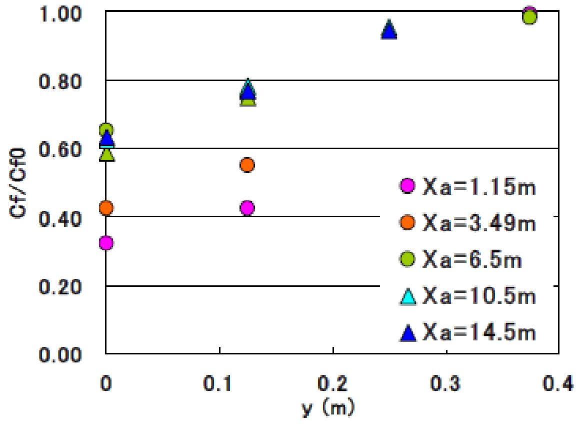

Figure 14(b) Spanwise direction

Figure 14 Distribution of skin friction (Kodama, et al, 2004)

As per the experiment conducted by (Kodama, et al, 2004) to determine the drag reduction effect in streamwise and spanwise direction, it is concluded that, as shown in Figure 14(a), the reduction effect quickly reduces at immediate downstream of injection and shows gradual reduction further downstream. As shown in Figure 14(b), there is no constant reduction region and that the reduction reduces linearly towards the side end spanwise, which suggests that injected bubbles steadily diffuse toward side ends and are lost steadily across them. It is also concluded that, the orientation of the wall also affects drag reduction. The wall-on-top condition gives the largest reduction. This can be easily explained by the fact that the bubble buoyancy favourably effects on the reduction. SWR surface paint was used by (Fukuda, et al, 2000), which is capable of forming a thin air film over an underwater surface and can stop the surface from becoming wet. Due to the surface tension of the water, the air film formed over the surface has the property of being able to take in air supplied. When air is supplied from the bow section to a ship's hull coated with SWR paint, it becomes attached to the SWR surface and forms an air film on it. Figure 15 shows a schematic view of a 7.2-m-long wooden scale model of a 280000-ton VLCC equipped with the SWR. The frictional drag on the SWR surface of the tanker bottom is reduced by about 40% at Froude number 0.20.

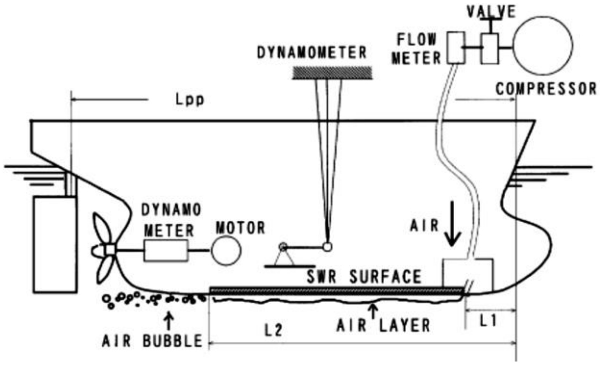

Figure 15 Schematic view of a model ship equipped with the SWR & A technique (Fukuda, et al, 2000)

7. EFFECT OF SURFACTANT SOLUTION AND SALINITY OF WATER ON BUBBLE SIZE FORMATION

It is also important to note that, for the application related to ships, friction drag reduction is sought mostly for the open sea with salt and other surfactants, majority of experiments on MBDR were conducted under laboratory conditions with fresh water. In a particular study carried out by (Shen, et al, 2006), under different aqueous conditions, it found that, the average bubble size was reduced by a factor of 2 in the surfactant solution and by a factor of 4 in saltwater. Table 2 gives the information about the bubbles sizes produced in different aqueous conditions, which clearly shows reduction in the diameter of bubbles produced with increase in the salinity of water.

Table 2 Basic properties of the bubble size for each drag reduction experiment (Shen, et al, 2006).

Aqueous conditions	**Mean (μm)**	**d^+**
Water nitrogen injection	476	200
20 ppm Triton X-100 nitrogen injection	322	134
35 ppt Saltwater nitrogen injection	254	106
Lipid bubble injection	44	18

Experiments were performed by (Winkel, et al, 2004) in freshwater (tap water), at four different concentrations of saltwater (Instant Ocean, Aquarium Systems), and at three different concentrations of a soluble surfactant (Triton-X-100, Union Carbide). Saltwater concentrations of 9, 19, 33 and 38 parts per thousand (ppt) were investigated.

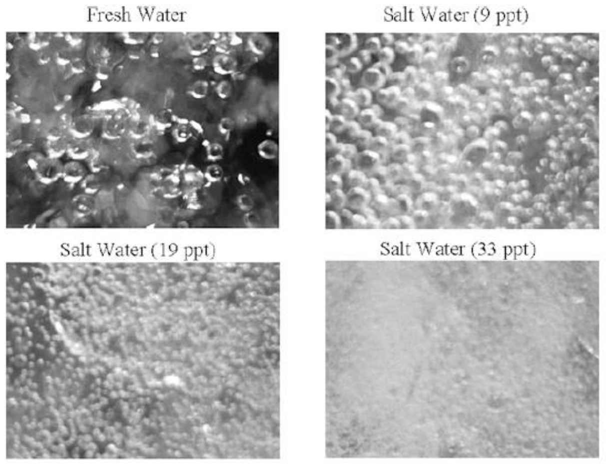

Figure 16 Sample photographs for all the bubble injection conditions tested (Winkel, et al, 2004)

Figure 16 Shows the sample photographs of bubble population, taken near the wall. From the photographs, it can be concluded that, as the solute concentration increases, the bubbles become smaller in size, and are also more evenly distributed over the viewing area. In another experiment conducted by (Takahashi, et al, 2001), CTAC was added to water with concentration up to 40ppm for the speed range up to 10m/sec. Figure 17 shows skin friction reduction as a function of average void ratio at three different CTAC concentration, at one speed of V=5m/sec. It is observed that, the effect of CTAC on skin friction reduction is very small at this flow speed.

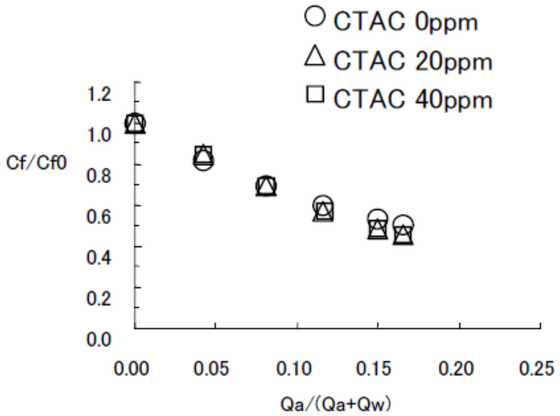

Figure 17 Relation between average void ratio and skin friction ratio ta v=5m/s sec (Takahashi, et al, 2001).

Winkel, et al, (2004) concluded that, one of the physical mechanisms for the reduction in bubble size is probably due to the ionic repulsion between bubbles in saltwater that prevents bubble coalescence near the injector reducing the mean bubble diameter with reduction in surface tension.

8. EFFECT OF POSITION OF MICROBUBBLE INJECTION POINT ON DRAG REDUCTION

Micro bubble injection location is one of the important parameters that need to be considered in reviewing the effectiveness of skin friction reduction by micro bubbles. Resistance tests of the 66K Supramax bulk carrier were performed at design draft to investigate MBDR effect (Yoshiaki, et al, 2000). Six air injection units that operate independently were analysed as shown in Figure 18. Figure 19 represents total percentage reduction in the ship's resistance (ΔR_{TM}) as compared to when air was not injected. It is understood that, a transitional air layer was well developed over the wide area of the bottom as shown in the captured image of Figure 20. However, it was observed that air leakage around the 12th station has caused an additional increase in the resistance by disturbing the flow around the hull.

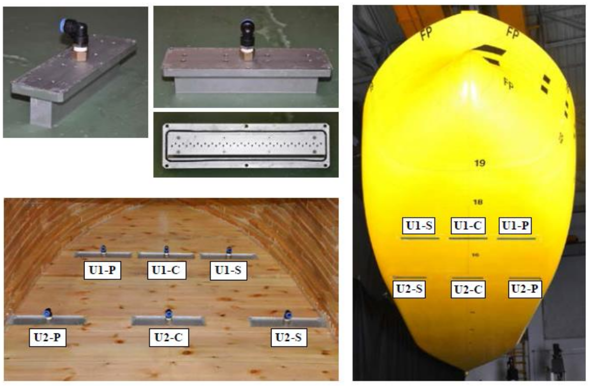

Figure 18 Arrangement of air injection units (Yoshiaki, et al, 2000)

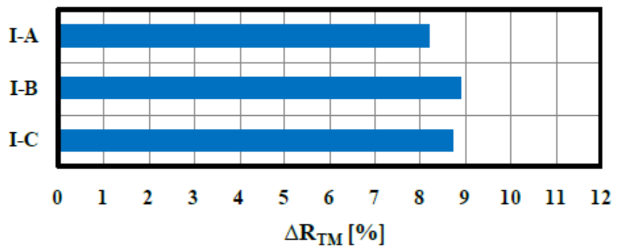

Figure 19 Reduction in the resistance and effective power at VS = 14.5knots (Yoshiaki, et al, 2000).

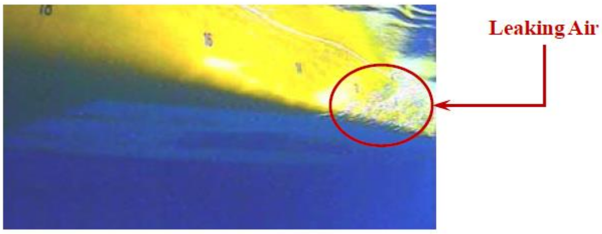

Figure 20 Captured air layer at VS = 14.5knots (Yoshiaki, et al, 2000)

Secondly, air was injected from the only centre injection units at the same towing speed as the previous case. These Results shown in Figure 21 conclude that, more resistance reduction was attained when air was injected from the centre units only, compared to the case of air injection from all units including the side. In other words, the side injection units did not make any contribution to the reduction in the resistance.

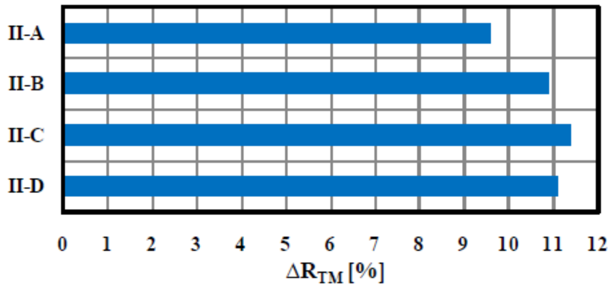

Figure 21 Reduction in the resistance and effective power at VS = 14.5knots (Yoshiaki, et al, 2000)

A series of model tests were conducted on a navy fast patrol boat (FPB) for a Froude number of up to 0.65 by (Sunaryo & Jamaluddin, 2012) and (Thomas, et al, 2016). The influence of the location of micro bubble injection and bubble velocity was investigated in both experiments. Figure 22 shows the lines plan for test model and the positions of bubble injectors placed behind the mid-ship. Positions varied from position 1, position 2, and position 3. These positions were investigated and compared regarding the influence of micro-bubble injection. Position 1 was 5 cm in front of the midship, position 2 was exactly at midship, and position 3 was 5 cm behind the midship. From the experimental results as shown in Figure 23, it was found that, the ship model with bubble injection at position 3, has a smallest value of C_T and found that the skin friction reduction is highest when the position of bubbles was located at the rear. It is clear that drag reduction for position 3 is greater than position 1 and position 2.

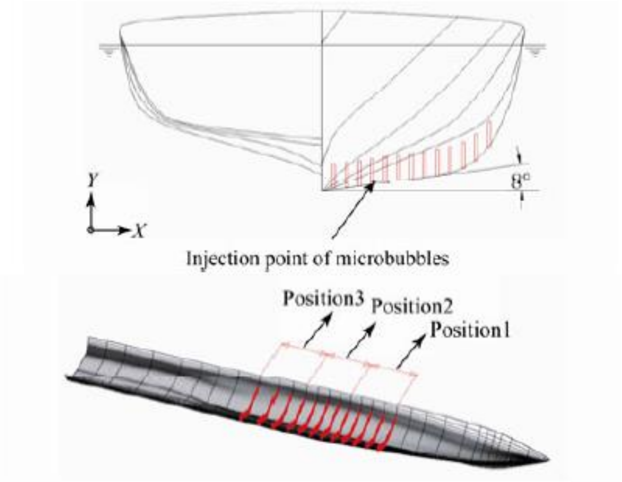

Figure 22 Lines plan and positioning bubble injector (Sunaryo & Jamaluddin, 2012)

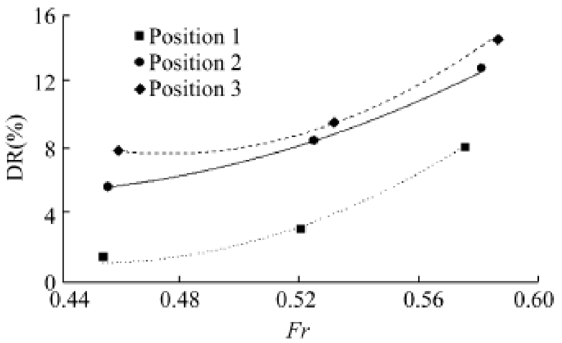

Figure 23 Relationship between drag reduction and Froude Number (Sunaryo & Jamaluddin, 2012)

9. EFFECT OF DEPTH OF WATER ON REDUCTION IN FRICTIONAL DRAG

In the nitrogen injection test by (Shen, et al, 2006), the bubble size was varied from 476 µm in fresh water, to 322 µm in a 20 ppm Triton X-100 solution, to 254 µm in a 35 ppt saltwater solution. From the experimental results placed at Figure 24, it can be concluded that, the most important parameter in determining MBDR effect is the effective gas phase volumetric flow rate, which is influenced both by the injection rate and the static pressure under the test conditions i.e. the pressure of water flow. Increasing the static pressure causes the volumetric flow rate of the injected gas phase to decrease proportionally. These results show that when using void fraction to compare MBDR results, the gas volumetric inflow rate must be corrected for the static pressure in the test section. Moreover, the efficiency of the same would decrease significantly with increasing depth if all other parameters are held constant.

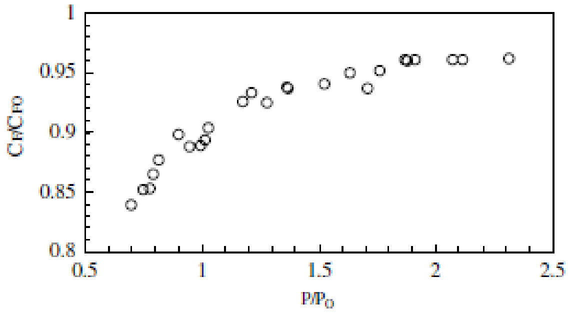

Figure 24 Effects of static pressure on friction drag reduction. Tap water with nitrogen injection, plate-on-top (Shen, et al, 2006)

As per the study carried out by (Yoshiaki, et al, n.d), to increase the MBDR effect, it is recommended to increase Froude number based on depth of water, which is given by $F_d = \frac{U}{\sqrt{gD}}$. It suggests that, either increase the flow speed and/or operate the vessel in shallow water, as it may require less work for the injection of air. (Mäkiharju, et al, 2012) stated that, the cost of pumping the air goes up with the square of the draft, since an increase in draft increases both the back pressure against which the compressor or blower must work, and the required mass flux of air and the gas volume must be compressed when injected into the higher-pressure flow beneath the hull.

10. EFFECT MICROBUBBLES ON THE PERFORMANCE OF PROPELLER

It is anticipated that, injection of bubbles below the hull will interfere with the operation of propeller and may reduce its efficiency. It is also expected that, it might increase the cavitation effect. Considering above, researchers worldwide are keen in finding out the effect. To investigate effects of air layers on the propulsion performance, self-propulsion tests of the 66K Supramax bulk carrier were performed by (Jinho, et al, 2014). From the experimental result, it is detected that, the axial velocity increased significantly and the nominal wake fraction, has reduced. Moreover, it was observed that, downward flow in the upper area of the propeller shaft has reduced. It is thought that, increase in the momentum of the flow along the hull bottom by the reduction in frictional drag accelerated flow into the propeller plane and this might have led to the reduction in the propeller thrust and torque. Experimental results also confirm that, relative rotative efficiency is reduced by less than 1%, hull efficiency decreased by about 5~6%, but open water efficiency increased by about 5% as the propeller loading was reduced. Consequently, the quasi-propulsive efficiency was reduced by about 0.6~0.9% and finally, the delivered power was reduced by 7~9.5%. Similar observation was made (Kato & Kodama, 2003), where the efficiency of the propeller was reduced by 3%-6% by the air ejection. It is opined that, the reduction in the thrust generated by the propeller was due to the reduction in the density of flow by injection of air. From the study by the Mitsubishi Air Lubrication System (MALS) (Kawabuchi, et al, 2011), significant observations were made. It was found that, the amount of air bubbles flowing into the propeller disk area decreased as the air bubble diameter increased. This may have been due to the buoyancy force, which increased with the air bubble diameter. However, the peak position of the void fraction did not vary substantially with the air bubble diameter. Judging from the average void fraction distribution on the propeller disk, the propeller efficiency of this ship remained nearly unchanged by the bubbles. Furthermore, it is predicted that, the intrusion of bubbles on the area of propeller disks, which could deteriorate the performance, and confirmed that the deterioration in propeller disk performance was negligible. Experiments have been performed by (MARIN, 2011) on ships with and without air-bubble injected at model and full scale. The results of model scale experiments showed a small increase in resistance and a small increase in propulsion efficiency, both around 1-2%. A trial with the ship with air injection at full scale showed 2.6% reduction in required propulsive power with air.

11. NET SAVINGS IN POWER CONSIDERING POWER REQUIRED TO INJECT MICROBUBBLES AND EFFECT ON PROPELLER PERFORMANCE

In order to evaluate the applicability of MBDR method to ships, it is essential to discuss its net drag reduction effect by taking into account the energy required to inject air or gas bubbles into water. Simplest format for estimating the net savings in the work, was given by (Kodama, et al, 2004).

$$Savings_{net} = \frac{W - W_{Pump}}{W} = \frac{(\Delta W)}{W}$$

Using the equations derived above, net savings in power for the cement carrier was estimated and it was found that, the drag of the ship in the fully loaded condition decreased by 7.38%. The pumping power needed for injecting air was found to be 1.94% and hence the net power-saving found to be 5.44%. Yoshiaki, et al, (n.d) proposed modified and upgraded methodology to predict net power savings, wherein, it was proposed to calculate net work (r_w) ratio as follows

$$r_w = \frac{W_{net}}{W_o} = \frac{R_T U + W_{Pump}}{R_{TO} U} = \frac{R_T}{R_{TO}} + \frac{W_{Pump}}{R_{TO} U}$$

Where,

r_w=1.0 when net drag reduction is zero
r_w<1.0 when there is drag reduction effect

W_{Pump} is expressed by taking into account energy loss due to head pressure at injection point and the local pressure there. Ship's Drag in non-bubble condition can be expressed in conventional non-dimensional form

$$R_T = [(1+K)C_{Fo} + C_W] * \frac{1}{2}\rho S U^2$$

Thus, by putting relevant expressions, we get

$$r_w = \frac{R_T}{R_{TO}} + \frac{W_{Pump}}{R_{TO}U}$$

$$r_W = \frac{r_D + \frac{\overline{C_{FO}}}{C_{FO}}}{1 + r_D} + \frac{Q_a}{SU_\infty}\frac{C_P + \frac{2}{F_d^2}}{(1+K)C_{FO}(1+r_D)}$$

Where,

$$r_D = \frac{C_W}{(1+K)C_{FO}}$$

Based on the experiments carried out by (Jinho, et al, 014), as shown in Figure 25, the net power savings, was estimated to be 5~6% in the speed range of 13.0~16.0knots, which is in line to observations made earlier.

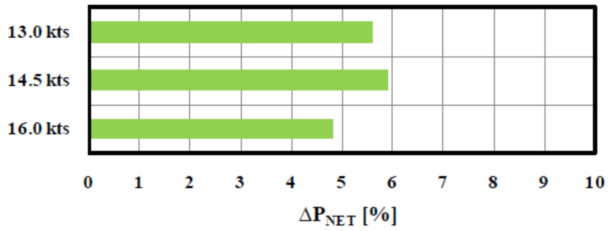

Figure 25 Net power savings at mean tAL = 8.2mm (Jinho, et al, 2014)

Mäkiharju, et al, (2012) presented an energy cost-benefit analysis for ALDR and PCDR for a ship with a large flat bottom. It was assumed that the ship's form drag is not appreciably changed by the air injector and the air layer persists along the entire length of the hull. Only the fraction of the ship's energy consumption for propulsion is considered in order to develop the possible net power savings, $\%P_{saved}$, compared to the power consumption required to pump the lubricating air:

$$\frac{\%P_{Saved}}{100} \cong \frac{P_{saved}}{P_D/\eta_{Prop}}$$

The net work ratio is estimated for a large tanker with 300m length and the speed of 14kts (Yoshiaki, et al, n.d). From the experimental and theoretical analysis, the net work ratio was calculated as 1.078, which is slightly greater than 1, which means that net drag reduction is not obtained. On the other hand, in the ballast condition (empty condition), the draft reduces and hence the r_W reduces to 0.979, approximately 2% net reduction was obtained. This means that, a tanker that runs between Japan and the Middle East can get net drag reduction one way. If the amount of air can be economized to half, the net work ratio becomes 0.952 even at full load condition. In general, in order for an energy-saving effect not to be embedded into measurement errors, it has to be 5% at least. This rough estimation suggests that, in order to put microbubbles into practical use, it is necessary to improve drag reduction efficiency at least twice as much and/or to combine the technique with other efforts such as developing a new hull form suited for microbubbles like one with very shallow draft and very wide flat bottom.

12. NUMERICAL INVESTIGATION ON CHANNEL FLOW

The experimental study was conducted by (Moriguchi & Kato, 2002) using recirculating water channel as shown in Figure 26. The test section, which is 10 mm high, 100 mm wide, and 2000 mm long generates a fully developed turbulent flow. Compressed air is injected into the channel for different flow rates and its effect is measured using shear stress transducers placed at 750mm and 1250mm from the injection point. Similar setup is used here to enhance the study using CFD technique. 3D numerical investigations into frictional drag reduction by microbubbles are carried out in Star CCM+ in a channel for different flow velocities, different void fraction and for different cross sections of flow at the injection point. The experimental investigation was carried at only two longitudinal locations and no observation was made at spanwise locations, which is easily possible in CFD technique. In the numerical setup, microbubbles were injected through series of holes of 1mm in diameter in the test section at the upstream upper surface, generating air–liquid flow. Coefficient of friction and void fraction values were measured at 12 longitudinal positions and at each longitudinal position, 11 in number transverse and depth wise positions were observed. In all, for one simulation, data at more than 1000 positions were collected. Simulations were performed at flow velocities ranging 4–7 m/s in the interval of 1 m/s, and at different air flow rate (12 values of Void fraction). More than 60 simulations were carried out to study the effect of these flow parameters on coefficient of friction. Effect on C_F was also studied by changing the depth of channel at the injection point, which changes flow parameters.

12.1 NUMERICAL SETUP & VALIDATION WITH EXPERIMENTAL RESULTS

The numerical and mesh setup used for this exhaustive study is shown in Figure 26 & Figure 27. Grid independency study was also carried out to optimize and finalize the meshing. Initially, uniform mesh was generated throughout the channel, which, based on flow regime of air bubbles, is optimised for the further study. Dense meshing was generated for both with and without injection of air till no change in final result is obtained. Optimized mesh is shown in Figure 27. For the simulation of three-dimensional, Implicit Unsteady Segregated flow, Volume of Fluid (VOF) approach was used to solve Reynolds Average Navier-Stokes Equations (RANS) and Eulerian multiphase equations of state with multiphase interactions based on density and surface tension of air and water. To account for the Boundary layer effect, Exact wall distance, Two layer all y+ wall treatment and Realizable K-Epsilon Two Layer approach was effectively utilised. For the simulation of Turbulence, K- Epsilon Turbulence model was used. Velocity inlet boundary condition was used to setup the flow velocity of water at water inlet boundary. Similarly, for setting up of air inlet, mass flow rate boundary condition was used. At the outlet, pressure outlet boundary condition is used. For all other sides of channel, typical wall boundary condition with No Slip condition was used.

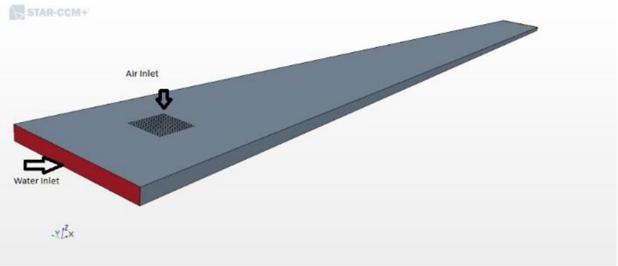

Figure 26 Geometry used for simulations

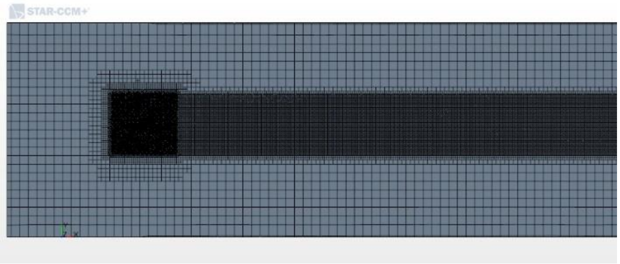

Figure 27 Optimised Mesh used for simulations

Figure 28 shows the comparison of C_{FO} values with experiment without injection of air at a location of 750mm from the injection point. Moreover, Figure 29 & Figure 30 shows the comparison of reduction in C_F values with experimental values, with and without injection of air at flow speed of 5m/s & 6m/s respectively. Here C_{FO} refers to coefficient of friction without the injection of bubbles and C_F refers to coefficient of friction with the injection of bubbles. Results obtained through CFD studies are in accordance with results obtained by experiments carried out by Moriguchi, et al, (2002), Kato, et al, (1998) and Madavan, et al, (1984).

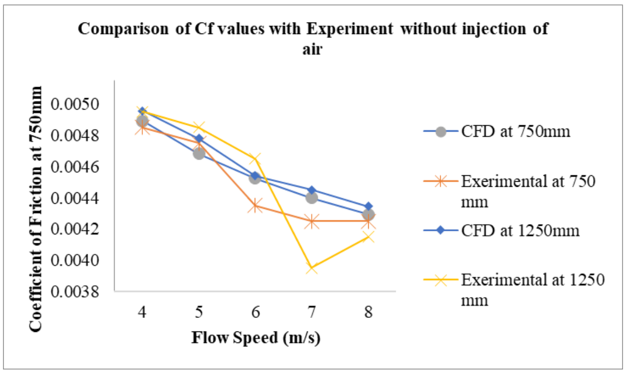

Figure 28 Comparison of CF values with experiment without injection of air

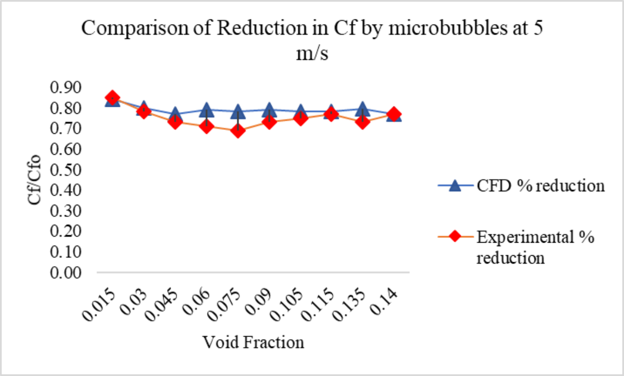

Figure 29 Comparison of reduction in CF with experiment, with and without injection of air at flow speed of 5m/s

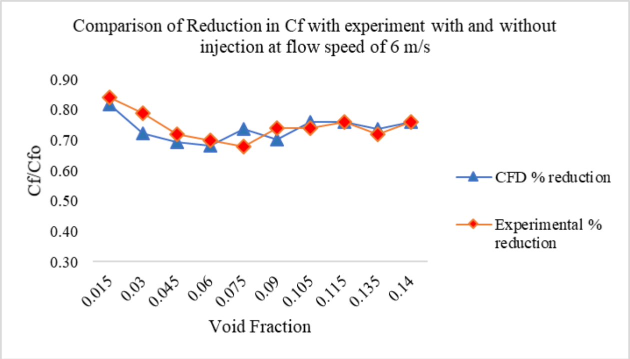

Figure 30 Comparison of reduction in CF with experiment, with and without injection of air at flow speed of 6m/s

12.2 VARIATION OF CF VALUES IN THE LONGITUDINAL DIRECTION FOR DIFFERENT SPEEDS & VF

Investigation on effect of flow speed on MBDR effect in longitudinal direction for different void fraction was carried out. From the Figure 31 & Figure 33, it can be concluded that, for Void fraction values of 3% and 9%, in general, MBDR effect is more for flow speed of 5m/s giving lowest values of coefficient of friction. However, as shown in Figure 32, MBDR effect was found to be maximum at higher speed of 7m/s at void friction of 6%. In most of the cases, MBDR effect reduced with increase in distance from the injection point, except for few cases at Void fraction of 9%, where in, MBDR effect increased from a point having distance 800mm onwards for speed of 7m/s and 600mm onwards for 4m/s. Reason for the same may be, as the distance increases in the longitudinal direction, bubbles coalesce with each other and form air pockets. This is the major reason for variation in C_F values in longitudinal direction, as bubbles coalesce to form air pockets avoiding any contact of water with the surface and thus reducing the coefficient of friction.

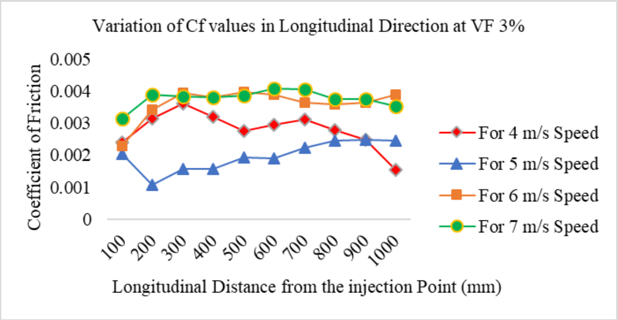

Figure 31 variation CF values in longitudinal direction for different flow speeds at VF of 3%

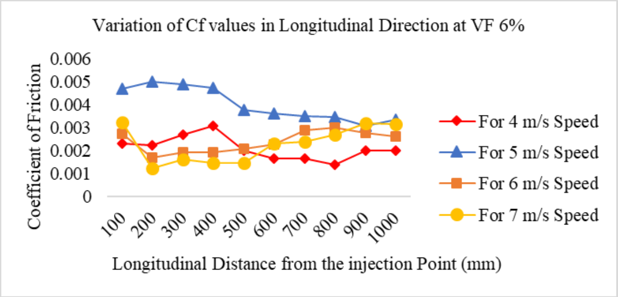

Figure 32 variation CF values in longitudinal direction for different flow speeds at VF of 6%

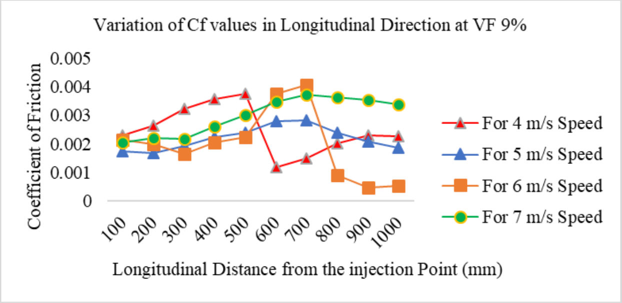

Figure 33 variation CF values in longitudinal direction for different flow speeds at VF of 9%

12.3 VARIATION OF C_F VALUES IN TRANSVERSE DIRECTION FOR DIFFERENT SPEEDS & VF

Similar investigation on effect of flow speed on MBDR effect in transverse direction for different values of void fraction was carried out. From the Figure 35 & Figure 36, it can be concluded that, for Void fraction values of 6% and 9%, MBDR effect is reduced with increase in distance from the injection point. For the case at Void fraction of 3% (Figure 34), similar observation was made for lower speeds of 4m/s and 5m/s, however, at higher speeds, due to more turbulence created, air bubbles distributed more in spanwise direction, causing increase in MBDR effect in spanwise direction.

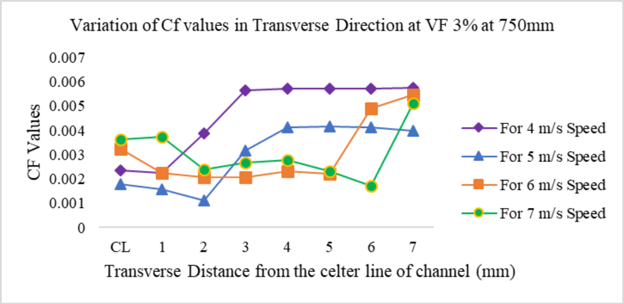

Figure 34 Variation CF values in Transverse direction for different flow speeds at VF of 3%

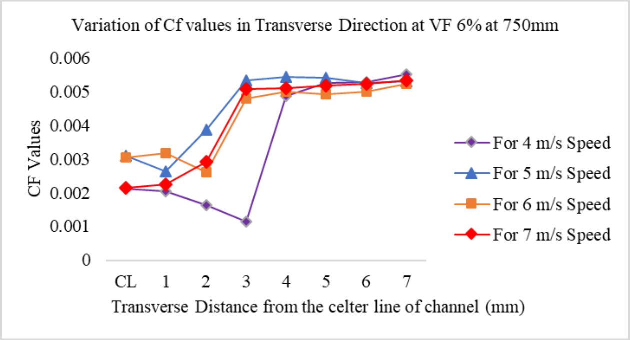

Figure 35 variation CF values in Transverse direction for different flow speeds at VF of 6%

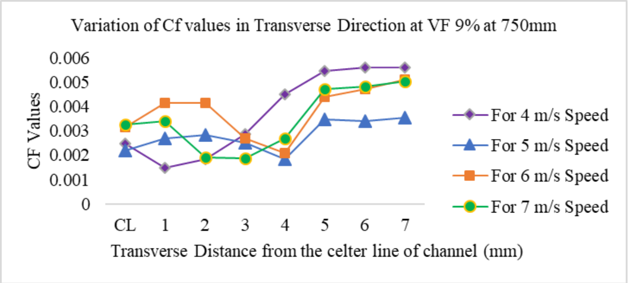

Figure 36 variation CF values in Transverse direction for different flow speeds at VF of 9%

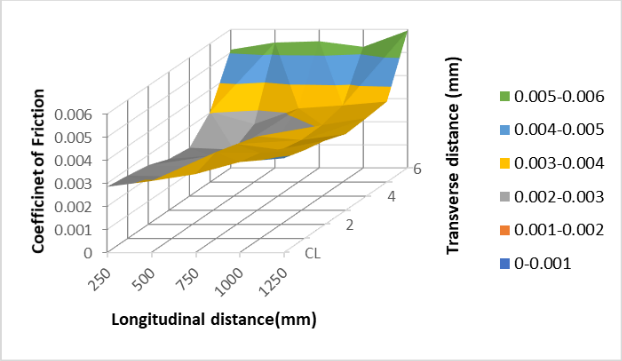

Figure 37 Variation of CF values at different longitudinal and transverse locations at flow speed of 6m/s and VF 11.5%

Figure 37 describes Variation of C_F values at different longitudinal and transverse locations at flow speed of 6m/s and VF of 11.5%, which clearly shows that, C_F value increases with increase in longitudinal and transverse distance from the air injection point. Moreover, it can be seen that, there is a variation in C_F values in longitudinal direction, which is mostly due to coalescence and breaking of bubbles with the distance from the injection point. To conclude, MBDR effect quickly reduces in the streamwise direction at immediate downstream of injection and gradually decreases further downstream. In the spanwise direction, there is no constant reduction region and the reduction effect reduces linearly towards the side end. Figure 38 describes the Longitudinal variation of C_F values for different values of void fraction. From the Figure 18, it can be concluded that, C_F value decreases till void fraction of 7.5%, beyond which, these values start increasing. This may be due the fact that, additional turbulence created by the injection of air bubbles. To conclude, as the MBDR effect depends upon the presence of Microbubbles, C_F values keep varying from point to point and do not follow a particular pattern.

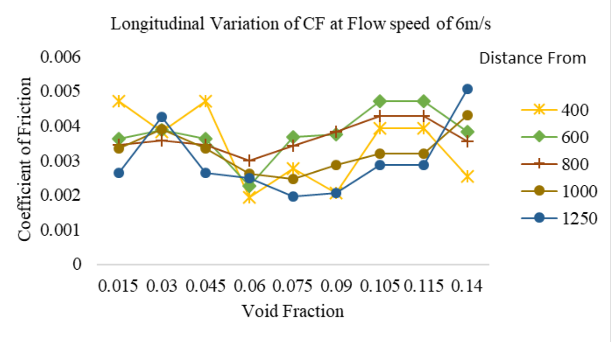

Figure 38 Longitudinal variation of CF at flow speed of 6m/s and different void fraction

To conclude, the distance from the injection point is the most important parameter in obtaining the reduction in frictional drag, and that the boundary layer thickness of top plate has little effect on the skin friction reduction by microbubbles. MBDR effect mostly depends on local void fraction than the injection void fraction. Local void fraction depends on the coalescence and breaking of bubbles. Formation of air pockets increases the local void fraction and in turn reduces coefficient of fraction, which has been found in many cases, where in, MBDR effect was found to be more after certain distance from the injection point

12.4 INVESTIGATION OF ALTERATION OF FLOW PARAMETERS AND C_F VALUES FOR DIFFERENT DEPTHS OF CHANNEL AT THE INJECTION POINT

It is well known fact that, diameters of microbubbles generated depends on the flow parameters at the injection point. Hence to investigate this effect, three different channels as used in experiments by (Morguchi & Kato, 2002) are modelled here in the CFD study. All three channels have the same test section height of 10 mm throughout the length except at the injection point. Channel 1, 2 & 3 have channel heights of 10mm, 5mm and 20mm at the injection point respectively. Channel 2 and Channel 3 are shown in Figure 39 along with velocity distribution throughout the length. Investigation has been carried out to check the changes in MBDR effect due to this variation in flow parameters for three different speeds of 5m/s, 6m/s and 7m/s at constant volume fraction of 6%.

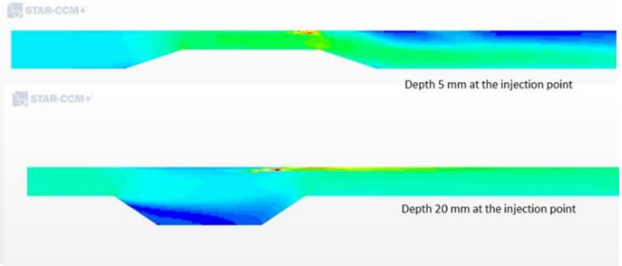

Figure 39 Channel 2 & 3 with velocity distribution

Figure 40 shows the variation of Void Fraction and in turn distribution of microbubbles for different depths of channel at the injection of point. As seen from the figure, for 5mm depth of the channel, due to reduction of pressure at the injection point, flow velocity increases which in turn causes increase in turbulence. This is forcing microbubbles to widely distribute in transverse direction and giving equal reduction in frictional drag in the transverse direction as well.

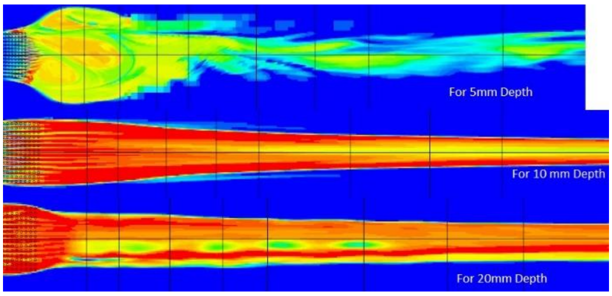

Figure 40 Variation of Void Fraction for different depths at the injection of point

Figure 41 depicts the variation of Turbulent Kinetic Energy for different depths at 750mm from the injection point. From the distribution, it is confirmed that, for 5mm depth of channel, as more number of bubbles are distributed in spanwise direction, turbulent kinetic energy reduces and for 20mm depth of channel, the same is increased due to injection of air. This implies that, out of three channels tested, channel with depth of 5mm gives best results to reduce frictional drag.

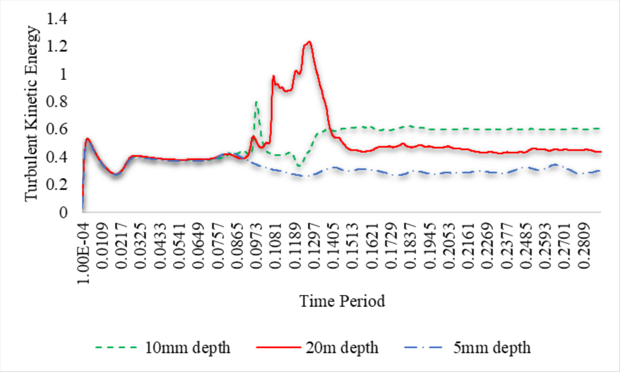

Figure 41 Variation of Turbulent Kinetic Energy for different depths at 750mm from the injection of point

Figure 42, Figure 43 & Figure 44 shows variation of C_F values in Transverse Direction at 750mm from the injection point and at constant value of Volume Fraction of 6% for different Flow Speeds of 5m/s, 6m/s and 7m/s respectively and of course for different depths of channel. From these figures, it can be safely concluded that, 5mm depth at the injection point gives best results for the MBDR effect, attaining minimum values of Coefficient of friction. Moreover, it can be seen that, for 5mm depth of channel, MBDR effect is almost equal in transverse direction. Also, it can be observed that, MBDR effect is maximum for lower flow speed of 5m/s as compared to other speeds. At higher flow speeds, additional turbulence created is increasing the turbulent viscosity and in turn the Reynolds stress.

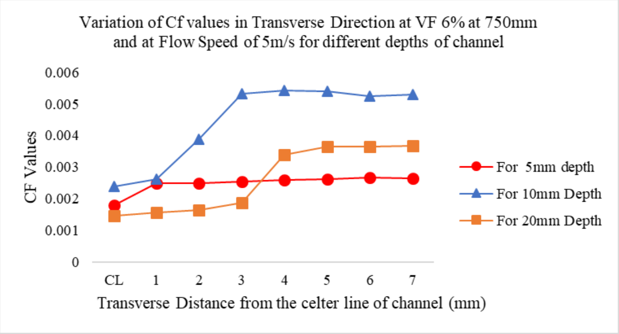

Figure 42: Variation of CF values in Transverse Direction at VF 6% at 750mm and at Flow Speed of 5m/s for different depths of channel

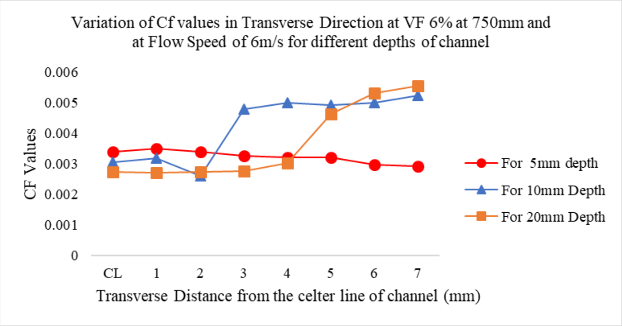

Figure 43: Variation of CF values in Transverse Direction at VF 6% at 750mm and at Flow Speed of 6m/s for different depths of channel

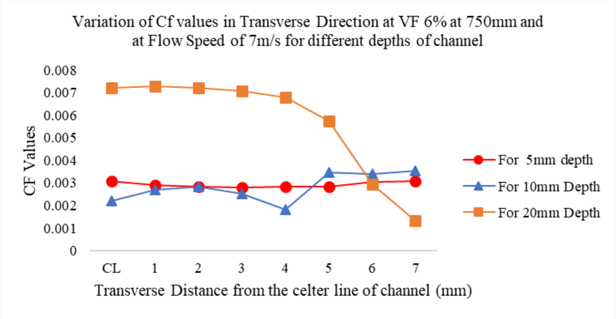

Figure 44 Variation of CF values in Transverse Direction at VF 6% at 750mm and at Flow Speed of 7m/s for different depths of channel

13. SUGGESTIONS TO IMPROVE THE DRAG REDUCTION/ FUTURE SCOPE FOR RESEARCHERS

Based on the exhaustive investigation carried out on MBDR studies carried out in past, following proposed concepts/opinions can become significant in increasing MDDR effect.

- As mentioned in the expression of net-work ratio (r_w), it is recommended to reduce ratio of wave drag to viscous drag (r_D), which implies that, one must choose a hull form that has small wave drag. The hull form of a large tanker is regarded suitable for MBDR method, as it has flat and very wide bottom, which will help the bubbles injected at the bow will stay close to the bottom due to the action of buoyancy.
- To increase MBDR effect, increase $F_d = \frac{U}{\sqrt{gD}}$, which can be implemented by reducing the depth at which the air bubbles needed to be injected.
- Moreover, reduce C_P, i.e., inject air at a location that has low pressure. This implies that, a ship operating in shallow water with micro bubbles injected will provide better results for MBDR method as compared to same ship operating in deep water.
- To re-develop or re-calibrate bubble coalescence based on the flow conditions.
- In the future, one can expect to carry out a detailed investigation into the bubble deformation effect to comprehensively clarify the mechanism of the frictional drag reduction due to microbubbles.
- Many researchers have struggled to investigate the effectiveness of micro bubbles on ships. Further research should be continued to enable the development of modification of turbulent boundary layer and thus increasing the ship efficiencies.
- Further studies of the hull features on the air-cavity boat performance, including aftbody deadrise, wetted skegs with finite width, multi-cavity setups, and propulsor is needed.
- Contradictory conclusions have been made based on the experimental results, which suggests that, there may be reduction in propulsive efficiency due to

microbubble injection. This needs further investigation.
- Experimentally validate the simulation results using towing tank experiments of ship model.
- One of the major problems faced in air lubricated methods is the uncontrolled bubble migration resulting in spending more energy for continuous bubble injection, which needs an urgent attention.
- Effect of SWR paint on the reduction can be further investigated, as, it is projected that, microbubbles will stick to the paint, however, it may also force liquid to stick to the paint and thus may increase the drag.
- Further study on comparison of reduction in drag by injecting bubbles at forward and/or midship of hull or at different locations may be carried out. Authors are of the opinion that, to increase effectiveness of MBDR, researchers can increase locations of injection points below the hull, which obviously needs further study.
- To study the effect of ALS in restricted area viz. motion in shallow water, restricted channel on reduction of frictional drag. Authors are of the opinion that, increase in drag for Inland and Coastal vessels where ship motion is restricted by channel width or depth will be compensated by reduction in friction frictional drag by MBDR. Moreover, motion in restricted area will assist the proper distribution of air bubbles below the hull.
- To Investigate the effect of microbubbles on the performance of propeller, cavitation and in turn the erosion, vibration, rudder control force reduction, echo sounder used by naval and research vessels.

14. CONCLUSIONS

The frictional resistance forms an integral part of total resistance of displacement ship of medium and low speed. Numerous technologies (Sindagi, et al, 2016), have been studied in past and utilized to reduce the frictional drag of a surface. It is concluded that, MBDR has added advantages over other drag reducing technologies, such as environmental friendly, easy operations, low costs and high saving of energy. It is also reported that, the MBDR is able to achieve 80% reduction in frictional drag, which can result in a substantial fuel savings for both commercial and naval ships. Literature review on MBDR suggests that, the skin friction reduction behaviour is a complicated phenomenon and depends on many factors such as Gas or Air Diffusion which depends on, Bubble size distributions and coalescence, which in turn depends on salinity of water, void fraction, location of injection points, depth of water in which bubbles are injected. To summarize, following inferences can be really vital in understanding the applying the methodology to reduce the frictional drag:

- Review opined that, MBDR effect is due to the alteration of local effective viscosity and density of the fluid which might reduce the Reynold's Stress. Bubble Stratification, near wall Phase composition, reduction of Turbulence intensity in the Streamwise direction, prevention of formation of spanwise vorticity near the wall are the other possible reasons.
- Diameter of bubbles depends mainly on flow parameters, which reduces by reducing the pressure at the point of injection. Pressure reduction can be achieved changing the height of channel or diameter of pipe at the injection point or by using venture tube.
- Detailed investigation on Bubble sizes and shapes after injection indicated that, bubble splitting is not dominant, however, bubble coalescence must be more prevalent as bubbles move downstream.
- MBDR effect quickly reduces in the streamwise direction at immediate downstream of injection and gradually decreases further downstream. In the spanwise direction, there is no constant reduction region and the reduction effect reduces linearly toward the side end. This suggests that, injected bubbles steadily diffuse toward side ends and are vanished steadily across them.
- The distance from the injection point is the most important parameter in obtaining the reduction in frictional drag and that the boundary layer thickness has little effect on the skin friction reduction by microbubbles
- It is found that the most important parameter in determining the fraction of drag reduction during gas injection is the effective void fraction, which is influenced by both, the injection rate and the static pressure under the test conditions.
- The formation of smaller bubbles, for the same gas injection rate, increased drag reduction when surfactant or salt exists in the aqueous environment.
- The reduction increases with increasing ship's length, as the benefit of the air injection extends to a greater fraction of the ship area downstream. Moreover, the cost of pumping the air goes as the square of the draft, since an increase in draft increases the back pressure against which the compressor or blower must work.

19. REFERENCES

1. ARNDT, R., HAMBLETON, W., KAWAKAMI, E. & AMROMIN, E. L., 2009. *Creation and Maintenance of Cavities Under Horizontal Surfaces in Steady and Gust Flows*. Journal of Fluids Engineering, Volume 131.
2. BUTUZOV, A., 1967. *Artificial cavitation flow behind a slender wedge on the lower surface of a horizontal wall.*. Fluid Dynamics, Volume 3, pp. 56-58.
3. BUTUZOV, A., SVERCHKOV, A., POUSTOSHNY, A. & CHALOV, S., 1999. *State of art in investigations and development for the ship on the air cavities*. China, International Workshop on Ship Hydrodynamics.

4. CECCIO, S. L., 2010. *Friction Drag Reduction of External Flows with Bubble and Gas Injection*. Annual Review of Fluid Mechanics, Volume 42, pp. 183-203..
5. ELBING, B. R. et al., 2008. *Bubble-induced skin-friction drag reduction and the abrupt transition to air-layer drag reduction*. Journal of Fluid Mechanics, Volume 612, pp. 201-236.
6. FOETH, E., n.d. *Decreasing frictional resistance by air lubrication*. Netherlands, 20th International Hiswa Symposium on Yacht Design and Yacht Construction & Maritime Research Institute of the.
7. FUKUDA, K. et al., 2000. *Frictional drag reduction with air lubricant over a super-water repellent surface*. J Mar Sci Technol, Volume 5, p. 123–130.
8. GOKCAY, S., INSEL, M. & ODABASI, A. Y., 2004. *Revisiting artificial air cavity concept for high speed craft*. Ocean Engineering, Volume 31, pp. 253-267.
9. JINHO, J. et al., 2014. *Experimental investigation of frictional resistance reduction with air layer on the hull bottom of a ship*. Int. J. Nav. Archit. Ocean Eng, Volume 6, pp. 363-379.
10. KANAI, A. & MIYATA, H., 2001. *Direct numerical simulation of wall turbulent flows with microbubbles*. Int. J. Numer. Meth. Fluids, Volume 35, pp. 593-615.
11. KATO, H. & KODAMA, Y., 2003. *Microbubbles as a Skin Friction Reduction Device - A Midterm Review of the Research, Japan:* Center for Smart Control of Turbulence National Maritime Research Institute, Japan.
12. KATO, H., MIURA, K., *YAMAGUCHI, H. & MIYANAGA, M., 1998. Experimental study on microbubble ejection method for frictional drag reduction*. J Mar Sci Technol, Volume 3, pp. 122-129.
13. KAWABUCHI, M. et al., 2011. CFD *Predictions of Bubbly Flow around an Energy-saving Ship with Mitsubishi Air Lubrication System*. Mitsubishi Heavy Industries Technical Review, 48(1).
14. KAWASHIMA, H. et al., n.d. *Experimental study of frictional drag reduction by microbubbles: Laser measurement and bubble generator,* Tokyo, Japan: Center for Smart Control of Turbulence, National Maritime Research Institute.
15. KIM, J., 2011. *Physics and control of wall turbulence for drag reduction.* Phil. Trans. R. Soc. A, pp. 1396-1411.
16. KITAGAWA, A. et al., n.d. *Turbulence structures of microbubble flow measured by PIV/PTV and LIF techniques.* Japan, Smart Control of Turbulence, Ministry of Education, Culture, Sports, Science and Technology.
17. KITAGAWA, A., HISHIDA, K. & KODAMA, Y., 2005. *Flow structure of microbubble-laden turbulent channel flow measured by PIV combined with the shadow image technique*. Experiments in Fluids, Volume 38, pp. 466-475.
18. KODAMA, Y. et al., 2004. *Practical application of microbubbles to ships - Large scale model experiments and a new full scale experiment*. National Maritime Research Institute, Toyo University, Azuma Shipping, Osaka Univ & Chugoku Marine Paints.
19. LAY, K. A. et al., 2010. *Partial cavity drag reduction at high Reynolds numbers*. Journal of Ship Research, 54(2), pp. 109-119.
20. LEWIS, E. V., n.d. *Principles of Naval Architecture, Second Revision*. Volume II Resistance & Propulsion. s.l.:Library of Congress Catalog Card No. 88-60829 ISBN No. 0-939773-01-5.
21. MADAVAN, K., DEUTSCH, S. & MERKLE, C. L., 1983. *Reduction of Turbulent Skin Friction by Microbubbles*. Technical Memorandum, The Pennsylvania State University, 9 MARCH, pp. File No. TM 83-23.
22. MADAVAN, K., DEUTSCH, S. & MERKLE, C. L., 1985. *Numerical Investigations Into the Mechanisms of Microbubble Drag Reduction*. Transactions of the ASME, Volume 107, pp. 370-377.
23. MADAVAN, K., DEUTSCH, S. & MERKLE, C. L., 24 Aug 1984. *Measurements of local skin friction in a microbubble modified turbulent boundary layer,* s.l.: echnical Memorandum, File No. TM 84-136, The Pennsylvania State University.
24. MÄKIHARJU, S. A., PERLIN, M. & CECCIO, S. L., 2012. *On the Energy Economics of Air Lubrication Drag Reduction*. Inter J Nav Archit Oc Engng, 4(4), pp. 412-422.
25. MÄKIHARJU, S. et al., 2010. *Perturbed Partial Cavity Drag Reduction at High Reynolds Numbers*. Pasadena, CA, Proc. 28th Symp. on Naval Hydrodynamics,.
26. MARIN, 2011. *The efficacy of air-bubble lubrication for decreasing friction resistance*. MARITECH NEWS, pp. 118-122.
27. MATVEEV, K. I., 2003. *On the limiting parameters of artificial cavitation*. Ocean Engineering, Volume 30, pp. 1179-1190.
28. MCCORMICK, M. & BHATTACHARYYA, R., 1973. *Drag reduction of a submersible hull by electrolysis*. Naval Engineering Journal 85, pp. 11-16.
29. MIZOKAMI, S. et al., 2010. *Experimental study of air lubrication method and verification of effects on actual hull by means of sea trial*. Mitsubishi Heavy Ind Techn Rev, 47(3), p. 41–47.
30. MOHANARANGAM, K., CHEUNG, S. C. P., TU, J. Y. & CHEN, L., 2009. *Numerical simulation of microbubble drag reduction using*

population balance model. Ocean Engineering, Volume 36, pp. 863-872.

31. MORIGUCHI, Y. & KATO, H., 2002. *Influence of microbubble diameter and distribution on frictional resistance reduction*. J Mar Sci Technol, Volume 7, pp. 79-85.
32. SANDERS, W. C. et al., 2006. *Bubble friction drag reduction in a high-Reynolds-number flat-plate turbulent boundary layer.* J. Fluid Mech, Volume 552, pp. 353-380.
33. SHEN, X., CECCIO, S. L. & PERLIN, M., 2006. *Influence of bubble size on micro-bubble drag reduction.* Experiments in Fluids, Volume 41, pp. 415-424.
34. SHEN, X., CECCIO, S. & PERLIN, M., 2006. *Influence of bubble size on microbubble drag reduction*. Exp Fluids, Volume 41, p. 415–424.
35. SINDAGI, S., VIJAYKUMAR, R. & SAXENA, B. k., 2016. *Frictional Drag Reduction: An EFD and CFD Based Review of Mechanisms*. IIT Madras, India, International conference on EFD and CFD – MARHY 2016.
36. SUNARYO, Y. G. & JAMALUDDIN, A., 2012. *Micro-bubble Drag Reduction on a High Speed Vessel Model*. J. Marine Sci. Appl, Volume 11, pp. 301-304.
37. TAKAHASHI, T. et al., 2001. *Mechanisms and Scale Effects of Skin Friction Reduction by Microbubbles*, Japan: Ship Research Institute, Shipbuilding Research Association of Japan.
38. THOMAS, I., KRISHNAN, R. G., SALOOP, T. S. & VISHNU M, M., 2016. *Mechanisms and Factors Affecting Microbubble Drag Reduction in Ship.* IOSR Journal of Mechanical and Civil Engineering (IOSR-JMCE), 13(3), pp. 97-102.
39. WATANABE M, 1991. *Air pollution from ship engines in maritime Transport*. Mar Eng Soc Jpn 26 (9).
40. WINKEL, E. S., CECCIO, S. L., DOWLING, D. R. & PERLIN, M., 2004. *Bubble-size distributions produced by wall injection of air into flowing freshwater, saltwater and surfactant solutions*. Experiments in Fluids, Volume 37, p. 802–810.
41. WU, S.-J., OUYANG, K. & SHIAH, S.-W., 2008. *Robust design of microbubble drag reduction in a channel flow using the Taguchi method.* Ocean Engineering, Volume 35, p. 856–863.
42. YOSHIAKI, K., AKIRA , K., TAKAHITO , T. & HIDEKI, K., 2000. *Experimental study on microbubbles and their applicability to ships for skin friction reduction*. International Journal of Heat and Fluid Flow 21, pp. 582-588.
43. YOSHIAKI, K. et al., n.d. *Drag Reduction of Ships by Microbubbles.* National Maritime Research Institute of Japan.
44. ZVERKHOVSKYI, O. et al., 2015. s.l.: MARIN Academy, Wageningen, NL; MARIN, Wageningen, NL Delft University of Technology, NL ; DAMEN Shipyards Gorinchem, NL.

A FUZZY DEMATEL MODEL PROPOSAL FOR THE CAUSE AND EFFECT OF THE FAULT OCCURRING IN THE AUXILIARY SYSTEMS OF THE SHIPS' MAIN ENGINE

(DOI No: 10.3940/rina.ijme.2018.a2.465)

A Balin, Istanbul University, Department of Transportation and Logistic, Istanbul, Turkey, **H Demirel**, Bülent Ecevit University, Department of Marine Engineering Operations, Zonguldak, Turkey, **E Celik**, Munzur University, Department of Industrial Engineering, Tunceli, Turkey and **F Alarcin**, Yildiz Technical University, Department of Marine Engineering Operations, Istanbul, Turkey

SUMMARY

The ship engine room has a structure that meets a number of needs related to administrative conditions. Even if a simple mechanical error is considered to be the addition of human errors into the complex structure of the engine room, it can lead to undetected loss. How the causes and effects of the detected faults affect the system is as important as an effective fault detection system to detect the fault and take immediate action against any possible engine failure. This study reveals the causes of problems occurring in the main engine auxiliary systems including cooling, lubricating, cooling oil and fuel systems, and the extent of these problems affecting the system. While the Decision Making Trial and Evaluation Laboratory supports to identify and analyze the error detection of auxiliary systems with respect to causal effect relation diagram, fuzzy sets deal with the uncertainty in decision-making and human judgements through the DEMATEL. Therefore, fuzzy DEMATEL approach is applied to examine the causes and the weights of the faults and their relation to each other in the auxiliary systems. When we look at the result of the proposed approach, fuel oil pump failures has more impact on the all system and air cooler problems has the second highest place among the all errors.

1. INTRODUCTION

In the engine room, all engines work in an integrated manner and must work perfectly to achieve the desired power and rotation. The engine room is designed to meet all the operational requirements of fuel, oil, exhaust, cooling, air supply and control systems which are expressed as main engine auxiliary systems designed to provide the necessary power for ship operation. Engine room is a system of high complexity systems and consists of subsystems that meet a number of needs. Diesel engines are the main source of generating power to operate the ship. Marine diesel engines are more likely to encounter sudden and unexpected failures due to long-term use. It is among the reasons for large-scale failures to ignore details or to notice small disorders. (Özsoysal, 2010).

Any simple engine failure can cause another one unless it is noticed shortly and necessary precautions are taken. These failures later become large enough to cause a loss that cannot be reversed. The important thing is to take action and take the necessary precautions before it becomes impossible to overcome these failures. Any probable engine failure can be detected easily with effective main engine failure detection. In addition to the observed symptoms and the identified failures, the frequency of failures and their cause and effect on auxiliary systems should also be taken into account in order to increase productivity and to account for possible causes of failures.

In addition to controlling the pressure and temperature of the exhaust, combustion air, oil and cooling water, checking the turbo charger with marine diesel engine would also be the occasion to detect failures (Calder, 1992). Sharma et al. (2008) has implemented a failure mode and effect analysis (FMEA) that expresses all possible failure modes and causes of the industrial system in a hierarchical structure. Çebi et al. (2009) suggested an expert diagnostics system to identify and evaluate frequent failures in ship engine auxiliaries using the PROLOG programming language. They developed an application for the ship cooling system and created action charts showing what types of faults were encountered in the event of an emergency and what they would do by changing the indicative value limits. As a result of their work, it is underlined shortening the intervention period of merchant ships and timely correcting failures that will increase operational efficiency when maneuvering on merchant ships in critical seas. Özsoysal (2010) investigated the damages and causes of exhaust failure in high speed marine diesel engines on Turkish ambulance boats. Gourgoulis (2010) worked on the turbine engine electric generators used in marine engineering for the auxiliary power supply system of the ship. The author made a failure analysis in order to solve real operating problems. Alarcin et al. (2014) applied fuzzy analytic hierarchy process (AHP) and TOPSIS (Technique for Order Preference by Similarity to Ideal Solution) methods that can be applied for failure detection in auxiliary systems. Balin et al. (2015) also implemented fuzzy AHP and fuzzy VIKOR methods applied for the importance of the effective use of time in determining and responding to the failures. Demirel et al. (2015) aimed to manage troubleshooting in marine engine auxiliary systems for maintenance processes for marine engineering operators using fuzzy AHP determine solution methods. Chen-Yi et al. (2007) used Fuzzy decision making trial and evaluation laboratory (FDEMATEL) to find the key factors in building the structure relations of an ideal customer's choice behavior. Wu and Lee (2007) applied FDEMATEL to segment competencies for better promoting the competency development of global managers. Furthermore, Liou et al. (2008) applied the model to establish an effective safety management system in aviation industry. Chang et al. (2011) applied FDEMATEL to find influential factors in selecting SCM suppliers. Moreover, the FDEMATEL has been successfully adopted in knowledge management (Patil and Kant, 2014), supply chain management (Govindan et al., 2015; Jeng, 2015), safety management (Zhou et al., 2013), human resource management (Chou et al., 2014), risk management (Mentes et al., 2015), emergency management (Zhou et al., 2011), critical operational hazards (Akyuz and Celik, 2015), and energy management (Luthra et al., 2016).

This paper presents an important methodological approach to mention causes and effects of the detected faults on the auxiliary systems of the ships' main engine. The proposed methodology enhances the maintenance processes for operators as well as property marine engineering. Although the method has already identified some scientific articles in different areas, there are few studies on the importance ratings of mistakes that occur mainly in auxiliary systems in the maritime industry. Therefore, this study will remedy about gap and contribute to the marine engineering area the rest of this paper is organized as follows: Section 2 presents the fundamental of the FDEMATEL approach. The case study is presented in Section 3. Finally, discussion and conclusion are presented in Section 4.

2. FUZZY DEMATEL METHOD

Decision making trial and evaluation laboratory (DEMATEL) method was proposed at Battelle Memorial Institute of Geneva Research Center for understanding and solving the real world problems (Gabus and Fontela, 1973, Gul et al., 2014; Gölcük and Baykasoğlu, 2016). It aims to reveal the direct and indirect relation between criteria, causal and effect dimensions (Dalahan et al., 2011). However, it is usually assumed that human perceptions (linguistic assessments) on decision criteria are usually evaluated subjectively. In many real cases, the human perception is uncertain and human(s) might be unwilling or unable to allocate exact numerical values to describe the preferences (Lin, 2013; Celik et al., 2015; Akyuz and Celik, 2016). While it is a good technique for evaluating problems and making decisions, fuzzy logic reflects the linguistic assessment in a healthier manner. Fuzzy logic is a robust tool for dealing with the vagueness, ambiguity and uncertainty of human perception and assessment in making decisions process that is proposed in 1965 by Lotfi A. Zadeh. Many decision making problems involve imprecision since goals, constraints, and possible actions are not known precisely in real world decision making problems, (Zadeh, 1965). Hence, it is better to convert the linguistic terms into fuzzy numbers in decision making problems (Gul et al, 2016). The FDEMATEL method can convert the relationship between the causes and effects of criteria into an intelligible structural model of the system. The FDEMATEL method has been successfully applied in many fields (Gölcük and Baykasoğlu, 2016). In recent years, the FDEMATEL method has become very popular, because it is specifically realistic to visualize the structure of complicated causal relationships with digraphs (Akyuz and Celik, 2015). The corresponding relationship between the linguistic terms and triangular fuzzy numbers is determined with respect to Table 1. The fuzzy ratings and their membership function is presented in Figure 1.

Table 1. Corresponding relationship between linguistic terms and fuzzy numbers

Linguistic terms	Triangular fuzzy numbers
No influence (No)	(0, 0, 0.25)
Very low influence (VL)	(0, 0.25, 0.5)
Low influence (L)	(0.25, 0.5, 0.75)
High influence (H)	(0.5, 0.75, 1)
Very high influence (VH)	(0.75, 1, 1)

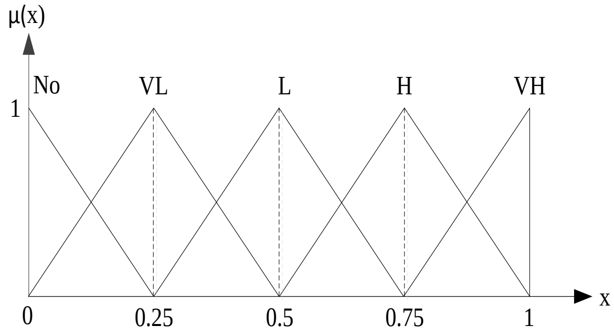

Figure 1. Fuzzy ratings and their membership function

The main steps of the method that is also presented in Figure 2 are defined as follows (Chen-Yi et al., 2007; Wu and Lee, 2007; Liou et al., 2008; Akyuz and Celik, 2015).

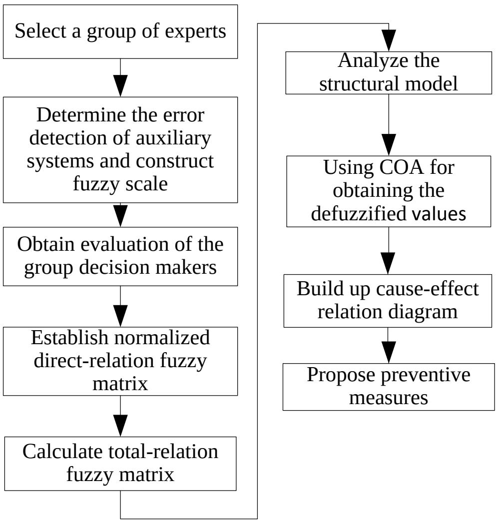

Figure 2. Flow diagram of the proposed approach

Step 1: Select a group of experts who have enough knowledge and experience about the problem in order to obtain consistent judgements.

Step 2: Determine error and construct fuzzy scale. Then, linguistic variable is applied with five scales (no influence, very low influence, low influence, high influence, and very high influence) with respect to the linguistic terms and triangular fuzzy numbers.

Step 3: Obtain the evaluation of the group decision makers: The pair wise comparison is obtained in terms of linguistics variables. Furthermore, the fuzzy assessments are transformed into defuzzified and aggregated as a crisp value. As a result, initial direct-relation fuzzy matrix ($\tilde{E}$) of group decision makers is constructed. $\tilde{e}_{ij}$ is the fuzzy evaluation of the ith failure to jth failure, can be indicated by $\tilde{e}_{ij} = (l_{ij}, m_{ij}, u_{ij})$. Here l_{ij}, m_{ij} and u_{ij} stand for the lower, middle and upper values of the fuzzy numbers.

$$\tilde{E} = \begin{bmatrix} 0 & \cdots & \tilde{E}_{1n} \\ \vdots & \ddots & \vdots \\ \tilde{E}_{n1} & \cdots & 0 \end{bmatrix} \tag{1}$$

$$\tilde{e}_{ij} = (l_{ij}, m_{ij}, u_{ij}) \tag{2}$$

Step 4: Calculate the normalized direct-relation fuzzy matrix. Once the initial direct-relation matrix is constructed, the normalization is applied. The following calculations are done respectively.

$$\tilde{\beta}_i = \sum \tilde{e}_{ij} = \left(\sum_{j=1}^{n} l_{ij}, \sum_{j=1}^{n} m_{ij}, \sum_{j=1}^{n} u_{ij}\right) \tag{3}$$

$$\gamma = max\left(\sum_{j=1}^{n} u_{ij}\right) \tag{4}$$

where $\tilde{\beta}_i$ and γ as triangular fuzzy numbers.

Thereafter, the linear scale transformation is applied to convert the errors into comparable scales. The normalized direct-relation fuzzy matrix $(\tilde{F})$ of the group decision makers can be represented as follows.

$$\tilde{F} = \begin{bmatrix} \tilde{\tilde{F}}_{11} & \cdots & \tilde{F}_{1n} \\ \vdots & \ddots & \vdots \\ \tilde{F}_{n1} & \cdots & \tilde{F}_{nn} \end{bmatrix} \tag{5}$$

where $\tilde{f}_{ij} = \frac{\tilde{e}_{ij}}{\gamma} = \left(\frac{\tilde{e}_{ij}}{\gamma}, \frac{\tilde{e}_{ij}}{\gamma}, \frac{\tilde{e}_{ij}}{\gamma}\right)$

Step 5: After having established normalized direct-relation fuzzy matrix, a total-relation fuzzy matrix is calculated by ensuring of $\lim_{\omega\to\infty} F^{\omega} = 0$. Then, the crisp case of the total-relation fuzzy matrix is obtained as follows.

$$\tilde{T} = \lim_{\omega\to\infty}\left(\tilde{F} + \tilde{F}^2 + \cdots + \tilde{F}^{\omega}\right) \tag{6}$$

$$\tilde{T} = \begin{bmatrix} \tilde{t}_{11} & \cdots & \tilde{t}_{1n} \\ \vdots & \ddots & \vdots \\ \tilde{t}_{n1} & \cdots & \tilde{t}_{nn} \end{bmatrix} \tag{7}$$

Where $\tilde{t}_{ij=} = (l''_{ij}, m''_{ij}, u''_{ij})$

$$Matrix\left[l''_{ij}\right] = F_l \; x \; (I - F_l)^{-1} \tag{8}$$
$$Matrix\left[m''_{ij}\right] = F_m \; x \; (I - F_m)^{-1} \tag{9}$$
$$Matrix\left[u''_{ij}\right] = F_u \; x \; (I - F_u)^{-1} \tag{10}$$

Step 6: Analyze the structural model. After having calculated matrix $\tilde{T}$, $\tilde{r}_i + \tilde{c}_j$and $\tilde{r}_i - \tilde{c}_j$ are calculated. In the formula, $\tilde{r}_i$ and $\tilde{c}_j$ denote the sum of the rows and columns of matrix $\tilde{T}$. While $\tilde{r}_i + \tilde{c}_j$ presents the importance of factor i, $\tilde{r}_i - \tilde{c}_j$ presents the net effect of factor i.

Step 7: Defuzzify $\tilde{r}_i + \tilde{c}_j$ and $\tilde{r}_i - \tilde{c}_j$. Next, $\tilde{r}_i + \tilde{c}_j +$ and $\tilde{r}_i - \tilde{c}_j$ are defuzzified by using center of area defuzzification technique which is introduced by Ross (1995) in order to determine the best non-fuzzy performance value. For a convex fuzzy number $\tilde{\delta}$, a real number z^* corresponding to its centre of area can be calculated as follows (Gumus et al., 2013):

$$z^* = \frac{\int \mu_{\tilde{\delta}}(z) z dz}{\int \mu_{\tilde{\delta}}(z) dz} \tag{11}$$

The BNP value of a fuzzy number $\tilde{G} = (l_{ij}, m_{ij}, u_{ij})$ can be found with following formula.

$$BNP_{ij} = \frac{u_{ij} - l_{ij} + m_{ij} - l_{ij}}{3} + l_{ij} \tag{12}$$

Step 8: Furthermore**,** depict a cause-effect relation diagram. In the last step, the cause and effect relation diagram is illustrated by mapping the dataset of $r_i + c_j$ and r_i-c_j.

3. A REAL-CASE APPLICATION FOR FAILURE IN AUXILIARY SYSTEMS OF THE SHIP MAIN ENGINE

When the causes and effect of faults in the marine diesel engines are examined, it is seen that each failure is connected to a different cause depending on the operating conditions. This led to the necessity of examining the causes and effects of faults affecting the systems of ship diesel engines.

In general when technically separated engine failures based on the basic features with the intention of categorizing are examined, each of which seems to have an association with a different system. Critical heat operating value for operation of marine diesel engines, are the cooling water and oil values functioning as a major factor in engine cooling and keeps the heat from the fuel coming out of the running engine. In addition to these values, it is expressed as a factor giving important information about the heat value of exhaust gases, combustion process, combustion efficiency and power obtained from the engine.

Ships in operation, due to irregular changes in the marine diesel engine load, a comprehensive intervention to control the temperature of the oil and cooling water is required. Keeping the values of the cooling water and oil temperature at optimum levels ensures more efficient energy recovery and safer marine diesel engine operation. The formation of oil film on the cylinder wall may affected by the heat of the cylinder wall cooling water. The operating structure of the central cooling system, which is frequently encountered in marine diesel engines, is shown in Figure 3.

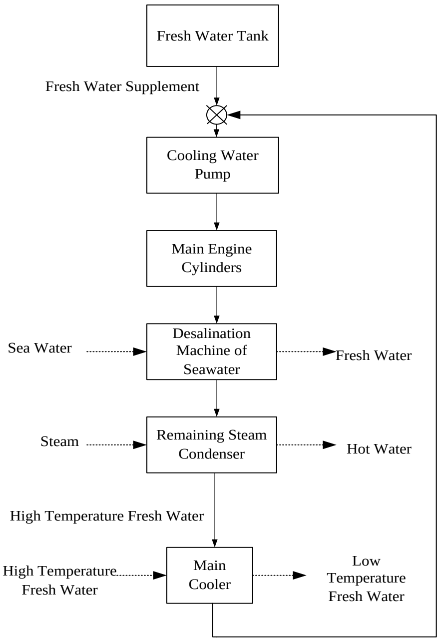

Figure 3. Structure of main engine HTFW system (Xiaoyan, 2007)

In diesel engines, fuel and governor systems must work perfectly to achieve the desired power and rotation. In order for the engines to operate safely, the rotation intervals are determined by the engine manufacturer. Exhaust heat value increases when the engine is out of range and running for longer. As the engine rotation speeds up, the emission of the exhaust gas flow increases, resulting in an increase in turbine rotation. The amount of fuel delivered from the fuel pump to the injector is controlled by the valve at a steady speed.

High-level exhaust gas temperatures, blocked filters, unwanted substances trapped in the compressor or turbine prevent the diesel engine and turbocharger from functioning properly. Fire occurs in the suction manifold due to excessive dirt and clogging of the air supply filter. Difficulties in pushing the gases generated by counter-pressure through the chimney and decrease in the inlet pressure cause the engine to fail to lift the load.

In the paper the main elements of the criteria for the selection and evaluation of machine operating systems were identified as a result of extensive exploration and consultation with three groups, including a professor from Naval Architecture and Ship Engineering. They were asked to rate the adequacy, appropriateness, and eligibility of the criteria and dimensions and to verify their "content validity" in terms of the functioning of the machine evaluation. The reasons for failures in the main engine systems were created from previous records and the daily maintenance books, and they were integrated with the staff experience. Failures are encoded as C_i where i is the number of related failure.

High heat level in all exhaust cylinders of the engine:

C_1: Fuel oil quality: It is important to determine the preheating temperature. Because the preheating is directly influence the combustion quality, it may cause increased cylinder wear related to liners and rings. Fuel oils are generally contaminated by water, sludge etc. and thus, the fuel oil must be wholly cleaned for solid as well as liquid contaminants via operators before sending it to the main engine or the auxiliary engines.

C_2: Fuel injector problems: Fuel injector has a critical role in atomization of fuel and combustion. If any part of the injector damaged or broke this results in the loss of power and efficiency. After that, The engine is also affected adversely in long term. Pressure and temperature should be monitored properly and necessary changes must be done on time.

C_3: Fuel oil pump failures: Fuels used incorrectly temperature and pressure cause these failures. After, power and efficiency decrease and suddenly engine can stop. The characteristics of the fuel must be noted and maintenance must be done regularly.

C_4: Fuel oil leakage in cylinders: Fuel oil leakage in cylinders generally occurs due to the injector problems. The leakage effects the combustion quality badly and can damage the turbine equipment. The injector maintenance must be done and the pressures and the temperatures must be checked properly.

C_5: Air fan is not working properly: If air fan is not working properly, the necessary amount of air for combustion does not enter the cylinders. Thus, the fuel cannot be burned completely. As a result, exhaust temperature increases and turbine equipment can be damaged. The amount of air for combustion must be checked periodically and the necessary precautions must be done on time.

Fluctuation in engine rotations:
C_6: Dirty fuel oil filter: In this case, fuel at a desired pressure is not sent to engine. Fuel pump may be damaged and the engine power decreases. The fuel filter should be cleaned regularly.

C_7: Fuel oil pump pressure: Higher or lower pressure than normal damage the oil pump and effect badly all the circuit. In addition, this can disrupt the other equipments and leads to affect combustion adversely. Therefore, the pump pressure should be checked regularly.

C_8: Fuel oil temperature: The temperature of the fuel affects its viscosity. This decreases the combustion quality and may lead to damage the engine. The temperature of the fuel must be controlled by operators.

C_9: Mechanical failure in the turbocharger: One of the most important problems in turbocharging is surging. This situation causes mechanical damages such as rotor and/or compressor blades. Any abnormality in the fuel system must be evaluated and fouling in the gas/air system must be timely cleaned by operators

C_{10}: Wrong adjustment of governor: This situation negatively effects the injected fuel quantity and the injection time. As a result, combustion quality decreases and the desired speed and power cannot be obtained. Injected fuel quantity and the injection time must be evaluated periodically.

Sudden shut down of the engine during normal operation:
C_{11}: Low level fuel oil tank: In this case, enough fuel may not be taken from storage tank or fuel is exhausted. Thus, the engine may be stopped suddenly. The level of the fuel tank should be checked regularly.

C_{12}: Insufficient intake air: Blower or dirty filter causes this situation. In this case, the desired combustion is not be obtained and engine performance decreases. Filters should be cleaned on time and periodic maintenance of blower should be noted.

C_{13}: Oil pressure: Oil pressure effects all the circuit. Pump failure, dirty filter and a leak on the circuit or the engine can cause the oil pressure failure. Without the required oil pressure, it is not ensured that whether the adequate cooling of the engine is satisfied. As a result, engine may damaged. The oil pressure must be checked regularly via operators.

C_{14}: Oil leakage: Oil leakage cause the decline in the oil pressure. As a result, adequate lubrication is not occur and the engine may be damaged. The oil level and pressure must be checked regularly via operators

C_{15}: Insufficient cooling water: A leak on the system or the end of the water in the cooling water tank can cause insufficient cooling water. Engine overheats without sufficient cooling water and engine may damaged. Cooling water level tanks, cooling water pressure and temperature must be checked regularly by operators.

Rise in the oil level in crankcase while the engine is working:
C_{16}: Cooling water leakage: A hole, crack on the system or worn O-rings can cause cooling water leakage. In this case, the amount of cooling water and pressure decrease. Thus, it is not ensured that whether the adequate cooling of the engine is satisfied and the engine may be damaged. Cooling water tank levels and pressure should be checked regularly.

C_{17}: Shut off valve on oil tank open: This situation causes a rise in the oil level in crankcase while the engine is working and engine is affected adversely. Oil tank level should be checked and noted.

C_{18}: Fuel oil leakage: All of the fuel pumps are connected with drain pipes to a common drain tank which involves a level switch. If there is a problem in pipes or any other equipments, oil level in crankcase rise and engine may be damaged. The drain pipes of all fuel pumps and oil levels should be checked regularly.

Fire in the Scavenging area:
C_{19}: Dirty scavenging manifold inlet: Dirty scavenging manifold inlet increases the fire in the scavenging area. This situation damage the engine. Scavenging manifold inlet should be cleaned periodically.

C_{20}: Abrasive oil ring and piston: In this case, abrasive oil ring and piston negatively affect scavenging area and increase the temperature. Increasing temperature in the system causes power loss Lubrication, maintenance of oil ring and piston should be done on time.

C_{21}: Air cooler problem: In this case, air cooler does not not work properly or stop suddenly. When the system temperatures increase and engine efficiency affect negatively. Air cooler filters and temperature levels should be checked regularly.

Surge in the turbocharger:
C_{22}: Exhaust valve burns: Especially, false opening of exhaust valve causes this case. As a result, surge occur in the turbocharger and this damages the system mechanically. Exhaust valve timing should be examined and applied carefully.

C_{23}: Insufficient turbocharger oil: Insufficient turbocharger oil causes surge in the turbocharger. Without the required lubrication, engine performance decreases. Oil level in turbocharger should be checked periodically.

C_{24}: Low level oil in the governor: Low level oil in the governor negatively affects the combustion quality and may cause surge in the turbocharger. This situation decreases the engine power. Oil level in the governor should be controlled periodically.

C_{25}: Scavenging pressure high: High scavenging pressure may cause mechanical failure in the turbocharger. If scavenge air system work properly, there is no surge in the turbocharger. Scavenge air system should be checked periodically.

3.1 APPLICATION OF THE PROPOSED APPROACH

After determining the key dimensions of the criteria for evaluation and selection of machine operation systems, then, experts assess the relation among the hazards through the use of fuzzy linguistic scale.

According to the three marine experts, Table 2 presents the linguistic assessment of the three marine experts' decisions. For example, C_1 is evaluated with respect to C_2 as High (H), Very High (VH) and High (H) by three experts, respectively. (shown in Table 2, row 1 and column 2). The all evaluations for failure with respect to all failure are presented in the same manner, in Table 2. Then, the initial direct-fuzzy matrix is constructed using linguistic variables that are presented in Table 1. Table 3 presents the aggregated fuzzy initial-direct matrix. In this step, the aggregation of the row 1 (C_1) and column 2 (C_2) is obtained as follows:

$$e_{C1,\,C2} = \frac{(0.5,\,0.75,\,1)+(0.75,\,1,\,1)+(0.5,\,0.75,\,1)}{3}$$

$$e_{C1,\,C2} = \frac{(1.75,\,2.5,\,3)}{3} = (0.58,\,0.83,\,1)$$

In the same manner, all calculations are applied for obtaining initial direct-fuzzy matrix. After having constructed initial direct-fuzzy matrix, normalized direct-relation fuzzy matrix is obtained by using the equations (3 - 5) respectively. The normalized initial direct-relation fuzzy matrix is presented in Table 4. Next, total-relation fuzzy matrix can be computed by using equations (6-10) that is provided Table 5. As a consequences of outcomes, the fuzzy values of $\tilde{r}_i, \tilde{c}_j,\ \tilde{r}_i + \tilde{c}_j, \tilde{r}_i\text{-}\tilde{c}_j$ are computed as presented in Table 6. Then, defuzzification process is applied to convert the fuzzy numbers into crisp numbers. The crisp values of the $r_i,\ c_j,\ r_i + c_j, r_i\text{-}c_j$ are presented in Table 7. According to the crisp numbers, the cause-effect relation diagram is build up. In the last step of the proposed approach, the cause and effect relationship diagram is figured based on the above outcomes.

The following Tables are contained in the Appendices at the end of this Paper:
Table 2. Linguistic assessment of the three marine experts
Table 3. The fuzzy direct-influence matrix
Table 4. Normalized initial direct-relation fuzzy matrix
Table 5. Total-relation fuzzy matrix
Table 6. Fuzzy values of $\tilde{r}_i, \tilde{c}_j,\ \tilde{r}_i + \tilde{c}_j, \tilde{r}_i\text{-}\tilde{c}_j$
Table 7. Crisp values of $r_i,\ c_j,\ r_i + c_j, r_i\text{-}c_j$

3.2 FINDINGS

By considering the calculation of the r_i, c_j, $r_i + c_j, r_i - c_j$, the Figure 4 presents the cause-effect relation diagram. The finding group can be considered as cause and effect group. While the effect group is under the axis, the cause group remains on the axis.

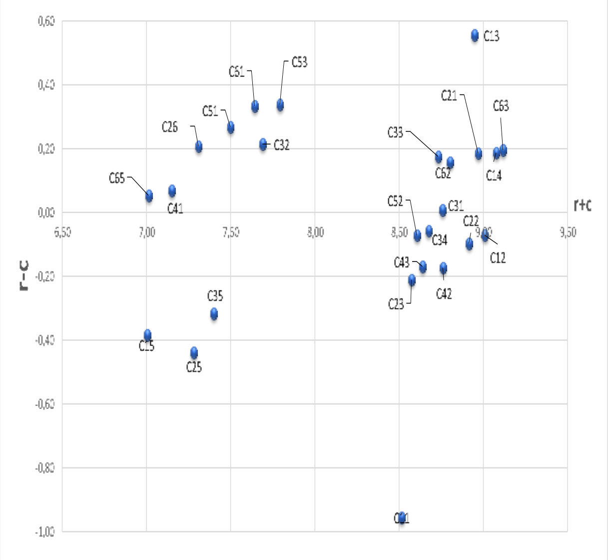

Figure 4. Cause-effect relation diagram

In order to evaluate error detection of auxiliary systems of ship main engines, it is significant to concentrate on the cause factor (error) analysis which have net and great impact on the all system. According to the Figure 4, C_3 (Fuel oil pump failures) has the highest $r_i - c_j$ value among the all error in cause group. It means that C_3 has more impact on the all system. In addition, C_3 has the highest r_i value (4.75) among the causal factors from the view of influential impact degree. It shows that C_3 has major impact on the other errors. C_{21} (Air cooler problem) has the second highest $r_i - c_j$ value since it ranks second place among the all errors. The third most critical factors among the entire process is C_{22} (Exhaust valve burns) while its $r_i - c_j$ value (0.33) ranks third place among the process.

Since effect factors are simply influenced by the other factors and, it may be still necessary to analyze effect factors (errors) which can lead to severe results in error detection of auxiliary systems of ship main engines. In the light of cause-effect relation diagram, apparently C_2 (Fuel injector problems) has the highest $r_i + c_j$ value (9.01) among the all system. The $r_i - c_j$ value (-0,07) of C_2 is very low when compared to other factors in effect group. Hence, C_2 has the significant impact on the other factors. Next, C_7 (fuel oil pump pressure) and C_{17} (shut off valve on oil tank open) have the second and third highest $r_i + c_j$values (respectively 8.91 and 8.76) in the all system. On the other hand, their $r_i - c_j$ values are very low (-0,10 and 0,17-) that means they are very easily influenced by the other factors. The rest of factors have moderate $r_i + c_j$values as it can be seen in diagram.

3.3 PREVENTIVE MEASURES PROPOSAL

In the light of the above findings, C_2, C_3, C_7, C_{17} C_{21}, C_{22}, H_5, H_4 and H_{11} are critical factors in the course of error detection the auxiliary systems of the ships' main engine. Preventive measures are presented in the view of marine experts who have enough experience on the auxiliary systems of the ships' main engine for a long year. Considering the marine experts' wide experience and knowledge, the preventive measures proposed by them are the most effective measures to avoid similar errors for auxiliary systems of the ships' main engines in the future. For all failures, operators have a critical role because of checking all the changes in the system. Therefore, practical and technical training of operators are most important for the prevention of failures. Table 8 provides the preventive measures against the critical error.

Table 8. Preventive measures.

Failure code	Preventive measures
C_3	Making regular maintenance of pump, cleaning of fuel and evaluating properties of the fuel carefully.
C_2	Monitoring of pressure and temperature changes regularly and making timely maintenance of the injector.
C_7	Considering the abrupt pump pressure changes and inspection of the fuel quality regularly.
C_{17}	Making regular maintenance of valve and checking the oil level periodically.
C_{21}	Cleaning the air cooler filters regularly and monitoring the system temperatures.
C_{22}	Applying exhaust valve timing carefully and making regular maintenance of valve.

4. CONCLUSIONS

The entire system must operate in an integrated manner in the Ship Engine room. Therefore, any failure in any system will quickly affect the entire system. A small mistake can sometimes become a non-compensating vital danger and adversely affect the entire system. Any Engine failures must always be solved by the engine operators as quickly as possible. For this reason, the causes and the weights of the faults and their relation to each other in the motor auxiliaries need to be addressed well.

As a result of the proposed approach, C_3 (Fuel oil pump failures) has more impact on the all system. On the other hand, while C_{21} (Air cooler problem) has the second highest place among the all errors, C_{22} (Exhaust valve burns) is the third most critical factors among the entire process. In the light of the above findings, C_2, C_3, C_7, C_{17} C_{21}, C_{22}, H_5, H_4 and H_{11} is obtained as crucial factors for the error detection of auxiliary systems of a ships' main engines.

The proposed hybrid method can be extended to interval type-2 fuzzy sets. The study is also thought to be a good reference for maintenance processes for ship engine officers.

5. REFERENCES

1. AKYUZ, E., & CELIK, E. (2015). *A fuzzy DEMATEL method to evaluate critical operational hazards during gas freeing process in crude oil tankers*. Journal of Loss Prevention in the Process Industries, 38, 243-253.
2. AKYUZ, E., & CELIK, E. (2016). *A modified human reliability analysis for cargo operation in single point mooring (SPM) off-shore units*. Applied Ocean Research, 58, 11-20.
3. ALARCIN, F., BALIN, A., & DEMIREL, H. (2014). *Fuzzy AHP and Fuzzy TOPSIS integrated hybrid method for auxiliary systems of ship main engines*. Journal of Marine Engineering & Technology,13(1), 3-11.
4. BALIN, A., DEMIREL, H., & ALARCIN, F. (2015). *A hierarchical structure for ship diesel engine trouble-shooting problem using fuzzy AHP and fuzzy VIKOR hybrid methods*. Brodogradnja, 66(1), 54-65.
5. CELIK, E., GUL, M., AYDIN, N., GUMUS, A. T., & GUNERI, A. F. (2015). *A comprehensive review of multi criteria decision making approaches based on interval type-2 fuzzy sets*. Knowledge-Based Systems, 85, 329-341.
6. CHANG, B., CHANG, C. W., & WU, C. H. (2011). *Fuzzy DEMATEL method for developing supplier selection criteria*. Expert systems with Applications, 38(3), 1850-1858.
7. DALALAH, D., HAYAJNEH, M., & BATIEHA, F. (2011). *A fuzzy multi-criteria decision making model for supplier selection*. Expert systems with applications, 38(7), 8384-8391.
8. DEMIREL, H., UNLÜGENÇOĞLU K., ALARCIN, F. & BALIN, A (2015). *Application of Fuzzy Analytical Hierarchy Proses for Error Detection of Auxiliary Systems of Ship Main Diesel Engines*. International Journal Maritime Engineering, 157, 105-111.
9. GABUS, A., & FONTELA, E., (1973). *Perceptions of the world problematique: communication procedure, communicating with those bearing collective responsibility*. Battelle Geneva Research Centre, Switzerland, Geneva.

10. GÖLCÜK, İ., & BAYKASOĞLU, A. (2016). *An analysis of DEMATEL approaches for criteria interaction handling within ANP*. Expert Systems with Applications, 46, 346-366.
11. GOURGOULIS, D. (2010). *Troubleshooting of marine steam turbo electro generators using engine control room simulator*, Journal of Maritime Research, 7(1), 13-26.
12. GOVINDAN, K., KHODAVERDI, R., & VAFADARNIKJOO, A. (2015). *Intuitionistic fuzzy based DEMATEL method for developing green practices and performances in a green supply chain*. Expert Systems with Applications, 42(20), 7207-7220.
13. GUL, M., GUNERI, A. F., & DERIN, B. (2014). *Evaluation of service quality criteria for a private medical center by using SERVQUAL and DEMATEL methods*. Sigma, 32, 240-253.
14. GUL, M., CELIK, E., AYDIN, N., GUMUS, A. T., & GUNERI, A. F. (2016). *A state of the art literature review of VIKOR and its fuzzy extensions on applications*. Applied Soft Computing, 46, 60-89.
15. GUMUS, A.T., YAYLA, A.Y., CELIK, E., & YILDIZ, A., (2013). *A combined fuzzy-ahp and fuzzy-gra methodology for hydrogen energy storage method selection in Turkey*. Energies 6 (6), 3017e3032.
16. HSU, C. Y., CHEN, K. T., TZENG, G. H., 2007. *FMCDM with fuzzy DEMATEL approach for customers' choice behavior model*. International Journal of Fuzzy Syst. 9 (4), 236-246.
17. JENG, D. J. F. (2015). *Generating a causal model of supply chain collaboration using the fuzzy DEMATEL technique*. Computers & Industrial Engineering, 87, 283-295.
18. LIN, R. J. (2013). *Using fuzzy DEMATEL to evaluate the green supply chain management practices*. Journal of Cleaner Production, 40, 32-39.
19. LIOU, J.J., YEN, L., & TZENG, G.H., (2008). *Building an effective safety management system for airlines*. J. Air Transp. Manag. 14 (1), 20-26.
20. LUTHRA, S., GOVINDAN, K., KHARB, R. K., & MANGLA, S. K. (2016). *Evaluating the enablers in solar power developments in the current scenario using fuzzy DEMATEL: An Indian perspective*. Renewable and Sustainable Energy Reviews, 63, 379-397.
21. MENTES, A., AKYILDIZ, H., YETKIN, M., & TURKOGLU, N. (2015). *A FSA based fuzzy DEMATEL approach for risk assessment of cargo ships at coasts and open seas of Turkey*. Safety Science, 79, 1-10.
22. ÖZSOYSAL, O. A. (2010). *Siphoning sea water back into the engine in fast boats*, Journal of Marine Science and Technology, 18(4), 496-503.
23. PATIL, S. K., & KANT, R. (2014). *A hybrid approach based on fuzzy DEMATEL and FMCDM to predict success of knowledge management adoption in supply chain*. Applied Soft Computing, 18, 126-135.
24. SHARMA, R.K., KUMAR, D., & KUMAR, P. (2005). *Systematic failure mode effect analysis (FMEA) using fuzzy linguistic modelling*, International Journal of Quality & Reliability Management, 22, 986 – 1004
25. ROSS, T.J., (1995). *Fuzzy Logic with Engineering Applications*. McGraw-Hill, Inc, USA.
26. CEBI, S., CELIK, M., KAHRAMAN, C., & ER, I. D. (2009). *An expert system auxiliary machinery troubleshooting: Shipamtsolver*, Expert Systems with Applications, 36, 7219-7227.
27. UNLUGENCOGLU, K. (2012). *Development and application of simulator algorithm in accordance with ship main engine auxiliary systems*. MSc Thesis, Yildiz Technical University, İstanbul, Turkey.
28. WU, W.W., & LEE, Y.T., (2007). *Developing global managers' competencies using the fuzzy DEMATEL method*. Expert Systems with Applications, 32 (2), 499-507.
29. ZADEH, L.A., (1965). *Fuzzy sets*. Information and Control 8, 338–353.
30. ZHOU, Q., HUANG, W., & ZHANG, Y., (2011). *Identifying critical success factors in emergency management using a fuzzy DEMATEL method*. Safety Science, 49 (2), 243e252.
31. ZHOU, S., SUN, J., LI, K. P., & YANG, X. (2013). *Development of a Root Cause Degree Procedure for measuring intersection safety factors*. Safety Science, 51(1), 257-266.

APPENDICES

Table 2. Linguistic assessment of the three marine experts

	C1	C2	C3	C4	C22	C23	C24	C25
C1	(No, No, No)	(H, VH, H)	(H, VH, VH)	(VH, VH, H)	(H, H, VH)	(L, L, L)	(VL, L, L)	(VL, VL,
C2	(H, VH, H)	(No, No, No)	(H, L, H)	(H, VL, VL)	(L, VL, VL)	(H, H, H)	(VH, H, H)	(L, L, L)
C3	(VL, VH, VH)	(H, VH, H)	(No, No, No)	(L, L, H)	(L, VL, VL)	(H, H, H)	(VH, VH, VH)	(L, VL, L)
C4	(VH, VH, VH)	(H, VH, VL)	(H, VL, H)	(No, No, No)	(VL, L, L)	(VH, VH, VH)	(VH, VH, VH)	(L, L, L)
C5	(VL, VH, VL)	(VL, VL, L)	(L, VL, VL)	(VH, L, VL)	(VH, VH, VH)	(VL, VL, VL)	(VL, VL, VL)	(H, VH, VH)
C6	(VH, H, H)	(VH, VH, H)	(H, H, H)	(VH, VH, VH)	(VL, VL, VL)	(H, H, H)	(H, H, H)	(VL, VL,
C7	(VH, H, H)	(VH, VH, VH)	(VH, VH, VH)	(VH, VH, VH)	(VL, L, L)	(VH, VH, VH)	(H, VH, VH)	(VL, L, L)
C8	(H, H, H)	(H, VH, VH)	(L, L, L)	(H, H, H)	(VL, VL, VL)	(VH, H, H)	(H, H, VH)	(VL, VL,
C9	(L, VL, VL)	(L, L, L)	(L, VL, VL)	(VL, L, L)	(L, L, L)	(L, L, L)	(L, L, L)	(L, VL, VL)
C10	(L, L, L)	(VH, H, H)	(VL, VL, VL)	(H, H, VH)	(L, L, L)	(VL, L, L)	(VH, H, H)	(L, VL, VL)
C11	(VH, VH, VH)	(VL, L, VL)	(VH, H, H)	(VH, VH, VH)	(VL, VL, VL)	(VH, VH, VH)	(VH, VH, VH)	(L, L, L)
C12	(L, L, L)	(H, H, H)	(VL, VL, VL)	(VL, VL, VL)	(H, VH, VH)	(L, L, L)	(L, VL, VL)	(H, H, H)
C13	(VH, VH, VH)	(H, VH, VH)	(VH, VH, VH)	(VH, H, H)	(VL, VL, VL)	(VH, VH, VH)	(VH, VH, H)	(VL, VL,
C14	(VH, VH, VH)	(VH, H, H)	(VH, H, H)	(VH, H, H)	(VL, L, L)	(VH, H, H)	(VH, VH, VH)	(VL, VL,
C15	(L, L, L)	(VL, VL, VL)	(VL, VL, VL)	(VL, VL, VL)	(H, H, H)	(L, L, VL)	(VL, L, VL)	(L, L, L)
C16	(L, VL, VL)	(VL, VL, VL)	(VL, L, L)	(VL, VL, L)	(L, L, L)	(VL, VL, VL)	(VL, L, L)	(L, L, L)
C17	(VH, VH, VH)	(H, H, H)	(VH, VH, H)	(VH, H, H)	(VL, VL, L)	(VL, VL, L)	(VH, VH, VH)	(VL, L, L)
C18	(VH, VH, VH)	(VH, VH, VH)	(VH, VH, VH)	(VH, VH, VH)	(VL, L, VL)	(L, L, L)	(VH, VH, VH)	(VL, VL,
C19	(L, L, VL)	(L, L, L)	(VL, VL, VL)	(VL, VL, VL)	(H, H, VH)	(H, H, VH)	(L, L, L)	(H, H, H)
C20	(VH, VH, VH)	(H, H, H)	(H, VH, VH)	(VH, VH, VH)	(VL, VL, VL)	(L, VL, VL)	(H, H, H)	(L, L, L)
C21	(H, H, H)	(VH, VH, VH)	(VL, L, L)	(L, L, L)	(H, VH, VH)	(H, H, H)	(VL, VL, L)	(H, VH, VH)
C22	(H, H, H)	(L, VL, L)	(VL, VL, VL)	(L, L, L)	(No, No, No)	(VH, L, VL)	(VL, H, L)	(VL, H, H)
C23	(VH, H, H)	(H, H, H)	(H, H, H)	(H, VH, VH)	(VH, VH, L)	(No, No, No)	(VL, VH, VH)	(L, H, VL)
C24	(VH, VH, VH)	(H, H, H)	(VH, VH, VH)	(H, H, H)	(VL, L, H)	(L, VH, VH)	(No, No, No)	(VL, L, H)
C25	(VL, L, L)	(L, VL, VL)	(VL, L, VL)	(VL, L, L)	(VL, H, H)	(L, H, VL)	(VL, VL, VL)	(No, No, No)

Table 3. The fuzzy direct-influence matrix

	C1	C2	C3	C4	C22	C23	C24	C25
C1	(0, 0, 0.25)	(0.58, 0.83, 1)	(0.67, 0.92, 1)	(0.67, 0.92, 1)	(0.58, 0.83, 1)	(0.25, 0.5, 0.75)	(0.17, 0.42, 0.67)	(0, 0.25, 0.5)
C2	(0.58, 0.83, 1)	(0, 0, 0.25)	(0.42, 0.67, 0.92)	(0.17, 0.42, 0.67)	(0.08, 0.33, 0.58)	(0.5, 0.75, 1)	(0.58, 0.83, 1)	(0.25, 0.5, 0.75)
C3	(0.5, 0.75, 0.83)	(0.58, 0.83, 1)	(0, 0, 0.25)	(0.33, 0.58, 0.83)	(0.08, 0.33, 0.58)	(0.5, 0.75, 1)	(0.75, 1, 1)	(0.17, 0.42, 0.67)
C4	(0.75, 1, 1)	(0.42, 0.67, 0.83)	(0.33, 0.58, 0.83)	(0, 0, 0.25)	(0.17, 0.42, 0.67)	(0.75, 1, 1)	(0.75, 1, 1)	(0.25, 0.5, 0.75)
C5	(0.25, 0.5, 0.67)	(0.08, 0.33, 0.58)	(0.08, 0.33, 0.58)	(0.33, 0.58, 0.75)	(0.75, 1, 1)	(0, 0.25, 0.5)	(0, 0.25, 0.5)	(0.67, 0.92, 1)
C6	(0.58, 0.83, 1)	(0.67, 0.92, 1)	(0.5, 0.75, 1)	(0.75, 1, 1)	(0, 0.25, 0.5)	(0.5, 0.75, 1)	(0.5, 0.75, 1)	(0, 0.25, 0.5)
C7	(0.58, 0.83, 1)	(0.75, 1, 1)	(0.75, 1, 1)	(0.75, 1, 1)	(0.17, 0.42, 0.67)	(0.75, 1, 1)	(0.67, 0.92, 1)	(0.17, 0.42, 0.67)
C8	(0.5, 0.75, 1)	(0.67, 0.92, 1)	(0.25, 0.5, 0.75)	(0.5, 0.75, 1)	(0, 0.25, 0.5)	(0.58, 0.83, 1)	(0.58, 0.83, 1)	(0, 0.25, 0.5)
C9	(0.08, 0.33, 0.58)	(0.25, 0.5, 0.75)	(0.08, 0.33, 0.58)	(0.17, 0.42, 0.67)	(0.25, 0.5, 0.75)	(0.25, 0.5, 0.75)	(0.25, 0.5, 0.75)	(0.08, 0.33, 0.58)
C10	(0.25, 0.5, 0.75)	(0.58, 0.83, 1)	(0, 0.25, 0.5)	(0.58, 0.83, 1)	(0.25, 0.5, 0.75)	(0.17, 0.42, 0.67)	(0.58, 0.83, 1)	(0.08, 0.33, 0.58)
C11	(0.75, 1, 1)	(0.08, 0.33, 0.58)	(0.58, 0.83, 1)	(0.75, 1, 1)	(0, 0.25, 0.5)	(0.75, 1, 1)	(0.75, 1, 1)	(0.25, 0.5, 0.75)
C12	(0.25, 0.5, 0.75)	(0.5, 0.75, 1)	(0, 0.25, 0.5)	(0, 0.25, 0.5)	(0.67, 0.92, 1)	(0.25, 0.5, 0.75)	(0.08, 0.33, 0.58)	(0.5, 0.75, 1)
C13	(0.75, 1, 1)	(0.67, 0.92, 1)	(0.75, 1, 1)	(0.58, 0.83, 1)	(0, 0.25, 0.5)	(0.75, 1, 1)	(0.67, 0.92, 1)	(0, 0.25, 0.5)
C14	(0.75, 1, 1)	(0.58, 0.83, 1)	(0.58, 0.83, 1)	(0.58, 0.83, 1)	(0.17, 0.42, 0.67)	(0.58, 0.83, 1)	(0.75, 1, 1)	(0, 0.25, 0.5)
C15	(0.25, 0.5, 0.75)	(0, 0.25, 0.5)	(0, 0.25, 0.5)	(0, 0.25, 0.5)	(0.5, 0.75, 1)	(0.17, 0.42, 0.67)	(0.08, 0.33, 0.58)	(0.25, 0.5, 0.75)
C16	(0.08, 0.33, 0.58)	(0, 0.25, 0.5)	(0.17, 0.42, 0.67)	(0.08, 0.33, 0.58)	(0.25, 0.5, 0.75)	(0, 0.25, 0.5)	(0.17, 0.42, 0.67)	(0.25, 0.5, 0.75)
C17	(0.75, 1, 1)	(0.5, 0.75, 1)	(0.67, 0.92, 1)	(0.58, 0.83, 1)	(0.08, 0.33, 0.58)	(0.08, 0.33, 0.58)	(0.75, 1, 1)	(0.17, 0.42, 0.67)
C18	(0.75, 1, 1)	(0.75, 1, 1)	(0.75, 1, 1)	(0.75, 1, 1)	(0.08, 0.33, 0.58)	(0.25, 0.5, 0.75)	(0.75, 1, 1)	(0, 0.25, 0.5)
C19	(0.17, 0.42, 0.67)	(0.25, 0.5, 0.75)	(0, 0.25, 0.5)	(0, 0.25, 0.5)	(0.58, 0.83, 1)	(0.58, 0.83, 1)	(0.25, 0.5, 0.75)	(0.5, 0.75, 1)
C20	(0.75, 1, 1)	(0.5, 0.75, 1)	(0.67, 0.92, 1)	(0.75, 1, 1)	(0, 0.25, 0.5)	(0.08, 0.33, 0.58)	(0.5, 0.75, 1)	(0.25, 0.5, 0.75)
C21	(0.5, 0.75, 1)	(0.75, 1, 1)	(0.17, 0.42, 0.67)	(0.25, 0.5, 0.75)	(0.67, 0.92, 1)	(0.5, 0.75, 1)	(0.08, 0.33, 0.58)	(0.67, 0.92, 1)
C22	(0.5, 0.75, 1)	(0.17, 0.42, 0.67)	(0, 0.25, 0.5)	(0.25, 0.5, 0.75)	(0, 0, 0.25)	(0.33, 0.58, 0.75)	(0.25, 0.5, 0.75)	(0.33, 0.58, 0.83)
C23	(0.58, 0.83, 1)	(0.5, 0.75, 1)	(0.5, 0.75, 1)	(0.67, 0.92, 1)	(0.58, 0.83, 0.92)	(0, 0, 0.25)	(0.5, 0.75, 0.83)	(0.25, 0.5, 0.75)
C24	(0.75, 1, 1)	(0.5, 0.75, 1)	(0.75, 1, 1)	(0.5, 0.75, 1)	(0.25, 0.5, 0.75)	(0.58, 0.83, 0.92)	(0, 0, 0.25)	(0.25, 0.5, 0.75)
C25	(0.17, 0.42, 0.67)	(0.08, 0.33, 0.58)	(0.08, 0.33, 0.58)	(0.17, 0.42, 0.67)	(0.33, 0.58, 0.83)	(0.25, 0.5, 0.75)	(0, 0.25, 0.5)	(0, 0, 0.25)

Table 4. Normalized initial direct-relation fuzzy matrix

Normaliz	C1	C2	C3	C4	C22	C23	C24	C25
C1	(0, 0, 0.01)	(0.03, 0.04, 0.05)	(0.03, 0.04, 0.05)	(0.03, 0.04, 0.05)	(0.03, 0.04, 0.05)	(0.01, 0.02, 0.03)	(0.01, 0.02, 0.03)	(0, 0.01, 0.02)
C2	(0.03, 0.04, 0.05)	(0, 0, 0.01)	(0.02, 0.03, 0.04)	(0.01, 0.02, 0.03)	(0, 0.02, 0.03)	(0.02, 0.03, 0.05)	(0.03, 0.04, 0.05)	(0.01, 0.02, 0.03)
C3	(0.02, 0.03, 0.04)	(0.03, 0.04, 0.05)	(0, 0, 0.01)	(0.02, 0.03, 0.04)	(0, 0.02, 0.03)	(0.02, 0.03, 0.05)	(0.03, 0.05, 0.05)	(0.01, 0.02, 0.03)
C4	(0.03, 0.05, 0.05)	(0.02, 0.03, 0.04)	(0.02, 0.03, 0.04)	(0, 0, 0.01)	(0.01, 0.02, 0.03)	(0.03, 0.05, 0.05)	(0.03, 0.05, 0.05)	(0.01, 0.02, 0.03)
C5	(0.01, 0.02, 0.03)	(0, 0.02, 0.03)	(0, 0.02, 0.03)	(0.02, 0.03, 0.03)	(0.03, 0.05, 0.05)	(0, 0.01, 0.02)	(0, 0.01, 0.02)	(0.03, 0.04, 0.05)
C6	(0.03, 0.04, 0.05)	(0.03, 0.04, 0.05)	(0.02, 0.03, 0.05)	(0.03, 0.05, 0.05)	(0, 0.01, 0.02)	(0.02, 0.03, 0.05)	(0.02, 0.03, 0.05)	(0, 0.01, 0.02)
C7	(0.03, 0.04, 0.05)	(0.03, 0.05, 0.05)	(0.03, 0.05, 0.05)	(0.03, 0.05, 0.05)	(0.01, 0.02, 0.03)	(0.03, 0.05, 0.05)	(0.03, 0.04, 0.05)	(0.01, 0.02, 0.03)
C8	(0.02, 0.03, 0.05)	(0.03, 0.04, 0.05)	(0.01, 0.02, 0.03)	(0.02, 0.03, 0.05)	(0, 0.01, 0.02)	(0.03, 0.04, 0.05)	(0.03, 0.04, 0.05)	(0, 0.01, 0.02)
C9	(0, 0.02, 0.03)	(0.01, 0.02, 0.03)	(0, 0.02, 0.03)	(0.01, 0.02, 0.03)	(0.01, 0.02, 0.03)	(0.01, 0.02, 0.03)	(0.01, 0.02, 0.03)	(0, 0.02, 0.03)
C10	(0.01, 0.02, 0.03)	(0.03, 0.04, 0.05)	(0, 0.01, 0.02)	(0.03, 0.04, 0.05)	(0.01, 0.02, 0.03)	(0.01, 0.02, 0.03)	(0.03, 0.04, 0.05)	(0, 0.02, 0.03)
C11	(0.03, 0.05, 0.05)	(0, 0.02, 0.03)	(0.03, 0.04, 0.05)	(0.03, 0.05, 0.05)	(0, 0.01, 0.02)	(0.03, 0.05, 0.05)	(0.03, 0.05, 0.05)	(0.01, 0.02, 0.03)
C12	(0.01, 0.02, 0.03)	(0.02, 0.03, 0.05)	(0, 0.01, 0.02)	(0, 0.01, 0.02)	(0.03, 0.04, 0.05)	(0.01, 0.02, 0.03)	(0, 0.02, 0.03)	(0.02, 0.03, 0.05)
C13	(0.03, 0.05, 0.05)	(0.03, 0.04, 0.05)	(0.03, 0.05, 0.05)	(0.03, 0.04, 0.05)	(0, 0.01, 0.02)	(0.03, 0.05, 0.05)	(0.03, 0.04, 0.05)	(0, 0.01, 0.02)
C14	(0.03, 0.05, 0.05)	(0.03, 0.04, 0.05)	(0.03, 0.04, 0.05)	(0.03, 0.04, 0.05)	(0.01, 0.02, 0.03)	(0.03, 0.04, 0.05)	(0.03, 0.05, 0.05)	(0, 0.01, 0.02)
C15	(0.01, 0.02, 0.03)	(0, 0.01, 0.02)	(0, 0.01, 0.02)	(0, 0.01, 0.02)	(0.02, 0.03, 0.05)	(0.01, 0.02, 0.03)	(0, 0.02, 0.03)	(0.01, 0.02, 0.03)
C16	(0, 0.02, 0.03)	(0, 0.01, 0.02)	(0.01, 0.02, 0.03)	(0, 0.02, 0.03)	(0.01, 0.02, 0.03)	(0, 0.01, 0.02)	(0.01, 0.02, 0.03)	(0.01, 0.02, 0.03)
C17	(0.03, 0.05, 0.05)	(0.02, 0.03, 0.05)	(0.03, 0.04, 0.05)	(0.03, 0.04, 0.05)	(0, 0.02, 0.03)	(0, 0.02, 0.03)	(0.03, 0.05, 0.05)	(0.01, 0.02, 0.03)
C18	(0.03, 0.05, 0.05)	(0.03, 0.05, 0.05)	(0.03, 0.05, 0.05)	(0.03, 0.05, 0.05)	(0, 0.02, 0.03)	(0.01, 0.02, 0.03)	(0.03, 0.05, 0.05)	(0, 0.01, 0.02)
C19	(0.01, 0.02, 0.03)	(0.01, 0.02, 0.03)	(0, 0.01, 0.02)	(0, 0.01, 0.02)	(0.03, 0.04, 0.05)	(0.03, 0.04, 0.05)	(0.01, 0.02, 0.03)	(0.02, 0.03, 0.05)
C20	(0.03, 0.05, 0.05)	(0.02, 0.03, 0.05)	(0.03, 0.04, 0.05)	(0.03, 0.05, 0.05)	(0, 0.01, 0.02)	(0, 0.02, 0.03)	(0.02, 0.03, 0.05)	(0.01, 0.02, 0.03)
C21	(0.02, 0.03, 0.05)	(0.03, 0.05, 0.05)	(0.01, 0.02, 0.03)	(0.01, 0.02, 0.03)	(0.03, 0.04, 0.05)	(0.02, 0.03, 0.05)	(0, 0.02, 0.03)	(0.03, 0.04, 0.05)
C22	(0.02, 0.03, 0.05)	(0.01, 0.02, 0.03)	(0, 0.01, 0.02)	(0.01, 0.02, 0.03)	(0, 0, 0.01)	(0.02, 0.03, 0.03)	(0.01, 0.02, 0.03)	(0.02, 0.03, 0.04)
C23	(0.03, 0.04, 0.05)	(0.02, 0.03, 0.05)	(0.02, 0.03, 0.05)	(0.03, 0.04, 0.05)	(0.03, 0.04, 0.04)	(0, 0, 0.01)	(0.02, 0.03, 0.04)	(0.01, 0.02, 0.03)
C24	(0.03, 0.05, 0.05)	(0.02, 0.03, 0.05)	(0.03, 0.05, 0.05)	(0.02, 0.03, 0.05)	(0.01, 0.02, 0.03)	(0.03, 0.04, 0.04)	(0, 0, 0.01)	(0.01, 0.02, 0.03)
C25	(0.01, 0.02, 0.03)	(0, 0.02, 0.03)	(0, 0.02, 0.03)	(0.01, 0.02, 0.03)	(0.02, 0.03, 0.04)	(0.01, 0.02, 0.03)	(0, 0.01, 0.02)	(0, 0, 0.01)

Table 5. Total-relation fuzzy matrix

	C1	C2	C3	C4	C22	C23	C24	C25
C1	(0.01, 0.07, 0.37)	(0.04, 0.1, 0.4)	(0.04, 0.1, 0.37)	(0.04, 0.1, 0.39)	(0.03, 0.08, 0.34)	(0.02, 0.08, 0.37)	(0.02, 0.08, 0.37)	(0.01, 0.05, 0.31)
C2	(0.05, 0.12, 0.46)	(0.02, 0.08, 0.42)	(0.04, 0.1, 0.42)	(0.03, 0.09, 0.42)	(0.01, 0.07, 0.36)	(0.04, 0.1, 0.43)	(0.04, 0.11, 0.44)	(0.02, 0.07, 0.36)
C3	(0.05, 0.12, 0.47)	(0.05, 0.12, 0.47)	(0.02, 0.08, 0.41)	(0.04, 0.11, 0.45)	(0.01, 0.07, 0.38)	(0.04, 0.11, 0.45)	(0.05, 0.13, 0.46)	(0.02, 0.07, 0.37)
C4	(0.06, 0.14, 0.47)	(0.04, 0.11, 0.45)	(0.03, 0.1, 0.42)	(0.02, 0.08, 0.41)	(0.02, 0.08, 0.37)	(0.05, 0.12, 0.44)	(0.05, 0.13, 0.45)	(0.02, 0.08, 0.37)
C5	(0.02, 0.08, 0.35)	(0.01, 0.06, 0.34)	(0.01, 0.06, 0.32)	(0.02, 0.07, 0.34)	(0.04, 0.08, 0.31)	(0.01, 0.06, 0.33)	(0.01, 0.06, 0.33)	(0.04, 0.08, 0.3)
C6	(0.05, 0.12, 0.47)	(0.05, 0.12, 0.46)	(0.04, 0.11, 0.43)	(0.05, 0.12, 0.45)	(0.01, 0.07, 0.37)	(0.04, 0.11, 0.44)	(0.04, 0.11, 0.45)	(0.01, 0.06, 0.36)
C7	(0.05, 0.12, 0.45)	(0.05, 0.12, 0.44)	(0.05, 0.12, 0.41)	(0.05, 0.12, 0.43)	(0.02, 0.07, 0.36)	(0.05, 0.12, 0.42)	(0.05, 0.12, 0.43)	(0.01, 0.07, 0.35)
C8	(0.04, 0.11, 0.44)	(0.04, 0.11, 0.43)	(0.03, 0.09, 0.39)	(0.04, 0.1, 0.42)	(0.01, 0.06, 0.34)	(0.04, 0.1, 0.41)	(0.04, 0.11, 0.42)	(0.01, 0.06, 0.33)
C9	(0.01, 0.07, 0.36)	(0.02, 0.07, 0.36)	(0.01, 0.06, 0.33)	(0.01, 0.07, 0.35)	(0.02, 0.06, 0.31)	(0.02, 0.07, 0.35)	(0.02, 0.07, 0.35)	(0.01, 0.05, 0.29)
C10	(0.02, 0.09, 0.4)	(0.04, 0.09, 0.4)	(0.01, 0.06, 0.35)	(0.04, 0.09, 0.39)	(0.02, 0.06, 0.33)	(0.02, 0.07, 0.37)	(0.04, 0.1, 0.39)	(0.01, 0.05, 0.31)
C11	(0.06, 0.13, 0.44)	(0.02, 0.09, 0.42)	(0.05, 0.11, 0.41)	(0.05, 0.12, 0.43)	(0.01, 0.07, 0.35)	(0.05, 0.12, 0.42)	(0.05, 0.12, 0.43)	(0.02, 0.07, 0.35)
C12	(0.02, 0.09, 0.41)	(0.03, 0.09, 0.41)	(0.01, 0.07, 0.36)	(0.01, 0.07, 0.38)	(0.04, 0.09, 0.35)	(0.02, 0.08, 0.39)	(0.01, 0.08, 0.38)	(0.03, 0.08, 0.34)
C13	(0.06, 0.13, 0.45)	(0.05, 0.12, 0.44)	(0.05, 0.12, 0.41)	(0.05, 0.12, 0.43)	(0.01, 0.07, 0.35)	(0.05, 0.12, 0.42)	(0.05, 0.12, 0.43)	(0.01, 0.06, 0.34)
C14	(0.05, 0.13, 0.44)	(0.04, 0.11, 0.43)	(0.04, 0.11, 0.41)	(0.05, 0.11, 0.42)	(0.01, 0.07, 0.35)	(0.04, 0.11, 0.42)	(0.05, 0.12, 0.42)	(0.01, 0.06, 0.34)
C15	(0.02, 0.08, 0.38)	(0.01, 0.06, 0.36)	(0.01, 0.06, 0.33)	(0.01, 0.06, 0.35)	(0.03, 0.07, 0.33)	(0.01, 0.07, 0.35)	(0.01, 0.07, 0.35)	(0.02, 0.06, 0.31)
C16	(0.01, 0.07, 0.38)	(0.01, 0.07, 0.36)	(0.01, 0.07, 0.35)	(0.01, 0.07, 0.36)	(0.02, 0.06, 0.32)	(0.01, 0.06, 0.35)	(0.02, 0.07, 0.36)	(0.02, 0.06, 0.31)
C17	(0.05, 0.13, 0.44)	(0.04, 0.11, 0.43)	(0.05, 0.11, 0.41)	(0.04, 0.11, 0.42)	(0.01, 0.07, 0.35)	(0.02, 0.08, 0.4)	(0.05, 0.12, 0.42)	(0.01, 0.07, 0.34)
C18	(0.06, 0.13, 0.43)	(0.05, 0.12, 0.42)	(0.05, 0.12, 0.4)	(0.05, 0.12, 0.41)	(0.01, 0.07, 0.34)	(0.03, 0.09, 0.4)	(0.05, 0.12, 0.41)	(0.01, 0.06, 0.33)
C19	(0.02, 0.08, 0.4)	(0.02, 0.08, 0.4)	(0.01, 0.06, 0.36)	(0.01, 0.07, 0.37)	(0.03, 0.08, 0.35)	(0.04, 0.09, 0.39)	(0.02, 0.08, 0.39)	(0.03, 0.07, 0.34)
C20	(0.05, 0.12, 0.44)	(0.04, 0.11, 0.43)	(0.05, 0.11, 0.41)	(0.05, 0.12, 0.42)	(0.01, 0.06, 0.35)	(0.02, 0.08, 0.4)	(0.04, 0.11, 0.42)	(0.02, 0.07, 0.35)
C21	(0.04, 0.1, 0.43)	(0.05, 0.11, 0.42)	(0.02, 0.08, 0.38)	(0.02, 0.09, 0.4)	(0.04, 0.09, 0.36)	(0.03, 0.09, 0.4)	(0.01, 0.08, 0.39)	(0.04, 0.09, 0.35)
C22	(0.04, 0.1, 0.42)	(0.02, 0.08, 0.4)	(0.01, 0.07, 0.37)	(0.02, 0.08, 0.39)	(0.01, 0.05, 0.32)	(0.03, 0.08, 0.39)	(0.02, 0.08, 0.39)	(0.02, 0.07, 0.34)
C23	(0.05, 0.12, 0.46)	(0.04, 0.11, 0.45)	(0.04, 0.1, 0.42)	(0.05, 0.12, 0.44)	(0.03, 0.09, 0.38)	(0.02, 0.07, 0.4)	(0.04, 0.11, 0.43)	(0.02, 0.07, 0.36)
C24	(0.06, 0.14, 0.47)	(0.04, 0.12, 0.46)	(0.05, 0.12, 0.43)	(0.04, 0.12, 0.45)	(0.02, 0.08, 0.38)	(0.04, 0.11, 0.44)	(0.02, 0.08, 0.41)	(0.02, 0.08, 0.37)
C25	(0.02, 0.08, 0.37)	(0.01, 0.07, 0.36)	(0.01, 0.06, 0.34)	(0.01, 0.07, 0.36)	(0.02, 0.07, 0.32)	(0.02, 0.07, 0.35)	(0.01, 0.06, 0.35)	(0.01, 0.04, 0.28)

Table 6. Fuzzy values of $\tilde{r}_i, \tilde{c}_j,\ \tilde{r}_i + \tilde{c}_j, \tilde{r}_i - \tilde{c}_j$

	$\tilde{r}_i$	$\tilde{c}_j$	$\tilde{r}_i + \tilde{c}_j$	$\tilde{r}_i - \tilde{c}_j$
C1	(0.55, 1.9, 8.89)	(0.95, 2.66, 10.6)	(1.5, 4.56, 19.48)	(-10.05, -0.75, 7.94)
C2	(0.8, 2.37, 10.24)	(0.83, 2.43, 10.35)	(1.63, 4.8, 20.59)	(-9.55, -0.07, 9.41)
C3	(0.91, 2.58, 10.76)	(0.73, 2.24, 9.62)	(1.64, 4.82, 20.38)	(-8.71, 0.34, 10.03)
C4	(0.91, 2.58, 10.41)	(0.82, 2.42, 10.09)	(1.73, 5, 20.5)	(-9.18, 0.16, 9.58)
C5	(0.37, 1.57, 7.99)	(0.5, 1.81, 8.77)	(0.87, 3.39, 16.76)	(-8.4, -0.24, 7.49)
C6	(0.83, 2.43, 10.47)	(0.79, 2.36, 10.03)	(1.62, 4.79, 20.5)	(-9.2, 0.07, 9.68)
C7	(0.83, 2.42, 9.98)	(0.82, 2.42, 10.28)	(1.65, 4.84, 20.26)	(-9.45, 0.01, 9.15)
C8	(0.66, 2.12, 9.76)	(0.77, 2.33, 10.07)	(1.44, 4.45, 19.83)	(-9.41, -0.21, 8.98)
C9	(0.36, 1.57, 8.33)	(0.53, 1.88, 9.17)	(0.9, 3.45, 17.5)	(-8.8, -0.31, 7.8)
C10	(0.5, 1.82, 8.95)	(0.44, 1.71, 8.5)	(0.94, 3.53, 17.46)	(-8, 0.11, 8.51)
C11	(0.83, 2.43, 9.88)	(0.81, 2.39, 9.93)	(1.64, 4.82, 19.8)	(-9.09, 0.05, 9.07)
C12	(0.58, 1.96, 9.31)	(0.49, 1.81, 8.91)	(1.07, 3.77, 18.22)	(-8.33, 0.16, 8.82)
C13	(0.87, 2.49, 10)	(0.76, 2.3, 9.77)	(1.63, 4.79, 19.77)	(-8.91, 0.19, 9.24)
C14	(0.77, 2.32, 9.83)	(0.76, 2.31, 10.03)	(1.54, 4.63, 19.86)	(-9.26, 0.02, 9.07)
C15	(0.43, 1.69, 8.51)	(0.56, 1.92, 9.1)	(0.98, 3.61, 17.61)	(-8.67, -0.23, 7.95)
C16	(0.45, 1.73, 8.65)	(0.42, 1.66, 8.54)	(0.87, 3.39, 17.19)	(-8.09, 0.06, 8.23)
C17	(0.76, 2.3, 9.82)	(0.85, 2.46, 10.08)	(1.61, 4.76, 19.91)	(-9.33, -0.17, 8.98)
C18	(0.78, 2.34, 9.58)	(0.8, 2.38, 10.03)	(1.59, 4.72, 19.61)	(-9.24, -0.04, 8.77)
C19	(0.55, 1.91, 9.19)	(0.46, 1.74, 8.65)	(1.01, 3.65, 17.84)	(-8.1, 0.18, 8.73)
C20	(0.72, 2.23, 9.84)	(0.76, 2.3, 9.95)	(1.49, 4.53, 19.8)	(-9.23, -0.07, 9.08)
C21	(0.64, 2.08, 9.47)	(0.49, 1.81, 8.88)	(1.14, 3.89, 18.35)	(-8.23, 0.27, 8.98)
C22	(0.58, 1.97, 9.41)	(0.49, 1.79, 8.69)	(1.07, 3.76, 18.1)	(-8.11, 0.18, 8.93)
C23	(0.79, 2.36, 10.29)	(0.75, 2.28, 9.93)	(1.54, 4.64, 20.22)	(-9.14, 0.07, 9.54)
C24	(0.93, 2.62, 10.42)	(0.84, 2.45, 10.09)	(1.77, 5.07, 20.51)	(-9.16, 0.16, 9.58)
C25	(0.43, 1.68, 8.49)	(0.4, 1.63, 8.41)	(0.83, 3.31, 16.9)	(-7.98, 0.05, 8.09)

Table 7. Crisp values of $r_i,\ c_j,\ r_i + c_j, r_i - c_j$

	r_i	c_j	$r_i + c_j$	$r_i - c_j$
C1	3.78	4.73	8.51	-0.96
C2	4.47	4.54	**9.01**	**-0.07**
C3	4.75	4.20	**8.95**	**0.56**
C4	4.63	4.44	9.08	0.19
C5	3.31	3.69	7.00	-0.38
C6	4.58	4.39	8.97	0.19
C7	4.41	4.51	**8.91**	**-0.10**
C8	4.18	4.39	8.57	-0.21
C9	3.42	3.86	7.28	-0.44
C10	3.76	3.55	7.31	0.21
C11	4.38	4.37	8.76	0.01
C12	3.95	3.74	7.69	0.21
C13	4.45	4.28	8.73	0.17
C14	4.31	4.37	8.67	-0.06
C15	3.54	3.86	7.40	-0.32
C16	3.61	3.54	7.15	0.07
C17	4.29	4.47	**8.76**	**-0.17**
C18	4.23	4.40	8.64	-0.17
C19	3.88	3.61	7.50	0.27
C20	4.27	4.34	8.60	-0.07
C21	4.06	3.73	**7.79**	**0.34**
C22	3.99	3.65	**7.64**	**0.33**
C23	4.48	4.32	8.80	0.16
C24	4.66	4.46	9.12	0.20
C25	3.53	3.48	7.01	0.05

Trans RINA, Vol 160, Part A2, Intl J Maritime Eng, Apr-Jun 2018

EFFECT OF THE BOUNDARY CONDITIONS ON THE DYNAMIC BEHAVIOURS OF SUBSEA FREE-SPANNING PIPELINES

(DOI No: 10.3940/rina.ijme.2018.a2.467)

T T Li, **C An*** and **M L Duan**, Institute for Ocean Engineering, China University of Petroleum – Beijing, China, **H Huang**, Petroleum Exploration and Production Research Institute, Sinopec, China, and **W Liang**, College of Mechanical and Transportation Engineering, China University of Petroleum – Beijing, China

SUMMARY

This paper establishes a fast and accurate solution of the dynamic behaviours of subsea free-spanning pipelines under four different boundary conditions, based on GITT - the generalised integral transform technique. The fluid-structure interaction model is proposed by combining a linear structural equation and a non-linear distributed wake oscillator model, which simulates the effect of external current acting on the pipeline. The eigenvalue problems for the cross-flow vibration of the free-spanning submarine pipeline conveying internal fluid for four different boundary conditions are examined. The solution method of the natural frequency based on GITT is proposed. The explicit analytical formulae for the cross-flow displacement of the pipeline free span are derived, and the mode shapes and dynamic behaviours of the pipeline free span are discussed with different boundary conditions. The methodology and results in this paper can also expand to solving even more complicated boundary-value problems.

1. INTRODUCTION

Due to seabed unevenness, pipeline crossings, tie-in to subsea structures, sleepers, soil scouring, sand waves, etc., it is inevitable that the free span of subsea pipelines develops in offshore/underwater projects. When a free span forms, the structural behaviours of the free spanning part will be different from the shoulder parts which rest on the seabed (Ronold, 1995). Under the backdrop that the oil supplies onshore and even in shallow waters which are easily accessible are declining, the exploration of oil and gas is now targeting at deeper waters (Bouchonneau et al, 2010; Fyrileiv et al, 2013 and Sollund et al, 2015). The existence of subsea free-spanning pipelines brings rigorous challenges for offshore/underwater engineering. Sollund et al. (2015) summarised the three major categories of risks that the free span poses to pipeline integrity, i.e. extensive bending/local buckling due to static weight, free spans being hooked by anchors or trawling equipment, and vortex-induced vibrations (VIV).

Vortex-induced vibrations (VIV) is defined as motions triggered on bluff bodies by interaction with an external flow. It determines, to a large extent, the dynamic characteristics of the subsea free-spanning pipeline, and the boundary conditions is one of the factors that affect the VIV behaviours of the free span. DNV-RP-F105 (2006) suggested that the free-spanning pipeline can be simplified as a beam model with pinned-pinned or fixed-fixed ends for VIV analysis. And there are a large number of theoretical, numerical and experimental studies that follow the above mentioned principle. For instance, Lou et al. (2005) conducted a finite element analysis of pinned-pinned subsea free-spanning pipelines; Kaewunrue et al. (2005) studied the nonlinear free vibration of marine pipes to determine the natural frequencies and mode shapes based on a pinned-pinned pipe model; Brushi and Vital (1991) carried out an experiment for the VIV behaviours of pipes with pinned-pinned, and clamped-clamped boundary conditions; Gu et al. (Gu et al, 2013a and Gu et al, 2013b) studied the VIV of a pinned-pinned flexible cylinder by carrying out a towing tank experiment and adopted an integral transform technique to solve the dynamic characteristics of a clamped-clamped pipe.

Due to the complexity of the harsh marine environment and the vibration behaviour of the pipeline system per se, proposing the appropriate boundary value problems to describe the boundary conditions for subsea free-spanning pipelines is not easy, not to mention solving the eigenvalue problems of structures with complicated boundary conditions. That said, attempts are done by researchers to study more complicated boundary condition problems. Choi (2001) proposed a calculation formula for the maximum allowable span length under fixed-fixed, pinned-pinned, fixed-pinned and fixed-free boundary conditions. Meng et al. (2017) studied the cross-flow vibration of a fixed-free pipe discharging fluid, and Cui and Tani (2008) studied the stability of a fixed-free pipe discharging and aspirating fluid. To make the boundary condition of the subsea free-spanning pipeline more close to the reality, Ai et al. (2009) proposed a spring-supported model to simulate the pipe-soil interaction at the span shoulders, while the two ends of the free-spanning pipeline system remain simple-supported.

However, free-spanning pipeline analyses typically involve a significant amount of parametric studies due to variations in span lengths, axial forces, flow and current velocities, boundary conditions, etc. (Tang et al, 2015, and Yang et al, 2017). Methods such as numerical simulation or large-scale experiments are quite time-consuming. It is highly desirable to establish a method based on analytical approaches, which can radically reduce the calculation time. The present paper is aimed at exploring a fast and accurate method for solving complicated boundary value problems. Firstly, a fluid-structure interaction model which combines a linear structural equation and non-linear distributed wake oscillator model simulating the effect of external current acting on the free-spanning pipeline is proposed, and the eigenvalue problems of the cross-flow vibration of the free-spanning pipeline under four different boundary conditions are solved. Secondly, the governing equation system is solved by GITT - the generalised integral transform technique, and the explicit analytical formulae for the cross-flow displacement of the pipeline free span are derived. Thirdly, the natural frequency of the free span system is solved based on GITT, which is validated against the theoretical results. In addition, the mode shapes and the dynamic behaviours are discussed.

2. PROBLEM DEFINITION

2.1 MODEL DESCRIPTION

Consider an elastic free-spanning submarine pipeline conveying internal fluid as shown in Figure 1. A Cartesian coordinate with its origin at the left end of the free span is set up, where the *x*-axis is the initial axis of a static pipeline, the *y*-axis is parallel to the direction of the current flow, and the *z*-axis is in the direction opposing gravity, along which the free-spanning pipeline vibrates. The Bernoulli-Euler beam equation is adopted to describe the transverse vibration of the pipeline. The governing equation system of the cross-flow vibration of the free-spanning submarine pipeline is given as (Lou et al, 2005 and Li et al, 2016):

$$\begin{cases} EI\dfrac{\partial^4 z}{\partial x^4}+(m_\mathrm{i}U^2+PA_\mathrm{i}-T_\mathrm{a})\dfrac{\partial^2 z}{\partial x^2}+2m_\mathrm{i}U\dfrac{\partial^2 z}{\partial x\partial t}+ \\ (r_\mathrm{s}+r_\mathrm{f})\dfrac{\partial z}{\partial t}+m\dfrac{\partial^2 z}{\partial t^2}=\dfrac{\rho_\mathrm{e}V^2DC_\mathrm{L0}}{4}q \\ \dfrac{\partial^2 q}{\partial t^2}+\varepsilon\Omega_\mathrm{f}(q^2-1)\dfrac{\partial q}{\partial t}+\Omega_\mathrm{f}{}^2q=\dfrac{\alpha}{D}\dfrac{\partial^2 z}{\partial t^2} \end{cases} \tag{1}$$

The pipeline is assumed to be cylindrical with both constant outer and inner diameters, respectively symbolised as *D* and D_i; its inner cross section area is symbolised as A_i; the free-spanning pipeline is subject to steady internal flow, with a constant velocity of *U*, and to uniform current, with a constant velocity of *V*; the axial tension is T_a; the internal pressure is *P*; the spanlength is *L*. m_p, m_i and m_e is the mass per unit length of the pipeline, the internal fluid and the added mass due to external fluid, and *m* is the summation of the three; m_e can be calculated by $m_\mathrm{e}=\dfrac{C_\mathrm{M}\pi\rho_\mathrm{e}D^2}{4}$, where C_M is the added mass coefficient, and ρ_e is the density of the external fluid; *EI* is the flexural stiffness; *St* is the Strouhal number; r_s is the structural damping; r_f is the fluid added damping, equalling to $\gamma\,\Omega_\mathrm{f}\rho_\mathrm{e}D^2$, where γ is a coefficient related to the mean sectional drag coefficient of the pipe - C_D, expressed as $C_\mathrm{D}/(4\pi St)$; the term on the right side of the first equation $\dfrac{\rho_\mathrm{e}V^2DC_\mathrm{L0}}{4}q$ denotes the lift force exerted on the pipeline by the current; $q=2C_\mathrm{L}(x,t)/C_\mathrm{L0}$ is the reduced fluctuating lift coefficient, where C_L0 is the reference lift coefficient that can be obtained through the observation of a fixed structure subject to vortex shedding, and C_L is the lift coefficient.

The second equation in the governing equation system Equation 1 is a wake oscillator model (Facchinetti et al, 2004). It is to simulate the fluid force acting on the free span. $\Omega_\mathrm{f}=2\pi StU/D$ denotes the vortex-shedding frequency; $\dfrac{\alpha}{D}\dfrac{\partial^2 z}{\partial t^2}$ describes the effect of the pipe motion on the near wake. It can be seen that the coupling is through acceleration. The values of the van der Pol parameter *ε* and scaling parameter *α* can be derived from the experimental results from Facchinetti et al. (2004). Under the acceleration coupling model the value of *ε* is 0.3, and *α* 12. The values of other fluid parameters in the mathematical model are as follows: C_D = 1.2, C_M = 1, *St* = 0.2.

By introducing the following dimensionless variables:

$$x^*=\frac{x}{L}\ ,\ z^*=\frac{z}{D}\ ,\ t^*=\frac{t}{L^2}\sqrt{\frac{EI}{m_\mathrm{p}}}\ ,\ U^*=UL\sqrt{\frac{m_\mathrm{p}}{EI}}\ , \\ V^*=VL\sqrt{\frac{m_\mathrm{p}}{EI}}\ ,\ \Omega_\mathrm{f}{}^*=\Omega_\mathrm{f}L^2\sqrt{\frac{m_\mathrm{p}}{EI}}\ ,\ \beta=\frac{\rho_\mathrm{e}U^{*2}C_\mathrm{L0}L^2}{4m_\mathrm{p}} \tag{2}$$

the governing equation system Equation 1 is then turned to (omitting the asterisks for simplicity):

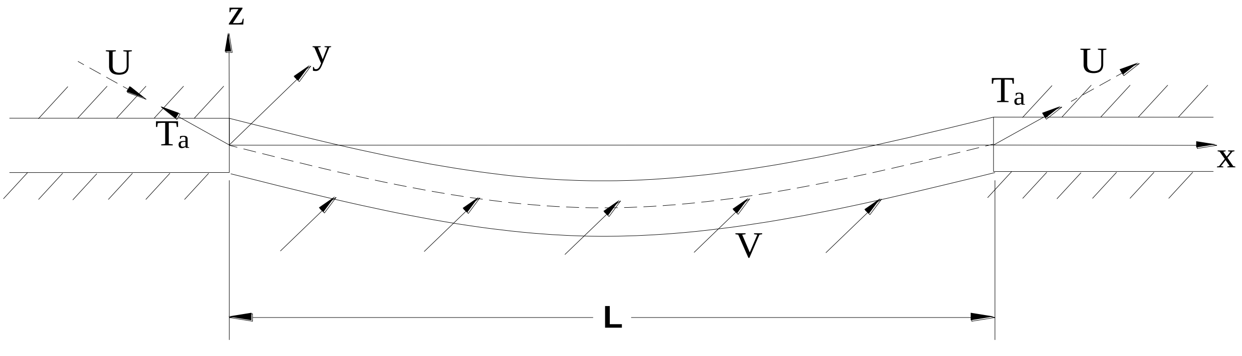

Figure 1: Schematic diagram of a fluid-conveying free-spanning submarine pipeline.

$$\begin{cases} \dfrac{\partial^4 z}{\partial x^4} + (\dfrac{m_\mathrm{i} U^2}{m_\mathrm{p}} + \dfrac{PA_\mathrm{i} L^2}{EI} - \dfrac{T_\mathrm{a} L^2}{EI})\dfrac{\partial^2 z}{\partial x^2} + \dfrac{2m_\mathrm{i} U}{m_\mathrm{p}}\dfrac{\partial^2 z}{\partial x \partial t} + \\ (r_\mathrm{s} + r_\mathrm{f})\dfrac{L^2}{\sqrt{m_\mathrm{p} EI}}\dfrac{\partial z}{\partial t} + \dfrac{m}{m_\mathrm{p}}\dfrac{\partial^2 z}{\partial t^2} = \beta q \\ \dfrac{\partial^2 q}{\partial t^2} + \varepsilon \Omega_\mathrm{f}(q^2 - 1)\dfrac{\partial q}{\partial t} + \Omega_\mathrm{f}{}^2 q = \alpha \dfrac{\partial^2 z}{\partial t^2} \end{cases} \tag{3}$$

2.2 EIGENVALUE PROBLEMS

The eigenvalue problems of the transverse displacement of the free span and the wake variable can be written respectively as:

$$\frac{\mathrm{d}^4 X_i(x)}{\mathrm{d}x^4} = \phi_i{}^4 X_i(x),\ 0 < x < 1 \tag{4a}$$

$$\frac{\mathrm{d}^4 Y_k(x)}{\mathrm{d}x^4} = \varphi_k{}^4 Y_k(x),\ 0 < x < 1 \tag{4b}$$

where X_i and ϕ_i are the eigenfunction and the eigenvalue of problem Equation 4a; likewise Y_k and φ_k are the eigenfunction and the eigenvalue of problem Equation 4b. The eigenfunctions both satisfy the following orthogonality,

$$\int_0^1 X_i(x) X_j(x)\,\mathrm{d}x = \delta_{ij} N_i \tag{5a}$$

$$\int_0^1 Y_k(x) Y_l(x)\,\mathrm{d}x = \delta_{kl} N_k \tag{5b}$$

where δ_{ij} and δ_{kl} is the Kronecker delta. For $i \neq j$, $\delta_{ij} = 0$; and for $i \neq j$, $\delta_{ij} = 1$. Likewise, for $k \neq l$, $\delta_{kl} = 0$; for $k = l$, $\delta_{kl} = 1$.

The normalised integrals are

$$N_i = \int_0^1 X_i{}^2(x)\,\mathrm{d}x \tag{6a}$$

$$N_k = \int_0^1 Y_k{}^2(x)\,\mathrm{d}x \tag{6b}$$

Hence, the general solution for the eigenfunctions are given by

$$X_i(x) = C_1 \cos\phi_i x + C_2 \sin\phi_i x + C_3 \cosh\phi_i x + C_4 \sinh\phi_i x \tag{7a}$$

$$Y_k(x) = D_1 \cos\varphi_k x + D_2 \sin\varphi_k x + D_3 \cosh\varphi_k x + D_4 \sinh\varphi_k x \tag{7b}$$

The unknowns (C_1, C_2, C_3, C_4, ϕ and C_1, C_2, C_3, C_4, φ) are determined by the boundary conditions. The four different boundary conditions discussed in the present paper are expressed as:

- fixed-fixed boundary condition:

$$X_i(0) = 0\ ,\ \frac{\mathrm{d}X_i(0)}{\mathrm{d}x} = 0\ ,\ X_i(1) = 0\ ,\ \frac{\mathrm{d}X_i(1)}{\mathrm{d}x} = 0 \tag{8a}$$

$$Y_k(0) = 0\ ,\ \frac{\mathrm{d}Y_k(0)}{\mathrm{d}x} = 0\ ,\ Y_k(1) = 0\ ,\ \frac{\mathrm{d}Y_k(1)}{\mathrm{d}x} = 0 \tag{8b}$$

- fixed-pinned boundary condition:

$$X_i(0) = 0\ ,\ \frac{\mathrm{d}X_i(0)}{\mathrm{d}x} = 0\ ,\ X_i(1) = 0\ ,\ \frac{\mathrm{d}^2 X_i(1)}{\mathrm{d}x^2} = 0 \tag{9a}$$

$$Y_k(0) = 0\ ,\ \frac{\mathrm{d}Y_k(0)}{\mathrm{d}x} = 0\ ,\ Y_k(1) = 0\ ,\ \frac{\mathrm{d}^2 Y_k(1)}{\mathrm{d}x^2} = 0 \tag{9b}$$

- fixed-free boundary condition:

$$X_i(0) = 0\ ,\ \frac{\mathrm{d}X_i(0)}{\mathrm{d}x} = 0\ ,\ \frac{\mathrm{d}^2 X_i(1)}{\mathrm{d}x^2} = 0\ ,\ \frac{\mathrm{d}^3 X_i(1)}{\mathrm{d}x^3} = 0 \tag{10a}$$

$$Y_k(0) = 0\ ,\ \frac{\mathrm{d}Y_k(0)}{\mathrm{d}x} = 0\ ,\ \frac{\mathrm{d}^2 Y_k(1)}{\mathrm{d}x^2} = 0,\ \frac{\mathrm{d}^3 Y_k(1)}{\mathrm{d}x^3} = 0 \tag{10b}$$

- pinned-pinned boundary condition:

$$X_i(0) = 0\ ,\ \frac{\mathrm{d}^2 X_i(0)}{\mathrm{d}x^2} = 0\ ,\ X_i(1) = 0\ ,\ \frac{\mathrm{d}^2 X_i(1)}{\mathrm{d}x^2} = 0 \tag{11a}$$

$$Y_k(0) = 0\ ,\ \frac{\mathrm{d}^2 Y_k(0)}{\mathrm{d}x^2} = 0\ ,\ Y_k(1) = 0\ ,\ \frac{\mathrm{d}^2 Y_k(1)}{\mathrm{d}x^2} = 0 \tag{11b}$$

The eigenvalue problems (4a) and (4b) are now solved for four different conditions:

- fixed-fixed boundary condition:

$$X_i(x) = \sin\phi_i x - \sinh\phi_i x + \frac{(\sinh\phi_i - \sin\phi_i)(\cosh\phi_i x - \cos\phi_i x)}{\cosh\phi_i - \cos\phi_i} \tag{12a}$$

$$Y_k(x) = \sin\varphi_k x - \sinh\varphi_k x + \frac{(\sinh\varphi_k - \sin\varphi_k)(\cosh\varphi_k x - \cos\varphi_k x)}{\cosh\varphi_k - \cos\varphi_k} \tag{12b}$$

where

$$\cosh\phi_i \cos\phi_i = 1\ (i = 1,\ 2,\ 3,\ \ldots) \tag{13a}$$

and

$$\cosh\varphi_k \cos\varphi_k = 1\ (k = 1,\ 2,\ 3,\ \ldots) \tag{13b}$$

- fixed-pinned boundary condition:

$$X_i(x) = \sin\phi_i x - \sinh\phi_i x + \frac{(\sinh\phi_i - \sin\phi_i)(\cosh\phi_i x - \cos\phi_i x)}{\cosh\phi_i - \cos\phi_i} \tag{14a}$$

$$Y_k(x)=\sin\varphi_k x-\sinh\varphi_k x+\frac{(\sinh\varphi_k-\sin\varphi_k)(\cosh\varphi_k x-\cos\varphi_k x)}{\cosh\varphi_k-\cos\varphi_k} \tag{14b}$$

where

$$\tanh\phi_i\tan\phi_i=1\ (i=1,\ 2,\ 3,\ \ldots) \tag{15a}$$

and

$$\tanh\varphi_k\tan\varphi_k=1\ (k=1,\ 2,\ 3,\ \ldots) \tag{15b}$$

- fixed-free boundary condition:

$$X_i(x)=\sin\phi_i x-\sinh\phi_i x+\frac{(\sinh\phi_i+\sin\phi_i)(\cosh\phi_i x-\cos\phi_i x)}{\cosh\phi_i+\cos\phi_i} \tag{16a}$$

$$Y_k(x)=\sin\varphi_k x-\sinh\varphi_k x+\frac{(\sinh\varphi_k+\sin\varphi_k)(\cosh\varphi_k x-\cos\varphi_k x)}{\cosh\varphi_k+\cos\varphi_k} \tag{16b}$$

where

$$\cosh\phi_i\cos\phi_i=-1\ (i=1,\ 2,\ 3,\ \ldots) \tag{17a}$$

and

$$\cosh\varphi_k\cos\varphi_k=-1\ (k=1,\ 2,\ 3,\ \ldots) \tag{17b}$$

- pinned-pinned boundary condition:

$$X_i(x)=\sin(\phi_i x) \tag{18a}$$

$$Y_k(x)=\sin(\varphi_k x) \tag{18b}$$

where

$$\phi_i=i\pi\ (i=1,\ 2,\ 3,\ \ldots) \tag{19a}$$

and

$$\varphi_k=i\pi\ (k=1,\ 2,\ 3,\ \ldots) \tag{19b}$$

3. INTEGRAL TRANSFORM SOLUTION

When the eigenvalue problems are solved, one can proceed with using GITT to solve the governing equation system Equation 3. Following the principle of GITT, the integral transform pair - the integral transform itself and the inversion formula is put forward.

For the transverse displacement of the free span:

$$\bar{z}_i(t)=\int_0^1\tilde{X}_i(x)z(x,t)\,\mathrm{d}x\text{ , transform} \tag{20a}$$

$$z(x,t)=\sum_{i=1}^{\infty}\tilde{X}_i(x)\bar{z}_i(t)\text{ , inversion} \tag{20b}$$

For the wake variable:

$$\bar{q}_k(t)=\int_0^1\tilde{Y}_k(x)q(x,t)\,\mathrm{d}x\text{ , transform} \tag{21a}$$

$$q(x,t)=\sum_{k=1}^{\infty}\tilde{Y}_k(x)\bar{q}_k(t)\text{ , inversion} \tag{21b}$$

where $\tilde{X}_i(x)=\dfrac{X_i(x)}{N_i^{1/2}}$ and $\tilde{Y}_k(x)=\dfrac{Y_k(x)}{N_i^{1/2}}$ are the normalised eigenfunctions.

The next step is to use GITT to transform the governing equation system in order that it is in the appropriate form that the results can be calculated. Multiplied by operators $\int_0^1\tilde{X}_i(x)\,\mathrm{d}x$ and $\int_0^1\tilde{Y}_k(x)\,\mathrm{d}x$ respectively, the partial differential equation system (3) is transferred to the following set of ordinary differential equation system, where the spatial coordinate *x* is eliminated:

$$\begin{cases}\phi_{\mathrm{i}}^{4}\bar{z}_i(t)+(\dfrac{m_{\mathrm{i}}U^2}{m_{\mathrm{p}}}+\dfrac{PA_{\mathrm{i}}L^2}{EI}-\dfrac{T_{\mathrm{a}}L^2}{EI})\displaystyle\sum_{j=1}^{\infty}A_{ij}\bar{z}_j(t)+\dfrac{2m_{\mathrm{i}}U}{m_{\mathrm{p}}}\sum_{j=1}^{\infty}B_{ij}\dfrac{\mathrm{d}\bar{z}_j(t)}{\mathrm{d}t}+\\ (r_{\mathrm{s}}+r_{\mathrm{f}})\dfrac{L^2}{\sqrt{EIm_{\mathrm{p}}}}\dfrac{\mathrm{d}\bar{z}_i(t)}{\mathrm{d}t}+\dfrac{m}{m_{\mathrm{p}}}\dfrac{\mathrm{d}^2\bar{z}_i(t)}{\mathrm{d}t^2}=\beta\displaystyle\sum_{k=1}^{\infty}C_{ik}\bar{q}_k(t)\\ \dfrac{\mathrm{d}^2\bar{q}_k(t)}{\mathrm{d}t^2}+\varepsilon\Omega_{\mathrm{f}}\displaystyle\sum_{l=1}^{\infty}\sum_{r=1}^{\infty}\sum_{s=1}^{\infty}D_{klrs}\bar{q}_l(t)\bar{q}_r(t)\dfrac{\mathrm{d}\bar{q}_s(t)}{\mathrm{d}t}-\\ \varepsilon\Omega_{\mathrm{f}}\dfrac{\mathrm{d}\bar{q}_k(t)}{\mathrm{d}t}+\Omega_{\mathrm{f}}^{2}\bar{q}_k(t)=\alpha\displaystyle\sum_{i=1}^{\infty}E_{ki}\dfrac{\mathrm{d}^2\bar{z}_i(t)}{\mathrm{d}t^2}\end{cases} \tag{22a}$$

where the coefficients are determined by the following integrals:

$$\begin{aligned}&A_{ij}=\int_0^1\tilde{X}_i(x)\frac{\mathrm{d}^2\tilde{X}_j(x)}{\mathrm{d}x^2}\mathrm{d}x,\ B_{ij}=\int_0^1\tilde{X}_i(x)\frac{\mathrm{d}\tilde{X}_j(x)}{\mathrm{d}x}\mathrm{d}x,\\ &C_{ik}=\int_0^1\tilde{X}_i(x)\tilde{Y}_k(x)\,\mathrm{d}x,\ D_{klrs}=\int_0^1\tilde{Y}_k(x)\tilde{Y}_l(x)\tilde{Y}_r(x)\tilde{Y}_s(x)\,\mathrm{d}x,\\ &E_{ki}=\int_0^1\tilde{Y}_k(x)\tilde{X}_i(x)\,\mathrm{d}x\end{aligned} \tag{22b}$$

For calculation, the expansions for $z(x,t)$ and $q(x,t)$ are truncated to *N* orders. When $\bar{z}_i(t)$ and $\bar{q}_k(t)$ are numerically evaluated with *N* orders, the inversion formulas Equations 20b and 21b are than applied to obtain the semi-analytical expressions for the non-dimensional $z(x,t)$ and $q(x,t)$.

4. RESULTS AND DISCUSSION

4.1 NATURAL FREQUENCIES BY GITT

The main parameters for the pipeline free span and the fluid are shown in Table 1. The internal flow velocity is set as zero. And for the initial conditions, a random noise with an amplitude of order $O(10^{-3})$ is applied to $z(x,0)$:

$$z(x,0)=O(10^{-3})\ ,\ \frac{\partial z(x,0)}{\partial t}=0\ ,\ q(x,0)=0\ ,\ \frac{\partial q(x,0)}{\partial t}=0 \tag{23}$$

Table 1 Geometric and physical properties of submarine pipeline, internal flow and external current.

Symbol	Value	Unit
Submarine pipeline		
L	40	m
D	0.35	m
D_i	0.325	m
ρ_p	8200	kg/m^3
ξ	0.005	
E	2.0×10^{11}	Pa
Internal fluid		
ρ_i	908.2	kg/m^3
External fluid		
ρ_e	1025	kg/m^3
C_D	1.2	
C_M	1	
C_L0	0.3	
α	12	
ε	0.3	
St	0.2	

Table 2 Fundamental natural frequency of the pipeline free span under different boundary conditions

Boundary condition	Results by GITT	Fundamental natural frequency $f_{s,1}$ (Hz)
Fixed-fixed	2.20	0.81
Fixed-pinned	1.53	0.56
Fixed-free	0.35	0.13
Pinned-pinned	0.98	0.36

Figure 2 presents the free vibration time history and frequency analysis of the free span midpoint for four different boundary conditions. The spectrogram for each boundary condition is obtained by the Fast Fourier Transform of the time histories. Since the governing equation system is non-dimensional, results calculated by GITT is also non-dimensional. The dominant frequency in the spectrogram for each boundary condition is the fundamental natural frequency of the free span. By conversion, the fundamental structural natural frequency in Hz is summarised in Table 2.

In order to validate the correctness of GITT solutions, the results in Table 2 is verified against the theoretical result, calculated by Equation 24.

$$f_\mathrm{s}=\frac{\phi_i^2}{2\pi L^2}\sqrt{\frac{EI}{(m_\mathrm{p}+m_\mathrm{i}+m_\mathrm{e})}} \tag{24}$$

The first solution of the eigenvalue ϕ_1, obtained through Equations 13a, 15a, 17a, 19a, respectively are 4.730041, 3.926602, 1.875104, π。 And by introducing the values of ϕ_1 to Equation 24, the corresponding natural frequency of the free spanning pipeline conveying internal flow with zero velocity are 0.81 Hz, 0.56 Hz, 0.13 Hz, 0.36 Hz, respectively for boundary conditions of the fixed-fixed, the fixed-pinned, the fixed-free and the pinned-pinned. By comparison, the results calculated by GITT is consistent with the theoretical results. This also proves the validity of the GITT solution.

4.2 MODE SHAPE ANALYSIS

When the structural natural frequency is determined, the structural damping can then be evaluated by relating to the natural frequency with $r_\mathrm{s}=4\pi m f_\mathrm{s}\xi$, where ξ is the damping ratio, the value of which, in this case, is taken as 0.005. Figure 3 depicts the mode shapes of the pipeline free span under different boundary conditions, at U = 0.5 and Vr = 6, where Vr is a normalised current velocity (reduced velocity) calculated by $Vr=V/Df_\mathrm{s}$.

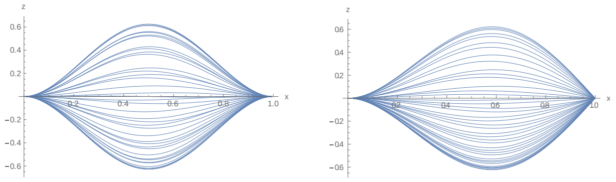

(a) the fixed-fixed (b) the fixed-pinned

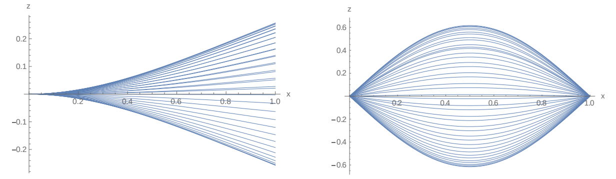

(c) the fixed-free (d) the pinned-pinned

Figure 3: Mode shapes of the free span under different boundary conditions

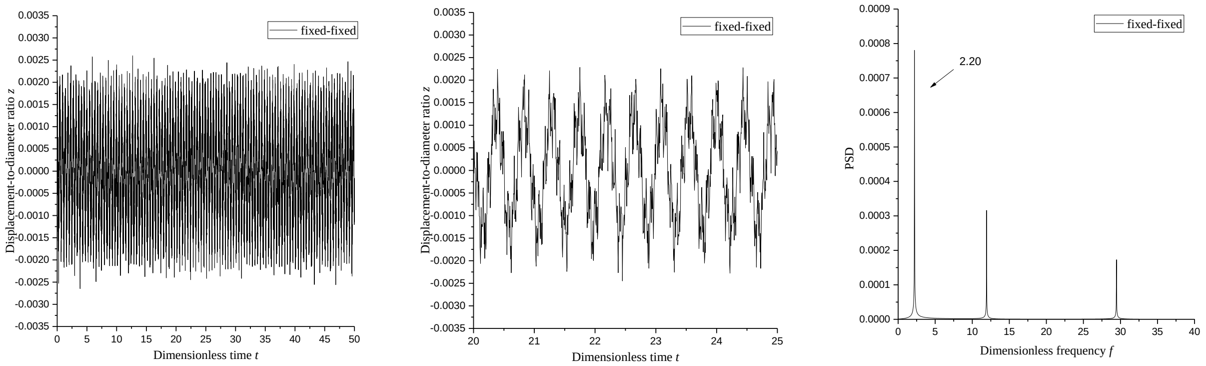

(a) fixed-fixed boundary condition

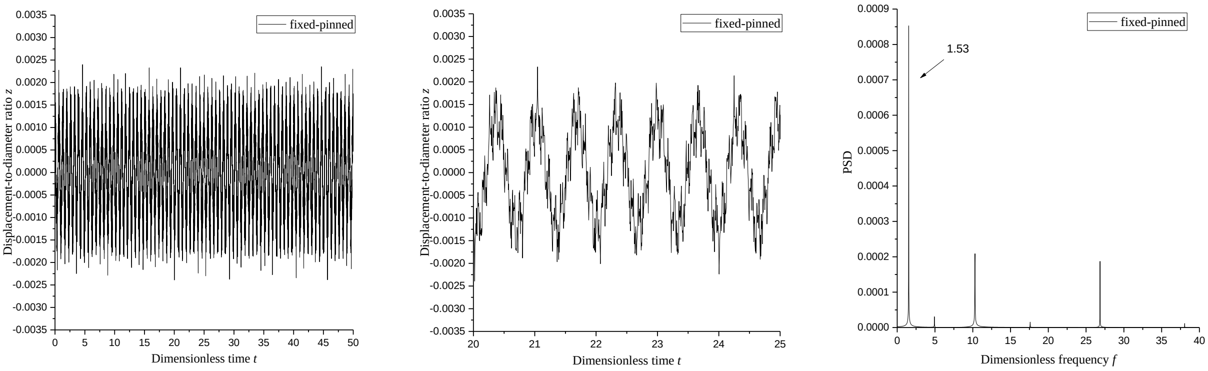

(b) fixed-pinned boundary condition

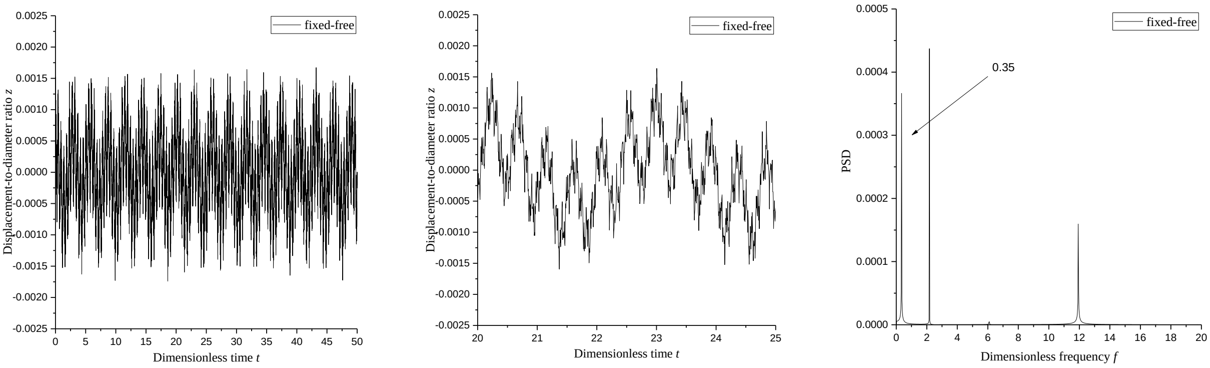

(c) fixed-free boundary condition

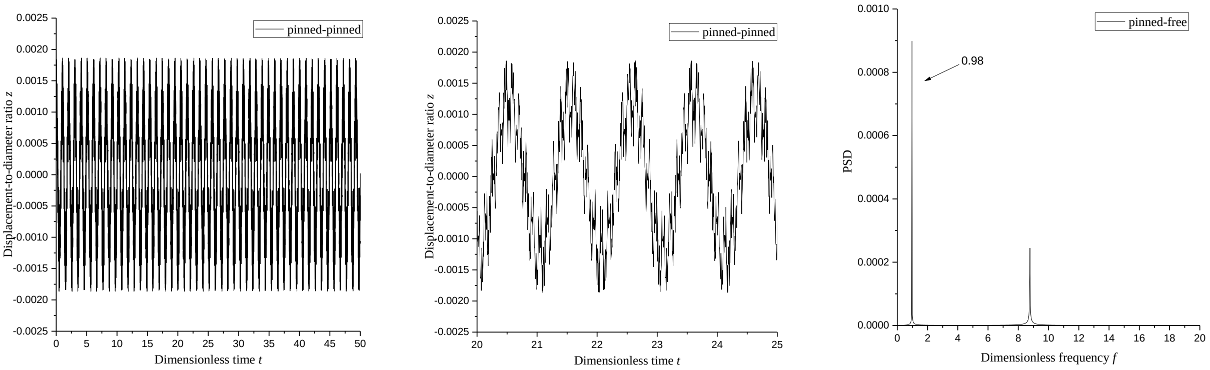

(d) pinned-pinned boundary condition

Figure 2: Free vibration time history and frequency analysis of the free span midpoint under different boundary conditions

The internal flow velocity ignored, the structural natural frequencies of the first three modes are calculated and presented in Table 3. For the free span under the fixed-fixed boundary condition, the vortex-shedding frequencies coincides with the first three structural natural frequencies when the external current velocities respectively are 1.42 m/s, 3.93 m/s, 7.70 m/s, according to Strouhal principle. In a similar manner, for the free span under the fixed-pinned boundary condition, the vortex-shedding frequencies coincides with the first three structural natural frequencies when the external current velocities respectively are 0.98 m/s, 3.18 m/s, 6.64 m/s. For the free span under the fixed-free boundary condition, the vortex-shedding frequencies coincides with the first three structural natural frequencies when the external current velocities respectively are 0.22 m/s, 1.40 m/s, 3.93 m/s. And for the free span under the pinned-pinned boundary condition, the vortex-shedding frequencies coincides with the first three structural natural frequencies when the external current velocities respectively are 0.63 m/s, 2.51 m/s, 5.65 m/s. Since the boundary conditions determines the natural frequency of the pipeline free span, the current velocity range that makes the lock-in occur varies when the boundary conditions changes. The results mentioned above are also summarised in Table 4.

Table 3 Fundamental natural frequency of the pipeline free span under different boundary conditions.

Boundary condition	1st mode natural frequency $f_{s,1}$ (Hz)	2nd mode natural frequency $f_{s,2}$ (Hz)	3rd mode natural frequency $f_{s,3}$ (Hz)
fixed-fixed	0.81	2.24	4.40
fixed-pinned	0.56	1.82	3.79
fixed-free	0.13	0.80	2.24
pinned-pinned	0.36	1.44	3.23

Table 4 Current velocity for vortex-shedding frequency equal to the structural natural frequency of the first three modes.

Boundary condition	Current velocity (m/s) $\Omega_f = f_{s,1}$	Current velocity (m/s) $\Omega_f = f_{s,2}$	Current velocity (m/s) $\Omega_f = f_{s,3}$
fixed-fixed	1.42	3.93	7.70
fixed-pinned	0.98	3.18	6.64
fixed-free	0.22	1.40	3.93
pinned-pinned	0.63	2.51	5.65

The mode shapes of the free span under four different boundary conditions at their corresponding three current velocities provided in Table 4 are shown in Figures 4-7. The boundary conditions determine the natural frequencies of the free-spanning pipeline system, thereby changing the lock-in region of the system. Results show that the lock-in happens at the lowest current velocity ranges with the fixed-free boundary condition, and at the highest current velocity ranges with the fixed-fixed boundary condition.

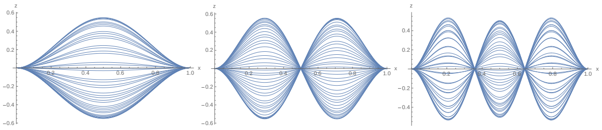
(a) 1.42 m/s (b) 3.93 m/s (c) 7.70 m/s

Figure 4: Mode shapes of the free span under the fixed-fixed boundary condition.

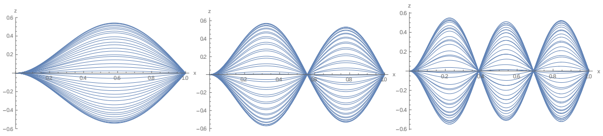
(a) 0.98 m/s (b) 3.18 m/s (c) 6.64 m/s

Figure 5: Mode shapes of the free span under the fixed-pinned boundary condition.

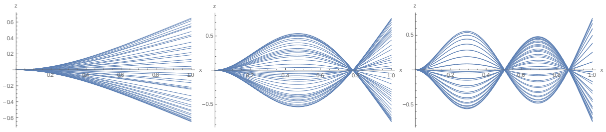
(a) 0.22 m/s (b) 1.40 m/s (c) 3.93 m/s

Figure 6: Mode shapes of the free span under the fixed-free boundary condition.

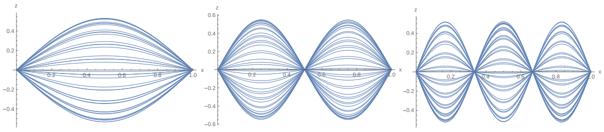
(a) 0.63 m/s (b) 2.51 m/s (c) 5.65 m/s

Figure 7: Mode shapes of the free span under the pinned-pinned boundary condition.

4.3 DYNAMIC ANALYSIS

Figure 8 presents how the reduced velocity Vr affects maximum RMS displacement-to-diameter ratio $z_{\text{RMS, Max}}$ of the free-spanning pipeline within the lock-in region. Results show that the lock-in occurs within the same reduced velocity region for the four boundary conditions discussed, i.e., $Vr \in [4, 8]$ and the tendency of $z_{\text{RMS, Max}}$ with the change of Vr is similar for the four boundary conditions. However, there is a distinct disparity for the value of $z_{\text{RMS, Max}}$ between different boundary conditions, with the fixed-free pipeline having the minimum $z_{\mathrm{RMS,\ Max}}$, followed by the fixed-fixed, the fixed-pinned, and the pinned-pinned which has the maximum $z_{\mathrm{RMS,\ Max}}$.

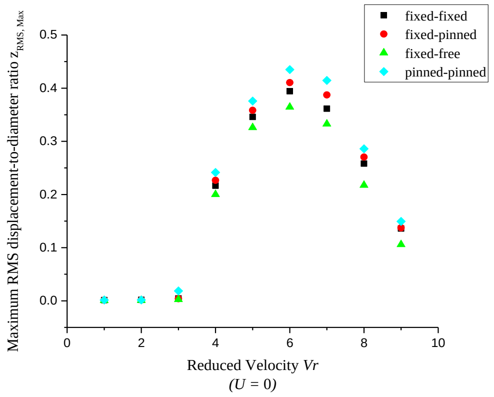

Figure 8: Effect of the reduced velocity on the maximum RMS displacement-to-diameter ratio.

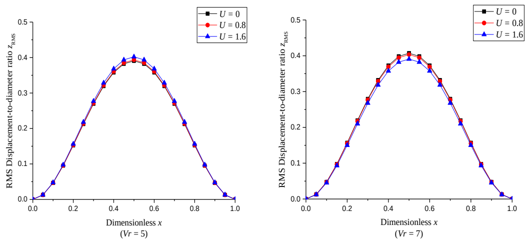

(a) the fixed-fixed

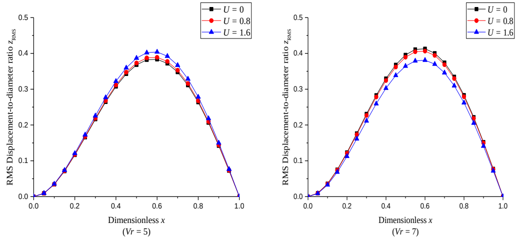

(b) the fixed-pinned

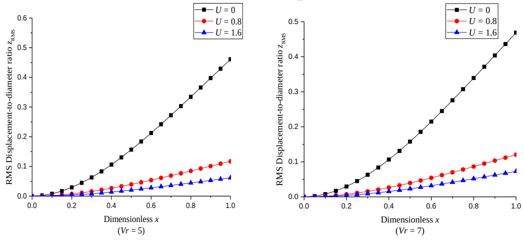

(c) the fixed-free

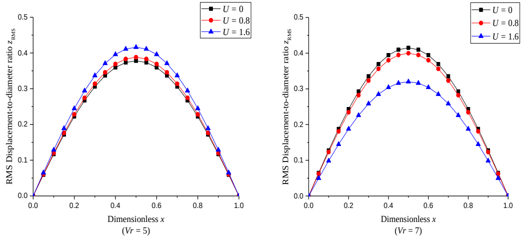

(d) the pinned-pinned

Figure 9: Distribution of RMS displacement-to-diameter ratio of the free-spanning pipeline.

Figure 9 demonstrates how the internal flow velocity *U* affects RMS displacement-to-diameter ratio z_{RMS} of the free-spanning pipeline under different boundary conditions. Results are calculated with *Vr* = 5, 7 and *U* = 0, 0.8, 1.6. Results show that the internal flow velocity will alter the z_{RMS} along the pipeline free span. When the internal flow velocity varies, there is a sharp change in the spanwise z_{RMS} for the free span with the fixed-free boundary condition. For the pinned-pinned free span, the change of the spanwise z_{RMS} is also remarkable.

Figure 10 exhibits the influence of internal flow velocity change on the natural frequency of the pipeline free span. For the free span with fixed-fixed, fixed-pinned or pinned-pinned boundary condition, the structural natural frequency declines with the increase of internal flow velocity. When the velocity of the internal flow surpasses a critical value, i.e. the dimensionless *U* = 7.56, 5.40, 3.78, respectively for the fixed-fixed, fixed-pinned or pinned-pinned ended free span, the pipeline system will lose its stability through first mode buckling due to the centrifugal force acting on the structure by the internal flow. However, the results in Figure 10 does not include the pipeline system with fixed-free boundary condition, since the vibration becomes non-conservative because the system can exchange energy with the environment as the free end discharges fluid (Meng, 2017).

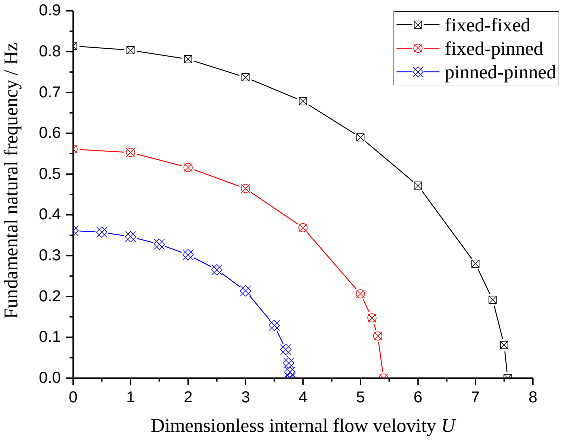

Figure 10: Effect of boundary conditions on the critical internal velocity

5. CONCLUSION

In the present paper, the eigenvalue problems for the cross-flow vibration of the free-spanning submarine pipeline conveying internal fluid are studied for four different boundary conditions, and the solution of natural frequency based on GITT is put forward and validated. Besides, the mode shapes and dynamic behaviours of the pipeline free span are discussed with different boundary conditions, and internal and external flow velocities are discussed. The methodology and results in this paper can also expand to solving even more complicated boundary-value problems. Findings are summarised as follows.

- Based on GITT, the structural natural frequencies of the free-spanning submarine pipeline constrained by four different boundary conditions are calculated and verified against the theoretical results.
- Since the boundary conditions determines the natural frequency of the pipeline free span, the current velocity range that makes the lock-in occur varies when the boundary condition changes. Under the fixed-fixed boundary condition, the lock-in happens at the highest current velocity range.
- The lock-in region is $Vr \in [4, 8]$ for all the boundary conditions, since the reduced velocity Vr is calculated based on the structural natural frequency, which changes according to the boundary conditions. The tendency of $z_{\mathrm{RMS,\ Max}}$ with the change of Vr is similar for the four boundary conditions discussed in the present paper. However, there is a distinct disparity for the value of $z_{\mathrm{RMS,\ Max}}$ between different boundary conditions.
- The boundary condition influences the natural frequency of the free-spanning pipeline system, and also the critical internal flow velocity for structural instability.

6. ACKNOWLEDGEMENTS

This work is supported by National Key Research and Development Plan of China (Grant No. 2016YFC0303700), National Natural Science Foundation of China (Grant No. 51509258), National Science and Technology Major Project of China (2016ZX05033-004-004) and Science Foundation of China University of Petroleum, Beijing (No. 2462013YJRC003 and No. 2462015YQ0403).

7. REFERENCES

1. RONOLD, K. O. (1995) *A probabilistic approach to the lengths of free pipeline spans*. Appl. Ocean Res. 17(4): 225-232.
2. BOUCHONNEAU, N., SAUVANT-MOYNOT, V., CHOQUEUSE, D., GROSJEAN, F., PONCET, E., PERREUX, D. (2010) *Experimental testing and modeling of an industrial insulated pipeline for deep sea application*. J. Pet. Sci. Eng. 73(1-2): 1-12.
3. FYRILEIV, O., AAMLID, O., VENAS, A., COLLBERG, L. (2013) *Deepwater pipelines - status, challenges and future trends*. Proc. IMechE M.: J. Eng. Marit. Environ. 227(4): 3 81-95.
4. SOLLUND, H. A., VEDELD, K., FYRILEIV, O. (2015) *Modal response of free spanning pipelines based on dimensional analysis*. Appl. Ocean Res. 50: 13-29.
5. DNV-RP-F105 (2006) *Free Spanning Pipelines*. Norway: Det Norske Veritas.
6. LOU, M., DING, J., GUO, H. Y., DONG, X. L. (2005) *Effect of internal flow on vortex-induced vibration of submarine free spanning pipelines*. China Ocean Eng. 19: 147-154.
7. KAEWUNRUEN, S., CHIRAVATCHRADEJ, J., CHUCHEEPSAKUL, S. (2005) *Nonlinear free vibrations of marine risers/pipes transporting fluid*. Ocean Eng. 32(3-4): 417-440.
8. BRUSCHI, R., VITALI, L. (1991) *Large amplitude oscillations of geometrically non-linear elastic beams subjected to hydrodynamic excitation*. J. Offshore Mech. Arct. Eng. 113(2).
9. GU, J. J., VITOLA, M., COELHO, J., PINTO, W. T., DUAN, M. L., LEVI, C. (2013a) *An experimental investigation by towing tank on VIV of a long flexible cylinder for deepwater riser application*. J. Mar. Sci. Technol. 18: 358-369.
10. GU, J. J., PINTO, W. T., LEVI, C., DUAN, M. L. (2013b) *An experimental study of the spanwise correlation of vortex shedding in the towing tank*. Ships. Offshore Struc. 8(5): 517-523.
11. CHOI, H. S. (2001) *Free spanning analysis for offshore pipeline*. Ocean Eng. 28(2001): 1325-1338.
12. MENG, S., KAJIWARA, H., ZHANG, W. (2017) *Internal flow effect on the cross-flow vortex-induced vibration of a cantilevered pipe discharging fluid*. Ocean Eng. 137: 120-128.
13. CUI. H., TANI, J. (2008) *Effect of boundary conditions on the stability of a cantilever pipe discharging and aspirating fluid*. JSME Int. J. 39(1): 20-24.
14. AI, S. M., SUN, L. P., MA, G. (2009). *The effect of soil non-linearity on VIV response of a free spanning pipeline*. In: Proceedings of the 28th international conference on ocean, offshore and arctic engineering, OMAE2009-79063, Hawaii.
15. TANG, M., YANG, C., YAN, J., YUE, Q. (2015). *Validity and limitation of analytical models for the bending stress of a helical wire in unbonded flexible pipes*. Appl. Ocean Res. 50: 58-68.
16. YANG, Z., YAN, J., CHEN, J., LU, Q., YUE, Q. (2017). *Multi-Objective Shape Optimization Design for Liquefied Natural Gas Cryogenic Helical Corrugated Steel Pipe*. J. Offshore Mech. Arct. Eng. 139(5), 051703.
17. LI, T. T., LI, X.Z., LIANG, W., SU, J., AN, C., DUAN, M. L. (2016) *A semi-analytical solution of the dynamic behaviour of free-spanning submarine pipelines conveying fluid*. In: Proceedings of the 26th international offshore and polar engineering conference, Rhodes.
18. FACCHINETTI, M.L., DE LANGRE, E., BIOLLEY, F. (2004) *Coupling of structure and wake oscillators in vortex-induced vibrations*. J. Fluids Struct. 19(2): 123-140.

Trans RINA, Vol 160, Part A2, Intl J Maritime Eng, Apr-Jun 2018

ANALYTICAL AND EXPERIMENTAL INVESTIGATION ON THE FREE VIBRATION OF SUBMERGED STIFFENED STEEL PLATE

(DOI No: 10.3940/rina.ijme.2018.a2.468)

S S Rezvani, and **M S Kiasat***, Department of Maritime Engineering, Amirkabir University of Technology, Tehran, Iran

SUMMARY

The approach developed in this paper applies to vibration analysis of rectangular stiffened plate coupled with fluid. It is obvious that the natural frequencies of a submerged structure are less than those of in vacuum and these are due to the effect of added mass of water to the structure. This paper focuses on the experimental, analytical and numerical solution of natural frequencies of submerged stiffened plate. The analytical solution based on the deflection equation of submerged orthotropic plate, Laplace's equation and Rayleigh's method in vibration analysis. By used the FEM software the numerical results for natural frequencies are derived. The natural frequencies of the stiffened plate are obtained practically by using Fast Fourier Transformation functions (FFT) in experimental analysis. Experimental results demonstrate the validity of analytical and numerical solution and results.

NOMENCLATURE

E	Young's modulus (N m^{-2})
G	Shear Young's modulus (N m^{-2})
ρ	Density of plate (kg m^{-3})
ρ_f	Fluid Density (kg m^{-3})
$\phi(x,y,z,t)$	Velocity Potential
μ	Plane Wave Number
m^*	Added Mass (kg)
m	Plate Mass (kg)
ω_{fluid}	Wet Natural Frequency (Hz)
P	Dynamic Pressures (N m^{-2})
[K]	Stiffness Matrix
[M]	Mass Matrix

1. INTRODUCTION

The plates are used in a wide range of engineering applications such as modern construction engineering, aerospace and aeronautical industries, aircraft construction, shipbuilding, and the components of nuclear power plants. The effect of the surrounding medium on the vibration of plates and shells is of primary interest to scientists and engineers working in aerospace, marine and reactor technology (Kerboua et al, 2008). It is therefore very important that the static and dynamic behavior of plates be clearly understood when subjected to different loading conditions so that they may be safely used in these industrial applications.

It is well known that the natural frequencies of structures in contact with fluid are different from those in vacuum. In general, the effect of the fluid force on the structure is represented as added mass, which lowers the natural frequency of the structure compared to what that would be measured in vacuum. This decrease in the natural frequency of the fluid-structure system is caused by increasing the kinetic energy of the coupled system without corresponding increase in strain energy (Kerboua et al, 2008). Many numerical methods have been used in fluid–structure interaction problems, including added mass formulation, finite element method (FEM), doubly asymptotic approximation (DAA), mixed boundary element and finite element method (BEM/FEM), and arbitrary Lagrangian–Eulerian formulation (ALE). The above numerical methods have also been developed into commercial codes, such as NASTRAN, ABAQUS, ANSYS, and USA (Kundu, 1990).

An enormous amount of effort has been carried out on problems involving dynamic interaction between an elastic structure and a surrounding fluid medium. Fluid–structure interaction problems have received extensive attention since 1965 (Kundu, 1990). An analytical solution studied for dynamic behavior of a rectangular reservoir partially filled with fluid using the Rayleigh–Ritz method (Kim et al, 1996). Hydro-elastic analysis investigated on a rectangular tank completely filled with liquid using a NASTRAN program and compared results with analytical solutions (Kim and Lee, 1997). Vibration modes numerically computed of an elastic thin structure in contact with a compressible fluid (Hernandez, 2006). Methods for modeling fluid effects are also available in some commercial finite element analysis (FEA) codes (Herting, 1997 and Hibbitt et al, 2001). Some aspects discussed of incorporating heavy fluid loading effects into SEA (Creighton, 1989). Based on Kwak's approach the problem of the axe symmetric vibration of circular and annular plates in contact with fluid studied (Liang et al, 1999). The natural frequencies were calculated for clamped, simply supported and free plates. Moreover, the results were compared with the experimental data. An energy finite element analysis (EFEA) formulation for computing the high frequency behavior of plate structures in contact with a dense fluid derived (Zhang et al, 2003).

The heavy fluid loading effect is incorporated in the derivation of the EFEA governing differential equations and in the computation of the power transfer coefficients between plate members. An energy finite element analysis (EFEA) formulation for high frequency vibration analysis of stiffened plates under heavy fluid loading derived (Zhang et al, 2005). G. Aksu used from a method based on the variational principles in conjunction with the finite difference technique to determine the dynamic characteristic of eccentrically stiffened plates (Aksu, 1982). Ömer Civalek developed the discrete singular convolution (DSC) method, for static analysis of thick symmetric cross-ply laminated composite plates based on the first-order shear deformation theory of Whitney and Pagano (Civalek, 2008). T. Holopainen, proposed a new finite element model for free vibration analysis of eccentrically stiffened plates (Holopainen, 1995). Murat Gürses, Ömer Civalek et al (Gürses, 2009) investigated discrete singular convolution (DSC) method for numerical solution of vibration problems. To overcome the complexities in the modal analysis of the fluid–structure interaction, the Mindlin plate theory and the potential flow theory are applied; the velocity potential is also expressed using double finite Fourier transforms (Li et al, 2011). In the paper, experimental, analytical and numerical analyses for submerged stiffened plate are studied. The numerical and analytical results are verified comparing to experimental results.

2. THEORETICAL ANALYSIS

In this section, theoretical analysis of stiffened plate is studied in the vacuum and fluid. In the analytical study, a stiffened plate undergoing a flexural bending vibration in a body of homogeneous, uncompressible and invisid fluid whose motion is irrotational, is considered. The governing equation for the surface displacement of the plate- fluid system is derived. The boundary conditions for the plate are considered as fixed on all sides. All of geometrical and physical properties of the stiffened plate as shown in Figure 1 are summarized in Table 1.

Table 1: Geometrical and Physical Properties of Stiffened Plate

$s(m)$	$a(m)$	$b(m)$	$c(m)$	$h(m)$	$l(m)$	$E(Gp$	$G(Gpa)$	$\rho(\frac{kg}{m^3})$
0.05	**0.3**	**0.3**	**0.004**	**0.004**	**0.02**	**208**	**70**	7800

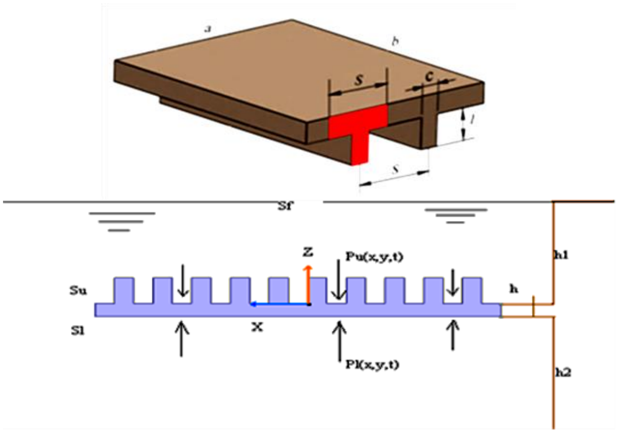

Figure 1: Stiffened plate schematics underwater

Where E is Young's modulus and G is shear Young's modulus. Consider a stiffened plate in which its both sides are exposed to still fluid as shown in Figure 1. The plate undergoes small amplitude free bending vibration. The fluid motion due to the vibration of the plate produces dynamic pressures $P_L(x,y,t)$ and $P_U(x,y,t)$ on the lower and upper fluid-plate interfaces S_L and S_U respectively. Governing equation of submerged deflection of stiffened plate is (Ventsel, 2001)

$$\begin{aligned} &D_x \frac{\partial^4 W(x,y,t)}{\partial x^4} + 2H \frac{\partial^4 W(x,y,t)}{\partial x^2 \partial y^2} + \\ &D_y \frac{\partial^4 W(x,y,t)}{\partial y^4} + \rho \frac{\partial^2 W}{\partial t^2} = P_L(x,y,t) - P_U(x,y,t) \end{aligned} \tag{1}$$

Where, $W(x,y,t)$ is the upward displacement of the plate measured from its static equilibrium position and ρ is density of the plate. $D_x = \frac{EI}{s}$ and $D_y = \frac{Eh^3}{12(1-\frac{c}{s}+\frac{ch^3}{s(h+l)^3})}$ are the flexural rigidities of an orthotropic plate. I is the moment of inertia of an inverse T-shaped section corresponding to one spacing of the rib location. Where $H = D_{xy} + 2D_s$, $D_s = \frac{Gh^3}{12}$ and D_{xy} is torsional rigidities and for stiffener with rectangular cross section is zero (Ventsel, 2001). The density of fluid ρ_f , is assumed to be homogeneous, incompressible, in viscid and its motion irrotational. Therefore, the velocity potential $\phi(x,y,z,t)$ satisfies Laplace's equation given by (Esmailzadeh, 2007):

$$\nabla^2 \phi(x,y,z,t) = 0 \tag{2}$$

Since the fluid motion is irrotational, the unsteady Bernoulli equation

$$\rho_f \frac{\partial \phi}{\partial t} + P + \frac{1}{2}\rho_f(\phi_x^2 + \phi_y^2 + \phi_z^2) + \rho_f gz = 0 \tag{3}$$

Where x, y and z indices denote to partial derivative variables. Neglecting the non-linear term $(\phi_x^2 + \phi_y^2 + \phi_z^2)$ for small amplitude waves, equation (3) can be replaced by its linearized form as:

$$\rho_f \frac{\partial \phi}{\partial t} + P + \rho_f gz = 0 \tag{4}$$

Since waves are assumed to be small, the free surface boundary condition

$$\frac{\partial \phi}{\partial z}\Big|_{z=0} - \frac{\omega^2}{g}\phi\Big|_{z=0} = 0 \tag{5}$$

Can be applied on S_F, where ω is the angular frequency of the wave motion caused by the vibration of the plate. On the bottom of the tank, the normal component of velocity is zero, i.e.

$$\frac{\partial \phi}{\partial z}\Big|_{z=-(h_1+h+h_2)} = 0 \tag{6}$$

The kinematics boundary conditions at plate-fluid interfaces S_L and S_U are given by

$$\frac{\partial \phi}{\partial z}\Big|_{z=-(h_1+h)} = \frac{\partial \phi}{\partial z}\Big|_{z=-h_1} = \frac{\partial W}{\partial t} \tag{7}$$

Using equation (4) we have:

On S_U

$$\rho_f \frac{\partial \phi}{\partial t}\Big|_{z=-h_1} + P_U - \rho_f g h_1 = 0 \tag{8}$$

And on S_L

$$\rho_f \frac{\partial \phi}{\partial t}\Big|_{z=-(h_1+h)} + P_L - \rho_f g(h_1 + h) = 0 \tag{9}$$

Substitution of equation (8) and (9) in to equation (3) gives the following governing equation

$$\begin{aligned}&\rho \frac{\partial^2 W}{\partial t^2} + \rho_f \left[\frac{\partial \phi}{\partial t}\Big|_{z=-(h_1+h)} - \frac{\partial \phi}{\partial t}\Big|_{z=-h_1} \right] + D_x \frac{\partial^4 W(x,y,t)}{\partial x^4} + \\ &2H \frac{\partial^4 W(x,y,t)}{\partial x^2 \partial y^2} + D_y \frac{\partial^4 W(x,y,t)}{\partial y^4} - \rho_f g h = 0\end{aligned} \tag{10}$$

Based on separation variable method, the displacement of the small amplitude bending vibration of the plate can be assumed as

$$W(x,y,t) = \overline{W}(x,y)T(t) \tag{11}$$

Let's also assume that the velocity potential $\phi(x,y,z,t)$ can be considered in the form of

$$\phi(x,y,z,t) = G(x,y)F(z)S(t) \tag{12}$$

Substituting Equation (12) into Equation (2) gives

$$F(z)\nabla^2 G(x,y) + G(x,y)\frac{d^2 F(z)}{dz^2} = 0 \tag{13}$$

$G(x,y)$, is a function of x and y, and F(z) is a function of z, so the following equation holds, viz.

$$\frac{\nabla^2 G}{G} = -\frac{\frac{d^2 F}{dz^2}}{F} = -\mu^2 \tag{14}$$

This can be written as

$$\nabla^2 G + \mu^2 G = 0 \tag{15}$$

$$\frac{d^2 F}{dz^2} - \mu^2 F = 0 \tag{16}$$

Where μ^2 is a real constant, and μ is the plane wave number, which is determined by the vibrating frequency of the submerged plate and fluid boundary conditions in the x-y plane. Substituting Equation (11) and (12) in to Equation (7) gives

$$G(x,y)S(t) = \overline{W}(x,y)\frac{T'}{F'\big|_{z=-(h_1+h)}} \tag{17}$$

Where, $T' = \frac{dT}{dt}$ and $F'(z) = \frac{dF}{dz}$

Applying Equation (17) to Equation (12) gives

$$\phi(x,y,z,t) = F(z)\overline{W}(x,y)\frac{T'(t)}{F'\big|_{z=-(h_1+h)}} \tag{18}$$

We also have

$$\phi(x,y,z,t) = F(z)\overline{W}(x,y)\frac{T'(t)}{F'\big|_{z=-h_1}} \tag{19}$$

The combination of Equations (11), (18), (19) and Equation (10) gives

$$T'' + \omega_{fluid}^2 T = 0 \tag{20}$$

$$\nabla^4 \overline{W} - \beta^4 \overline{W} = 0 \tag{21}$$

Applying Equation (11) gives

$$\frac{\partial^2 W}{\partial t^2} = \overline{W}\frac{d^2 T}{dt^2} = \overline{W}T'' \tag{22}$$

Applying Equation (18) and Equation (19) gives

$$\begin{aligned}&\frac{\partial \phi}{\partial t}\Big|_{z=-(h_1+h)} - \frac{\partial \phi}{\partial t}\Big|_{z=-h_1} = \\ &\overline{W}T'' \left[\frac{F}{F'}\Big|_{z=-(h_1+h)} - \frac{F}{F'}\Big|_{z=-h_1} \right]\end{aligned} \tag{23}$$

$$\nabla^4 = T\nabla^4 \overline{W} \tag{24}$$

Applying Equations (22), (23) and (24) to Equation (10) gives

$$\rho\bar{W}T'' + \rho_f\bar{W}T''\left[\frac{F}{F'}\bigg|_{z=-(h_1+h)} - \frac{F}{F'}\bigg|_{z=-h_1}\right] + D_x\frac{\partial^4 W(x,y,t)}{\partial x^4} + 2H\frac{\partial^4 W(x,y,t)}{\partial x^2\partial y^2} + D_y\frac{\partial^4 W(x,y,t)}{\partial y^4} - \rho_f gh = 0 \tag{25}$$

Where the term $\rho_f gh$ is a static load. It has effect only on the equilibrium position, but not on the dynamical response. So Equation (25) can be solved without considering this static term. Consider the equation

$$\rho\bar{W}T'' + \rho_f\bar{W}T''\left[\frac{F}{F'}\bigg|_{z=-(h_1+h)} - \frac{F}{F'}\bigg|_{z=-h_1}\right] + D_x\frac{\partial^4\bar{W}(x,y)}{\partial x^4}T(t) + 2H\frac{\partial^4\bar{W}(x,y)}{\partial x^2\partial y^2}T(t) + D_y\frac{\partial^4\bar{W}(x,y)}{\partial y^4}T(t) = 0 \tag{26}$$

Where $\rho^* = \rho_f\left[\frac{F}{F'}\bigg|_{z=-(h_1+h)} - \frac{F}{F'}\bigg|_{z=-h_1}\right]$ is the added mass due to the fluid- loading effect. That is

$$(\rho+\rho^*)\bar{W}T'' + D_x\frac{\partial^4 W(x,y,t)}{\partial x^4} + 2H\frac{\partial^4 W(x,y,t)}{\partial x^2\partial y^2} + D_y\frac{\partial^4 W(x,y,t)}{\partial y^4} = 0 \tag{27}$$

The combination of Equation 11, 18, 19 and Equation 10 gives

$$T'' + \omega_{fluid}^2 T = 0 \tag{28}$$

$$\nabla^4\bar{W} - \beta^4\bar{W} = 0 \tag{29}$$

$$\beta^4 = (\rho+\rho^*)\omega_{fluid}^2 \tag{30}$$

Where, ω_{fluid} is the natural frequency of the plate underwater; β is a constant determined by the plate boundary conditions. If the plate vibrates in air, the response equations corresponding to Equations 28, 29 can be obtained

$$T'' + \omega_{air}^2 T = 0 \tag{31}$$

$$D_x\frac{\partial^4 W(x,y,t)}{\partial x^4} + 2H\frac{\partial^4 W(x,y,t)}{\partial x^2\partial y^2} + D_y\frac{\partial^4 W(x,y,t)}{\partial y^4} - \beta'^4\bar{W} = 0 \tag{32}$$

Here

$$\beta'^4 = \omega_{air}^2\rho \tag{33}$$

The constant β' is determined by plate boundary conditions, which are the same whenever the plate is submerged in fluid or in air. Thus one has

$$\beta = \beta' \tag{34}$$

In this case we have the following basic equation

$$\omega_{fluid} = \omega_{air}\frac{1}{\sqrt{1+\frac{m^*}{m}}} \tag{35}$$

Equation (35) displays the relationship between natural frequency of the plate in fluid and that in air.

2.1 THE NATURAL FREQUENCY FOR DRY STIFFENED PLATE

In this section, Rayleigh's method is used to compute the natural frequencies in vacuum environment. The Rayleigh's method is based on following relation (Ventsel, 2001).

$$U_{\max} = K_{\max} \tag{36}$$

Where

$$U_{1\max} = \frac{1}{2}\int_0^a\int_0^b\left[D_x\left(\frac{\partial^2 W}{\partial x^2}\right)^2 + D_y\left(\frac{\partial^2 W}{\partial y^2}\right)^2 + 2D_{xy}\frac{\partial^2 W}{\partial x^2}\frac{\partial^2 W}{\partial y^2} + 4D_s\left(\frac{\partial^2 W}{\partial y\partial x}\right)^2\right]dxdy$$

$$D_x = \frac{EI}{t},\quad D_y = \frac{Eh^3}{12\left(1-\frac{b}{t}+\frac{bh^3}{tH_1^3}\right)},\quad D_{xy} = 0,\quad \mathrm{D}_s = \frac{Gh^3}{12}$$

$$H = D_{xy} + 2D_s$$

$$K_{\max} = K_{\max\, plate} + K_{\max\ stiffeners} = \frac{\omega^2}{2}\left(\int_0^a\int_0^b \rho_{plate}h\bar{W}(x,y)\,dxdy + n\int_0^c\int_0^b \rho_{stiff}\,l\,\bar{W}(x,y)\,dxdy\right)$$

Where n is the number of stiffeners. By satisfying the boundary conditions of fixed four sides (Equation(37)), the deflection of plate can be obtained as follow and this leads to achieving natural frequency as shown in Equation (38).

$$\overline{W} = A_{mn}(1-\cos\frac{2m\pi x}{a})(1-\cos\frac{2n\pi y}{b}) \tag{37}$$

$$\omega_{air} = \frac{22.79}{a^2}\sqrt{\frac{1}{\rho}\left[D_x + D_y(\frac{a}{b})^4 + \frac{2}{3}H(\frac{a}{b})^2\right]} \tag{38}$$

By using differential equation (14**)** and applying the Rayleigh's method**,** the natural frequency of submerged reinforced plate is obtained. When Rayleigh's method is written to find natural frequency under the water, the frequency is proportional to the ratio of the maximum potential energy to the sum of kinetic energy of reinforced plate T_p^* and fluid T_F^*. The values of V_p and T_p^* in fluid and vacuum are constant, so the natural frequency of reinforced plate in vacuum and fluid are related to each other as shown in Equation(35). Using Rayleigh's method for submerged stiffened plate leads to the following natural frequency.

$$\omega_{fluid} = \frac{22.79}{a^2}\sqrt{\frac{m}{\rho(m+m_a)}\left[D_x + D_y(\frac{a}{b})^4 + \frac{2}{3}H(\frac{a}{b})^2\right]} \tag{39}$$

There are different ways to calculate the added mass (m_a) for example Strip or Greenspon method (Goninan 2001 and Liu 1995).

3. NUMERICAL SIMULATIONS

In order to validate the present formulation, the natural frequency obtained by the present method under clamped boundary conditions is compared with finite element whose results was validated through natural frequency of the modal testing under free boundary conditions in section 4**.** The reason for using this method validation, is that clamped boundary conditions applied in practice and experimental setup is very difficult and inaccurate, therefore, FEM software is used as an intermediary to compare the results of the analytical and experimental procedure. In the modeling of the submerged plate, the shell elements are used to design the plate and stiffeners. To achieve the natural frequencies of the model, free vibration analysis is used without any external excitations. For the free vibration analysis the numerical solution is reduced to solving the problem (X.H. Wang, 2006).

$$[K]\times(u) = \omega\times[M]\times(u) \tag{40}$$

Where [K] and [M] are, respectively, the stiffness and mass matrix while (u) and ω are the modal vector and the frequency parameter. Numerical results of first two mode shapes of the dry stiffened plate are shown in Figure 2. As shown in Figure 2 (c), first mode shape of the dry stiffened plate is in twisted form but in it can be seen in Figure 2 (d) the second mode shape is in bended form. It is expected that the same mode shapes could be seen in the fluid with different frequency values.

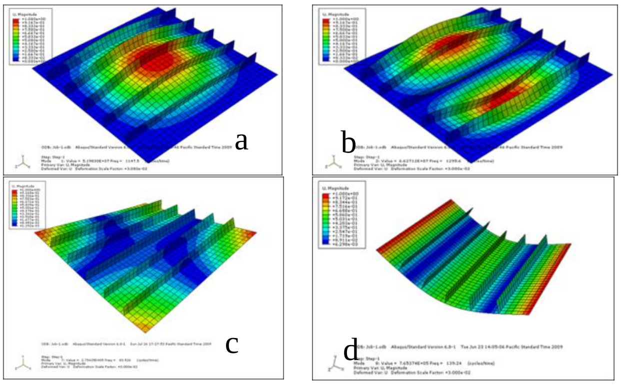

Figure 2: dry stiffened plate frequency; (a), (b) first and second natural frequency (1147 and 1295.6 Hz) in clamped boundary conditions; (c), (d) first and second natural frequency (83.5 and 139.2 Hz) in free boundary conditions

It should be noted that in the submerged case in order to improve the mode shape view, the fluid of upper side of the plate is hidden in the software results. Numerical results of mode shapes of the wet stiffened plate are shown in Figure 3.

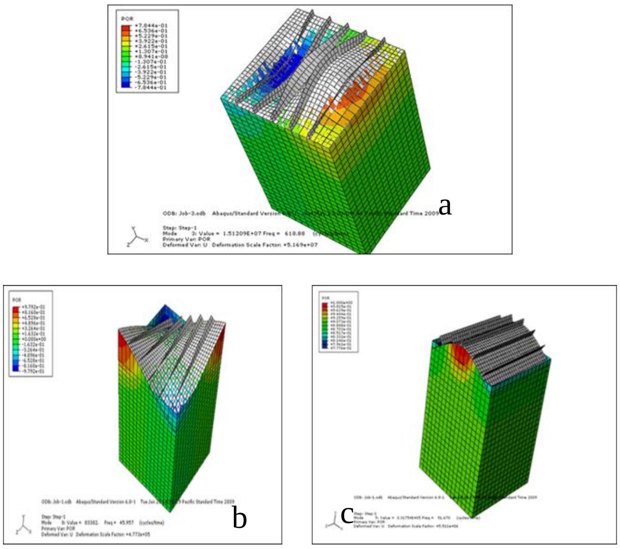

Figure 3:wet stiffened plate frequency; (a) first natural frequency (618.8 Hz) in clamped boundary conditions; (b) , (c) first and second natural frequency (45.95 and 91.6 Hz) in free boundary conditions

As shown in Figure 3 (b), first mode shape of the plate in the water environment is in twisted form but in Figure 3 (c) it can be seen that the second mode shape is in bended form. As expected previously, the obtained mode shapes in the vacuum and fluid are the same. Obviously, as mentioned in the literature the natural frequencies of structures in the fluid are less than of in the vacuum. This is due to the added mass of the fluid in the structure. Numerical results of the study verified the above claim. In all of simulations the density of water and its bulk modulus are considered as 1000 $({}^{kg}/_{m^3})$ and $2.7 \times 10^9 (pa)$ respectively.

4. EXPERIMENTAL ANALYSIS

The natural frequencies of the stiffened plate are obtained using modal analysis of frequency response functions (FRF) practically. The dynamic response of a mechanical structure while either in a development phase or an actual use environment can readily be determined by impulse force testing. These tests are performed by B&K modal testing equipment. Using an FFT (Fast Fourier Transformation) analyzer, the transfer function of the structure can be determined from a force pulse generated by the impact of a hammer and the response signal measured with an accelerometer. The impact force yields extensive information about the frequency and attenuation behavior of the system under test. By using FFT and phase analysis the natural frequencies can be easily obtained. The boundary conditions of stiffened plate are considered free on all sides. Thickness of stiffeners and plate are considered $4mm$. The test vessel, stiffened plate and Portable Vibration Analysis Toolbox (PVAT) system are shown in Figures 4.

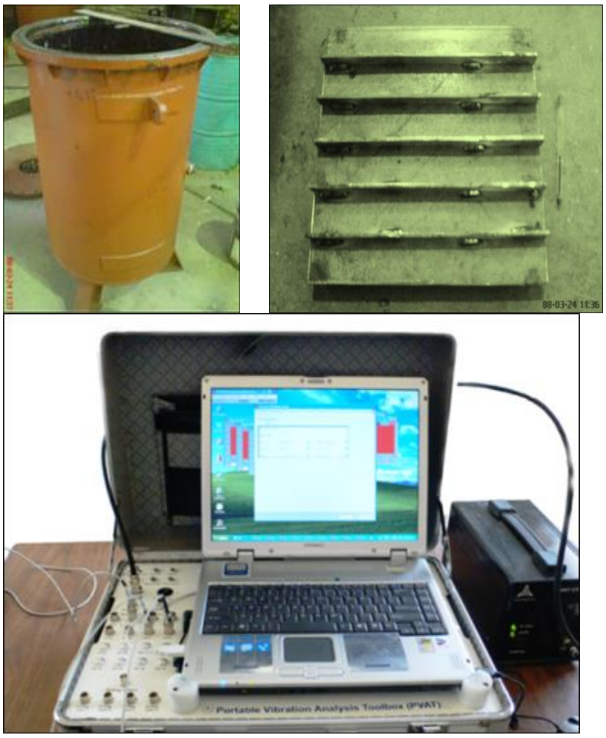

Figure 4: Modal test equipment

4.1 MODAL TEST RESULTS

Test specimens flouted in the air and submerged in the water are shown in Figures 5 (a) and 5 (b) respectively (The stiffeners could not be seen in the pictures because that was welded on the lower side of stiffened plate).

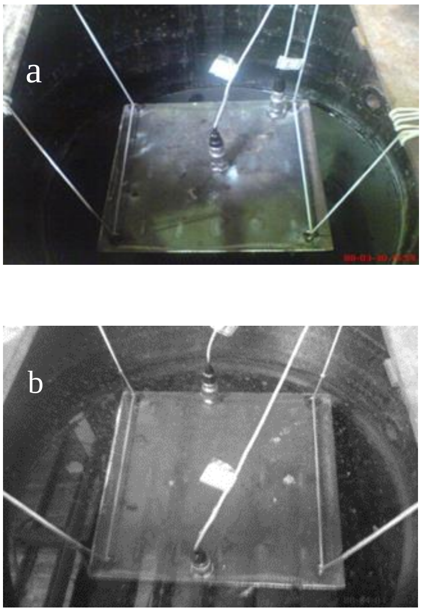

Figure 5: stiffened plate in air (a) and underwater (b).

In order to analyze stiffened plate in the air, each of accelerometers is connected to separate channels of the PVAT system analyzer. Some tests were done under different conditions. For example, two accelerometers are attached to plate can be seen in Figure 5. Hammer impacts are applied to specified points on the plate. The locations of attachment of accelerometers and points of hammer exciting impact are shown in Figure 6.

All points of the plate attached to the accelerometers are selected according to the obtained results from mode shapes in numerical simulations. Indeed, the accelerometer has to be attached to the point showing the maximum displacement in the particular mode. FFT responds are then obtained based on velocity and acceleration criterion. The FFT graphs in air are shown in Figure 6 (X values show the frequency).

The submerged sensors in the water, are isolated using water proof adhesive. Height of water on the upper side of stiffened plate in the vessel is $25cm$. All of the tests in the air environment are the same as in the fluid. The FFT graphs of underwater case are shown in Figure 7.

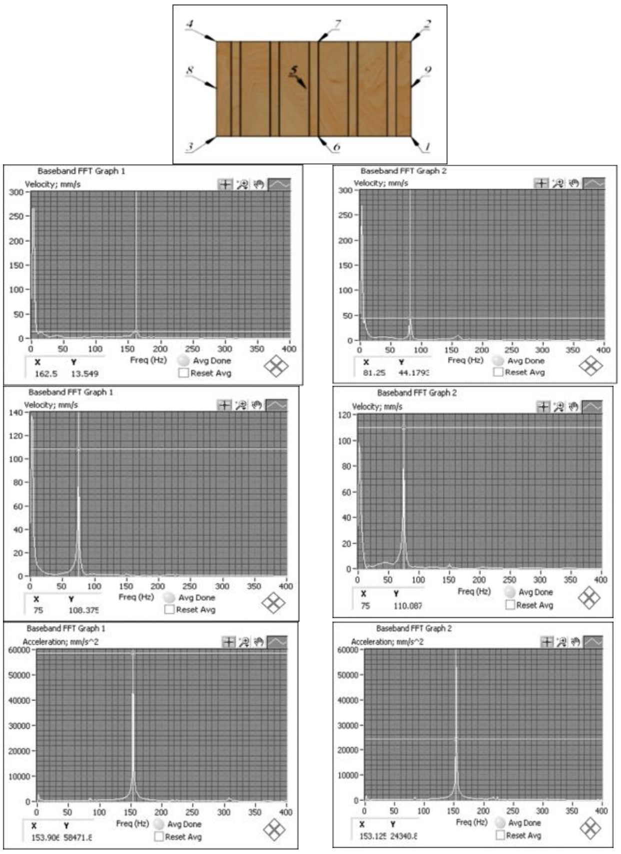

Figure 6: the FFT graphs of dry stiffened plate

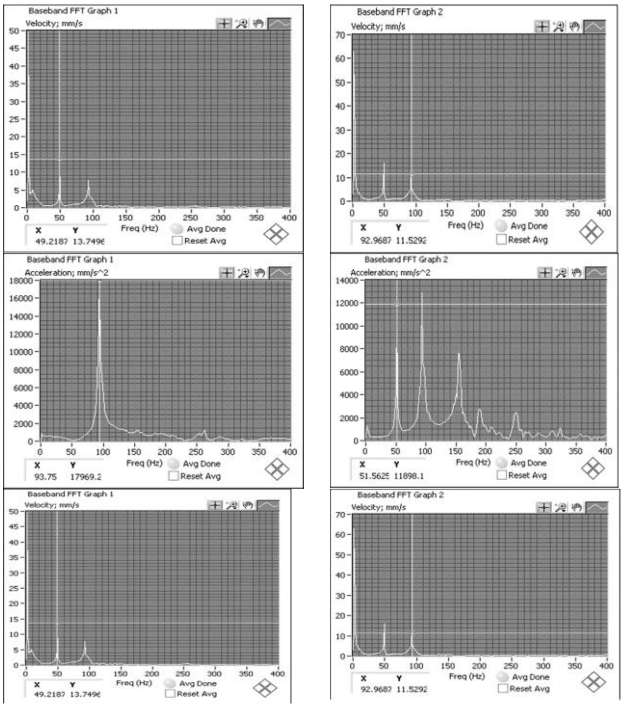

Figure 7: the FFT graphs of wet stiffened plate

5. RESULTS

To evaluate the coupled acoustic analysis in numerical solution the final solution was compared to the experimental results. The results and the relative error of both finite element solutions to the experiment are shown in Table 2 with free boundary conditions on all sides.

Table 2 Comparison of test and the numerical results for first two modes shapes frequency

	Numerical result	Test result	Error %
Wet frequency (Hz)	45.957	49.2	6.5
	91.670	93.7	2
Dry frequency (Hz)	83.526	78	7
	139.24	155	10.1

The previous calculations show that it was possible to simulate the vibration of the stiffened plate in the water tank. In building three models with an increasing number of elements, it was ensured that the solution be converged. It is therefore justified to use the numerical solution in the design process of vessels that should be used underwater which are subject to vibration. Comparison of the analytical and the numerical results for first mode shapes frequency are shown in Table 3.

Table 3 Comparison of the analytical and the numerical results for first mode shapes frequency

	Numerical result	Analytical result	Error %
Wet frequency (Hz)	618.88	649.026	4.6
Dry frequency (Hz)	1147.5	1295	11.3

Table 2 and 3 show the accuracy of numerical and analytical result. Strings as free boundary conditions for all sides of plate, make error in results. Also improper hammer impact produces an error.

6. CONCLUSIONS

In this study, the free vibration of a stiffened plate in contact with bounded water is investigated both theoretically and experimentally. The kinetic and potential energy for stiffened plate with the kinetic energy of the bounded water are obtained and used in Rayleigh's method to extract the natural frequency. The effect of contact with water on the vibration of stiffened plate is therefore appeared as an added mass in vertical displacement of the plate. Free-free boundary conditions are arranged for the stiffened plate in a hammer-accelerometer modal testing. The shape of the Fast Fourier Transform function versus frequency graph for the dry and wet stiffened plates are observed to be similar but shifted along the frequency axis with a factor of about 0.5 for frequency.

FEM is used as an intermediary to verify the present analytical results for a clamped stiffened plate. However, since the application of clamped boundary conditions is difficult in practice, free-free boundary conditions are set up for the plate experimentally. The results of FEM are on the other hand verified by the modal testing for free-free boundary conditions. Finally, the natural frequency obtained by the present method is compared and validated with FEM under clamped boundary conditions. So, with a good approximation, the Equation (39) can be used to calculate the natural frequency of stiffened plates in contact with any fluid.

7. REFERENCES

1. AKSU, G., 1982. *Free vibration analysis of stiffened plates by including the effect of inplane inertia*. ASME, Transactions, Journal of Applied Mechanics 49, 206-212.
2. CIVALEK, Ö., 2008. *Analysis of thick rectangular plates with symmetric cross-ply laminates based on first-order shear deformation theory*. Journal of Composite Materials 42 (26), 2853-2867.
3. HOLOPAINEN, T., 1995. *Finite element free vibration analysis of eccentrically stiffened plates*. Computers & structures 56 (6), 993-1007.
4. KERBOUA, Y., LAKIS, A.A., THOMAS, M., MARCOUILLER, L., 2008. *Vibration analysis of rectangular plates coupled with fluid*. Applied Mathematical Modelling 32,2570–2586.
5. KERBOUA, Y., LAKIS, A.A., THOMAS, M., MARCOUILLER, L., 2008. *Three- dimensional modeling of curved structures containing and/or submerged in fluid.* Finite Elements in Analysis and Design, Vol. 44,pp. 334 – 345.
6. KUNDU, P. K. ,1990. *Fluid mechanics*. Academic Press Inc., 638 pp
7. KIM, J.K., KOH, H.M., WAHK, I.J., 1996. *Dynamics response of rectangular flexible fluid containers*. Journal of Engineering Mechanics, Vol. 122 (9), pp. 807-817.
8. KIM, M.C., LEE, S.S., 1997. *Hydroelastic analysis of a rectangular tank*. In: MSC Aerospace User's Conference. Newport Beach, CA, pp. 17–20.
9. HERNANDEZ, E., 2006. *Approximation of the vibration modes of a plate and shell coupled with a fluid*. J. Appl. Mech. Trans. ASME 73, 1005–1010.
10. HERTING, D.N., 1997. MSC/NASTRAN, *Advanced Dynamics User's Guide*, Version 70. MacNeal-Schwendler Corporation.
11. HIBBITT., KARLSSON., ORENSEN., 2001. ABAQUS/ Standard, *User's Manual*, Version 6.2-1.
12. CRIGHTON, D.G., INNES, D., 1983. *Low frequency acoustic radiation and vibration response of locally excited fluid-loaded structures*. Journal of Sound and Vibration 91 , 293–314.
13. LIANG, C.C., TAI, Y.S., LI, P.L., 1999. *Letters to the editor Natural frequencies of annular plates having contact with fluid*. Journal of Sound and Vibration 228, 1167–1181.
14. ZHANG, W., WANG, A., VLAHOPOULOS, N., WU, K., 2003. *High-frequency vibration analysis of thin elastic plates under heavy fluid loading by an energy finite element formulation*. Journal of Sound and Vibration 263 , 21–46.
15. ZHANG, W., WANG, A., VLAHOPOULOS, N., WU, K., 2005. *A vibration analysis of stiffened plates under heavy fluid loading by an energy finite element analysis formulation*. Finite Elements in Analysis and Design 41 , 1056–1078.
16. LI., P-L., SHYU, R-J., WANG, W-H., CHENG. C-Y., 2011. *Analysis and reversal of dry and hydroelastic vibration modes of stiffened plates*. Ocean Engineering, Volume 38, Issues 8-9, Pages 1014-1026.
17. VENTSEL, E., KRAUTHAMMER, T., 2001. *Thin Plates and Shells*. The Pennsylvania State University University Park, Pennsylvania.
18. ESMAILZADEH, M., LAKIS, A.A., THOMAS, M., MARCOUILLER, L., 2007. *Three-dimensional modeling of curved structures containing and/or Submerged in fluid*. Finite Elements in Analysis and Design 44, 334 – 345.
19. LIU, B.-L., and O FARRELL, J.M., 1995. *High Frequency Flow/ Structural Interaction in Dense Subsonic Fluids*. NASA Contractor Report 4652 March
20. A. GONINAN & CO.¸ LTD., 2001. Broadmeadow Road, Broadmeadow, NS= 2292, Australia and CLAUSEN, P. D.,: *An added mass theory for the base plate in a partially filled rectangular tank for use with FEA*. Journal of Sound and Vibration 246(2), 211-223
21. WANG, X.H., XU, B., REDEKOP, D., 2006. *FEM free vibration and buckling analysis of stiffened toroidal shells*. Thin-Walled Structures 44, 2–9
22. GÜRSES, M., CIVALEK, Ö., KORKMAZ, A., ERSOY.H, *Free vibration analysis of symmetric laminated skew plates by discrete singular convolution technique based on first-order shear deformation theory*, International journal for numerical methods in engineering,Vol 79,pp. 290-313.
23. CHO, D., VLADIMIR N., and CHOI, T., 2013. *Natural vibration analysis of stiffened panels with arbitrary edge constraints using the assumed mode method*, Vol 229(4), pp.340-349.

VISCOSITY IN SEAKEEPING

(DOI No: 10.3940/rina.ijme.2018.a2.473)

M Pawłowski, Gdansk School of Higher Education, Poland

SUMMARY

Application of strip theory for the prediction of ship motions in waves relies on sectional hydrodynamic coefficients; i.e. the added mass and damping coefficients. These coefficients apply to linearised problems and are normally computed for inviscid fluids. It is possible to account for viscosity but this cannot be done by the RANS equations, as in linear problems there is no room for turbulence. The hydrodynamic coefficients can include the effect of viscosity but this can be done rightly through the classic Navier–Stokes equations for laminar (non-turbulent) flows. For solving these equations commercial RANS software can be used, assuming no Reynolds stresses.

NOMENCLATURE

$\forall$	sectional area
A	amplitude of oscillations
a	sectional added mass
B	sectional breadth of body
b	sectional damping coefficient
c	sectional coefficient of stiffness
h	distance from body surface
$\boldsymbol{I}$	unit matrix
k	$= (\omega/2\nu)^{1/2}$ – wave number
k'	$= (\omega/\nu)^{1/2} = 2^{1/2}k$
K	$= k'\sqrt{i}$, constant
k	$= 2\pi/\lambda$ – wave number of regular wave
k	kinetic energy of turbulence
k	unit vector of the z-axis
l	characteristic length of body
p	pressure
$\boldsymbol{P}$	stress tensor
$\overline{\boldsymbol{P}}$	stress tensor for smoothed motion
r	radius, distance from an axis
$\boldsymbol{R}$	tensor of turbulent fluctuations
Re	Reynolds number
RANS	Reynolds Averaged Navier–Stokes equations
$\boldsymbol{S}$	tensor of velocity
$\boldsymbol{S}_d$	tensor of deformations
T	period of oscillations
u	forward speed of ship
u_0	amplitude of velocity of oscillations
v	velocity field
β	incident angle between direction of wave propagation and ship speed
δ	$= 1/k = (2\nu/\omega)^{1/2}$ – skin depth (depth of penetration)
ϕ	velocity potential
λ	wave length
μ_t	dynamic coefficient of turbulent viscosity
μ	dynamic coefficient of viscosity
ν	$= \mu/\rho$ – kinematic coefficient of viscosity
ρ	density
ρ'	$k'r = 2^{1/2}kr$ – module of Kr
ρ	$= Kr$ – nondimensional radius (complex)
ω	$= 2\pi/T$ – circular frequency of oscillations
ω	circular frequency of regular wave

1. INTRODUCTION

A question arises if viscosity should be accounted for in ship's dynamics, particularly in seakeeping. When analysing a non-stationary ship's motion two hydrodynamic coefficients are used: the added mass and damping coefficients. Strictly speaking, they are applicable only to linearised equations of motion. In the case of inviscid fluids·, the field of velocity around the body has a potential ϕ, fulfilling the Laplace equation $\Delta\phi = 0$ along with boundary conditions. The said equation is linear, leaving no room for turbulence. In other words, such a velocity field is always smooth, both for viscous and inviscid fluids, clearly observed outside the boundary layer, where flow is potential, despite the viscosity of water. To show this, it is sufficient to observe that the Laplacian of velocity vanishes in potential flow, when $\boldsymbol{v} = \operatorname{grad}\phi$. Namely:

$$\Delta \boldsymbol{v} = \Delta \operatorname{grad}\phi = \operatorname{grad}\Delta\phi = 0.$$

We could change here the sequence of differentiation and account for the fact that the potential fulfils the Laplace equation $\Delta\phi = 0$. Hence, outside the boundary layer the fluid behaves, as if it was inviscid. The same conclusion can be obtained resorting to a useful identity:

$$\Delta \boldsymbol{v} \equiv \operatorname{grad}\operatorname{div}\boldsymbol{v} - \operatorname{rot}\operatorname{rot}\boldsymbol{v}. \qquad (1)$$

For incompressible ($\operatorname{div}\boldsymbol{v} \equiv 0$) and irrotational ($\operatorname{rot}\boldsymbol{v} \equiv 0$) flows, the Laplacian of velocity vanishes.

For rotational flows, the potential of velocity does not exist. Vorticity is due to viscosity, which comes to action in close vicinity of the wall, as e.g. in the boundary layer in a wall-bounded flow. In such a case, the governing equation for laminar flows, neglecting the unit mass force, is the Navier–Stokes equation:

$$\frac{\partial \boldsymbol{v}}{\partial t} + (\boldsymbol{v}\cdot\nabla)\boldsymbol{v} = -\tfrac{1}{\rho}\operatorname{grad} p + \tfrac{1}{3}\nu\operatorname{grad}\operatorname{div}\boldsymbol{v} + \nu\Delta\boldsymbol{v}, \qquad (2)$$

where μ and $\nu \equiv \mu/\rho$ are the dynamic and kinematic coefficients of viscosity, respectively, and ρ is the density of fluid. The two terms on the left hand-side represent the acceleration of a particle $d\boldsymbol{v}/dt$. This is a non-linear equation of motion. The only non-linear term – the second one on the left hand-side – is the acceleration related to the convection of the particle, known as the *convective acceleration*, which is the source of turbulence. For linearised equations, in which the non-linear term $(v \cdot \nabla)v$ is neglected, the averaging process introduces no Reynolds stresses and therefore the linearised equations of motion remain unchanged after averaging. In other words, solutions to linearised N–S equations, despite viscosity, are still smooth. Such equations are closed and need no turbulence models. For that reason, employing turbulence models for linear problems, which is widely applied in literature, is conceptually wrong, see for instance Salui *et al.* (2000), Quérard *et al.* (2009), and many others.

Linearised seakeeping analysis is normally based on the assumption of potential flow, applicable to inviscid fluids. Furthermore, in linear approach *physical* oscillations are replaced by *virtual* ones in which the body is assumed to be stationary, i.e. moving without oscillations. In such a case, motion of the fluid due to oscillations is depicted by the boundary condition on the surface of the body, crucial for the problem. That is, the normal component of fluid velocity on the outer surface of the body equals the normal component of velocity of the outer surface, which is such as on the body in real motion, completed by the boundary conditions on the free surface and in infinity. Fluid particles move (slide) along the surface of the body but this does not create any vorticity, as by assumption the fluid is inviscid.

Evidence shows (Salvesen *et al*, 1970) that the prediction of ship motions based on potential flow provides satisfactory results, except for roll, where viscous effects are considerable, particularly for damping. But, even then, there are serious doubts, if the hydrodynamic coefficients should be determined resorting to turbulence. Flow around a rolling ship contains vorticity, particularly for V-type and rectangular sections, but this does not mean necessarily that it is turbulent.

To overcome this problem a number of experimental and numerical methods have been developed for the prediction of roll damping. The most known is a semi-empirical method developed by Ikeda *et al.* (1978). The linearised-damping coefficient has been divided into a number of components, reflecting various effects. The idea of linearisation of the non-linear roll damping is thoroughly discussed by the author Pawłowski (2010). It is worth mentioning a substantial work on non-linear roll damping carried out by Spouge (1988). One common disadvantage of experimental methods is that the results obtained are limited to particular geometry of ships. To be free of this limitation, various numerical techniques are used for calculating the hydrodynamic coefficients for roll, such as discrete vortex method (DVM), random vortex method (RVM), and the Reynolds Averaged Navier–Stokes (RANS) equations, discussed briefly below. Vortex methods were popular in the past, as they require much smaller computing power than finite volume collocated grid approaches, part of which are RANS solvers. But nowadays, with rapid advancement in computing, FEM became widely applied, backed-up by the Volume of Fluid method, used for modelling the free surface. They are the best means for solving viscous flows. They can reproduce the creation of vorticity in the boundary layer and vortex shedding.

The hydrodynamic forces acting on the body in potential flows are found by integration of the dynamic pressure p, given by the Cauchy–Lagrange equation, over a wetted surface of the body in the mean position:

$$p = -\rho\left({}^{\partial\phi}/_{\partial t} + \tfrac{1}{2}v^2\right), \tag{3}$$

which results in the added mass m and damping coefficient N, both dependent on the circular frequency of *forced* oscillations $\omega = 2\pi/T$ [rad/s], where T is the period of oscillations, and $\boldsymbol{v} = \operatorname{grad}\phi$. The term $\tfrac{1}{2}v^2$ is usually neglected, as small quantity.

The convective acceleration can be expressed in two ways:

$$(v \cdot \nabla)v \equiv Sv \equiv \tfrac{1}{2}\operatorname{grad} v^2 - v \times \operatorname{rot} v, \tag{4}$$

where $S \equiv (\nabla \otimes v)^{\mathrm{T}}$ is the tensor of velocity. In potential flows $(v \cdot \nabla)v = \tfrac{1}{2}\operatorname{grad} v^2$.

Assuming that the convective acceleration is small relative to other terms, it can be neglected. The non-linear equation of motion (2) for viscous flows reduces then to the linear one:

$$\frac{\partial \boldsymbol{v}}{\partial t} = -\tfrac{1}{\rho}\operatorname{grad} p + \tfrac{1}{3}\nu \operatorname{grad}\operatorname{div}\boldsymbol{v} + \nu\Delta\boldsymbol{v}\,\cdot \tag{5}$$

As such, it leaves no room for turbulence provided that the Reynolds number for a given case of flow is less than the critical value, i.e. when $\mathrm{Re} < \mathrm{Re}_{crit}$. Its solutions are smooth then, though not necessarily of laminar type, due to the complexity of flow induced by vorticity, in particular – by trailing vortices. Complex flows are not the same as turbulent. Nonetheless, the said equation is typically solved using various RANS solvers along with turbulence models, though a plain FEM would be entirely sufficient.

The right-hand side of equation (5) equals to ${}^{1}/_{\rho}\operatorname{Div}P$, where $P = -pI + 2\mu(S_d - \tfrac{1}{3}I\operatorname{div}v)$ is the stress tensor, p is the pressure, I is the unit matrix, and S_d is the tensor of deformation. The stress tensor P is essential for calculating the stress vector $p_n = Pn$, where n is a unit vector normal to given surface element.

Once, the instantaneous stress tensor P is obtained by integrating equation (5) along with the equation of continuity and boundary conditions, instantaneous values of the hydrodynamic forces and moments can be obtained by integrating the elementary forces $p_n dS$ over the wetted surface S of the submerged body.

Frequently, the pressure field p is either constant or a function of the velocity field $\boldsymbol{v}$. In such cases, equation (5) reduces to the *equation of diffusion*:

$$\partial \boldsymbol{v}/\partial t = \nu \Delta \boldsymbol{v}, \tag{6}$$

well known in theoretical physics.

2. AVERAGED NAVIER–STOKES EQUATIONS

As we can see, the linearised Navier–Stokes equation (5) is capable of providing realistic solutions for the hydrodynamic coefficients in roll, accounting for viscosity. But we have to be cautious here. The above statement is valid for laminar flows only, when $\mathrm{Re} < \mathrm{Re}_{crit}$, which is in practice the case. Otherwise, instability of flow (turbulence) happens due to the omitted convective acceleration $(\boldsymbol{v}\cdot\nabla)\boldsymbol{v}$. The said instability opens room for turbulence stresses, important for analysis of the boundary layer, essential for the problem of steady resistance of the ship, and not for seakeeping.

When flow is turbulent the velocity field can be presented, as $\boldsymbol{v} = \bar{\boldsymbol{v}} + \boldsymbol{v}'$, where $\bar{\boldsymbol{v}}$ is the mean (time-averaged, *smoothed*) component, of laminar type, and $\boldsymbol{v}'$ is the *velocity of fluctuation* (turbulent pulsation), of stochastic nature. Similarly, the pressure $p = \bar{p} + p'$. Substituting $\boldsymbol{v}$ and p to equation (2), after averaging the following is obtained for the equation of turbulent flow:

$$\frac{\partial \bar{\boldsymbol{v}}}{\partial t} + \overline{(\boldsymbol{v}\cdot\nabla)\boldsymbol{v}} = -\tfrac{1}{\rho}\,\mathrm{grad}\;\bar{p} + \tfrac{1}{3}\nu\,\mathrm{grad}\;\mathrm{div}\,\bar{\boldsymbol{v}} + \nu\Delta\bar{\boldsymbol{v}}\,\cdot \tag{7}$$

If $\mathrm{div}\boldsymbol{v}' = 0$, the averaged convective acceleration equals:

$$\begin{aligned}\overline{(\boldsymbol{v}\cdot\nabla)\boldsymbol{v}} &= (\bar{\boldsymbol{v}}\cdot\nabla)\bar{\boldsymbol{v}} + \overline{(\boldsymbol{v}'\cdot\nabla)\boldsymbol{v}'} = \\ &= (\bar{\boldsymbol{v}}\cdot\nabla)\bar{\boldsymbol{v}} + \nabla\left(\overline{\boldsymbol{v}'\otimes\boldsymbol{v}'}\right) = (\bar{\boldsymbol{v}}\cdot\nabla)\bar{\boldsymbol{v}} + \mathrm{Div}\,\boldsymbol{R},\end{aligned} \tag{8}$$

where $R \equiv \overline{(v'\otimes v')}$ is a dyad (tensor) of averaged turbulent fluctuations made up of two the very same vectors $\boldsymbol{v}'$ and $\boldsymbol{v}'$, whose elements $R_{ij} = \langle v'_i v'_j \rangle$ are averaged with respect to time:

$$\boldsymbol{R} = \begin{bmatrix} \overline{v_1'^2} & \overline{v_1'v_2'} & \overline{v_1'v_3'} \\ \overline{v_2'v_1'} & \overline{v_2'^2} & \overline{v_2'v_3'} \\ \overline{v_3'v_1'} & \overline{v_3'v_2'} & \overline{v_3'^2} \end{bmatrix} = \begin{bmatrix} \overline{v_p'^2} & 0 & 0 \\ 0 & \overline{v_q'^2} & 0 \\ 0 & 0 & \overline{v_r'^2} \end{bmatrix},$$

where v'_1, v'_2, v'_3 are components of the velocity of fluctuation at any orthogonal co-ordinate system, while v'_p, v'_q, v'_r are components of fluctuations in the principal system. For a stationary flow (in terms of smoothed quantities) this tensor is independent of time, but dependent on space point, i.e. $R_{ij} = R_{ij}(\boldsymbol{r})$. Further, R is a symmetric tensor for which the principal co-ordinate system pqr can be found in which the cross-product elements vanish. For this reason, the tensor of turbulent fluctuations has *three* degrees of freedom (not six but three), i.e. three its elements are independent of the remaining ones. In other words, to define the tensor of fluctuations R it is sufficient to define the three degrees of freedom, e.g. the three principal values on the main diagonal. This opens room for modelling turbulence.

The easiest case for modelling is isotropic turbulence, invariant under rotations, with equal principal values on the main diagonal, as only one quantity has to be estimated. However, isotropic turbulence does not occur in technical applications. Another easy case for modelling is flow through a pipeline, where only one element of tensor R is meaningful: $R_{13} \equiv R_{rz}$.

The tensor of fluctuations R has the same properties, as any symmetric tensor of the third order, as e.g. the stress tensor known from strength of materials. Hence, the sum of elements on the main diagonal $R_{11} + R_{22} + R_{33}$ is independent of the orientation of the system and equals $2k$, where k is the turbulence kinetic energy (TKE). This quantity value is one of the three invariants of tensor R and the most important characteristic of turbulence. TKE vanishes on the surface of the body and on the outer surface of the boundary layer. Regarding the principal axes, it can be assumed they are parallel to the principal axes of the tensor of deformations S_d for smoothed velocity field $\bar{v}$.

Elements on the main diagonal R_{11}, R_{22}, R_{33} have the meaning of variance of fluctuations, whereas R_{12}, R_{13}, R_{23} have the meaning of covariance, representing correlation between fluctuating velocities.

For isotropic turbulence, elements on the main diagonal $R_{11} = R_{22} = R_{33} = \tfrac{2}{3}k$ are the same, the cross product terms $R_{12} = R_{13} = R_{23} = 0$ vanish, and the principal axes are indefinite. The fluid has then no turbulence sheer stresses. For instance, if flow through a pipeline featured isotropic turbulence, the velocity profile would be the same, as for laminar flow, which is contradictory to reality.

Substituting formulation (8) to equation (7), the following is obtained for the equation of motion for a turbulent flow:

$$\begin{aligned}&\frac{\partial \bar{\boldsymbol{v}}}{\partial t} + (\bar{\boldsymbol{v}}\cdot\nabla)\bar{\boldsymbol{v}} = \\ &-\tfrac{1}{\rho}\,\mathrm{grad}\;\bar{p} + \tfrac{1}{3}\nu\,\mathrm{grad}\;\mathrm{div}\,\bar{\boldsymbol{v}} + \nu\Delta\bar{\boldsymbol{v}} - \mathrm{Div}\boldsymbol{R},\end{aligned} \tag{9}$$

known as the RANS equations, where a bar above the notation denotes a smoothed (averaged) quantity. The first three terms on the right-hand side equal to ${}^{1}/_{\rho}\mathrm{Div}\bar{P}$, where $\overline{P} = -\overline{p}I + 2\mu(S_d - \tfrac{1}{3}I\,\mathrm{div}\,\overline{v})$ is the stress tensor for smoothed motion, $\overline{p}$ and S_d is the pressure and tensor of deformation for smoothed velocity field, respectively. With this notation, equation (9) can be written as:

$$\frac{d\overline{\boldsymbol{v}}}{dt} = \tfrac{1}{\rho}\,\mathrm{Div}\big(\overline{\boldsymbol{P}} - \rho\boldsymbol{R}\big), \tag{10}$$

where $\overline{P} - \rho R = -(\overline{p} + \tfrac{2}{3}\mu\,\mathrm{div}\,\overline{v})I + 2\mu S_d - \rho R$, and

$$-\rho\boldsymbol{R} = \begin{bmatrix} -\rho\,\overline{v_1'v_1'} & -\rho\,\overline{v_1'v_2'} & -\rho\,\overline{v_1'v_3'} \\ -\rho\,\overline{v_2'v_1'} & -\rho\,\overline{v_2'v_2'} & -\rho\,\overline{v_2'v_3'} \\ -\rho\,\overline{v_3'v_1'} & -\rho\,\overline{v_3'v_2'} & -\rho\,\overline{v_3'v_3'} \end{bmatrix}. \tag{11}$$

The tensor $-\rho R$ is the additional apparent stress tensor, owing to the fluctuating velocity field, called the *turbulent stress tensor*, or the *tensor of Reynolds stresses*.

The pressure terms on the main diagonal are negative, while the tangential terms must have the *same* sign, as corresponding elements of the tensor of deformation for smoothed velocity field $\boldsymbol{S_d}$, which follows from their physical meaning. By the very nature of things, turbulence increases the absolute value of all the stresses.

The divergence of the tensor of fluctuations R is directly connected to vorticity, hidden in the RANS equations. This is clearly seen if one resorts to equation (4):

$$\mathrm{Div}R = \overline{(v'\cdot\nabla)v'} \equiv \tfrac{1}{2}\mathrm{grad}\,\langle v'^2\rangle - \langle v'\times\mathrm{rot}\,v'\rangle, \tag{12}$$

where $\langle v'^2\rangle = R_{11} + R_{22} + R_{33} = 2k$. Equation (12) shows the importance of vorticity in generation of the Reynolds stresses. These stresses require relating them to characteristics of the averaged velocity field to close the RANS equation for solving, which has led to the creation of many turbulence models.

There are generally two types of turbulence models: algebraic and Reynolds-stress models. Models of the first group (k–ε, k–ω) are very popular. They resort to the idea of *turbulent viscosity*, introduced by Boussinesq in 1877, shortly discussed below.

The Reynolds stress tensor can be presented as:

$$-\rho R = -p_t I + (-\rho R + p_t I),$$

where $p_t = \tfrac{2}{3}\rho k$ is the mean turbulent pressure. It is assumed that the tensor in parentheses is proportional to the net tensor of deformation in smoothed flow, i.e.:

$$(-\rho R + p_t I) = 2\mu_t(S_d - \tfrac{1}{3}I\,\mathrm{div}\,\overline{v}), \tag{13}$$

where μ_t is the so-called (dynamic coefficient of) *turbulent viscosity*, termed also the *eddy viscosity*. Equation (13) is strict, if the principal directions of the two tensors are the same, which is true in the case of straight-linear flows. The whole stress tensor takes then the form:

$$\begin{aligned}\overline{P} - \rho R = -\big[\overline{p} + p_t + \tfrac{2}{3}(\mu + \mu_t)\,\mathrm{div}\,\overline{v}\big]I\,+ \\ +\,(\mu + \mu_t)2S_d.\end{aligned} \tag{14}$$

Velocity field is defined by equation (10) in which the divergence of the whole stress tensor is given by the following formulation:

$$\begin{aligned}\mathrm{Div}(P - \rho R) = -\mathrm{grad}\,(\overline{p} + p_t) + (\mu + \mu_t)\Delta\overline{v}\,+ \\ +\,\tfrac{1}{3}(\mu + \mu_t)\,\mathrm{grad}\,\mathrm{div}\,\overline{v} - \tfrac{2}{3}\mathrm{div}\,\overline{v}\,\mathrm{grad}\,\mu_t + 2\,\mathrm{grad}\,\mu_t S_d.\end{aligned} \tag{15}$$

The above equation requires some comments. Firstly, the Reynolds stress tensor $-\rho R$ and the tensor $(-\rho R + p_t I)$ yield the same sheer stresses. Secondly, in close vicinity of the surface of the body the turbulent pressure $p_t = \tfrac{2}{3}\rho k$ varies mainly in a plane normal to the average velocity $\overline{\boldsymbol{v}}$. Therefore, for the sake of simplicity the longitudinal component of $\mathrm{grad}\,p_t$ (along $\overline{\boldsymbol{v}}$) can be neglected. A good example is flow through a boundary layer or a pipeline, where the longitudinal component of the $\mathrm{grad}\,p_t$ is ignored. The rejection of p_t does not affect the sheer stresses.

TKE and turbulent viscosity vanish on surface of the body and outside the boundary layer. Equation (15) implies that a turbulent flow can be viewed as the laminar one with a varying viscosity. The latter depends on the Reynolds number and distance from the surface of the body, with a maximum value somewhere inside the boundary layer. However, none of the publications available in literature, including the two mentioned earlier, shows how turbulent viscosity varies across the boundary layer or how its thickness varies along the body.

In the k–ε model the kinematic coefficient of turbulent viscosity $\nu_t \equiv \mu_t/\rho$ is approximated by $\nu_t = 0.09k^2/\varepsilon$, where k is the TKE and ε is the rate of dissipation of TKE. The model comprises as well two PDE (transport equations) for k and ε. The equation for ν_t is clearly ill conditioned on extremes of the boundary layer, as k and ε vanish. Therefore k–ε models have generally poor performance in realistic flow situations, discussed in detail by McDonough (2007). Somewhat better results provide Reynolds stress models in which transport equations are derived for elements R_{ij}, but they are expensive in terms of computational time. Still, a complete description of turbulence remains one of the unsolved problems in classical physics.

Turbulence models have been developed mainly for stationary flows within the boundary layer. Stationary – in terms of smoothed quantities. There are doubts if turbulence exists at all outside the body (in the wake), behind the separation point. These doubts are due to decay of the normal derivative of velocity at the separation point and, what goes with it, the vanishing of turbulent stresses just at this point. This follows immediately from Prandtl's mixing-length hypothesis.

No turbulence models exist for non-stationary flows, and oscillatory motions in particular. Further, these models would have to be time dependent, which is not feasible. Presumably, all models have been developed and calibrated for stationary flows. Use of any turbulence model for oscillating bodies is therefore strongly speculative, and of little real merit.

3. HYDRODYNAMIC COEFFICIENTS

The idea of the hydrodynamic coefficients, i.e. the added mass and damping coefficients is solely applicable to linear problems, in which the body hardly moves, if at all. In such circumstances there is no room for developing turbulence. Hence, it can be assumed that there are no Reynolds stresses at all, which reduces RANS equation (9) to regular N–S equations (2). Hence, the same solver can be used for solving both the N–S and RANS equations, e.g. commercial RANS solvers ANSYSCFX10.0, COMET, CFDSHIP-IOWA, etc., assuming no Reynolds stresses.

In non-linear harmonic oscillations of finite amplitude in calm water the hydrodynamic coefficients are not constant in respect to time and, apart from that, they are dependent on the amplitude of oscillations. Consequently, they have to be averaged over time.

In linear problems the body is stationary, performing no oscillations. Its motion is depicted by the kinematic boundary conditions. Though it is acceptable to assume that the body physically oscillates calculations become cumbersome and results less accurate.

In the case the body physically oscillates, equations for the hydrodynamic sectional forces are as follows:

$$\begin{aligned} &\text{sway:} && -a_{22}\ddot{y}-b_{22}\dot{y}=F_y(t), \\ &\text{heave:} && -a_{33}\ddot{z}-b_{33}\dot{z}-c_{33}z=F_z(t), \\ &\text{roll:} && -a_{44}\ddot{\alpha}-b_{44}\dot{\alpha}-c_{44}\alpha=M_x(t), \end{aligned} \tag{16}$$

where in general a is the added mass (in kg/m – for a_{22} and a_{33}, in kgm – for a_{44}), b is the damping coefficient (in kg/sm – for N_{22} and N_{33}, and in kgm/s – for N_{44}), and c is the coefficient of stiffness, all per unit length. For heave, $c_{33} = B\rho g$ [N/m^2], where B is breadth of the body at the waterline. For roll, $c_{44} = \rho g\forall GM$ [N], where $\forall$ is the sectional underwater area, and GM is the height of the metacentre above the waterline (the origin G is normally taken at the centreline of the waterline) .The right hand-sides represent the hydrodynamic forces, obtained by measurements or by integration of the pressure p and tangential stresses τ over the wetted surface of the body.

In the case of virtual oscillations, the hydrostatic terms vanish, as $z = \alpha = 0$. The hydrodynamic forces are obtained by integrating the linearized pressure over the wetted surface of the body, the same as in the *mean* position of the oscillating body (Faltinsen, 1990; Salvesen *et al*., 1970).

The main difficulty is to extract from the whole dynamic force, the time dependent harmonic part, which should be resolved next into the inertial and damping components.

The hydrodynamic forces on the right hand sides of equations (16), i.e. $F_y(t)$, $F_z(t)$, $M_x(t)$ are provided measurements or by numerical calculations per unit length as time histories. They are calculated for forced harmonic oscillations in calm water for y, z, and α, of general form $A\sin\omega t$, with given amplitude A and circular frequency ω.

Applying Fourier analysis to equations (16), after performing simple mathematics, we get in general the following expressions for the sectional added mass and damping coefficients:

$$a=\frac{c}{\omega^2}+\frac{1}{A\pi\omega}\int_t^{t+T}F(t)\sin\omega t\,dt, \tag{17}$$

$$b=\frac{1}{A\pi}\int_t^{t+T}F(t)\cos\omega t\,dt, \tag{18}$$

where $T = 2\pi/\omega$ is the period of oscillations, A is the amplitude of forced oscillations, and $F(t)$ stands for the time varying hydrodynamic force or moment for given circular frequency ω and amplitude A. These forces deviate from harmonic runs, if the equations of motion are non-linear. The coefficient of stiffness c in equation (17) is treated as known quantity.

4. THE EFFECT OF FORWARD SPEED

Regarding seakeeping, most research has been devoted to calculating the hydrodynamic coefficients for a stationary ship oscillating in calm water. As will be shown later, in such a case the boundary layer is marginal, and can be ignored. The hydrodynamic coefficients, except for roll, can be therefore calculated traditionally, assuming no viscosity of water, and, what goes with it, assuming potential flow, governed by the Laplace equation $\Delta\phi = 0$. For roll, however, the hydrodynamic coefficients have to be calculated accounting for viscosity.

Measured values of the added mass a_{44} are *smaller*, while for the damping coefficient b_{44} – *higher* from those for potential flow in proportion to the amplitude of roll (Figure. 1). The effect is noticeable. Measured values, denoted by points for three different amplitudes A: 0.05, 0.1, 0.2 rad (2.875°, 5,75°, 11.5°) are taken from Vugts (1968). Values for potential flow (thick line) were obtained by Dudziak (1988) with the help of multi-pole potentials. To obtain the hydrodynamic coefficients with the effect of viscosity, a FEM can be used for the integration of equations of conservation, or any RANS solver, ignoring the Reynolds stresses.

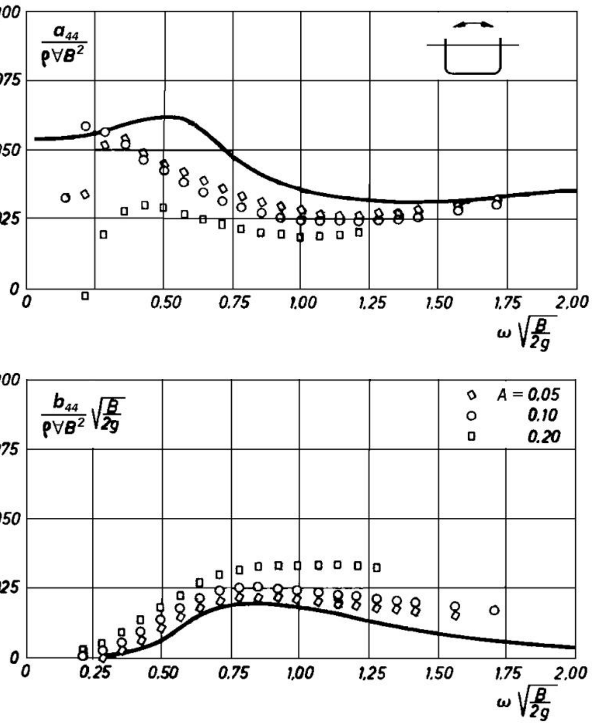

Figure. 1. Nondimensional hydrodynamic coefficients for roll of a rectangular section

For a ship advancing with forward speed in regular seas, the hydrodynamic coefficients can be calculated in two ways. 1), assuming that they are the same as for forced oscillations in calm water with circular frequency equal to the encounter frequency ω_E, given by the equation:

$$\omega_E = |\omega - ku\cos\beta|, \tag{19}$$

where ω is the circular frequency of regular wave, $k \equiv 2\pi/\lambda$ is the wave number, λ is the wave length, *u* is the forward speed of the ship, and β is the heading angle between the ship speed and direction of wave propagation. And 2), predicting the hydrodynamic coefficients from the solution of equations of conservation for the viscous flow, including the boundary layer. As shown by Weymouth *et al*. (2005), such a problem is extremely complex. The thickness of the boundary layer varies in the course of motion, and outside the boundary layer – as shown earlier – flow is irrotational, i.e. potential. Hence, turbulence occurs solely inside the boundary layer, while outside it – the flow is potential.

The first approach ignores simply the boundary layer. Here arises the question, if the hydrodynamic coefficients could be determined accounting for the boundary layer, but not in the so complicated way, as discussed by Weymouth *et al*. (2005). It seems there is such a possibility. Note that 1) outside the boundary layer flow is potential, and 2) the boundary layer moves with the ship, as if being fixed to it. Hence, we can assume that the mass of the ship is augmented by the mass of the boundary layer, while the hydrodynamic forces are such, as if the wetted surface of the ship coincided with the outer surface of the boundary layer. Hence, the key meaning in this approach has the thickness δ of the turbulent boundary layer. As first approximation, it could be taken the same as for a flat plate:

$$\delta = 0.37\left(\frac{\nu}{ux}\right)^{1/5} x\,, \tag{20}$$

where ν is the kinematic viscosity of water, *u* is the forward speed of the ship, and *x* is distance from the forward end of the ship below water. The fraction inside the parentheses is the inverse of the Reynolds number, related to *x*. Behind the separation point, the thickness of the boundary layer can be taken as δ = 0. Numerical values of δ are shown in Table. 1 for the coefficient of viscosity $\nu = 10^{-6}$ m^2/s, and two vessel's speeds *u* = 5 m/s and 10 m/s.

Table. 1. Thickness of turbulent boundary layer

	u = 5 m/s		*u* = 10 m/s	
x [m]	Re	δ [m]	Re	δ [m]
10	$5.0\cdot10^7$	0.107	$1.0\cdot10^8$	0.093
20	$1.0\cdot10^8$	0.186	$2.0\cdot10^8$	0.162
50	$2.5\cdot10^8$	0.387	$5.0\cdot10^8$	0.337
100	$5.0\cdot10^8$	0.674	$1.0\cdot10^9$	0.586
200	$1.0\cdot10^9$	1.173	$2.0\cdot10^9$	1.021

It is worth realising that accurate prediction of the hydrodynamic coefficients is not required for the satisfactory prediction of ship motion in a seaway. Coefficients of stiffness c_{33}, c_{44}, c_{55} are at least an order of magnitude larger (the first and third are usually more than two orders larger) than the added mass and damping coefficients. The overwhelming dominance of hydrostatic stiffness and highly linear wave excitation allow the strip theory to predict ship motions with reasonably high degree of accuracy. Things are improved further by the counteracting non-linear effects of hydrodynamic coefficients a_{44} and b_{44} (Figure. 1).

5. CASE STUDIES

To shed some light on the effect of viscosity in ship dynamics it is worth recalling four case studies, known in literature: 1) sliding oscillations of a flat surface, 2) angular oscillations of a cylinder, 3) sliding oscillations of a cylinder, and 4) oscillations of an arbitrary body.

5.1 SLIDING OSCILLATIONS OF A FLAT SURFACE

This is a classic problem, discussed in almost every textbook on fluid mechanics, solved by Stokes in 1851. Consider an infinite surface at the *x*-plane, performing harmonic oscillations in the *z* direction with the velocity $u = u_0\cos\omega t$. By assuming that the field of velocity $\boldsymbol{v} = v\boldsymbol{k}$ is of laminar type, i.e. it has one component only in the direction of the z-axis, where $v = v(x)$ is a function of x (distance from the plane), N–S equation (2) reduces to two scalar equations: $p = const$, and the equation of diffusion:

$$\frac{\partial v}{\partial t} = \nu \frac{\partial^2 v}{\partial^2 x}, \tag{21}$$

Its solution is as follows:

$$v = u_0 e^{-kx} \cos(kx - \omega t), \tag{22}$$

where $k = (\omega/2\nu)^{1/2}$ is the wave number. The inverse of the wave number, denoted by $\delta \equiv 1/k = (2\nu/\omega)^{1/2}$ is the *depth of penetration*, known better as the *skin depth*. At a distance $x = 3\delta$ the velocity drops to $e^{-3} \approx 5\%$ of the value at the oscillating surface. And at a distance $x = 5.3\,\delta$ it drops to 0.5%. We can assume then that the thickness of the boundary layer equals $\sim 5\delta$. The depth of penetration increases with the kinematic viscosity ν and *decreases* with the circular frequency ω. For a finite plate, the depth of penetration is presumably much thinner.

For example, for water the kinematic coefficient of viscosity $\nu \approx 10^{-6}$ m^2/s, and for air $\nu \approx 15{\cdot}10^{-6}$ m^2/s. Assuming the circular frequency of oscillations $\omega = 1$ rad/s, the depth of penetration for water equals $\delta = 1.4$ mm, and for air $\delta = 5.5$ mm. At a distance 5δ, i.e. 7 mm for water, and 27 mm for air, the fluid is practically at rest, despite the oscillations. These quantities are inversely proportional to $\surd\omega$. Real frequencies occurring in seakeeping are from the range $\omega \in \langle 0.2,\ 4\rangle$ rad/s. Hence, the skin depth is small. Note that this quantity value is at least two orders of magnitude smaller than the values for a stationary boundary layer (Table. 1).

Knowing the velocity field, the tangential stress on the surface can be found by the equation $\tau = \mu\partial v/\partial x$. Substituting $x = 0$, the following is obtained for the stresses:

$$\tau = -\mu k u_0(\cos\omega t - \sin\omega t),$$

where $\mu k = (½\rho\mu\omega)^{1/2}$. Hence, a phase shift exists between stress and speed. Since the acceleration of the surface $\dot{u} = -\omega u_0 \sin\omega t$, the above can be written as:

$$\tau = -(\mu k/\omega)\dot{u} - \mu k u = -(½\rho\mu/\omega)^{1/2}\dot{u} - (½\rho\mu\omega)^{1/2} u \equiv -m\dot{u} - Nu, \tag{23}$$

where $m = (½\rho\mu/\omega)^{1/2}$ is the added mass per unit area, while $N = (½\rho\mu\omega)^{1/2}$ is the coefficient of damping per unit area. If the fluid is on both sides of the surface, the expressions for m and N should be doubled. Both components of the stress, which are the same as the frictional resistance per unit area, are directed against the appropriate parameters of motion.

Friction is associated with dissipation of energy. The said quantity can be obtained as work of friction forces. Dissipation of energy per unit time and unit area is equal to mean value of the product of the tangential stress and the speed of the surface:

$$\langle \tau u \rangle = -{}^1\!/_T \int_0^T (m\dot{u}u + Nu^2)\,dt,$$

where T is the period of oscillations. Since $\dot{u}udt = d½u^2$, the first term provides no contribution due to the oscillations of velocity. A contribution provides the other term, equal to: $\langle \tau u \rangle = -½Nu_0^2$.

As can be seen, the coefficient of damping $N = (½\rho\mu\omega)^{1/2}$ is responsible for dissipation, not the added mass. This can be taken as a general rule.

5.2 ANGULAR OSCILLATIONS OF A CYLINDER

Consider now the velocity field around an infinitely long cylinder of radius r_0, performing angular oscillations around its axis in infinite fluid with a circular frequency ω. The z-axis coincides with the axis of the cylinder (Figure. 2).

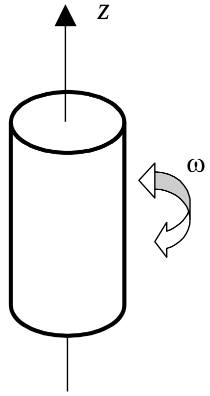

Figure. 2

It is assumed again that the velocity field is of laminar type, i.e. it has only a circumferential component $\boldsymbol{v} = v\boldsymbol{e}_\theta$, a value of which depends on the co-ordinate r (distance from the axis of the cylinder) and on time t, i.e. $v = v(r, t)$. This component is constant for a given r at a fixed time instant, which results from the equation of continuity. Similarly, the pressure field $p = p(r, t)$. Note that the problem is 2-D, therefore no quantity can depend on the variable z.

With these assumptions grad$p$ has only a radial component. Similarly, the convective acceleration $(v\cdot\nabla)v$ has solely a radial component, equal to the centrifugal acceleration. The two remaining terms in equation of motion (2), i.e. the local acceleration and Laplacian of velocity have only circumferential components, as $\Delta(v\boldsymbol{e}_\theta) = (v'' + v'/r - v/r^2)\boldsymbol{e}_\theta$, where $'$ means differentiation with respect to r. Equation (2) yields then two scalar equations, one for the pressure field $dp/dr = \rho v^2/r$, and the other for the velocity field, which has a form of the equation of diffusion:

$$\partial v/\partial t = \nu(v'' + v'/r - v/r^2). \tag{24}$$

As can be seen, the pressure field $p = p(r, t)$ is obtained by integrating the centrifugal accelerations, dependent on the instantaneous velocity field. On the other hand, the velocity field $v = v(r, t)$ is determined by decoupled equation (24).

Determination of the velocity field around an oscillating cylinder is not as easy as for an oscillating plane. Equation (24) suggests that we can seek its solution by a separation of variables. Namely, we can postulate that $v = u_0 e^{-\mathrm{i}\,\omega t}R$, where $R = R(r)$ is a function of variable r only, whereas $v = u_0 e^{-\mathrm{i}\,\omega t}$ is the velocity on the surface of the cylinder at $r = r_0$.

Substituting v to equation (24) yields a characteristic equation for the function R:

$$\begin{gathered} -\mathrm{i}\omega R = \nu(R'' + R'/r - R/r^2), \\ \nu(R'' + R'/r - R/r^2) + \mathrm{i}\omega R = 0, \\ R'' + R'/r - R/r^2 + (\mathrm{i}\omega/\nu)R = 0. \end{gathered}$$

Introducing notation $K^2 \equiv \mathrm{i}\,\omega/\nu$, the above equation will take the form:

$$R'' + R'/r + (K^2 - {}^{1}\!/_{r^2})R = 0.$$

This is a Bessel equation of the first order [the Bessel equation of the n-th order is defined as: $R'' + R'/r + (K^2 - {}^{n^2}\!/_{r^2})R = 0$]. Multiplying it by r^2 yields the characteristic equation in an equivalent form:

$$r^2R'' + rR' + (K^2r^2 - 1)R = 0.$$

Introducing a nondimensional radius $\rho = Kr$, the function R becomes a function $R = R(\rho)$. The characteristic equation will become a normalised Bessel equation of the first order:

$$R'' + R'/\rho + (1 - {}^{1}\!/_{\rho^2})R = 0, \tag{25}$$

defining the function $R(\rho)$, where ' means now differentiation with respect to ρ. Its solution are cylindrical functions of the first and second kind $J_1(\rho)$ and $N_1(\rho)$. The asymptotic form of the two functions for large arguments $\rho = Kr$ is as follows (Abramowitz & Stegun, 1970):

$$\begin{aligned} J_1 &= (2/\pi\rho)^{1/2}\sin(\rho - {}^1\!/_4\pi), \\ N_1 &= -(2/\pi\rho)^{1/2}\cos(\rho - {}^1\!/_4\pi). \end{aligned} \tag{26}$$

Graphs of the functions J_1 and N_1 for a real argument ρ are shown in Figure. 3. For $\rho > \sim 3$ they can be replaced the asymptotic approximations.

The parameter K is given by the equation: $K^2 \equiv \mathrm{i}\omega/\nu$. Hence, $K = k'\sqrt{\mathrm{i}}$, where $k' = (\omega/\nu)^{1/2}$. Thus, the nondimensional variable $\rho \equiv Kr = k'r\sqrt{\mathrm{i}} \equiv \rho'\sqrt{\mathrm{i}}$ is a complex number, where $\rho' \equiv k'r = |\rho|$ is the module of the variable ρ. Considering that $\sqrt{\mathrm{i}} = \pm(1 + \mathrm{i})/\sqrt{2}$, the variable ρ can be presented in the equivalent form:

$$\rho = \pm(1 + \mathrm{i})k'r/\sqrt{2} = \pm(kr + \mathrm{i}kr), \tag{27}$$

where $k = k'/\sqrt{2} = (\omega/2\nu)^{1/2}$.The choice of the sign depends on the condition in infinity. We will see later that the sign should be negative, i.e. corresponding to the phase $-{}^3\!/_4\pi$.

Real and imaginary parts of the cylindrical functions can be obtained by substituting $\rho = \rho'\sqrt{\mathrm{i}}$ in the polynomial expansions; they are functions of the amplitude $\rho' \equiv k'r = \sqrt{2}kr$ and are called the *Kelvin* (*Thomson*) functions.

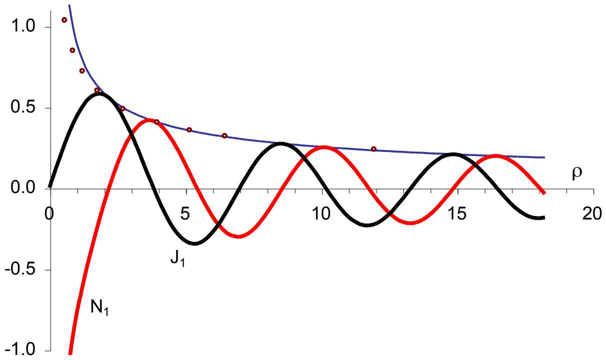

Figure. 3. Runs of cylindrical functions J_1, N_1 and the amplitude $(J_1^2 + N_1^2)^{1/2}$ for real ρ

The number $\sqrt{\mathrm{i}}$ has two phases $-{}^3\!/_4\pi$ and ${}^1\!/_4\pi$. In electrical engineering, for analysing the so-called *skin effect*, the variable $\rho = \rho'\sqrt{(-\mathrm{i})}$ is of importance, which has two phases: ${}^3\!/_4\pi$ and $-{}^1\!/_4\pi$. Skin effect is the tendency of an alternating electric current to become distributed within a conductor in such a way that the current density is largest near the surface of the conductor, and decreases towards its centre. The electric current flows mainly at the conductor "skin", between the outer surface and a level called the skin depth δ. This effect increases effective resistance of the conductor at higher frequencies where the skin depth is smaller, thus reducing the effective cross-section of the conductor. Hence, the determination of current density in the conductor is an *inner* problem, contrary to the determination of the velocity field outside an oscillating cylinder. The inner problem in fluid mechanics means determination of the velocity field *inside* the cylinder.

The Kelvin functions solely concern the variable $\rho = \rho' e^{\pm 3/4\pi\mathrm{i}}$, with phases $\pm{}^3\!/_4\pi$. They are denoted as follows:

$$\begin{aligned} J_1(\rho' e^{\pm 3/4\pi\mathrm{i}}) &\equiv \mathrm{ber}_1\,\rho' \pm \mathrm{i}\,\mathrm{bei}_1\,\rho', \\ N_1(\rho' e^{\pm 3/4\pi\mathrm{i}}) &\equiv \mathrm{yer}_1\,\rho' \pm \mathrm{i}\,\mathrm{yei}_1\,\rho'. \end{aligned}$$

When a complex argument ρ tends to infinity, cylindrical functions become unbounded. For a real variable, they present damped oscillations, as in Figure. 3.

A general solution of equation (25) is a linear combination of the fundamental solutions, i.e. $R(\rho) = \alpha J_1(\rho) + \beta N_1(\rho)$, where α and β are arbitrary constants. We have to find a combination where the function $R(\rho)$ decays with growth of the complex argument ρ. To ease the answer to this question, consider the asymptotic form of the two functions, given by equation (26). Substituting $\rho = x + \mathrm{i}y$, the following is obtained:

$$J_1 = (2/\pi\rho)^{1/2}[\cosh y \sin(x - \tfrac14\pi) + \mathrm{i}\sinh y \cos(x - \tfrac14\pi)],$$
$$N_1 = -(2/\pi\rho)^{1/2}[\cosh y \cos(x - \tfrac14\pi) - \mathrm{i}\sinh y \sin(x - \tfrac14\pi)],$$

where $x = y = kr$. When the imaginary part y tends to $\pm\infty$, both functions grow to infinity. Create then a new cylindrical function called the *Hankel function*: $H_1 \equiv J_1 - \mathrm{i}N_1$, denoted in literature by $H_1^{(2)}$. After simplifications, the following is obtained:

$$H_1 = (2/\pi\rho)^{1/2}e^{y}[\sin(x - \tfrac14\pi) + \mathrm{i}\cos(x - \tfrac14\pi)].$$

The Hankel function vanishes in infinity in the lower half-domain, when $y < 0$. This happens, when the nondimensional variable ρ, given by equation (27), is taken with the minus sign: $\rho = -(kr + \mathrm{i}kr) = -\sqrt{2}kre^{\mathrm{i}\pi/4} = -\rho' e^{\mathrm{i}\pi/4} = \rho' e^{-\frac34\pi\mathrm{i}}$, which gives the phase $-\tfrac34\pi$. Considering that $x = y = -kr$, after simplifications we get an asymptotic form of the Hankel function:

$$H_1(kr) = -2^{1/4}(\pi kr)^{-1/2}e^{-kr}e^{\mathrm{i}(kr + \frac18\pi)} = M_1 e^{\mathrm{i}(kr + \frac18\pi)}, \qquad (28)$$

where $M_1 = -2^{1/4}(\pi kr)^{-1/2}$ is the amplitude of the function $H_1(kr)$. We will see that the sign is unimportant. For a finite argument ρ the expression for the Hankel function $H_1(kr)$ is far more complicated. It can be obtained from the polynomial expansions of the cylindrical functions. For a variable $\rho = \rho' e^{\pm\frac34\pi\mathrm{i}}$, the real and imaginary parts are denoted, as below:

$$H_1(\rho' e^{\pm\frac34\pi\mathrm{i}}) \equiv \mathrm{her}_1(\rho') \mp \mathrm{i}\,\mathrm{hei}_1(\rho').$$

These functions are related in a simple way to modified Bessel functions: $\mathrm{ker}_1\rho' \equiv -\tfrac12\pi\mathrm{hei}_1\rho'$ and $\mathrm{kei}_1\rho' \equiv \tfrac12\pi\mathrm{her}_1\rho'$. And the modified Bessel functions are related in turn to the first derivatives of the functions $\mathrm{ker}\,\rho'$ and $\mathrm{kei}\,\rho'$ of the zero order:

$$\mathrm{ker}_1\rho' = (\mathrm{ker}'\rho' - \mathrm{kei}'\rho')/\sqrt{2},$$
$$\mathrm{kei}_1\rho' = (\mathrm{ker}'\rho' + \mathrm{kei}'\rho')/\sqrt{2}.$$

Hence, to calculate the real and imaginary parts of the Hankel function $H_1(\rho)$ it is sufficient to know the derivatives of the Hankel functions of the zero order $\mathrm{ker}'\rho'$ and $\mathrm{kei}'\rho'$. They are given by effective polynomial approximations (Abramowitz & Stegun, 1970). Their graphs are shown in Figure. 4. For large values of $\rho' \equiv k'r = \sqrt{2}kr$, both functions oscillate, passing through the same zeros.

With the increase of the module of the nondimensional radius $\rho' = |\rho|$, decrement of damping of the amplitude of the Hankel function H_1 increases monotonically from $-\infty$ to an asymptotic value $-1/\sqrt{2} \approx -0.707$ (Figure. 5). It means that for large enough $\rho' > \sim 4$ the velocity field vanishes as $(\rho'/\sqrt{2})^{-1/2}e^{-\rho'/\sqrt{2}}$. In other words, the variable ρ' becomes the variable $\rho'/\sqrt{2} = kr$. The solution must be then expressed in terms of the variable kr, as seen in equation (28).

Now, a general solution of equation (25) is a function $R(\rho) = \alpha H_1(\rho)$. It fulfils the condition in infinity, as it vanishes to zero. The constant α is chosen from the kinematic condition on the surface of cylinder $\rho = \rho_0$ to be equal to 1. Hence, $\alpha = 1/H_1(\rho_0)$. The velocity field is given then by the equation: $v = u_0 e^{-\mathrm{i}\omega t}H_1(\rho)/H_1(\rho_0)$. Taking the real part, the following is obtained:

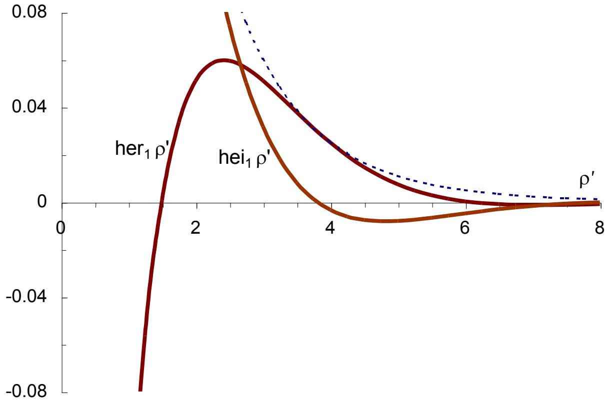

Figure. 4. Run of real and imaginary parts of Hankel function H_1 and their amplitude

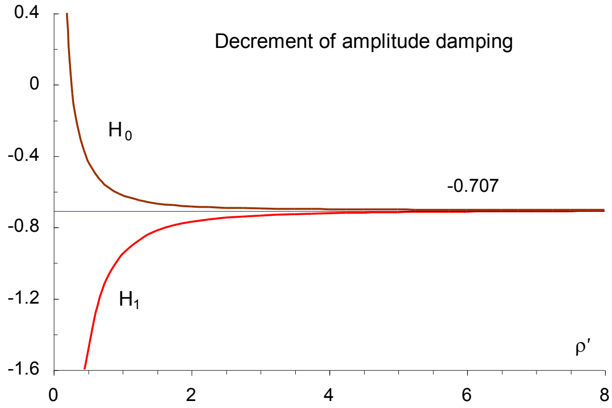

Figure. 5. Decrement of amplitude damping of Hankel function H_0 and H_1

$$v = u_0[(AA_0 + BB_0)\cos\omega t + (AB_0 - A_0B)\sin\omega t]/(A_0^2 + B_0^2), \qquad (29)$$

where $A \equiv \mathrm{her}_1(\rho')$ and $B \equiv \mathrm{hei}_1(\rho')$ are the real and imaginary parts of the Hankel function $H_1(\rho)$, A_0 and B_0 are the values on the cylinder surface. On the surface of cylinder $r = r_0$, the above equation yields $v = u_0\cos\omega t$. As can be seen from Figure. 4, for $\rho' < \sim 8$ the functions A and B are not of oscillatory character, therefore the solution has the character of a standing wave.

Equation (29) can be largely simplified for arguments $\rho' \equiv k'r > \sim 8$, which happens, when the radius $r > r_{min} \equiv \sim 8/k' = 8/\surd 2k = 4\surd 2/k = 4\surd 2\delta \approx 5.7\delta$. For water, for circular frequency $\omega = 1$ rad/s, $r_{min} = \sim 8$ mm, and for air $r_{min} = \sim 32$ mm. The quantity r_{min} is inversely proportional to $\surd\omega$; it is then generally small. Resorting to equation (28), it is easy to find the real part of the velocity $v = u_0 e^{-i\omega t} H_1(\rho)/H_1(\rho_0)$:

$$v = u_0(r_0/r)^{1/2} e^{-k(r-r_0)} \cos[k(r-r_0) - \omega t] =$$
$$= u_0(r_0/r)^{1/2} e^{-kh} \cos(kh - \omega t),$$

valid for $r > r_{min}$, where $h \equiv r - r_0$ is the distance from the cylinder surface, and $k = (\omega/2\nu)^{1/2}$. Expressing the ratio of radii in terms of h, we get eventually:

$$v = \frac{u_0}{\sqrt{1+\frac{h}{r_0}}} e^{-kh} \cos\left(kh - \omega t\right)\cdot \qquad (30)$$

For $h > \sim 5\delta$, $v \approx 0$. If r_0 grows indefinitely, the velocity field tends to the field of a flat surface, given by equation (22), with $x \equiv h$. The velocity field in the case of a cylinder vanishes somewhat faster than for a flat surface. However, the depth of penetration $\delta = 1/k$ is the same in both cases. When $r < r_{min}$, i.e. for cylinders with small radii, the velocity field has to be found using equation (29), which requires the knowledge of the Hankel function $H_1(\rho)$.

It can be shown that the error, with which the Hankel function $H_1(kr)$, given by equation (28), fulfils Bessel equation (25), very quickly decreases with a growth of the nondimensional radius kr. The absolute value of the error equals $\frac{3}{4}\cdot 2^{1/4}(\pi kr)^{-1/2} e^{-kr}$. For $kr = 2, 3, 4$ the error equals merely 4.8%, 1.4%, and 0.5%.

When the cylinder rotates in one direction with a constant angular velocity ω, it induces a stationary velocity field, as for a rectilinear vortex, given by the equation:

$$v = u_0 r_0/r = u_0/(1 + h/r_0), \qquad (31)$$

where u_0 is the velocity on the surface of the cylinder at $r = r_0$. As can be seen, the velocity field has now a completely different character than in the case of an oscillating cylinder. 1°, despite viscosity, the velocity field is potential and independent of viscosity. 2°, if r_0 grows indefinitely, it tends to a uniform flow $v = u_0$, with an infinitely thick boundary layer. 3°, it decays much slower than for an oscillating cylinder. The velocity drops to $1/n$ of the value u_0 at the surface at a distance $h = (n - 1)r_0$, independent of viscosity. For instance, it drops to $0.5\% = {}^{1}/_{200}$, at a distance $h = 199r_0$, extremely large in comparison to an oscillating cylinder. By the sheer fact that the body oscillates, the boundary layer reduces to amazingly small dimensions.

5.3 SLIDING OSCILLATIONS OF A CYLINDER

Consider now an infinitely long cylinder of radius r_0, performing sliding oscillations along its axis in infinite fluid with a circular frequency ω (Figure. 6). It is assumed again that the velocity field has only a longitudinal component $\boldsymbol{v} = v\boldsymbol{e}_z$, which can be solely a function of the co-ordinate r (distance from the axis of the cylinder) and on time t, i.e. $v = v(r, t)$. This results from the equation of continuity, symmetry of the problem and its 2-D character.

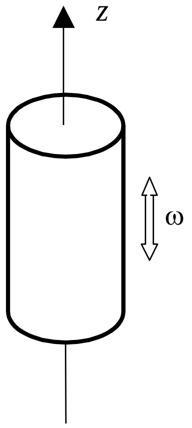

Figure. 6.

With these assumptions, the convective acceleration $(v\cdot\nabla)v$ vanishes, and equation (2) reduces to two scalar equations: i.e. $p = const$, and the diffusion equation: $\partial v/\partial t = \nu\Delta v$, where the Laplacian $\Delta v = (rv')'/r = v'' + v'/r$ (the sign $'$ means differentiation with respect to r). Hence:

$$\partial v/\partial t = \nu(v'' + v'/r). \qquad (32)$$

We can postulate, as before, that the solution of equation (32) is of the form: $v = u_0 e^{-i\omega t} R$, where $R = R(r)$ is a function of the variable r only, whereas $v = u_0 e^{-i\omega t}$ is the velocity of the cylinder. Substituting v in equation (32) yields a characteristic equation for the function R:

$$-i\omega R = \nu(R'' + R'/r),$$
$$R'' + R'/r + (i\omega/\nu)R = 0.$$

Introducing the notation $K^2 \equiv i\omega/\nu$, the above will take the form: $R'' + R'/r + K^2 R = 0$. Introducing the nondimensional radius $\rho = Kr$, the function R becomes a function $R = R(\rho)$, for which the characteristic equation is as follows:

$$R'' + R'/\rho + R = 0, \qquad (33)$$

where $'$ means now differentiation with respect to ρ. This is a Bessel equation of the zero order, defining the function $R = R(\rho)$. Its solution are cylindrical functions of the first and second kind $J_0(\rho)$ and $N_0(\rho)$. At zero these functions have values as follows: $J_0(0) = 1$, $N_0(0) = -\infty$. The asymptotic form of the two functions for large arguments $\rho = Kr$ is as follows (Abramowitz, Stegun, 1970):

$$J_0 = (2/\pi\rho)^{1/2}\cos(\rho - \tfrac{1}{4}\pi),\quad N_0 = -(2/\pi\rho)^{1/2}\sin(\rho - \tfrac{1}{4}\pi). \tag{34}$$

Graphs of the functions J_0 and N_0 for a real argument ρ are shown in Figure. 7. For $\rho > \sim 1$ they can be replaced the asymptotic approximations.

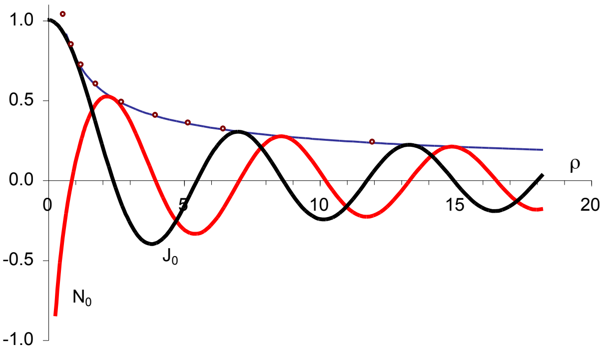

Figure. 7. Runs of cylindrical functions J_0, N_0 and the amplitude $(J_0^2 + N_0^2)^{1/2}$ for real ρ

The non-dimensional radius ρ is a complex quantity, given by equation (27). Substituting to the Bessel functions $\rho = \rho' e^{\pm\frac{3}{4}\pi i}$, where $\rho' \equiv \sqrt{2}kr$, we get

$$J_0(\rho' e^{\pm\frac{3}{4}\pi i}) \equiv \mathrm{ber}\,\rho' \pm i\,\mathrm{bei}\,\rho',$$
$$N_0(\rho' e^{\pm\frac{3}{4}\pi i}) \equiv \mathrm{yer}\,\rho' \pm i\,\mathrm{yei}\,\rho'.$$

When the complex argument ρ tends to infinity, both functions become unbounded. For a real variable, they present damped oscillations, as in Figure. 7. As before, the Hankel function $H_0 \equiv J_0 + iN_1$, denoted in literature by $H_0^{(1)}$ (note the change of the sign), vanishes in infinity in the lower half-domain, when $y < 0$. Its asymptotic expansion for large ρ is as follows:

$$H_0 = (2/\pi\rho)^{1/2}e^{y}[\cos(x - \tfrac{1}{4}\pi) - i\sin(x - \tfrac{1}{4}\pi)].$$

This happens, when the nondimensional variable $\rho = \rho' e^{\pm\frac{3}{4}\pi i}$ is taken with the phase $-\frac{3}{4}\pi$. Considering that $x = y = -kr$, the asymptotic form of the Hankel function is as follows:

$$H_0(kr) = 2^{1/4}(\pi kr)^{-1/2}e^{-kr}e^{i(kr + \frac{5}{8}\pi)} = M_0 e^{i(kr + \frac{5}{8}\pi)}, \tag{35}$$

where $M_0 = 2^{1/4}(\pi kr)^{-1/2}$ is the amplitude of the function $H_0(kr)$. For a finite argument ρ the expression for the Hankel function $H_0(kr)$ can be obtained from the polynomial expansions of the cylindrical functions. For a variable $\rho = \rho' e^{\pm\frac{3}{4}\pi i}$, the real and imaginary parts are denoted, as:

$$H_0(\rho' e^{\pm\frac{3}{4}\pi i}) \equiv \mathrm{her}(\rho') \pm i\,\mathrm{hei}(\rho'),$$

where the real and imaginary parts of the function $H_0(\rho' e^{\pm\frac{3}{4}\pi i})$, i.e. $\mathrm{her}(\rho')$ and $\mathrm{hei}(\rho')$, shown in Figure. 8, are calculated with the help of the function $\mathrm{ker}\rho' \equiv -\frac{1}{2}\pi\mathrm{hei}(\rho')$ and $\mathrm{kei}\rho' \equiv \frac{1}{2}\pi\mathrm{her}\rho'$; the functions $\mathrm{ker}\rho'$ and $\mathrm{kei}\rho'$ are given by effective polynomial approximations (Abramowitz & Stegun, 1970). For large values of $\rho' \equiv k'r = \sqrt{2}kr$, both functions oscillate, passing through the same zeros.

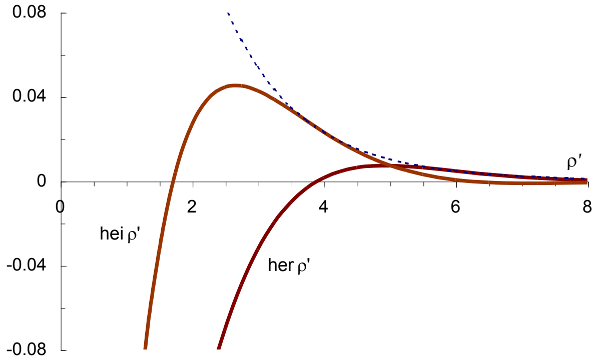

Figure. 8. Runs of real and imaginary parts of Hankel function H_0 and their amplitude

As before, with the increase of the nondimensional radius $\rho' = |\rho|$, decrement of damping of the amplitude of the Hankel function H_0 decreases monotonically from $+\infty$ to an asymptotic value $-1/\sqrt{2} \approx -0.707$ (Figure. 5). It means that for large $\rho' > \sim 2$ the velocity field vanishes as $(\rho'/\sqrt{2})^{-1/2}e^{-\rho'/\sqrt{2}}$. In other words, the variable ρ' becomes the variable $\rho'/\sqrt{2} = kr$. The solution must be then expressed in terms of the variable kr, as seen in equation (35).

A general solution of equation (33) is a function $R(\rho) = \alpha H_0(\rho)$. It fulfils the condition in infinity, as it vanishes to zero. The velocity field is given by the equation: $v = u_0 e^{-i\omega t}H_0(\rho)/H_0(\rho_0)$. Taking the real part, we get:

$$v = u_0[(AA_0 + BB_0)\cos\omega t - (AB_0 - A_0B)\sin\omega t]/(A_0^2 + B_0^2), \tag{36}$$

where $A \equiv \mathrm{her}_1(\rho')$ and $B \equiv \mathrm{hei}_1(\rho')$ are the real and imaginary parts of the Hankel function $H_1(\rho)$, A_0 and B_0 are the values on the cylinder. As can be immediately checked, on the surface of cylinder $r = r_0$, the above equation yields $v = u_0\cos\omega t$. For $\rho' < \sim 8$ the functions A and B have no oscillatory character (see Figure. 8), therefore the solution has the character of a standing wave.

Equation (36) can be largely simplified for arguments $\rho' \equiv k'r > \sim 8$, which happens, when the radius $r > r_{min} \equiv \sim 8/k' = 8/\sqrt{2}k \approx 5.7\delta$. Resorting to equation (35), it is easy to find the real part of the velocity $v = u_0 e^{-i\omega t}H_1(\rho)/H_1(\rho_0)$, reducing to equation (30), the same as for angular oscillations, valid for $r > r_{min} \approx 5.7\delta$. For $h > \sim 5\delta$, $v \approx 0$.

It is interesting that in the three case studies the boundary layer is the same and at least two orders of magnitude smaller than the values for a stationary boundary layer

(Table. 1). Further, the velocity field is found from equation of diffusion (6), without resorting to the idea of vorticity. This feature of the field is a resultant quantity, having no impact on the calculations.

5.4 OSCILLATIONS OF AN ARBITRARY BODY

As we could see in the foregoing three case studies, contrary to stationary flows the boundary layer is thin on oscillating bodies. It can be shown that the same holds for an arbitrary oscillating body. A proof is provided below.

In the case of sliding oscillations of a flat surface or a cylinder the convective acceleration $(v \cdot \nabla)v$ vanishes everywhere. In the case of an arbitrary surface, this no longer holds. In linear problems, non-linear terms are ignored by definition, irrespective of their size. We are entitled to do it, if they are small in relation to the remaining terms in the governing equations.

The convective acceleration $(v \cdot \nabla)v$ is the only non-linear term in N–S equation (2). It is relatively easy to assess its magnitude (Landau & Lifszic, 2009). The operator $(v \cdot \nabla)$ means differentiation along the direction of velocity. In close vicinity of the body the velocity is basically parallel to its surface. Therefore $(v \cdot \nabla)v \sim v^2/l$, where l is a characteristic dimension of the body. In an oscillatory motion the velocity $v \sim \omega A$, where A is the amplitude of oscillations. Hence,

$$(v \cdot \nabla)v \sim (\omega A)^2/l.$$

On the other hand, the following holds for the local acceleration:

$$\partial \mathbf{v}/\partial t \sim \omega v \sim \omega^2 A.$$

Comparing the two expressions, we get $(v \cdot \nabla)v << \partial v/\partial t$, if $A << l$, i.e. if the amplitude of oscillations is small in relation to the size of the body. In addition, it is easy to show that the terms $\partial \mathbf{v}/\partial t$ and $\nu \Delta \mathbf{v}$ are of the same magnitude.

The Reynolds number is normally defined for stationary flows, when a body moves at constant speed. For oscillatory motion this number is defined as $\mathrm{Re} = \omega A l/\nu$. In linear problems amplitudes of motion are assumed to be small, as we say – infinitely small. The Reynolds numbers are, therefore, small by definition, leaving little room for turbulence, if at all.

With the help of the above considerations, some properties of motion can be deduced from the linearised equation (5). The operator of rotation (curl) can be applied to both its sides. As the rotation of the gradient vanishes, and introducing notation $\Omega \equiv \mathrm{rot}v$ for the vorticity, we get:

$$\partial/_{\partial t}\Omega = \nu \Delta \Omega, \tag{37}$$

i.e. Ω fulfils the equation of diffusion (6). It follows from the foregoing that such an equation leads to exponential decay of the quantity described by it, in this case the vorticity. In other words, the motion of the fluid induced by oscillating body is rotational in some layer around the body. Vorticity decays rapidly with a distance from the body, turning at some distance to a potential flow, despite viscosity. The depth of penetration of the vorticity is identical, as for the velocity, equal to $\delta = 1/k = (2\nu/\omega)^{1/2}$.

The quantity δ can be large or small in relation to the body. The case of $\delta \gg l$ occurs, if $\omega l^2 \ll \nu$, i.e. when oscillations are extremely slow, far below the range of interest. In such cases changes of velocity are very slow. The motion of the fluid is therefore quasi-stationary. That is to say, at each time instant fluid motion is the same as for a uniform motion of the body with the speed at given time instant. The boundary layer as such stretches practically over the entire domain.

The opposite case $\delta << l$, i.e. of *thin* boundary layer occurs, when $\omega l^2 >> \nu$. As ν is small, this occurs practically at the entire range of frequency of oscillations ω that are of interest. In seakeeping, it is from the range $\omega \in \langle 0.2, 4\rangle$ rad/s. As the boundary layer is thin the effect of viscosity on the hydrodynamic coefficients is generally minimal.

6. CONCLUSIONS

Based on the results and arguments presented in this work the following conclusions can be drawn:

- it is possible to account for viscosity in the hydrodynamic coefficients (added mass and damping coefficient) but this should not be done by the RANS equations employing turbulence models, as in linear problems there is no room for turbulence
- hydrodynamic coefficients for roll can include the effect of viscosity through the linearised Navier–Stokes equations that do not need any turbulence models. For other degrees of freedom the effect of viscosity is vestigial
- contrary to stationary flows, the boundary layer on oscillating ships is thin; therefore its effect on the hydrodynamic coefficients can only be of secondary meaning
- viscosity opens room for memory effects even in an unbounded domain
- commercial RANS software can be used in seakeeping for solving the Navier–Stokes equations provided no turbulence stresses are assumed
- advanced turbulence models should be based on modelling Reynolds stresses

7. REFERENCES

1. ABRAMOWITZ M., STEGUN J. A. *Handbook of mathematical functions*, Dover Publications, Inc., New York 1970, 9th edition

2. DUDZIAK J. *Teoria okrętu*, Wydawnictwo Morskie, Gdańsk, 1988
3. FALTINSEN O. M. *Sea loads on ships and offshore structures*, Cambridge University Press, 1990
4. IKEDA Y., HIMENO Y., TANAKA N. *A prediction method for ship roll damping*, Dept. of Naval Architecture, University of Osaka Prefecture, Report 00405, 1978
5. LANDAU L., LIFSZIC E. *Hydrodynamika*, Wydawnictwo Naukowe PWN, Warszawa 2009
6. McDONOUGH J. M. *Introductory lectures on turbulence: physics, mathematics and modeling*, Dept. of Mechanical Engineering and Mathematics, University of Kentucky, 2007, http://web.engr.uky.edu/~acfd/lctr-notes634.pdf
7. PAWŁOWSKI M. *Approximation of the non-linear roll damping*, Proc., 11th Intl. Ship Stability Workshop, Wageningen, 2010, 7 pp., http://shipstab.org/index.php/conference-workshop-proceedings
8. QUÉRARD A.B.G., TEMAREL P., TURNOCK S.R. *Hydrodynamics of ship-like sections in heave, sway and roll motions predicted using an unsteady RANS method*, Proc. IMechE, Vol. 223, Part M: J. Engineering for the Maritime Environment, No 2/2009, p.227–238, DOI 10.1243/14750902JEME114
9. SALUI K. B., SARKAR T., VASSALOS D. *An improved method for determining hydrodynamic coefficients in roll motion using CFD techniques*, Ship Technology Research, Vol. 47, 2000, pp. 161–174
10. SALVESEN N., TUCK, E. O., FALTINSEN O.: *Ship motions and sea loads*, Trans. Society of Naval Architects and Marine Engineers, Vol. 78, pp 250–279, Discussion: 279–287 (1970)
11. SPOUGE J. R. *Non-linear analysis of large amplitude rolling experiments*, Intl. Shipbuilding Progress, Vol. 35, No. 403, 1988, pp. 271-320
12. VUGTS J. H *The hydrodynamic coefficients for swaying, heaving and rolling cylinders in a free surface*, Intl. Shipbuilding Progress, No. 167, Vol. 15, 1968, pp. 251–276
13. WEYMOUTH G. D., WILSON R. V., STERN F. *RANS computational fluid dynamics predictions of pitch and heave motions in head seas*, Journal of Ship Research, Vol. 49, No. 2, June 2005, pp. 80–97

A RESEARCH ON TECHNIQUES, MODELS AND METHODS PROPOSED FOR SHIP COLLISION AVOIDANCE PATH PLANNING PROBLEM

(DOI No: 10.3940/rina.ijme.2018.a2.476)

R Fışkın, **H Kişi**, Dokuz Eylül University, Maritime Faculty, Turkey and **E Nasibov**, Dokuz Eylül University, Faculty of Science, Turkey

SUMMARY

The development of soft computing techniques in recent years has encouraged researchers to study on the path planning problem in ship collision avoidance. These techniques have widely been implemented in marine industry and technology-oriented novel solutions have been introduced. Various models, methods and techniques have been proposed to solve the mentioned path planning problem with the aim of preventing reoccurrence of the problem and thus strengthening marine safety as well as providing fuel consumption efficiency. The purpose of this study is to scrutinize the models, methods and technologies proposed to settle the path planning issue in ship collision avoidance. The study also aims to provide certain bibliometric information which develops a literature map of the related field. For this purpose, a thorough literature review has been carried out. The results of the study have pointedly showed that the artificial intelligence methods, fuzzy logic and heuristic algorithms have greatly been used by the researchers who are interested in the related field.

NOMENCLATURE

CPA	Closest Point of Approach
TCPA	Time to Closest Point of Approach
DCPA	Distance to Closest Point of Approach
COLREG	International Regulation for Preventing Collisions at Sea
WoS	Web of Science
ARPA	Automatic Radar Plotting Aid
AIS	Automatic Identification System
OS	Own Ship
TS	Target Ship
f	Frequency
IF	Impact Factor
N/A	Not Available
USV	Unmanned Maritime Surface Vehicle
PC	Computer

1. INTRODUCTION

Over the years, ship navigation has conventionally been carried out thoroughly by human endeavour (Statheros et al., 2008), and it brings some human based errors (Nguyen et al., 2012; Su et al., 2012; Yıldırım et al., 2015; Yıldırım et al., 2017). Nowadays, developing technology has contributed to ship crew for minimizing these errors. These technologies may create some intelligent navigation systems in a close future. These types of systems will provide guidance to navigators and operators in planning optimal collision avoidance route (Statheros et al., 2008). Ships manoeuvres that might lead to substantial risk encounter situation. These matters may be overcome by providing ship handling procedures training. Marine officer's experience relevant with ship handling can play a vital role in safe navigation. On the other hand, they have also some limitations because of economical and human constrains. Besides, well-experienced marine officers might make wrong navigation judgments that can cause collision with human casualties and environmental disasters. For instance, an experienced marine officer can be affected by unexpected inadequacy of ship movement and communication failures under various environmental conditions (Perera et al., 2015). Limiting subjective decision by human in sea navigation and changing them with an intelligent decision-making system can reduce collision at sea (Perera et al., 2011).

Technological developments have led to increase ship traffic that causes navigation to become more difficult for marine officers. Performing navigation at sea is a complicated operation because continually analysing a large amount of data is required and assessing navigational situations improperly can cause to collision situations. In this respect, it is necessary to support marine officers in collision avoidance decision-making process (Lazarowska, 2012). If decision support systems are utilized the decision-making process in an encounter situation, human originated errors, resulting from subjective judgment, can be decreased and sea navigational safety can be improved (Tsou and Hsueh, 2010).

Collision avoidance process is a multi-criteria and non-linear programming problem and there has also to be equilibrium between navigational safety and economy simultaneously (Smierzchalski and Michalewicz, 2000). In other words, the collision avoidance process should not only keep on the danger assessment and action to avoid collision but also take into consideration optimizing the amount of yaw from the original trajectory (Su et al., 2012). In recent years, the optimization methods to solve ship encounter situation and ship collision avoidance planning problem proposed by researchers have increased and the field has become a popular subject. In this respect, the study aims to look over the methods in the literature proposed to solve ship collision avoidance path planning problem.

Review articles recently introduced by Tam et al. (2009) and Statheros et al. (2008) discussed published papers on autonomous ship navigation and encounter situation methods for ship particularly in close range encounters. The main difference of our study from these studies is the idea that our study reviews and discusses the related articles in four subtitles according to their approach types and gives bibliometric information without any time interval constraint.

2. THE PRINCIPLE AND PROCEDURE OF SHIP COLLISION AVOIDANCE

One of the most important safety issue for a vessel at sea is the risk of collision with other ships or objects that endangers sea navigation. The ship crew has the highest priorities to be sure of such a risk to be minimized. The officer on watch is responsible for this task by observing the environment around the vessel and advising the other crew on board (Ward and Leighton, 2010).

The data such as course, speed, ship position, Time to Closest Point of Approach (TCPA), Distance to Closest Point of Approach (DCPA), weather information provided from navigation equipment located on the bridge is crucial for the ship domain calculation and determination of a collision avoidance model. The encounter situation at sea is regulated by the International Regulations for Preventing Collisions at Sea (COLREG) for deciding the state of encounter for the give-way vessel and stand-on vessel. If the vessel is the give-way vessel that should act to avoid collision, recommendation of collision avoidance route by a decision support system is crucial for navigators and operators. This might be changeable due to different task phases, the trajectory solution to avoid collision can be divided into four phases (Tsou and Hsueh, 2010);

a. *Cruising Phase:* In this phase, the system is in alert and search condition continually. The alert range is set throughout collision avoidance considering the current navigation environment and ship safety domain size.
b. *Initial Warning Phase:* The phase consists of two steps as collision avoidance alert encountered by a single target ship and multiple target ships. For former one, if a target ship gets into the observation range, the encounter state and collision risk is determined. If there is a collision risk with target ship (CPA less than the safety domain) and the give-way vessel is an own vessel, route planning to avoid collision will be proceeded. On the other hand, when there are lots of targets in the vicinity, the encounter state and collision risk are determined for each ship. Then, the CPA for each target ship is calculated. If CPA is less than the safety domain, it is assumed to be a risk of collision. The target ship with the smallest TCPA has the highest risk of collision. This target ship is the first ship to be avoided (Davis et al., 1982 as cited in Tsou and Hsueh, 2010).
c. *Collision Avoidance Navigation Phase:* The small alterations of route for collision avoidance trajectory should be avoided, so the target ship is able to perceive the intention of the own ship (COLREG rule 8b). On the other hand, it should not be so large to prevent yawing too much from the original route.
d. *Return to Original Route Phase:* While deciding to return to the original route after collision avoidance is achieved, it needs to be made sure that the return course will not result any other collision risk.

3. METHODOLOGY

The purpose of making a literature review is often to evaluate and to map the existing literature to identify and to highlight the limit and boundaries of related literature (Tranfield et al., 2003). Literature reviews are applied into steps and categories in order to conduct systematic and transparent evaluation as an effective tool. For example, Seuring and Gold (2012) conducted their study in four steps such as material collection, descriptive analysis, category selection and material evaluation. In another study, Davarzani et al. (2016), inspired by Seuring and Gold (2012) and Rowley and Slack (2004), formed their study with the steps of identifying appropriate search terms, evaluating search results and generating bibliometric statistics, network and literature map (Fışkın and Bitiktaş, 2016).

This study basically comprises four steps. In the first step, appropriate search terms were determined, and initial results were evaluated regarding to the subject. In the second step, the proposed approaches were divided into categories according to their types. In the third stage, bibliometric statistics and literature map were presented. Finally, in the last stage, the findings were evaluated and conclusion and discussion about the findings were conducted. This study, covering a period of 41 years from 1976 to 2017, utilized some search engines such as Scopus, Google Scholar, Dokuz Eylül University Library Search Engine, Science Direct, WoS to reach existing studies in related literature. *The searching terms were defined as following: (“ship” OR “maritime” OR “marine” OR “USV” OR “vessel”) AND (“route” OR “trajectory” OR “path” OR “encounter” OR “safe” OR “intelligent”) AND (“collision” OR “avoidance” OR “guidance” OR "decision support" OR "decision making" OR “autonomous” OR “automatic”) AND (“planning” OR “optimal” OR “optimization” OR “optimisation”).* Besides, the reference lists of the accessed studies were examined, and the related studies were also obtained. As a result, a total of 180 published papers about the topic were reached. Master and PhD dissertations, notes, unpublished papers, news, reviews and analysis were excluded from the scope of the study. For this purpose, the following steps were followed to design an effective search process:

- identification and structure of searching terms,
- control of accessed papers regarding the scope of the study,

- selection of appropriate papers.

The selection criteria and evaluation framework applied in the study are given in Figure 1 in detail.

Contribution of each author, institution and country was analysed quantitatively and ranked using the model created by Howard et al. (1987). Single authored papers allocated to the author a single unit of point. In multi-authored papers, point was allocated to the authors proportionally according to equation (1):

$$\text{Score} = \frac{\left(1.5^{n-1}\right)}{\sum_{i=1}^{n} 1.5^{n-1}} \tag{1}$$

where n is the total number of authors and i is the specific author's ordinal position. Therefore, for example, in a co-authored paper 0.60 point was given to the first author; the second author in a three-authored paper was given to 0.32 points and so on. By this model, the accumulated productivity score for each author, institution and country was calculated to reveal the contribution map of the related literature. The model was also recently implemented and used by researchers (such as Tsai and Wen, 2005; Fışkın and Nas, 2013; Yi and Chan, 2014; Greenbaum et al., 2016) in the literature.

4. THE TECHNIQUES, MODELS AND METHODS PROPOSED TO SOLVE SHIP COLLISION AVOIDANCE PATH PLANNING PROBLEM

The accident occurring in marine industry can lead to casualty, enormous entity loss and sea pollution. The related field researches have concentrated on anti-collision systems for maritime navigation especially in the last decade. Such problem has become a popular topic within the field and many methods and models have been proposed by researchers. The problem is the development of the systems that will take efficient action to avoid collision in compliance with the COLREGs. Additionally, development of the systems mimicking the behaviour of experienced navigators that can avoid collision automatically has come in the focus of the recent research. In case of encounter situation at sea, Automatic Radar Plotting Aid (ARPA) located on ships provides assistance to navigator. The aid reports that there is a potential collision risk between the ships (Chen et al., 2010), it cannot, however, propose any optimal manoeuvre to avoid collision. But, it has trail manoeuvre feature to simulate the effect on all tracked targets. The feature has been adopted by IMO in Resolution A.823(19) Performance Standards for Automatic Radar Plotting Aids (SOLAS Reg V/12). According to the resolution, the ARPA should be able to simulate the trajectories of all tracked targets and own ship (IMO, 1995).

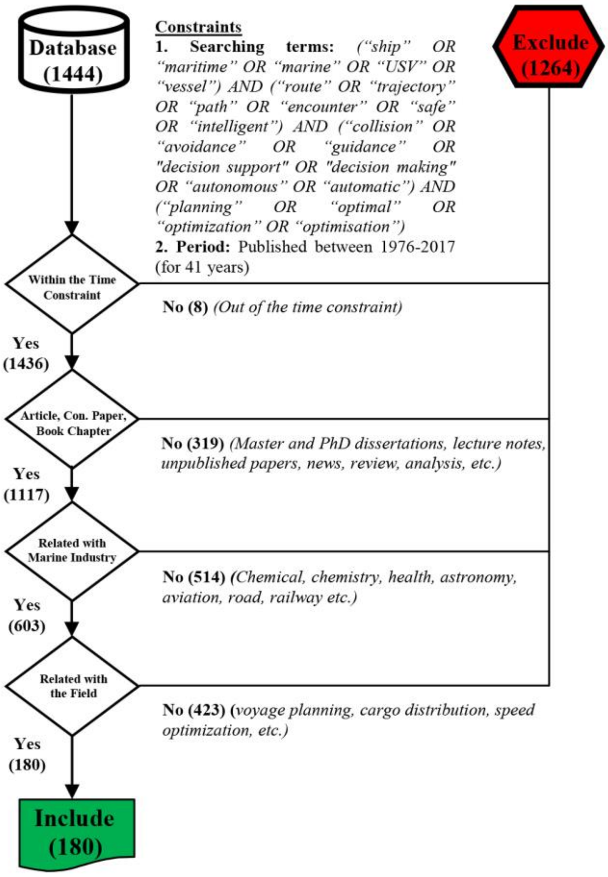

Figure 1. Selection criteria and evaluation framework.

In related literature, there have been many methods, techniques and models proposed to solve ship encounter situation. These approaches can be divided into four main subtitles as *deterministic approaches, artificial intelligence approaches*, *hybrid systems*, and *simulation approaches*.

Deterministic approaches refer to certain mathematical definition of navigation environment. This type of approaches (Tam and Bucknall, 2013; Szlapczynski, 2008; Szlapczynski, 2007; Yavin et al., 1997) utilizes a precise description to solve ship encounter situation problem. These algorithms are important in terms of providing exact and same solutions compared to heuristic algorithms, but the calculation of a solution may take a long time.

Artificial intelligence approaches comprise primarily fuzzy logic (Zadeh, 1965) (Grinyak and Devyatisil'nyi, 2016; Su et al., 2012; Perera et al., 2011; Lee et al., 2015; Perera et al., 2009), stochastic and heuristic approaches (Hao et al., 2007; Tsou et al., 2010; Cheng et al., 2007; Lazarowska, 2015b; Lazarowska, 2014a), and neural networks (Simsir et al., 2014; Lisowski, 2000). These types of algorithms can make complicated problem easier by means of their high computational efficiency and learning capacities. The computational time is shorter than deterministic approaches, but it usually provides a sub-optimal solution rather than an exact solution.

Hybrid systems to solve related problem (Perera et al., 2015; Zhuo and Hearn, 2008; Ying et al., 2007; Mohamed-Seghir, 2012a) propose a combination of the methods mentioned above. Neuro-Fuzzy, Fuzzy-Bayesian and Bayesian-Genetic algorithms are mostly implemented methods to solve the problem.

Simulation based approaches can provide a useful platform for optimal collision avoidance decision making (Liu et al., 2007b). The approaches which are significant in modelling and simulating system are generally based on multi-agent (Liu et al., 2007b; Liu et al., 2006a; Robert et al., 2003; Liu et al., 2008). Other type simulation based approaches (Itoh et al., 2003; Johansen et al., 2016a; Yang et al., 2006; Yang et al., 2007) apart from multi-agent based are also implemented to simulate ship collision avoidance decision-making problem.

Methods, models and techniques proposed to solve related problem according to their approach types are listed in Table 1.

Table 1. Distribution of articles according to the approach type.

Approach Type	Solution Method	Main Topic	References
Artificial Intelligence	Fuzzy Logic	A fuzzy based decision-making system	Grinyak and Devyatisil'nyi, 2016; Su et al., 2012; Perera et al., 2011; Lee et al., 2015; Perera et al., 2009; Kao et al., 2007a; Pietrzykowski and Chomski, 2003; Hwang, 2002; Hwang et al., 2001; Perera et al., 2010b; Hasegawa and Kouzuki, 1987; Kijima and Furukawa, 2002; Hara and Hammer, 1993; Rhee and Lee, 1996; You et al., 2013; Brcko et al., 2013; Pietrzykowski et al., 2010; Kao et al., 2007b; Mohamed-Seghir, 2017; Mohamed-Seghir, 2016
		Ontology-based fuzzy support system	Park et al., 2007
		Structure design for navigation collision avoidance	Liu and Yang, 2004
		Intelligent control system for collision avoidance	Shtay and Gharib, 2009; Feng and Li, 2012
		Fuzzy logic based autonomous collision avoidance	Lee, S. M. et al., 2004; Lee and Kim, 2004; Wen et al., 2016; Mao et al., 2015
	Bacterial Foraging Algorithm	To plan the dynamic collision avoidance process of ships	Hongdan et al., 2015a
		Tool for optimal collision avoidance strategy	Nguyen et al., 2012
		Optimization of ship collision avoidance	Ma and Yang, 2013
	Trajectory Base Algorithm	Trajectory base method for collision avoidance	Lazarowska, 2016
	Linear Extension Algorithm	A distributed anti-collision decision supporting formulation in multi-ship encounter situations	Zhang et al., 2015
	Cat Swarm Biological Algorithm	Heuristic algorithm based collision avoidance action	Wei et al., 2015
	Genetic Algorithm	Multi-objective route optimization for onboard decision support system	Hao et al., 2007; Xu et al., 2014; Vettor and Guedes Soares, 2014
		Heuristic algorithm based safe ship trajectory planning	Tsou et al., 2010; Cheng et al., 2007; Zeng, 2003; Zeng and Ito, 2001; Zeng et al., 2000a; Zeng et al., 2000b; Ito et al., 1999; Cheng and Liu, 2006; Fan et al., 2016; Zeng et al., 2001; Hornauer and Hahn, 2013
	Evolutionary Algorithm	Modelling of ship trajectory in collision situations	Smierzchalski and Michalewicz, 2000; Kolendo and Smierzchalski, 2015; Szlapczynski, 2011; Smierzchalski, 1999; Smierzchalski and Michalewicz, 1998; Smierzchalski, 2003; Kaminski and

			Smierzchalski, 2001; Kuczkowski and Smierzchalski, 2014; Tsou, 2016; Kuczkowski and Smierzchalski, 2017; Szlapczynski and Szlapczynska, 2012; Tam and Bucknall, 2010; Szlapczynski, 2009
	Ant Colony Algorithm	Heuristic algorithm based safe ship trajectory planning	Lazarowska, 2015b; Lazarowska, 2014a; Lazarowska, 2015a; Lazarowska, 2012; Lazarowska, 2015c; Lazarowska, 2015d; Tsou and Hsueh, 2010; He and Qi, 2007; Lazarowska, 2013; Lazarowska, 2014b; Escario et al., 2012
	Wolf Colony Search Algorithm	Heuristic algorithm based ship collision avoidance	Hongdan et al., 2015b
	Danger Immune Algorithm	Intelligent optimization algorithm based collision avoidance strategy	Xu, 2014; Yiming et al., 2012
	Artificial Neural Network	Decision support guidance for strait passing vessels	Simsir et al., 2014; Lisowski, 2000
	Game Control	Game control method in ship collision avoidance	Lisowski, 2012; Olsder and Walter, 1978; Lisowski, 2008; Miloh and Pachter, 1989; Lisowski, 2005; Lisowski, 2001; Lisowski, 2013a; Lisowski, 2013b
		Searching optimal collision avoidance route	Chang et al., 2003
	Modified Gaussian Mixture Model	Intelligent ship bridge collision avoidance	Zhang and Zheng, 2011
		Intelligent decision-making for vessel collision avoidance	Chen et al., 2010
		Ship trajectory control optimization in anti-collision manoeuvring	Zhang et al., 2013
		Automatic trajectory planning and collision avoidance	Xue et al., 2008
	Expert System	Method for personifying intelligent decision making for collision avoidance	Li et al., 2008
		Expert systems approach to collision avoidance	Li et al., 2003; Koyama and Yan, 1987
	Artificial Fish Swarm Algorithm	Decision support for collision avoidance	Ma et al., 2014a; Li and Ma, 2016
	Simulated Annealing Algorithm	Turning angle to avoid collision	Liu et al., 2007a
	Artificial Potential Field	Ship auto collision avoidance system	Zhong et al., 2008; Xue et al, 2012; Zhang and Shi; 2007; Wei and Xue, 2013 ; Wang, T. et al., 2017
	Tabu Search Algorithm	Heuristic algorithm based ship collision avoidance	Kim et al., 2015; Kim et al., 2017
	A* Algorithm	Trajectory planning for collision avoidance	Hornauer et al., 2015; Blaich et al., 2012a; Campbell and Naeem, 2012; Ma et al., 2014b; Naeem et al., 2012; Blaich et al., 2015; Zhang, 2013; Yang et al., 2012
	Lee's Algorithm	Extended grid based collision avoidance	Blaich et al., 2012b
	Differential Evolution	Generating optimal ship collision route	Zhao et al., 2014
	Particle Swarm Optimization	Decision support for encounter situation	Wang, K. et al., 2017; Chen and Huang, 2012
Hybrid Systems	Artificial Neural Network, Fuzzy Logic	Collision avoidance of ship manoeuvres by intelligent guidance	Perera et al., 2015; Zhuo and Hearn, 2008; Zhuo and Tang, 2008
		Expert system for path collision avoidance	Ahn et al., 2012
		The design of a fuzzy-neural	Liu et al., 2006b; Liu and Shi, 2005; Hiraga et al., 1995

		network for ship collision avoidance	
		Autonomous ship collision free trajectory navigation	Hong et al., 1999; Harris et al., 1999
	Fuzzy-Bayesian	Collision avoidance decision action model	Perera et al., 2012; Perera et al., 2010a
	Particle Swarm Optimization, Fuzzy Logic	Intelligent collision avoidance control approach for large ships	Zhuo and Hasegawa, 2014
	Bayesian Genetic Algorithm	Ship route designing for collision avoidance	Ying et al., 2007
	A* Search Algorithm, Fuzzy Logic	Expert system and search algorithm based collision avoidance system	Lee and Rhee, 2001
	Game Theory, Artificial Neural Network	Safe control in collision situation at sea	Lisowski, 2016; Lisowski, 2014; Lisowski, 2010; Lisowski, 2007;
	Particle Swarm Optimization, Bacterial Foraging Algorithm	Dynamic collision avoidance optimization	Hongdan et al., 2014; Liu et al., 2016
	Genetic Algorithm, Fuzzy Logic	Optimal safe ship trajectory in a collision situation	Mohamed-Seghir, 2012a
	Genetic Annealing Algorithm	Ship dynamic collision avoidance space model	Cheng and Liu, 2007
	Immune Particle Swarm Algorithm	Collision avoidance of ship manoeuvres by intelligent guidance	Tian and Pan, 2011
	Branch and Bound Method, Fuzzy Logic, Genetic Algorithm	Safe ship trajectory in fuzzy environment	Mohamed-Seghir, 1995; Mohamed-Seghir, 2014; Mohamed-Seghir, 2012b
	Analytic Hierarchy Process, Artificial Neural Network	Collision avoidance in complex water area	Wang, et al., 2016
Deterministic	Deterministic Solution Model	Cooperative path planning algorithm	Tam and Bucknall, 2013
		Planning collision avoidance manoeuvres for multi target encounter situation	Szlapczynski, 2008; Lazarowska, 2017
		Finding course alteration manoeuvre in a multi-target encounter situation	Szlapczynski, 2007; Johansen et al., 2016b
		Computation of feasible command strategies	Yavin et al., 1997
		Optimal control of a ship for collision avoidance manoeuvres	Miele et al., 1999; Miele and Wang, 2005; Miele and Wang, 2004; Kayano and Imazu, 2009; Wit and Oppe; 1979; Miele and Wang, 2006
		Methods to assign the safe trajectory avoiding collision	Lisowski and Smierzchalski, 1995
		Optimal turn manoeuvres for collision avoidance	Merz and Karmarkar, 1976
		Collision avoidance mechanism of ships at sea	Bi and Liu, 2015
		Modelling collision avoidance decisions support	Wang et al., 2010; Kwik, 1989; Curtis, 1986
		A negotiation framework for automatic collision avoidance	Qinyou et al., 2006

		The timing of collision avoidance manoeuvres	James, 1994
		Collision avoidance algorithm for USV	Oh et al, 2014
		Ship domain based collision avoidance	Chen et al., 2017
		Dynamic support system in close-quarters situation	Wang, X. et al., 2017
Simulation	Multi-Agent Information Fusion Model	Information fusion methods based ship collision avoidance model	Liu et al., 2008
	Multiagent-Based Simulation System	Multiagent-based simulation system for the decision-making	Liu et al., 2007b
		Direct perception interface for ship-ship collision avoidance	Liu et al., 2006a
		Cognitive demands of collision avoidance in simulated ship control	Robert et al., 2003
	Visualization-Based Simulation System	Visualization-based collision avoidance support system	Itoh et al., 2003
	Simulation-Based Model	Collision avoidance using simulation based control behaviour selection	Johansen et al., 2016a
		Analysing and assessment of manoeuvring for avoiding collision	Kumagai et al., 2012; Pedersen et al., 2003
		Finding safe passage for ships in collision situations	Xue et al., 2011
		The AIS assisted collision avoidance	Hsu et al., 2009
		CPA simulation model for automatic collision avoidance	Zhao et al., 1994; Svetak and Jakomin, 2005
		Construction of simulation platform	Yang et al., 2006; Yang et al., 2007
		Knowledge acquisition for collision avoidance	Hammer and Hara, 1990

5. BIBLIOMETRIC STATISTICS

5.1 AUTHORS AND AFFILIATIONS STATISTICS

Countries, authors, and institutions were selected from the data file, appearance frequency of them was recorded and productivity score was calculated using the method described in detail in methodology section. It was found that a total of 293 different authors from 92 different institutions and 24 different countries contributed to the related field. Table 2 shows the top ten most prolific authors, institutions and countries based on the productivity score. *Lisowski, J.* from Poland is the most prolific author with the score of 11.60 within a total of 293 different authors. *Lazarowska, A.* form Poland and *Mohamed-Seghir, M.* from Poland follow *Lisowski, J.* with the score of 10.00 and 6.00, respectively. The affiliations of the authors were selected from data file and statistical analysis was conducted. The city, where the institution is located, was obtained and the geographical location of the institutions contributing to related field was shown using the coordinates of these cities in *gpsvisualizer.com* as shown in Figure 2. The size of the circles represents the contribution level of each institution. It was revealed that the major density of contributing institutions was in North-western Europe and Eastern Asia. The statistics of the contributing countries, as seen in Table 2, shows that the *China* dominates the related research field by holding the highest productivity score which is 52.91. In terms of institutions, however, *Gdynia Maritime University* located in Poland is the most prolific institution with the score of 32.60.

Figure 2. The geographical dispersion of contributing institutions.

Table 2. Top contributing countries, institutions and authors.

Country Contributing Score		**Institution Contributing Score**			**Author Contributing Score**			
Country	**Score**	**Institution**	**Country**	**Score**	**Author**	**Country**	**f**	**Score**
China	52.91	Gdynia Maritime University	Poland	32.60	Lisowski, J.	Poland	12	11.60
Poland	43.00	Wuhan University of Technology	China	9.86	Lazarowska, A.	Poland	10	10.00
Japan	16.61	Dalian Maritime University	China	8.90	Mohamed-Seghir, M.	Poland	6	6.00
Taiwan	10.21	Shanghai Maritime University	China	8.63	Smierzchalski, R.	Poland	9	5.20
UK	11.54	Gdansk University of Technology	Poland	7.60	Szlapczynski, R.	Poland	5	4.60
South Korea	7.00	Technical University of Lisbon	Portugal	7.49	Liu, Y. H.	China	6	3.08
Portugal	7.49	Harbin Engineering University	China	7.07	Zeng, X. M.	Japan	5	3.01
Germany	6.05	Tokyo University of Mercantile Marine	Japan	6.00	Perera, L. P.	Portugal	6	2.73
USA	4.21	National Taiwan Ocean University	Taiwan	5.19	Miele, A.	USA	4	2.22
Netherlands	2.73	Jimei University	China	4.00	Tsou, M. C.	Taiwan	3	2.07
		Rice University	USA	4.00				

5.2 OTHER FUNDAMENTAL STATISTICS

An in-depth analysis was conducted to reveal the most frequent words used in the list of keywords, to determine the solution methods which were implemented to solve the related problem, the type of publication, and the approach type which was basically adopted in the articles. The results of the analysis are shown in Table 3 and Table 4 in detail. As seen in these tables, *Collision Avoidance* was the most frequently used keyword in the articles from a pool of 237 different keywords. Additionally, *Path Planning*, *Ship Collision Avoidance* and *COLREGs* were also commonly used by the authors as keywords in their studies. On the other hand, it was revealed that *Fuzzy Logic* was the most frequently applied solution method, the studies were mostly published in article type, *The Journal of Navigation* was the dominant publication media from a pool of 129 different journals and conference proceedings, and the *Artificial Intelligence* was basically adopted by authors in the studies as an approach type.

The dispersion of publications in each year was shown in Figure 3. Most of the publications were published in the last fifteen years in the 1976 – 2017 periods. Especially, the significant growth was more notable after 1999. Approximately, 80% of the studies were published after that year, but the diagram has showed a rolling graph over the years.

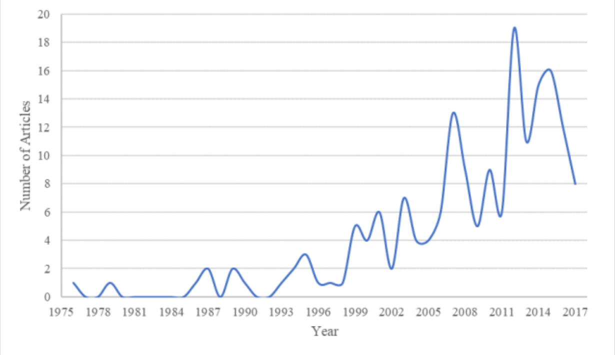

Figure 3. Dispersion of published articles by years.

Table 3. The statistical distribution of solution methods, keywords, publication types.

Solution Method	**f**	**%**	**Keyword**	**f**	**%**	**Publication Type**	**f**	**%**
Fuzzy Logic	45	18.7	Collision Avoidance	58	10.0	Article	94	52.2
Deterministic Solution Model	21	8.7	Path Planning	18	3.1	Conference Paper	78	43.3
Genetic Algorithm	19	7.9	Ship Collision Avoidance	16	2.8	Book Chapter	8	4.5
Artificial Neural Network	16	6.6	COLREGs	12	2.1	Total	180	100
Evolutionary Algorithm	14	5.8	Genetic Algorithm	10	1.7			
Game Theory	12	5.0	Ant Colony Optimization	9	1.6			
Ant Colony Optimization	11	4.6	Decision Support System	9	1.6			
Simulation-Based Model	10	4.1	Safe Ship Control	8	1.4			
Game Control	9	3.7	Evolutionary Algorithm	8	1.4			
A* Algorithm	9	3.7	Fuzzy Logic	7	1.2			
Particle Swarm Algorithm	6	2.5	Ship Navigation	7	1.2			
Bacterial Foraging Algorithm	5	2.1	Simulation	6	1.0			
Expert System	3	1.2	Others	409	71.5			
Others	61	25.3	Total	580	100			
Total	241	100						

Table 4. The statistical distribution of journals/conferences and approach types.

Journal / Conference	**f**	**%**	**Approach Type**	**f**	**%**
The Journal of Navigation (IF: 1,586)	12	6.7	Artificial Intelligence	116	64.4
Ocean Engineering (IF: 1,894)	6	3.3	Hybrid System	26	14.4
TransNav Journal (IF: N/A)	5	2.8	Deterministic	23	12.8
Journal of Optimization Theory and Applications (IF: 1,160)	5	2.8	Simulation	15	8.3
Journal of Marine Science and Technology (IF: 0,838)	5	2.8	Total	180	100
Maritime Research (IF: 0,776)	5	2.8			
International Conference on Machine Learning and Cybernetics	3	1.7			
International Conference on Knowledge Based and Intelligent Information and Engineering Systems Polish	3	1.7			
Navigation of China (IF: N/A)	3	1.7			
Journal of Oceanic Engineering (IF: 2,297)	2	1.1			
Others	131	72.8			
Total	180	100			

6. DISCUSSION

The deterministic approaches have the advantage of providing accurate and optimal results, but, generally, the longer-term solution process, comparing to heuristic algorithms, weakens real-time applicability, which is crucial for collision avoidance problem. The recent study introduced by Lazarowska (2017), however, showed that the deterministic based algorithm could also return more optimal solution in a shorter time than heuristic based method such as Ant Colony Optimization (ACO). When comparing the model with another deterministic model developed by Tam and Bucknall (2013) in terms of computational time, the former one returned the optimal solution in 1.77 second and the latter one returned 7.0 second, respectively, using the same processor PC for the similar scenarios (5 encounter ships cases). On the other hand, ACO and Genetic Algorithm (GA) based heuristic model proposed by Tsou et al. (2010) revealed through the experiments that ACO provided better results than GA. Hongdan et al. (2015a), Hongdan et al. (2015b) and Hongdan et al. (2014) proposed heuristic models based on Quantum Bacterial Foraging Algorithm (QBFA), Adaptive Wolf Colony Search Algorithm (AWSA) and Particle Swarm Optimization (PSO) based BFA to compare to each of them with BFA. The experimental results showed that the all of them outperformed than BFA in respect to both execution time and execution efficiency. The fuzzy logic method also implemented by researchers, especially to create a hybrid solution method by combining with other algorithms. Artificial Neural Network (ANN), GA, PSO, A* Algorithm were algorithms typically used for this purpose. Ahn et al. (2012), for example, proposed the neuro-fuzzy algorithm applied for developing the simply designed fuzzy system to deduce the enviable results, contentedly. The study revealed that the redesigned system was more practical and realistic than ordinary fuzzy inference system. This type of algorithms increased the performance of the execution efficiency.

In conclusion, the artificial intelligence approach has the advantage of real-time applicability due to short-term solution process but provides near optimal results rather than accurate and exact results. An integration of approaches such as fuzzy logic, neural network, GA, etc., which is called hybrid systems approaches, can constitute a ship collision avoidance intelligent system and had an advantage regarding execution efficiency. This type of approach will provide substantial contribution for the collision avoidance problem. The integration of the algortihm to create hybrid model, however, should be done well to get reliable and useful results. Deterministic approaches can provide exact and accurate solution, but execution process may take a long time. Simulation based algorithms can mimic the system to provide information about its behaviour, but detailed simulation structure may be toilsome regarding resources and time.

7. CONCLUSION

Research on ship collision avoidance route planning problem has begun to appear since the 1970s with the introduction of COLREGs. The problem has become a crucial research field with the increasing quantity of published articles, especially since 1999. In this respect, the study contributes to revealing the developments in the field via investigating solution methods and approach types used in the studies as well as providing authors, affiliations, publication types and keywords statistics.

Ship collision avoidance route planning problem stands as a complicated topic and the related literature shows that many methods and models have been proposed to solve this problem. Especially fuzzy logic, heuristic and artificial intelligence optimization methods are used to form a model for the related problem. Deterministic approaches and hybrid systems are also used but not as much as previously mentioned ones. It is revealed that most of the models have considered the COLREGs, while forming the algorithm structure but some others have ignored it. On the other hand, most of the models have used the terminology to define the ship that is operated by avoider and the ship to be avoided as own ship (OS) and target ship (TS), respectively. The geographical dispersion of the institutions shows that the ship collision avoidance and path planning optimization problem have attracted the research institutions from various parts of the world with several contributions especially from academicians and researchers in North-western Europe and Eastern Asia.

In this paper, various techniques, models and methods proposed to solve ship collision avoidance are briefly explained. In conclusion, intelligent collision avoidance systems will undoubtedly be beneficial for safe navigation as well as efficiency of fuel consumption by optimizing the route of ships and they will have a vital role in unmanned and autonomous ships.

8. FINANCIAL SUPPORT

This work was supported by Dokuz Eylül University Scientific Research Coordination Unit. Project Number: 2017.KB.SOS.005.

9. REFERENCES

1. AHN, J. H., RHEE, K. P. and YOU, Y. J. (2012). A Study on the Collision Avoidance of a Ship Using Neural Networks and Fuzzy Logic. *Applied Ocean Research,* 37, 162-173.
2. BI, X. and LIU, X. (2015). Research on Double Collision Avoidance Mechanism of Ships at Sea. *TransNav: International Journal on Marine Navigation and Safety of Sea Transportation,* 9(1), 13-16.

3. BLAICH, M., KÖHLER, S., REUTER, J. and HAHN, A. (2015). Probabilistic Collision Avoidance for Vessels. *IFAC-PapersOnLine*, 48(16), 69-74.
4. BLAICH, M., ROSENFELDER, M., SCHUSTER, M., BITTEL, O. and REUTER, J. (2012a). Fast Grid Based Collision Avoidance for Vessels Using A* Search Algorithm. *In 17th International Conference on Methods and Models in Automation and Robotics*, 385-390
5. BLAICH, M., ROSENFELDER, M., SCHUSTER, M., BITTEL, O. and REUTER, J. (2012b). Extended Grid Based Collision Avoidance Considering COLREGs for Vessels. *9th IFAC Conference on Manoeuvring and Control Marine Craft*, 45(27), 416-421.
6. BRCKO, T., DIMC, F. and SVETAK, J. (2013). On Testing the Fuzzy Logic Approach in Anti-Collision at Sea Decision Making. *GNSS Vulnerabilities and Solutions Conference*, 37-52.
7. CAMPBELL, S. and NAEEM, W. (2012). A Rule-Based Heuristic Method for COLREGs-Compliant Collision Avoidance for an Unmanned Surface Vehicle. *IFAC Proceedings Volumes,* 45(27), 386-391.
8. CHANG, K. Y., JAN, G. E. and PARBERRY, I. (2003). A Method for Searching Optimal Routes with Collision Avoidance on Raster Charts. *The Journal of Navigation*, 56(3), 371-384.
9. CHEN, G., LI, L., YIN, Y. and YANG, S. (2010). Mechanism and Simulation of Personifying Intelligent Decision-making for Vessel Collision Avoidance. *2010 International Conference on Computer Application and System Modelling.*
10. CHEN, L. J. and HUANG, L. W. (2012). Ship Collision Avoidance Path Planning by PSO Based on Maneuvering Equation. *Future Computing, Communication, Control and Management*, 675-682.
11. CHEN, Y., YANG, J., ZHANG, Q., GUO, F. and LIU, Y. (2017). Ship Collision Avoidance on the Basis of 3-d Model. *International Conference on Intelligent Transportation Engineering (ICITE),* (pp. 309-313). IEEE.
12. CHENG, X. D and LIU, Z. Y. (2007). Trajectory Optimization for Ship Navigation Safety Using Genetic Annealing Algorithm. *In Third International Conference on Natural Computation*, 4, 385-392.
13. CHENG, X. D. and LIU, Z. Y. (2006). Study on Ship Collision Avoidance Trajectory Optimization in Inland Waterways with Genetic Algorithm. *Navigation of China*, 67(2), 38-46.
14. CHENG, X. D., LIU, Z. Y. and ZHANG, X. T. (2007). Trajectory Optimization for Ship Collision Avoidance System Using Genetic Algorithm. *IEEE In OCEANS 2006-Asia Pacific*, 1-5.
15. CURTIS, R. G. (1986). A Ship Collision Model for Overtaking. *Journal of the Operational Research Society*, 37(4), 397-406.
16. DAVARZANI, H., FAHIMNIA, B., BELL, M. and SARKIS, J. (2016). Greening Ports and Maritime Logistics: A Review. *Transportation Research Part D: Transport and Environment*, 48, 473-487.
17. DAVIS, P. V., DOVE, M. J. and STOCKEL, C. T. (1982). A Computer Simulation of Multi-Ship Encounters. *The Journal of Navigation*, 35(2), 347-352.
18. ESCARIO, J. B., JIMENEZ, J. F. and GIRON-SIERRA, J. M. (2012). Optimization of Autonomous Ship Maneuvers Applying Ant Colony Optimization Metaheuristic. *Expert System with Applications*, 39, 10120-10139.
19. FAN, Y., SUN, X., WANG, G. and ZHAO, Y. (2016). On evolutionary genetic algorithm in path planning for a USV collision avoidance. *Express Letters*, 10(7), 1691-1696.
20. FENG, M. and LI, Y. (2012). Ship Intelligent Collision Avoidance Based on Maritime Police Warships Simulation System. *In Electrical & Electronics Engineering (EEESYM),* (pp. 293-296). IEEE.
21. FIŞKIN, R. and BITIKTAŞ, F. (2016). A Research on Models Proposed for Quay Crane Scheduling Problem in Container Terminals. *1st International Congress on Ship and Marine Technology.*
22. FIŞKIN, R. and NAS, S. (2013). A Content Analysis of the “International Journal on Marine Navigation and Safety of Sea Transportation” from 2007 to 2012. *TransNav: International Journal on Marine Navigation and Safety of Sea Transportation*, 7(1), 145-149.
23. GREENBAUM, H., MEYER, L., SMITH, M. C., BARBER, A., HENDERSON, H., RIEL, D. and ROBINSON, D. H. (2016). Individual and Institutional Productivity in Educational Psychology Journals from 2009 to 2014. *Educational Psychology Review*, 28(2), 215-223.
24. GRINYAK, V. M. and DEVYATISIL’NYI, A. S. (2016). Fuzzy Collision Avoidance System for Ships. *Journal of Computer and Systems Sciences International*, 55(2), 249–259.
25. HAMMER, A. and HARA, K. (1990). Knowledge Acquisition for Collision Avoidance Maneuver by Ship Handling Simulator, *International Conference on Marine Simulation and Ship Maneuverability*, 245-252.
26. HAO, J. L., ZHAO, L. N., HU, J. F. and YANG, X. B. (2007). Decision-Making Model for Multi-Ship Collision Avoidance Based on Adaptive Genetic Algorithm. *In International Conference on Transportation Engineering*, 606-611.

27. HARA, K. and HAMMER, A. (1993). A Safe Way of Collision Avoidance Maneuver Based on Maneuvering Standard Using Fuzzy Reasoning Model. In International Conference on Marine Simulation and Ship Maneuverability, 1, 163-170.
28. HARRIS, C. J., HONG, X. and WILSON, P. A. (1999). An Intelligent Guidance and Control System for Ship Obstacle Avoidance. *Journal of Systems and Control Engineering*, 213(14), 311-320.
29. HASEGAWA, K. and KOUZUKI, A. (1987). Automatic Collision Avoidance System for Ships Using Fuzzy Control. *Journal of the Kansai Society of Naval Architects*, 205.
30. HE, Z. J. and QI, L. (2007). Research of a Method for AUV to Avoid Collision with Moving Obstacles Based on Ant Colony Algorithm. *Ship Science and Technology*, 6(2007): 86-89.
31. HIRAGA, I., FURUHASHI, T., UCHIKAWA, Y. and NAKAYAMA, S. (1995). An Acquisition of Operator's Rules for Collision Avoidance Using Fuzzy Neural Networks. *IEEE Transactions on Fuzzy Systems*, 3(3), 280-287.
32. HONG, X., HARRIS, C. J. and WILSON, P. A. (1999). Autonomous Ship Collision Free Trajectory Navigation and Control Algorithms. *7th IEEE International Conference on Emerging Technologies and Factory Automation*, 2, 923-929.
33. HONGDAN, L., SHENG, L. and YONG, Z.L. (2015a). Ship Collision Avoidance Path Planning Strategy Based on Quantum Bacterial Foraging Algorithm. *2nd International Conference on Electrical, Computer Engineering and Electronics*, 612-621.
34. HONGDAN, L., SHENG, L. and ZHUO, Y. (2015b). Application of Adaptive Wolf Colony Search Algorithm in Ship Collision Avoidance. *International Journal of Simulation: Systems, Science and Technology*, 16 (2A), 14.1-14.7.
35. HONGDAN, L., SHENG, L., LANYONG, Z. and ZHENGGUO, G. (2014). The Application Research with Particle Swarm Bacterial Foraging Intelligent Algorithm in Ship Collision Avoidance. *International Conference on Mechatronics, Control and Electronic Engineering*, 69-74.
36. HORNAUER, S. and HAHN, A. (2013). Towards Marine Collision Avoidance Based on Automatic Route Exchange. *IFAC Proceedings Volumes*, 46(33), 103-107.
37. HORNAUER, S., HAHN, A., BLAICH, M. and REUTER, J. (2015). Trajectory Planning with Negotiation for Maritime Collision Avoidance. *TransNav: International Journal on Marine Navigation and Safety of Sea Transportation*, 9(3), 335-341.
38. HOWARD, G. S., COLE, D. A. and MAXWELL, S. E. (1987). Research Productivity in Psychology Based on Publication in the Journals of the American Psychological Association. *American Psychologist*, 42(11), 975-986.
39. HSU, H. Z., WITT, N. A., HOOPER, J. B. and MCDERMOTT, A. P. (2009). The AIS-Assisted Collision Avoidance. *The Journal of Navigation*, 62(4), 657-670.
40. HWANG, C. N. (2002). The Integrated Design of Fuzzy Collision-Avoidance and *H*∞-Autopilots on Ships. *The Journal of Navigation*, 55, 117-136.
41. HWANG, C. N., YANG, J. M. and CHIANG, C. Y. (2001). The Design of Fuzzy Collision-Avoidance Expert System Implemented by H∞-Autopilot. *Journal of Marine Science and Technology*, 9(1), 25-37.
42. International Maritime Organization. (1995). Resolution A.823(19) Performance Standards for Automatic Radar Plotting Aids.
43. ITO, M., ZHANG, F. and YOSHIDA, N. (1999). Collision Avoidance Control of Ship with Genetic Algorithm. *Proceedings of the International Conference on Control Applications*, 2, 1791-1796.
44. ITOH, H., NUMANO, M. and PEDERSEN, E. (2003). Modelling and Simulation of Sea Traffic and a Visualization-Based Collision Avoidance Support System. *International Congress on Modelling and Simulation (MODSIM)*, 1996-2001.
45. JAMES, M. K. (1994). The Timing of Collision Avoidance Maneuvers: Descriptive Mathematical Models. *The Journal of Navigation*, 47(2), 259-272.
50. JOHANSEN, T. A., CRISTOFARO, A. and PEREZ, T. (2016b). Ship Collision Avoidance Using Scenario-Based Model Predictive Control. *IFAC-PapersOnLine*, 49(23), 14-21.
51. JOHANSEN, T. A., PEREZ, T. and CRISTOFARO, A. (2016a). Ship Collision Avoidance and COLREGs Compliance Using Simulator-Based Control Behavior Selection with Predictive Hazard Assessment. *IEEE Transactions on Intelligent Transportation Systems*, 17(12), 3407-3422.
52. KAMINSKI, R. and SMIERZCHALSKI, R. (2001). An Evolutionary Method of Ship’s Anti-Collision Trajectory Planning: New Experiments. *WIT Transactions on The Built Environment*, 53, 125-132.
53. KAO, S. L., LEE, K. T., CHANG, K. Y. and KO, M. D. (2007a). A Fuzzy Logic Method for Collision Avoidance in Vessel Traffic Service. *The Journal of Navigation*, 60, 17-31.
54. KAO, S. L., SU, C. M., CHENG, C. Y. and CHANG, K. Y. (2007b). A New Method of Collision Avoidance for Vessel Traffic Service.

In International Conference on Maritime Technology ICMT, 153-159.

55. KAYANO, J. and IMAZU, H. (2009). A Study of a Collision Avoidance Support System. *International Conference on Systems, Man and Cybernetics*. (pp. 244-249). IEEE.
56. KIJIMA, K. and FURUKAWA, Y. (2002). Development of Collision Avoidance Algorithm Using Fuzzy Inference. *Proceeding of Pacific/Asia Offshore Mechanics Symposium*, 123-130.
57. KIM, D., HIRAYAMA, K. and OKIMOTO, M. (2015). Ship Collision Avoidance by Distributed Tabu Search. *TransNav: International Journal on Marine Navigation and Safety of Sea Transportation*, 9(1), 23-29.
58. KIM, D., HIRAYAMA, K. and OKIMOTO, T. (2017). Distributed Stochastic Search Algorithm for Multi-Ship Encounter Situations. *The Journal of Navigation*, 70(4), 699-718.
59. KOLENDO, P and SMIERZCHALSKI, R. (2015). Ship Evolutionary Trajectory Planning Method with Application of Polynomial Interpolation. *Activities in Navigation: Marine Navigation and Safety of Sea Transportation*, 161-166. Netherlands: CRC Press.
60. KOYAMA, T. and YAN, J. (1987). An Expert System Approach to Collision Avoidance. *Proceeding 8th Ship Control Systems Symposium*, 3, 234.
61. KUCZKOWSKI, L. and SMIERZCHALSKI, R. (2014). Comparison of Single and Multi-Population Evolutionary Algorithm for Path Planning in Navigation Situation. *In Solid State Phenomena*, 210, 166-177.
62. KUCZKOWSKI, L. and SMIERZCHALSKI, R. (2017). Path Planning Algorithm for Ship Collisions Avoidance in Environment with Changing Strategy of Dynamic Obstacles. *In Polish Control Conference* (pp. 641-650).
63. KUMAGAI, K., MOCHIDA, T., TANAKA, Y. and KAYANO, J. (2012). Basic Study on Analyzing of Maneuvering for Avoiding Collision in the Congested Sea Area Where Many Ships Are Crossing by Using OZT. *In 2012 Fifth International Conference on Emerging Trends in Engineering and Technology*, 270-275.
64. KWIK, K. H. (1989). Calculation of Ship Collision Avoidance Maneuvers: A Simplified Approach. *Ocean Engineering*, 16(5-6), 475-491.
65. LAZAROWSKA, A. (2012). Decision Support System for Collision Avoidance at Sea. *Polish Maritime Research*, 19, 19-24.
66. LAZAROWSKA, A. (2013). Application of Ant Colony Optimization in Ship's Navigational Decision Support System. *Marine Navigation and Safety of Sea Transportation: Navigational Problems*, 53. Crc Press.
67. LAZAROWSKA, A. (2014a). Ant Colony Optimization Based Navigational Decision Support System. *18th International Conference on Knowledge-Based and Intelligent Information & Engineering System*, 1014-1022.
68. LAZAROWSKA, A (2014b). Safe Ship Control Method with the Use of Ant Colony Optimization. *In Solid State Phenomena*, 210, 234-244. Trans Tech Publications.
69. LAZAROWSKA, A (2015a). Swarm Intelligence Approach to Safe Ship Control. *Polish Maritime Research*, 22(4), 34-40.
70. LAZAROWSKA, A (2015b). Parameters Influence on the Performance of an Ant Algorithm for Safe Ship Trajectory Planning. *IEEE 2nd Cybernetics International Conference*, 140-145.
71. LAZAROWSKA, A. (2015c). Ship's Trajectory Planning for Collision Avoidance at Sea Based on Ant Colony Optimization. *The Journal of Navigation*, 68(2), 291-307.
72. LAZAROWSKA, A. (2015d). Safe Ship Trajectory Planning Based on the Ant Algorithm - the Development of the Method. *Activities in Navigation: Marine Navigation and Safety of Sea Transportation*, 153-160. Netherlands: CRC Press.
73. LAZAROWSKA, A. (2016). A Trajectory Base Method for Ship's Safe Path Planning. *Procedia Computer Science*, 96, 1022-1031.
74. LAZAROWSKA, A. (2017). A New Deterministic Approach in a Decision Support System for Ship's Trajectory Planning. *Expert Systems with Applications*, 71, 469-478.
75. LEE, H. J. and RHEE, K. P. (2001). Development of Collision Avoidance System by Using Expert System and Search Algorithm. *International Shipbuilding Progress*, 48(3), 197-212.
76. LEE, I. L., KIM, S. G. and KIM, Y. G. (2015). Fuzzy Relational Product for Collision Avoidance of Autonomous Ships. *Intelligent Automation and Soft Computing*, 21(1), 21-38.
77. LEE, S. M., KWON, K.Y. and JOH, J. (2004). A Fuzzy Logic for Autonomous Navigation of Marine Vehicle Satisfying COLREG Guidelines. *International Journal of Control, Automation, and Systems*, 2(2), 171-181.
78. LEE, Y. I. and KIM, Y. G. (2004). A Collision Avoidance System for Autonomous Ship Using Fuzzy Relational Products and COLREGs. *In International Conference on Intelligent Data Engineering and Automated Learning*, 247-252. Springer Berlin Heidelberg.
79. LI, L. N., XIONG, Z. N. and REN, Q. S. (2003). Generation and Optimization of Intelligent Decisions for Multi-Ship Collision Avoidance. *Information and Control*, 32(2), 189-192.

80. LI, L., YANG, S., SUO, Y., CHEN, G. and WANG, J. (2008). Automation Method for Personifying Intelligent Decision-Making for Vessel Collision Avoidance. *International Conference on Automation and Logistics,* 1876-1881.
81. LI, W. and MA, W. (2016). Simulation on Vessel Intelligent Collision Avoidance Based on Artificial Fish Swarm Algorithm. *Polish Maritime Research*, 23(s1), 138-143.
82. LISOWSKI, J. (2000). Multistage Ship's Optimal Control in Collision Situations Using a Neural Network. *In II International Conference Safe Navigation Beyond*, 109-119.
83. LISOWSKI, J. (2001). Optimal and Safe Ship Control as a Multi-Step Matrix Game. Systems Science, 27(3), 97-113.
84. LISOWSKI, J. (2005). Dynamic Games Methods in Navigator Decision Support System for Safety Navigation. *In Proceedings of the European Safety and Reliability Conference* (Vol. 2, pp. 1285-1292).
85. LISOWSKI, J. (2007). Intelligent Safe Ship Control Methods in Collision Situations. *In European Control Conference (ECC),* (pp. 2250-2257). IEEE.
86. LISOWSKI, J. (2008). Optimal and Game Ship Control Algorithms for Avoiding Collisions at Sea. *WIT Transactions on Information and Communication Technologies*, 39, 525-534.
87. LISOWSKI, J. (2010). Optimization Decision Support System for Safe Ship Control. *Risk Analysis*, WIT Press, Southampton/Boston, MA, 259-272.
88. LISOWSKI, J. (2012). Game Control Methods in Avoidance of Ships Collisions. *Polish Maritime Research,* 19, 3-10.
89. LISOWSKI, J. (2013a). Sensitivity of Computer Support Game Algorithms of Safe Ship Control. *International Journal of Applied Mathematics and Computer Science*, 23(2), 439-446.
90. LISOWSKI, J. (2013b). Optimal and Game Control Algorithms of a Ship in Collision Situations at Sea. *Control and Cybernetics*, 42(4), 773-792.
91. LISOWSKI, J. (2014). Computational Intelligence Methods of a Safe Ship Control. *Procedia Computer Science*, 35, 634-643.
92. LISOWSKI, J. (2016). Analysis of Methods of Determining the Safe Ship Trajectory. *TransNav: International Journal on Marine Navigation and Safety of Sea Transportation*, 10(2), 223-228.
93. LISOWSKI, J. and SMIERZCHALSKI, R. (1995). Methods to Assign the Safe Maneuver and Trajectory Avoiding Collision at Sea. *WIT Transactions on the Built Environment*, 12: 495-502.
94. LIU, H., DENG, R. and ZHANG, L. (2016). The Application Research for Ship Collision Avoidance with Hybrid Optimization Algorithm. *International Conference on Information and Automation (ICIA),* (pp. 760-767). IEEE.
95. LIU, Q., PEDERSEN, E., OKAZAKI, T., FUKUTO, J. and TANAKA, K. (2006a). Direct Perception Interface for Ship-Ship Collision Avoidance. *International Conference on Systems, Man and Cybernetics*, 808-813.
96. LIU, Y. A., LIU, J., WU, J. and ZOU, X. H. (2007a). Application of Simulated Annealing Algorithm in Turning Angle to Avoid Collision between Ships. *Ship Building of China*, 4, 8.
97. LIU, Y. H. and SHI, C. J. (2005). A Fuzzy-Neural Inference Network for Ship Collision Avoidance. *International Conference on Machine Learning and Cybernetics*, 4754-4759.
98. LIU, Y. H. and YANG, W. L. (2004). The Structure Design of an Intelligent Decision Support System for Navigation Collision Avoidance. *International Conference on Machine Learning and Cybernetics,* 302-307.
99. LIU, Y. H., DU, X. M. and YANG, S. H. (2006b). The Design of a Fuzzy-Neural Network for Ship Collision Avoidance. *Advances in Machine Learning and Cybernetics*. Springer Berlin Heidelberg, 804-812.
100. LIU, Y. H., WANG, S. Z. and DU, X. M. (2008). A Multi-Agent Information Fusion Model for Ship Collision Avoidance. *International Conference on Machine Learning and Cybernetics,* 6-11.
102. LIU, Y. H., YANG, C. and DU, X. M. (2007b). A Multiagent-Based Simulation System for Ship Collision Avoidance. *Advanced Intelligent Computing Theories and Applications,* Springer-Verlag Berlin Heidelberg, 316-326.
103. MA, W. Y. and YANG, J. X. (2013). Optimization of Ship Collision Avoidance Route Based on Bacterial Foraging Algorithm. *Journal of Dalian Maritime University*, 39(2), 21-24.
104. MA, W. Y., WU, Z., YANG, J. and LI, W. (2014a). Decision Support from Artificial Fish Swarm Algorithm for Ship Collision Avoidance Route Planning. *Journal Navigation of China,* 2014(3): 63-67.
105. MA, Y., GAN, L., ZHENG, Y. and ZHANG, J. (2014b). Autonomous Ship Safe Navigation Using Smoothing A* Algorithm. *Open Cybernetics and Systemics Journal*, (8), 72-76.
106. MAO, Y. S., SONG, L. F., XIANG, Z. Q., ZHUO, Y. Q., MAO, P. X. and YAN, Z. (2015). Multi-Obstacle Intelligent Collision Avoidance Strategy for Unmanned Surface Vehicle. *Journal of Dalian Maritime University,* 41(4), 8-13.

107. MERZ, A. W. and KARMARKAR, J. S. (1976). Collision Avoidance Systems and Optimal Turn Maneuvers. *The Journal of Navigation,* 29(2), 160-174.
108 MIELE, A. and WANG, T. (2004). New Approach to the Collision Avoidance Problem for a Ship. *International Game Theory Review*, 6(01), 137-155.
109. MIELE, A. and WANG, T. (2005). Maximin Approach to the Ship Collision Avoidance Problem via Multiple-Subarc Sequential Gradient-Restoration Algorithm. *Journal of Optimization Theory and Applications*, 124(1), 29-53.
110. MIELE, A. and WANG, T. (2006). Optimal Trajectories and Guidance Schemes for Ship Collision Avoidance. *Journal of Optimization Theory and Applications,* 129(1), 1-21.
111. MIELE, A., WANG, T., CHAO, C. S. and DABNEY, J. B. (1999). Optimal Control of a Ship for Collision Avoidance Maneuvers. *Journal of Optimization Theory and Applications*, 103(3), 495-519.
112. MILOH, T. and PACHTER, M. (1989). Ship Collision-Avoidance and Pursuit-Evasion Differential Games with Speed-Loss in a Turn. *Computers & Mathematics with Applications*, 18(1-3), 77-100.
113. MOHAMED-SEGHIR, M. (1995). Application of Fuzzy Set Theory to Determinate Optimal Safety Trajectory of the Ship in a Collision Situation. *Modelling, Measurement and Control D,* 12(1), 49-54.
114. MOHAMED-SEGHIR, M. (2012a). Safe Ship's Control in a Fuzzy Environment Using a Genetic Algorithm. *In Solid State Phenomena*, 180, 70-75. Trans Tech Publications.
115. MOHAMED-SEGHIR, M. (2012b). The Branch-and-Bound Method and Genetic Algorithm in Avoidance of Ships Collisions in Fuzzy Environment. *Polish Maritime Research,* 19(s1), 45-49.
116. MOHAMED-SEGHIR, M. (2014). The Branch-and-Bound Method, Genetic Algorithm, and Dynamic Programming to Determine a Safe Ship Trajectory in Fuzzy Environment. *Procedia Computer Science*, 35, 348-357.
117. MOHAMED-SEGHIR, M. (2016). Computational Intelligence Method for Ship Trajectory Planning International *Conference on Methods and Models in Automation and Robotics* (MMAR), (pp. 636-640). IEEE.
118. MOHAMED-SEGHIR, M. (2017). The Fuzzy Properties of The Ship Control in Collision Situations. *International Conference on Innovations in Intelligent Systems and Applications (INISTA),* (pp. 107-112). IEEE.
119. NAEEM, W., IRWIN, G. W. and YANG, A. (2012). COLREGs-Based Collision Avoidance Strategies for Unmanned Surface Vehicles. *Mechatronics*, 22(6), 669-678.
120. NGUYEN, M. D., NGUYEN, V. T. and TAMARU, H. (2012). Automatic Collision Avoiding Support System for Ships in Congested Waters and at Open Sea. *2012 International Conference on Control, Automation and Information Sciences.*
121. OH, H. N. H., TSOURDOS, A. and SAVVARIS, A. (2014). Development of Collision Avoidance Algorithms for the C-Enduro USV. *IFAC Proceedings Volumes*, 47(3), 12174-12181.
122. OLSDER, G. J. and WALTER, J. L. (1978). A Differential Game Approach to Collision Avoidance of Ships. *In Optimization Techniques Part 1*, 264-271. Springer Berlin Heidelberg.
123. PARK, G. K., BENEDICTOS, J. L. R. M., LEE, C. S. and WANG, M. H. (2007). Ontology-based Fuzzy-CBR Support System for Ship's Collision Avoidance. *International Conference on Machine Learning and Cybernetics*, 1845-1850.
124. PEDERSEN, E., INOUE, K. and TSUGANE, M. (2003). Simulator Studies on a Collision Avoidance Display That Facilitates Efficient and Precise Assessment of Evasive Maneuvers in Congested Waterways. *The Journal of Navigation*, 56(03): 411-427.
125. PERERA, L. P., CARVALHO, J. P. and SOARES, C. G. (2009). Autonomous Guidance and Navigation Based on the COLREGs Rules and Regulations of Collision Avoidance. *Advanced Ship Design for Pollution Prevention*, Taylor & Francis Group, London, 205-216.
126. PERERA, L. P., CARVALHO, J. P. and SOARES, C. G. (2010a). Bayesian Network Based Sequential Collision Avoidance Action Execution for an Ocean Navigational System. 8th IFAC Conference on Control Applications in Marine Systems, 43(20), 266-271.
127. PERERA, L. P., CARVALHO, J. P. and SOARES, C. G. (2010b). Fuzzy-Logic Based Parallel Collisions Avoidance Decision Formulation for an Ocean Navigational System. *In Proceeding of the 8th IFAC Conference on Control Applications in Marine Systems,* 295-300.
128. PERERA, L. P., CARVALHO, J. P. and SOARES, C. G. (2011). Fuzzy Logic Based Decision-Making System for Collision Avoidance of Ocean Navigation Under Critical Collision Conditions. *Journal of Marine Science and Technology,* 16, 84-99.
129. PERERA, L. P., CARVALHO, J. P. and SOARES, C. G. (2012). Intelligent Ocean Navigation and Fuzzy-Bayesian Decision/Action Formulation. *IEEE Journal of Oceanic Engineering,* 37(2), 204-219.

130. PERERA, L. P., FERRARI, V., SANTOS, F. P., HINOSTROZA, M. A. and SOARES, C. G. (2015). Experimental Evaluations on Ship Autonomous Navigation and Collision Avoidance by Intelligent Guidance. *IEEE Journal of Oceanic Engineering,* 40(2), 374-378.
131. PIETRZYKOWSKI, Z. and CHOMSKI, J. (2003). A Navigator Decision Support System in Planning a Safe Trajectory. *4th IAMU General Assembly*.
132. PIETRZYKOWSKI, Z., MAGAJ, J., WOŁEJSZA, P. and CHOMSKI, J. (2010). Fuzzy Logic in the Navigational Decision Support Process Onboard a Sea-Going Vessel. *In International Conference on Artificial Intelligence and Soft Computing*, 185-193.
133. QINYOU, H., QIAOER, H. and CHAOJIAN, S. (2006). A Negotiation Framework for Automatic Collision Avoidance between Vessels. *In 2006 IEEE/WIC/ACM International Conference on Intelligent Agent Technology,* 595-601.
134. RHEE, K. P. and LEE, H. J. (1996). Development of a Collision Avoidance System Considering the Navigation Plan. *In Marine Simulation and Ship Manoeuvrability,* 96, 341-348.
135. ROBERT, G., HOCKEY, J., HEALEY, A., CRAWSHAW, M., WASTELL, D. G. and SAUER, J. (2003). Cognitive Demands of Collision Avoidance in Simulated Ship control. *The Journal of the Human Factors and Ergonomics Society*, 45(2), 252-265.
136. ROWLEY, J. and SLACK, F. (2004). Conducting a Literature Review. *Management Research News*, 27, 31–39.
137. SEURING, S. and GOLD, S. (2012). Conducting Content-Analysis Based Literature Reviews in Supply Chain Management. *Supply Chain Management,* 17, 544–555.
138. SHTAY, A. D. and GHARIB, W. (2009). An Intelligent Control System for Ship Collision Avoidance. *International Journal of Engineering and Technology*, 9(10), 36-41.
140. SIMSIR, U., AMASYALI, M. F., BAL, M., ÇELEBI, U. B. and ERTUĞRUL, S. (2014). Decision Support System for Collision Avoidance of Vessels. *Applied Soft Computing,* 25, 369-378.
141. SMIERZCHALSKI, R. (1999). An Intelligent Method of Ship's Trajectory Planning at Sea. *In Intelligent Transportation System,* 907-912.
142. SMIERZCHALSKI, R. (2003). Evolutionary Algorithm in Problem of Avoidance Collision at Sea. In *Artificial Intelligence and Security in Computing Systems* (pp. 81-90). Springer, Boston, MA.
143. SMIERZCHALSKI, R. and MICHALEWICZ, Z. (1998). Adaptive Modeling of a Ship Trajectory in Collision Situations at Sea. In Proceedings of IEEE World Congress on Computational Intelligence, pp. 342-347.
144. SMIERZCHALSKI, R. and MICHALEWICZ, Z. (2000). Modelling of Ship Trajectory in Collision Situations by an Evolutionary Algorithm. *IEEE Transactions on Evolutionary Computation*, 4(3), 227-241.
145. STATHEROS, T., HOWELLS, G. and MCDONALD-MAIER, K. (2008). Autonomous Ship Collision Avoidance Navigation Concepts, Technologies and Techniques. *The Journal of Navigation*, 61, 129-142.
146. SU, C. M., CHANG, K. Y. and CHENG, C. Y. (2012). Fuzzy Decision on Optimal Collision Avoidance Measures for Ships in Vessel Traffic Service. *Journal of Marine Science and Technology*, 20(1), 38-48.
147. SVETAK, J. and JAKOMIN, L. (2005). Model of Optimal Collision Avoidance Maneuver on the Basis of Electronic Data Collection. *Promet-Traffic & Transportation*, 17(6), 295-302.
148. SZLAPCZYNSKI, R. (2007). Determining the Optimal Course Alteration Maneuver in A Multi-Target Encounter Situation for a Given Ship Domain Model. *Annual of Navigation*, 12, 75-85.
149. SZLAPCZYNSKI, R. (2008). A New Method of Planning Collision Avoidance Maneuvers for Multi-Target Encounter Situations. *The Journal of Navigation,* 61, 307-321.
150. SZLAPCZYNSKI, R. (2009). Evolutionary Sets of Cooperating Trajectories in Multi-Ship Encounter Situations-Use Cases. *International Navigational Symposium on Marine Navigation and Safety of Sea Transportation,* pp. 443-448.
151. SZLAPCZYNSKI, R. (2011). Evolutionary Sets of Safe Ship Trajectories: A New Approach to Collision Avoidance. *The Journal of Navigation*, 64(1), 169-181.
152. SZLAPCZYNSKI, R. and SZLAPCZYNSKA, J. (2012). Customized Crossover in Evolutionary Sets of Safe Ship Trajectories. *International Journal of Applied Mathematics and Computer Science,* 22(4), 999-1009.
153. TAM, C. and BUCKNALL, R. (2010). Path-Planning Algorithm for Ships in Close-Range Encounters. *Journal of Marine Science and Technology*, 15(4), 395-407.
154. TAM, C. K. and BUCKNALL, R. (2013). Cooperative Path Planning Algorithm for Marine Surface Vessels. *Ocean Engineering,* 57, 25-33.
155. TAM, C., BUCKNALL, R. and GREIG, A. (2009). Review of Collision Avoidance and Path Planning Methods for Ships in Close Range Encounters. *The Journal of Navigation*, 62(3), 455-476.
156. TIAN, Y. B. and PAN, P. P. (2011). Application of Improved Immune Particle Swarm Algorithm

in Ship Collision Avoidance. *Navigation of China*, 34(1).

157. TRANFIELD, D., DENYER, D. and SMART, P. (2003). Towards a Methodology for Developing Evidence-Informed Management Knowledge by Means of Systematic Review. *British Journal of Management*, 14, 207–222.

158. TSAI, C. C. and WEN, M. L. (2005). Research and Trends in Science Education from 1998 to 2002: A Content Analysis of Publication in Selected Journals. *International Journal of Science Education*, 27(1): 3-14.

159. TSOU, M. C. (2016). Multi-Target Collision Avoidance Route Planning Under an ECDIS Framework. *Ocean Engineering*, 121, 268-278.

160. TSOU, M. C. and HSUEH, C. K. (2010). The Study of Ship Collision Avoidance Route Planning by Ant Colony Algorithm. *Journal of Marine Science and Technology,* 18(5), 746-756.

161. TSOU, M. C., KAO, S. L. and SU, C. M. (2010). Decision Support from Genetic Algorithms for Ship Collision Avoidance Route Planning and Alerts. *The Journal of Navigation*, 63, 167-182.

162. VETTOR, R. and GUEDES SOARES, C. (2014). Multi-Objective Evolutionary Algorithm in Ship Route Optimization. *Maritime Technology and Engineering,* London, UK: Taylor & Francis Group.

163. WANG, K., YAN, X., YUAN, Y., JIANG, X., LODEWIJKS, G. and NEGENBORN, R. R. (2017). PSO-Based Method for Safe Sailing Route and Efficient Speeds Decision-Support for Sea-Going Ships Encountering Accidents. International Conference on Networking, Sensing and Control (ICNSC), 14th (pp. 413-418). IEEE.

164. WANG, T., YAN, X., WANG, Y. and WU, Q. (2017). A Distributed Model Predictive Control Using Virtual Field Force for Multi-Ship Collision Avoidance Under COLREGs. *International Conference on Transportation Information and Safety (ICTIS),* (pp. 296-305). IEEE.

165. WANG, X., LIU, Z., and CAI, Y. (2017). The Ship Maneuverability Based Collision Avoidance Dynamic Support System in Close-Quarters Situation. *Ocean Engineering,* 146, 486-497.

166. WANG, X. Y., ZHENG, R. J., SIMSIR, U. and XIAO, Y. Y. (2016). An Intelligent Collision Avoidance Algorithm Research. *International Congress on Image and Signal Processing, BioMedical Engineering and Informatics (CISP-BMEI),* (pp. 2000-2004). IEEE.

167. WANG, Y. Y., DEBNATH, A. K. and CHIN, H. C. (2010). Modelling Collision Avoidance Decisions in Navigation. *In Proceedings of 10th Asian Conference on Marine Simulation and Simulator Research.*

168. WARD, N. and LEIGHTON, S. (2010). Collision Avoidance in the e-Navigation Environment. *In Proc. 17th Conf. Int. Assoc. Marine Aids Navig. Lighthouse Authorities* (pp. 4-10).

169. WEI, Y. and XUE, Y. Z. (2013). Simulation Research on Ship Automatic Collision Avoidance. *Journal of Dalian Maritime University*, 39(2), 18-20.

170. WEI, Z., ZHOU, K. and WEI, M. (2015). Decision-Making in Ship Collision Avoidance Based on Cat-Swarm Biological Algorithm. *International Conference on Computational Science and Engineering 2015*.

171. WEN, X., JIANGQIANG, H., JIANCHUAN, Y. and KE, L. (2016). Ship Automatic Collision Avoidance by Altering Course Based on Ship Dynamic Domain. *In Trustcom/BigDataSE/ISPA*, (pp. 2024-2030). IEEE.

172. WIT, C. and OPPE, J. (1979). Optimal Collision Avoidance in Unconfined Waters. *Navigation,* 26(4), 296-303.

173. XU, Q. (2014). Collision Avoidance Strategy Optimization Based on Danger Immune Algorithm. *Computer and Industrial Engineering*, 76, 268-279.

174. XU, Q., ZHANG, C. and WANG, N. (2014). Multiobjective Optimization Based Vessel Collision Avoidance Strategy Optimization. *Mathematical Problems in Engineering*, 2014: 1-9.

175. XUE, Y., CLELLAND, D., LEE, B. S. and HAN, D. (2011). Automatic Simulation of Ship Navigation. *Ocean Engineering*, 38(17), 2290-2305.

176. XUE, Y., LEE, B. S. and HAN, D. (2008). Automatic Collision Avoidance of Ships. *Journal of Engineering for the Maritime Environment,* 223(1), 33-46.

177. XUE, Y. Z., HAN, D. F. and TONG, S. Y. (2012). Automatic Trajectory Planning and Collision Avoidance of Ships in Confined Waterways. *Sustainable Maritime Transportation and Exploitation of Sea Resources*, 167. London: Taylor and Francis.

178. YANG, J. M., TSENG, C. M. and FAN, C. C. (2012). Collision-Free Path Planning for Unmanned Surface Vehicle by Using Advanced A* Algorithm. *Journal of Taiwan Society of Naval Architects and Marine Engineers*, 31(4), 173-184.

179. YANG, S. H., SHI, C. J., LI, L. and GUAN, K. (2006). Construction of Simulation Platform for Vessel Automatic Collision Avoidance with the Technologies of MAS and Navigational Simulator. *Journal of System Simulation*, 18, 686-690.

180. YANG, S., LI, L., SUO, Y. and CHEN, G. (2007). Study on Construction of Simulation Platform for Vessel Automatic Anti-Collision and Its Test Method. *In 2007 IEEE International Conference on Automation and Logistics,* 2414-2419.
181. YAVIN, Y., FRANGOS, C., MILOH, T. and ZILMAN, G. (1997). Collision Avoidance by a Ship with a Moving Obstacle: Computation of Feasible Command Strategies. *Journal of Optimization Theory and Applications,* 93(1), 53-66.
182. YILDIRIM, U., UĞURLU, Ö. and BAŞAR, E. (2015). Human Error in Grounding Accidents: Case Study for Container Ships. *Journal of ETA Maritime Science,* 3(1), 1-10.
183. YILDIRIM, U., UĞURLU, Ö., BAŞAR, E. and YÜKSEKYILDIZ, E. (2017). Human Factor Analysis of Container Vessel's Grounding Accidents. *International Journal of Maritime Engineering,* 159(A1), 89-98.
184. YIMING, B., XINJIE, H. and XIANYAO, M. (2012). Optimization of Strategy for Ship Collision Avoidance with Danger Model Immune Algorithm. *Navigation of China,* 35(2012), 29-32.
185. YI, W. and CHAN, A. P. (2014). Critical Review of Labor Productivity Research in Construction Journals. *Journal of Management in Engineering,* 30(2), 214-225.
186. YING, S., SHI, C. V and YANG, S. (2007). Ship Route Designing for Collision Avoidance Based on Bayesian Genetic Algorithm. *International Conference on Control and Automation,* 1807-1811.
187. YOU, Y., RHEE, K. P. and AHN, K. (2013). A Method of Inferring Collision Ratio Based on Manoeuvrability of Own Ship Under Critical Collision Conditions. *International Journal of Naval Architecture and Ocean Engineering,* 5(2), 188-198.
188. ZADEH, L. A. (1965) Fuzzy Sets. *Information and Control,* 8, 338–353.
189. ZENG, X. (2003). Evaluation of the Safe Path for Ship Navigation. *Applied Artificial Intelligence,* 17(2), 87-104.
190. ZENG, X. M. and ITO, M. (2001). Planning a Collision Avoidance Model for Ship Using Genetic Algorithm. *International Conference on Systems, Man, and Cybernetics,* 4, 2355-2360.
191. ZENG, X. M., ITO, M. and SHIMIZU, E. (2000a). Collision Avoidance of Moving Obstacles for Ship with Genetic Algorithm. *International Workshop on Advanced Motion Control,* 513-518.
192. ZENG, X. M., ITO, M. and SHIMIZU, E. (2000b). Planning and Keeping the Safe Course to Avoid Collision at Sea with Genetic Algorithms. Annual Conference of the Industrial Electronics Society, (Vol. 4, pp. 2388-2393).
193. ZENG, X. M., ITO, M. and SHIMIZU, E. (2001). Building an Automatic Control System of Maneuvering Ship in Collision Situation with Genetic Algorithms. *In Proceedings of American Control Conference,* 4, 2852-2853.
194. ZHANG, J., ZHANG, D., YAN, X., HAUGEN, S. and SOARES, C. G. (2015). A Distributed Anti-Collision Decision Support Formulation in Multi-Ship Encounter Situations under COLREGs. *Ocean Engineering,* 105, 336-348.
195. ZHANG, J.F., YAN, X.P., ZHANG, D. and HAUGEN, S. (2013). Ship Trajectory Control Optimization in Anti-Collision Maneuvering. *TransNav: International Journal on Marine Navigation and Safety of Sea Transportation,* 7(1), 89-93.
196. ZHANG, M. and SHI, C. (2007). Autonomous Collision Avoidance for Ships Using APF method. *In International Conference on Transportation Engineering,* (pp. 2687-2692).
197. ZHANG, W. and ZHENG, Y. (2011). Intelligent Ship-Bridge Collision Avoidance Algorithm Research Based on a Modified Gaussian Mixture Model. *International Conference on Multimedia Technology,* 6414-6419.
198. ZHANG, Y. L. (2013). A Method of Ship's Path Planning at Sea. *In Applied Mechanics and Materials* (Vol. 321, pp. 2038-2041). Trans Tech Publications.
199. ZHAO, J., TAN, M., PRICE, W. G. and WILSON, P. A. (1994). DCPA Simulation Model for Automatic Collision Avoidance Decision Making Systems Using Fuzzy Sets. *In OCEANS'94.'Oceans Engineering for Today's Technology and Tomorrow's Preservation Proceedings,* 2, 244-249.
200. ZHAO, Y. X., LI, W., FENG, S., OCHIENG, W. Y. and SCHUSTER, W. (2014). An Improved Differential Evolution Algorithm for Maritime Collision Avoidance Route Planning. *In Abstract and Applied Analysis (Vol. 2014).* Hindawi Publishing Corporation.
201. ZHONG, B. L., LIU, X. J., WU, J. S., QIU, J. N. and JIANG, H. (2008). Study on Ship Auto-Collision Avoidance System Based on Artificial Potential Field. *Journal of Guangzhou Maritime College,* 1, 004.
202. ZHUO, Y and TANG, T. (2008). An Intelligent Decision Support System to Ship Anti-Collision in Multi-Ship Encounter. *Proceedings of the 7th World Congress on Intelligent Control and Automation,* 1066-1071.
203. ZHUO, Y. and HASEGAWA, K. (2014). Intelligent Collision Avoidance Control for Large Ships. *In Information Science, Electronics and Electrical Engineering*

(ISEEE), 2014 International Conference on, 3, 1887-1891.

204. ZHUO, Y. and HEARN, G. E. (2008). A Ship Based Intelligent Anti-Collision Decision-Making Support System Utilizing Trial Maneuvers. *Chinese Control and Decision Conference*, 3982-3987.

DISCUSSION

VISCOSITY IN SEAKEEPING

M Pawłowski, Gdansk School of Higher Education, Poland

(Vol 160, A2, 2018)

COMMENT

Jacek Pozorski, Institute of Fluid-Flow Machinery, Polish Academy of Sciences

The paper addresses the issue of actuality in ship hydrodynamics: the estimation of ship's linear and angular oscillations with respect to the state of equilibrium. The prediction of seakeeping properties raises a question about a relative importance of viscous and free-surface effects (Quérard et al. 2009), yet this question remains of more general importance in fluid mechanics, since it is related to the dynamic characteristics of objects/bodies immersed in a liquid. From a theoretical standpoint, the problem refers to flows with moving boundaries. It can also be considered in terms of fluid-structure interaction (FSI), however, not necessarily linked with the computation of the body deformation and stresses due to the flow. As the Author correctly notices, the computational solution to this problem in its full setup reveals to be extremely costly due to the 3D and unsteady nature of the fluid motion under turbulent flow conditions at nominally high Reynolds numbers ($Re \sim 10^9$, as stated by the Author in Tab. 1) in presence of the free surface. For this reason, the full solution, or direct numerical simulation (DNS), of the governing Navier-Stokes (N-S) equations at these Re will remain unfeasible in the foreseeable future; see, e.g., Pozorski (2017) for an estimation of the DNS capability in simple wall-bounded turbulent flows. The situation gets even worse in ship hydrodynamics when a DNS of fluid flow would need to be coupled to the dynamics of the rigid body (of complex geometry, usually).

When the statistical approach to turbulent flow computation is adopted in terms of the Reynolds-averaged Navier-Stokes (RANS) closure, the mean hydrodynamic fields of velocity and pressure remain fully three-dimensional and time-dependent. Therefore, even a RANS computation of flow past a 3D hull is still quite costly, see Quérard et al. (2009) and references therein. As pointed out by those Authors, simpler methods based on the so-called strip theory are still of interest. In this theory, the 2D cross-sections (strips) of the hull are considered w.r.t. the ship's longitudinal axis. To describe the dynamics of such a section, the degrees of freedom correspond to rotational oscillations (roll) and to translational ones, both vertical (heave) and horizontal (sway). According to the strip theory, the governing equations to predict the seakeeping response in waves rely on a suitable estimation of the sectional added mass and viscous damping, see Eqs. (16). These two-dimensional hydrodynamic coefficients have often been determined using the assumption of potential flow. Quérard et al. (2009) adopted the RANS approach and a CFD commercial solver to obtain the added mass and damping coefficients in turbulent flow conditions.

Still staying on the grounds of strip theory, the IJME paper by M. Pawłowski discusses an important question about the role of viscosity when it comes to the estimation of the sectional coefficients for the added mass and damping. In the first part of the work, some concepts of turbulent flow modelling are revisited and discussed. For the sake of clarity and correct statement of these concepts, a number of comments to this part are due. First, the N-S equations are formulated for a compressible flow of the Newtonian fluid, with the $\nu\mathrm{grad}(\mathrm{div}\mathbf{V})/3$ term present on the RHS of Eq. (2); there, ν is the kinematic viscosity coefficient. Such a general form is fine, provided that one keeps in mind a natural consequence of the compressibility assumption, which is the variability of the fluid density ρ and the presence of density fluctuations ρ' in turbulent flows. Therefore, a rigorous derivation of the Reynolds-averaged momentum equation will give rise to a number of additional terms involving correlations of $\mathbf{V}'$ and p' with ρ'. Alternatively, the density-weighted (or Favre) averaging is most often applied, leading to a simpler form of the averaged equations. Since the problem considered in the paper basically refers to an incompressible flow, then the simplest way to keep the equations to their intended physical meaning would be to write Eq. (2) without the $\mathrm{grad}(\mathrm{div}\mathbf{V})$ right from the outset term for the sake of consistency. Another point that might come out unclear from the reading of the paper is the notion of linear equations. As far as I understand, the linearity is important when constructing the system of (and fitting the coefficients to) equations of sectional dynamics, Eqs. (16). Yet, the linearised N-S equation as written in the paper, Eq.(5), means that the Stokes flow dynamics is considered and the inertia forces are negligible with respect to the viscous forces. In other words, the viscous time scale L^2/ν is much shorter than the convective time scale L/V_0 and the Reynolds number (which can be expressed as the ratio of the two scales) is very small. Under such conditions, the flow will not become turbulent.

Another point that needs to be clarified here refers to the nature of the turbulent (Reynolds) stress tensor. As the Author recalls, this symmetric, second-rank tensor consists of six independent components and it can be represented by three diagonal elements, see the matrix expressions below Eq. (8), in the coordinate system determined by the eigenvectors of this tensor. Yet, to do so, a general transformation needs to be found at each point of the flow. It is given by the rotation matrix with three independent angles of rotation (the Euler angles).

Consequently, to fully describe the Reynolds stress tensor **R**, six quantities (and not just three) are needed anyway. The Author puts forward an assumption that the Reynolds stress tensor and the mean strain rate tensor **S** are aligned. Rigorously, on the grounds of the Boussinesq hypothesis, which makes the basis of the eddy-viscosity type closures in RANS, such an assumption should hold for the stress anisotropy tensor $\mathbf{a}=\mathbf{R}-(2k/3)\mathbf{I}$. In other words, $\mathbf{a}=-2\nu_t\mathbf{S}$, see for example Pope (2000), where ν_t is the turbulent (eddy) viscosity coefficient. Yet, an important caveat is in order. It is well known that the Boussinesq hypothesis is not true in general, in particular in complex flows, in the separation regions, etc. (BTW: the Prandtl mixing length hypothesis does not hold there, either). So, the assumption about the main axes of **a** and **S** being identical is also flawed for the same reason.

One more remark seems appropriate at this point. The turbulent viscosity ν_t used in RANS may be assessed *a priori* when complete information on the turbulent stresses and the mean velocity gradients is available. This is possible in DNS; a comprehensive study of the turbulent boundary layer (TBL), relevant for the present paper, was performed in a seminal paper by Spalart (1988). Based on this result, the profile of ν_t across the TBL can be determined, see Figure. 7.30 in the monograph by Pope (2000). This corresponds to the Author's intuition, with zero value of turbulent viscosity at the wall, a maximum somewhere in the BL, and then again a zero asymptotic value outside of the layer. Yet, in my opinion the statement about the computation of ν_t proportional to k^2/ε as being "clearly ill conditioned" has to be taken with caution. First, depending on the inflow (or free-stream) levels of the turbulence kinetic energy k and its dissipation rate ε, their values, albeit small, may not be strictly zero outside the TBL; then, ε does not vanish at the wall either. Second, outside the boundary layer, the mean velocity gradients are usually much smaller than the mean shear within the TBL and so will be the stresses **R** computed with the Boussinesq hypothesis. As the last remark to this part, it is appropriate to note that unsteady flows may also be dealt with in the statistical approach, called unsteady RANS (URANS). It reveals to be useful in some situations, in particular when the non-stationarity in the mean flow field is due to a regular, large-scale process, such as (quasi-periodic) vortex shedding in flow past a bluff body, or when an external forcing is present, as in the so-called synthetic jets or in the unsteady TBL around the hull due to incoming surface waves (e.g., in the head sea conditions).

Next, the paper discusses a number of analytical solutions of viscous flow problems, such as the oscillating plane, the oscillating and rotating cylinder, and a general rigid body. Thanks to the assumptions about the flow kinematics, true at small enough Re, these problems become linear and essentially 1D (the relevant spatial coordinate is wall-normal and goes across the BL-type region), allowing for an analytical, time-dependent solution. The respective solutions yield the estimate of the so-called penetration depth δ which is, basically, the viscous length scale. The Author nicely identifies the unsteady boundary layer thickness in the roll motion of the hull with δ to have an estimation of the damping coefficient for individual sections. He estimates the boundary layer thickness in oscillating flows (or forming on oscillating bodies) as considerably smaller than the BL forming on a respective body (on a ship hull) in a steady forward motion. The presented analyses are certainly of relevance for the roll motion. Yet, is it justified to separate the two cases (when the seakeeping features are to be studied at the cruise speed, for instance)? Also, as argued before, the conclusion about the N-S solvers to be used without any turbulent stresses does not seem to be general or well substantiated, at least for sufficiently large Re that may occur in the finite-amplitude oscillations. It seems that the account for the Reynolds stresses will make no harm, as they will appear as negligible in the laminar flow regions, after all. The computational overhead due to the RANS solver (rather than the one for unsteady 3D laminar flow) does not seem to be excessive. Finally, the discussion offered by the Author shows the main mechanisms how the viscosity acts (and where it should be accounted for) while estimating the hydrodynamic coefficients in seekeeping analyses.

AUTHORS' RESPONSE

The Author is grateful to **Professor Jacek Pozorski** for detailed discussion of the paper. It provides a good opportunity for some clarifications and elucidation. The subject of turbulence is not easy, and often misunderstood.

Firstly, it is worth recalling the reasons for turbulence. The sufficient condition for this phenomenon is vorticity, which occurs in the vicinity of the wall, whereas the necessary condition is that flow is fast enough, i.e. the Reynolds number for given problem is higher than the critical one.

Hence, the idea of turbulence does not apply to inviscid flows, as they are irrotational by nature. Fluid particles in such flows perform a translational motion, without rotation. Such flows have a potential ϕ that defines the velocity field $\boldsymbol{v} = \operatorname{grad}\phi$. The potential fulfils the Laplace equation $\Delta\phi = 0$ along with boundary conditions. As this problem is linear, it leaves no room for turbulence. Apart from that, its solutions are unique, which follows directly from the properties of the Neumann problem, well known in theoretical physics, in which the values of the normal derivatives of the potential (normal components of velocity) are specified at the boundaries of the domain. There is no such a theorem for viscous flows. Solutions of the N–S equations can be twofold: laminar or turbulent.

It is worth noting, however that viscous flows can also be potential (irrotational) provided that there are no solid walls, as in the case of surface waves, e.g. ocean waves, or other sources of vorticity, as in the case of baroclinic flows. In other words, no walls, no vorticity in barotropic flows, which means potential flows, free of turbulence, see equation (1) in the paper. In the case of atmospheric winds, turbulence occurs, the so-called free turbulence, when masses of the air have different velocities, rubbing against each other, and/or they are baroclinic. The latter comes from works of Vilhelm Bjerknes (1862–1951), a founder of modern meteorology and weather forecasting.

Hence, turbulence is associated with vorticity. By the way, when Newton established his formulation for the shear stress $\tau = \mu \partial \boldsymbol{v} / \partial y$, he did not realise that flow near the wall was rotational – this notion did not exist that time. Even nowadays, hardly anyone links the slipping of fluid films against each other with vorticity. Everybody links this phenomenon with the shear stress, but not with vorticity.

When the Reynolds number exceeds the critical one, the regular vorticity lines (rings – in flow through a pipeline or horseshoe lines – in flow past a flat plate) are no longer flat. They become irregular in shape, creating 3-D velocity pulsations, in otherwise stationary flow, that are next converted into the additional apparent stress tensor $-\rho\boldsymbol{R}$, see equation (11) in the paper. For this reason, turbulence is always 3-D. In other words, 2-D turbulence does not exist. The link between vorticity and velocity pulsations opens room for theoretical analysis of turbulence.

Going back to the Navier–Stokes equation – equation (2) in the paper – the Laplacian of velocity $\Delta\boldsymbol{v}$ is the source of velocity pulsations $\boldsymbol{v}'$ that are converted to the tensor of Reynolds stresses $-\rho\boldsymbol{R}$ by the non-linear convective acceleration $(\boldsymbol{v}\cdot\nabla)\boldsymbol{v}$. For potential flows the source of velocity pulsations vanishes ($\Delta\boldsymbol{v} \equiv 0$), therefore the convective term $(\boldsymbol{v}\cdot\nabla)\boldsymbol{v}$ has nothing to convert into the turbulent stress tensor ($-\rho\boldsymbol{R} \equiv 0$). Potential flows are therefore never turbulent.

For the sake of generality, equation (2) in the paper is written for a compressible flow. Professor Pozorski is right – in such a case the said equation should by complemented by a number of additional terms, providing correlations between $\boldsymbol{v}'$, p' and ρ'. Bearing in mind that the paper refers basically to incompressible flows ($\mathrm{div}\boldsymbol{v} = 0$), the simplest way to keep the equations to their intended meaning is to neglect all the terms containing $\mathrm{div}\boldsymbol{v}$, as e.g. $\mathrm{grad}\,\mathrm{div}\boldsymbol{v}$.

Another point worth discussing is the notion of linearity of the equations of ship motion in waves. If the said equations are linear, the response of the ship in realistic sea conditions, subjected to irregular waves, can be obtained with the help of superposition and spectral analysis. In particular, equations (16) are linear, if the hydrodynamic coefficients a_{ii}, b_{ii}, c_{ii} (for $i = 3$, 4, and 5) are independent of the amplitude of *forced* oscillations. This is the case, if equations for fluid motion are linear. Though roll is prone to viscosity and non-linear effects, evidence shows (Salvesen *et al.*, 1970) that the prediction of ship motions based on potential flow, with the omission of viscosity, provides satisfactory results.

Professor Pozorski is right saying that the Boussinesq hypothesis does not always hold, in particular in complex flows, in separation regions, for flows over curved surfaces, etc. Notwithstanding the above, the Boussinesq hypothesis is widely applied, without any criticism, as if it were universal. Nonetheless, it is worth knowing that in cases where it does hold, the net Reynolds stress tensor $(-\rho\boldsymbol{R} + p_t\boldsymbol{I})$ and net mean strain rate tensor of deformation $(\boldsymbol{S}_d - \tfrac{1}{3}\boldsymbol{I}\,\mathrm{div}\bar{\boldsymbol{v}})$ are aligned, and related to each other by equation (13) in the paper. The above statement is difficult to find in literature. In such a case, turbulence is entirely described by one quantity – the coefficient of turbulent viscosity ν_t, found with the help of any turbulent model.

It would be a good practice that papers dealing with turbulent boundary layers show the run of turbulent viscosity ν_t across the boundary layer. This quantity should vanish on the wall and on the outer surface of the layer. Regrettably, it is difficult to find information in literature on this topic. Figure 1, taken from the monograph of Pope (2000), one of the few shows how turbulent viscosity ν_t varies across a boundary layer. As can be seen, it does not vanish on the outer edge of the layer, as it should be expected.

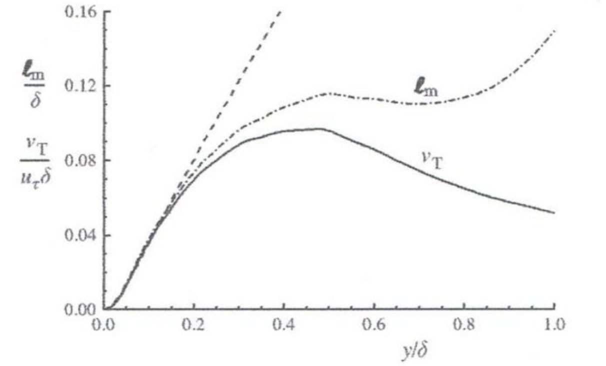

Figure 1. Turbulent viscosity and mixing length across a turbulent boundary layer (Spalart, 1988)

A much better profile of turbulent viscosity across the boundary layer on a flat plate can be found in the paper of Li *at al.* (2016). As seen in Figure 2, taken from this reference, the Reynolds shear stress $<u'v'>$ clearly vanishes at the extremities of the boundary layer. The resulting turbulent viscosity ν_t is shown in Figure 3. It vanishes at the extremities of the boundary layer, reaching a maximum value inside the layer. It is worth noting that this quantity is much larger than the kinematic coefficient of viscosity ν.

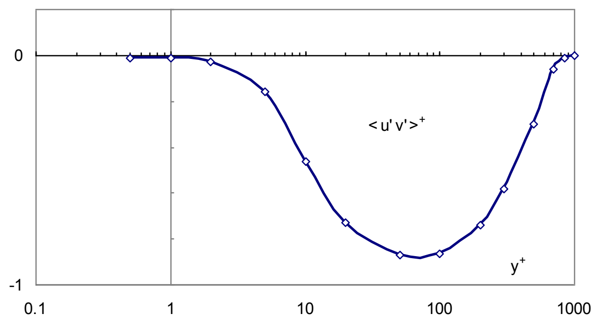

Figure 2. Turbulent shear stress $<u'v'>^+$ versus distance from wall y^+ in flow past a flat plate (Li *at al.*, 2016)

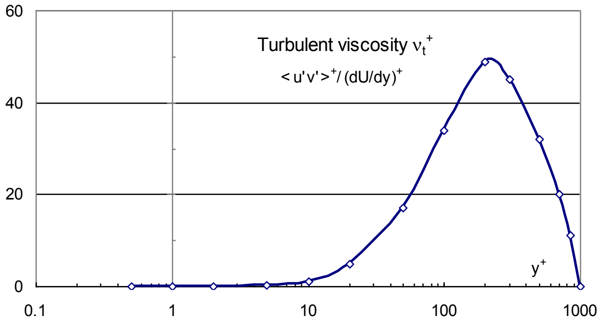

Figure 3. Turbulent viscosity across a turbulent boundary layer on a flat plate (Li *at al.*, 2016)

The Author's paper is mainly concerned with hydrodynamic forces acting on oscillating bodies. There is no problem to calculate them for potential flows. However, many researchers are concerned with the omission of viscosity, which means for them the omission of turbulence. The Author's opinion is that turbulence has little chance to develop on oscillating bodies. One of the symptoms proving this statement is a much thinner boundary layer, by about one order, than for stationary flows. Many researches do apply turbulence models, developed for steady flows, for unsteady flows, which is unreasonable. One could think that a neat remedy in this situation is the application of the unsteady RANS (URANS), but this can be tricky, if the time for averaging is improperly suited to oscillations. As discussed by McDonough (2007), the unsteady RANS methods are problematic.

We have to tell loudly that a good prediction of turbulence is not an easy task. To be not ungrounded, consider a well-known case of flow through a pipeline. In such a case, only one Reynolds stress component $R_{rz} \equiv \tau_t$ has to be estimated with the help of the mixing-length hypothesis:

$$-\rho\langle v_r' v_z'\rangle = \rho l_m^2 (du/dy)^2,$$

where du/dy is the derivative of the smoothed velocity profile with respect to the distance $y = R - r$ from the inner surface of the pipeline. According to Prandtl, the mixing length is given by the equation:

$$l_m/R = 0.14 - 0.08(r/R)^2 - 0.06(r/R)^4,$$

dependent on the relative radius r/R. On the other hand, the turbulent shear stress is given by the equation: $\tau_t = \mu_t(du/dy)$. Equating the two equations for the shear stress yields the equation for the kinematic turbulent viscosity: $\nu_t = l_m^2(du/dy)$. Assuming for the velocity profile $u = u_0 \cdot (y/R)^{1/7}$, the gradient of velocity equals:

$$du/dy = {}^1/_7(u_0/R)(y/R)^{-6/7},$$

where u_0 is the maximum velocity at the axis of a pipeline. A graph of turbulent viscosity ν_t is shown in Figure 4, while for turbulent shear stress – in Figure 5.

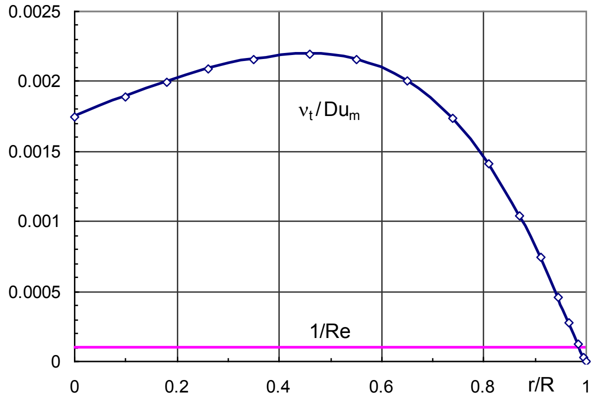

Figure 4. Run of turbulent viscosity ν_t in pipeline

The quantity $\nu_t/u_m D$ in Figure 4 plays the role of the inverse of a turbulent Reynolds number Re_t, where $u_m \equiv \bar{u}$ is the mean velocity of flow, and D is the diameter of a pipe. For instance, for $\mathrm{Re} = 10^4$, $1/\mathrm{Re} = 10^{-4}$, it is easy to deduce from Figure 4 that the turbulent viscosity ν_t is about 20 times larger than the molecular viscosity ν. Regarding the run of the turbulent viscosity ν_t it seems to be faulty, as it should vanish at the axis of a pipeline, for $r = 0$, where the vorticity and gradient of velocity vanish.

Of the key meaning for the analysis of flow in a boundary layer is the knowledge of the shear stress on the wall τ_w. For flow through a pipe this quantity results from the equation: $\Delta p \tfrac{1}{4}\pi D^2 = \pi D l \tau_w$, where $\Delta p = \lambda(l/D)\tfrac{1}{2}\rho\bar{u}^2$ is the drop of pressure along the pipeline of length l, and λ is the friction factor, dependent on the Reynolds number. The equation yields $\tau_w = \tfrac{1}{8}\lambda\rho\bar{u}^2$. Substituting for $\tau_w = \rho u_\tau^2$, where u_τ is the friction velocity, useful in applications, we get $u_\tau = (\tfrac{1}{8}\lambda)^{1/2}\bar{u}$.

The maximum flow velocity $u_{\square}$ is given by the equation: $u_0 = 8.74 u_\tau \mathrm{Re}_\tau^{1/7}$, where $\mathrm{Re}_\tau = u_\tau R/\nu = \tfrac{1}{4}(\tfrac{1}{2}\lambda)^{1/2}\mathrm{Re}$, and $\mathrm{Re} = \bar{u}D/\nu$ is the Reynolds number. Substituting for u_τ, the following is obtained: $u_0 = \bar{u}\,8.74(\tfrac{1}{2})^{13/7}\lambda^{4/7}\mathrm{Re}^{1/7}$. Substituting now the Blasius formulation for the friction factor $\lambda = 0.3164/\mathrm{Re}^{1/4}$, we get eventually that $u_0 = 1.25\bar{u}$, independent of the Reynolds number.

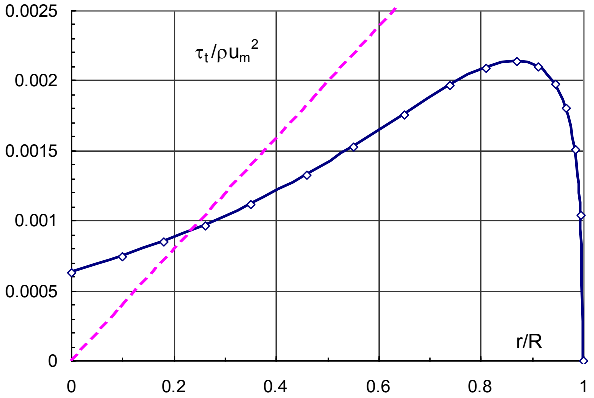

Figure 5. Turbulent sheer stress τ_t in pipeline – solid line, dashed line – total

Now, the nondimensional shear stress on the wall equals: $\tau_w/\rho u_0^2 = ⅛\lambda(\bar{u}/u_0)^2 = 0.08\lambda$, or $\tau_w/\rho\bar{u}^2 = 0.125\lambda$. Inside the pipe, the shear stress varies linearly: $\tau = \tau_w r/R$, as seen in Figure 5 (dashed line for Re = 10^4, with $\tau_w/\rho\bar{u}^2$ = 0.00396). The shear stress τ varies linearly inside a pipeline both in laminar and turbulent flows.

As can be seen in Figure 5, there is amazingly large discrepancy between the real and calculated values of turbulent shear stresses inside the pipeline. The former is dependent on the Reynolds number, while the latter – not. Such a situation indicates a conceptual error. The mixing length l_m should depend simply on the Reynolds number for any viscous flow, not only for flow through a pipe.

Regarding the application of CFD, it is equally well applicable to laminar and turbulent flows. Calculations for turbulent flows are, however, much more complex and time consuming, as there is need to solve more differential equations, needed for definition of the tensor of Reynolds stresses.

Figure 1 in the paper shows a comparison between experimental results of the hydrodynamic coefficients for roll with inviscid (potential) theory. The differences are modest even for extreme cases, such as a rectangular section. If we apply the N–S equations or RANS equations the improvement can be limited by the nature of things. The problem is that nearly everybody applies RANS equations instead of the N–S ones, because of the widely available commercial codes. Meanwhile, results obtained by the RANS equations are not sensational and dubious, which can be seen in literature, e.g. in the two references: Quérard *et al.* (2009) and Salui *et al.* (2000), cited in the paper. It should be obvious that applying steady turbulent models to unsteady cases cannot guarantee reliable results. But even if we apply the same turbulent models to the same case of steady flow as other researches it does not guarantee that we get similar results. As shown by McDonough (2007) (page 93, Figure 2.3), results obtained from various commercial flow codes are amazingly different. For potential flows such a situation is impossible – results obtained from different sources are practically the same.

The three analytical solutions for oscillating bodies, discussed in the paper, could be used as reference for validation of the commercial codes, assuming no Reynolds stresses.

The main purpose of the paper is to show that in the case of oscillating bodies resorting to turbulent models is unnecessary and conceptually wrong, due to the thin boundary layer and the lack of well developed turbulent models for unsteady flows. To some extent the situation resembles the flow around a wing –aerodynamic forces are found without resorting to turbulence. Note that in section 5.4 reference is made to Landau (2009), a Nobel Prize winner in physics for 1962.

REFERENCES

14. POPE S.B. *Turbulent Flows*, Cambridge University Press, 2000
15. POZORSKI J.: *Models of turbulent flows and particle dynamics*. In: (Minier J.P., Pozorski J., Eds.) Particles in Wall-Bounded Turbulent Flows, pp. 97-150. Springer, 2017
16. SPALART P.R. *Direct simulation of a turbulent boundary layer up to R_\theta=1410*, Journal of Fluid Mechanics, Vol. 187, 1988, pp. 61-98
17. LI D., LUO K., FAN J. *Direct numerical simulation of heat transfer in a spatially developing turbulent boundary layer*, Physics of Fluids 28, 105104 (2016); DOI: 10.1063/1.4964686

The Transactions of The Royal Institution of Naval Architects – Part A

International Journal of Maritime Engineering

GUIDANCE NOTES FOR AUTHORS

All papers, technical notes and discussions should be submitted in electronic form, normally in MSWord format. Authors wishing to submit in other formats should first contact RINA Headquarters. Submissions should be forwarded on PC compatible disks or CD-ROM, containing the full text, including inserted figures. Submissions less than 5Mb may be forwarded by email or online.

Authors are responsible for obtaining security clearance as required. If they so wish, authors may add a disclaimer stating that the opinions expressed are solely those of the author.

In submitting papers or technical notes for publication, authors implicitly assign copyright to the Royal Institution of Naval Architects if the paper or technical note is published. Where copyright is held elsewhere, authors must present evidence of approval to re-publish.

When submitting contributions for publication, authors must state if the paper or technical note has been published before and where, or whether it is being considered for publication by some other publisher

Papers: Papers should not normally exceed 6000 words (with up to 10 illustrations). Longer papers where the content justifies the extra length may be published at the Editor's discretion. The required format of papers submitted for publication may be obtained from the RINA website or from RINA Headquarters

Technical Notes: Technical notes should not normally exceed 1500 words (and up to 5 illustrations). The required format of technical notes submitted for publication may be obtained from the RINA website or from RINA Headquarters

Discussion: Discussion of published papers, or comment on published discussion, should not normally exceed 500 words (with up to 2 illustrations).

All submissions for publication should be forwarded to:

The Editor (IJME)
The Royal Institution of Naval Architects
8-9 Northumberland Street
London WC2N 5DA, UK
Tel: +44 (0)20 7235 4622 Fax: +44 (0)20 7259 5912
Email: ijme@rina.org.uk Online: www.rina.org.uk

THE ROYAL INSTITUTION OF NAVAL ARCHITECTS

The Royal Institution of Naval Architects is an internationally renowned professional institution and learned society, whose members are involved at all levels in the design, construction and repair of ships, boats and maritime structures, in over 80 countries. RINA is widely represented in the marine industry, universities and colleges, and maritime organisations worldwide.

Membership is open to those who are professionally qualified in naval architecture or a related subject, or who are involved or interested in the maritime industry. RINA members enjoy a wide range of benefits and services, including advice on education, training and professional development. The RINA also publishes a range of technical journals, books and papers, and organises an extensive programme of international conferences and training courses covering all aspects of naval architecture and maritime technology, available to members free or at reduced rates

The Transactions of The Royal Institution of Naval Architects

Vol 160 Part A2 2018 ISSN 1471-8751

International Journal of Maritime Engineering

CONTENTS

PAPERS

TECHNICAL NOTES

There are no Technical Notes published in this issue of IJME

DISCUSSION